Fluctuations collectives dans les systèmes de fermions fortement corrélés

Erik Linnér

INSTITUT POLYTECHNIQUE DE PARIS

NNT : 2023IPPAX090

Thèse de doctorat

Interplay of collective fluctuations in strongly correlated fermionic systems

Thèse de doctorat de l'Institut Polytechnique de Paris
préparée à l'École polytechnique

École doctorale n°626 de l'Institute Polytechnique de Paris (EDIPP)
Spécialité de doctorat : Physique

Thèse présentée et soutenue à Palaiseau, le 5 octobre, par

ERIK LINNÉR

Benoît Douçot Directeur de recherche, Sorbonne Université (Laboratoire de Physique Théorique et Hautes Energies)	Président
Massimo Capone Professeur, International School for Advanced Studies (SISSA)	Rapporteur
Marcello Civelli Maître de Conférences, Université Paris-Saclay (Laboratoire de Phyique des Solides)	Rapporteur
Yvan Sidis Directeur de recherche, Université Paris-Saclay, CEA (Laboratoire Léon Brillouin)	Examinateur
Silke Biermann Professeure, École Polytechnique (Centre de Physique Théorique)	Directrice de thèse
Evgeny Stepanov Chargé de recherche, École Polytechnique (Centre de Physique Théorique)	Invité

Interplay of collective fluctuations in strongly correlated fermionic systems

by

Erik Linnér

Thèse de doctorat de l'Institut Polytechnique de Paris
préparée au Centre de Physique Théorique
à
L'ÉCOLE POLYTECHNIQUE

Acknowledgements

I wish to express my deepest gratitude to my supervisor Silke; through more than four years in Paris, I have had the pleasure to be first tutored as a Master's student and then supervised as a doctorate student by you with incredible kindness and scientific expertise. As a period full of life-changing experiences is coming to an end, and as a new one is about to begin, I am sincerely happy that you have been the one to build a researcher out of me. Alike, I wish to extend my deepest gratitude to my close collaborator Zhenya; you have been more than essential in the completion of my doctorate. Through fruitful scientific discussions about everything between Heaven and Earth (which was surprisingly initialized by attending one of your group presentations) you have had an important role in the process of shaping me as a researcher. Within my doctorate studies, furthermore, I had the great pleasure of collaborating with Alexander Lichtenstein and Clément Dutreix. I am eternally grateful to Alexander Lichtenstein for his invitation to visit Hamburg within our collaboration, allowing for my first scientific visit after a world changed by a collection of little viruses. I want to warmly thank both Alexander Lichtenstein and Clément Dutreix for their hospitality, which I have had the pleasure to experience in both the old and new world.

I would like to express my appreciation for all the members of my committee. To the president of the committee, Benoît Douçot, I wish to thank you for perfectly orchestrating the soutenance de thèse. To the reviewers of the committee, Marcello Civelli and Massimo Capone, I wish to thank you both for accepting to read the manuscript. I am honored you read the manuscript so attentively, as displayed by the long-lasting question session filled with a large number of thought-provoking questions. To the examinator of the committee, Yvan Sidis, I wish to thank you for connecting the work to reality with your sharp questions from both your experimental and theoretical expertise.

Within my time in the Condensed Matter group of the CPHT laboratory, I have felt very warmly at home due to friendly corridor talks, scientific/non-scientific discussions over coffee/tea, and the overlong lunch breaks. I wish to thank all current and former members (in no particular order) of the Condensed Matter group which have in one way or another contributed to my wonderful doctorate experience: O. Dmytruk, M. Ferrero, A. Georges, K. Le Hur, L. Poyurovskiy, M.-O. Renou, L. Sanchez-Palencia, A. Subedi, F. Vicentini, *S. Backes*, M. Chatzieleftheriou, D. Mosca, V. Harkov, D. Johnstone, *A. Galler*, *A. Gómez Pueyo*, *B. Lenz*, *J.-H. Sim*, S. Al Saati, F. del Pozo, F. Fossati, A. Mukherjee, L. Rampon, J. Xiong, Z. Zhu, *E. Bernhardt*, *P. Besserve*, *R. Garioud*, *B. Bacq-Labreuil*, *J. Schneider*, *J. Boust*, *M. Turtulici*, F. Miljevic, X. Zhou, *P. Forni* and *M. Korolev*. In particular, I wish to thank Vitja and Mary for plenty of indispensable comments on the earlier drafts of this thesis. From scientific seminars, lectures and discussions to dinner parties and healthy excursions, I wish to thank everyone for, in their own way, positively contributing to my experience in Paris.

Outside the Condensed Matter group of the CPHT laboratory, there are plenty of people at École Polytechnique which I wish to thank. One of the rare aspects of the CPHT laboratory is the closeness between a selection of different theoretical topics: condensed matter physics, mathematical physics, particle physics, string theory and plasma physics. It has been a blessing to be able to discuss with researchers of such a mixture of theoretical fields, allowing one to be curious about topics outside my own field of expertise. Tout d'abord, je tiens à remercier le directeur du laboratoire J.-R. Chazottes et les deux sections les plus importantes du laboratoire: j'aimerais remercier chaleureusement Florence, Fadila et Malika à l'administration, Yannick, Vazoumana, Danh, Ilandirayane et tous les autres membres de l'équipe informatique. Grâce au soutien essentiel de Malika, nous avons été en mesure d'organiser des séminaires au laboratoire pour les jeunes chercheurs. Je suis très reconnaissant de la suggestion de J.-R. Chazottes et *B. Bacq-Labreuil* d'organiser les séminaires, et de l'aide de *D. van Egmond* lorsque j'ai été malade du Covid-19. Je suis très heureux d'avoir pu léguer avec succès l'organisation des séminaires à M. Vilatte et A. Loty. Returning to English, my doctorate experience has been positively influenced by many other current and former members of the CPHT laboratory. I wish to thank (in no particular order) A. Couairon, T. Nicolas, M. Petropoulos, G. Bossard, E. Dudas, B. Goutéraux, U. Reinosa, R. Boussarie, C. Lorcé, C. Marquet, C. Kopper, B. van Rees, D. Ramirez, M. Sanchez Garitaonandia, A. Shukla, C. Andres Casas, *J. Holguin*, *D. van Egmond*, A. Hebbar, M. Reehorst, *M. Rekhis*, M. Beauvillain, M. Vilatte, A. Loty, G. Casagrande, Y. Pano, D. Rivera Betancour, *F. Sottovia*, *W. Focillon*, D. Bansard-Tresse, P. Wang and *M. Borji*. It is impossible to thank everyone individual for how enjoyable they have made working at CPHT, and living in Île-de-France in general. From the friendly laboratory of CMLS, I wish to warmly thank *S. Sadeghi Arjmand*. Outside the world of research, within my doctorate studies, I was lucky to teach tutorials under J. Faure from the laboratory of LOA and A. Couairon from the laboratory of CPHT. I wish to warmly thank both of them for their wonderful support, in addition to the indispensable support from Alice, Nadège and everyone else at the academic office of the Bachelor program. Enfin, je tiens à remercier la présidente du département de physique S. Biermann, ainsi que Nouria, Patricia et tous les autres membres de l'administration du département de physique pour tout leur soutien et pour avoir permis à toute cette machine académique compliquée de fonctionner.

Extending our praise from École Polytechnique to the whole Saclay plateau, I have very much appreciated the kind people over at LPS in Orsay and their wonderful seminar series for condensed matter physics, with special thanks to A. Mesaros, P. Simon, M. Civelli and M. Uldemolins, and the friendly people at CEA, in particular Y. Sidis and *P. André*. Leaving"Province" and turning towards Paris, I wish to give special thanks to L. de Medici, Z. Zeravcic, *M. Muñoz Basagoiti* and *M. Crispino* within ESPCI, B. Douçot, M. Saitta, M. Casula, B. Lenz, *A. Rotaru*, A. Keliri, A. Ritz-Zwilling and M. Peria within Sorbonne Université, L. Fratino within CY Cergy Paris Université, and S. Mougiakakos within Université Paris Cité, and to express my appreciation to everyone at the condensed matter team within Collège de France for their hospitality. Outside France, I am grateful to A.I. Lichtenstein, M. Eckstein, A. Galler, *V. Harkov*, *M. Vandelli*, F. Valiera and others in Hamburg, and A. Rubtsov and Y. Lyakhova in Moscow. I wish to finally express my deepest gratitude to my previous supervisor Ferdi in Lund. Without your enormous support, there would not have been any four-year journey to Paris.

I want to really thank my friends Paul, Robin and Maitane, who have been close friends for many years, and who were important companions on this academic ("coming-of-age") journey in Paris. This journey in Paris has been associated with meeting many new friends, especially through the ICFP program and Cité Universitaire. I have found many wonderful friends which due to the Covid-19 pandemic already feel like life-long friendships. To my cultured friends Andriani, Anna and Matteo, thank you for all the cultured experiences we have planned throughout all the seasons of all the years. In addition, I wish to thank Andriani and Anna for their valuable comments on earlier drafts of the thesis. Without vital proofreading by Anna for the sections using "la langue de Molière", one and a half years of French classes would arrive to an embarrassing conclusion. To my competitive friends Mateo, Arfor and Louis, thank you for all the dinners together, the competitive game sessions and for all the simple pleasant moments together. To my Garrician friends Manu, Sol, Johanna and Giulia, thank you for all the cozy days in Garric, all the unforgettable moments and all the mate drinking. To my hard-working friends Diana, and Regina, I wish to thank you both for plenty of cozy library study sessions and for everything else as well. To my friends Mirjana, Lucia and many more from Maison de l'Italie, I want to thank you for the film sessions, the yoga sessions, the dinners, and the incredible warmness and support between everyone in the first lockdown. There are so many more I wish to thank from Cité Universitaire that the acknowledgement would look like the author list of a paper by the ATLAS collaboration. See you all somewhere on this tiny little globe.

On a final note, I wish to thank all my friends in Sweden and around the world for their support. Even though we have been separated by a spatial and temporal distance, I am happy to have kept such a natural and close relationships with my friends back home in Sweden. Slutligen vill jag tacka hela min släkt i Sverige, speciellt min pappa Mats; sekä kiittää koko sukuani Suomessa, erityisesti äitiäni Pirjoa.

Tack pappa ja kiitos äiti!

Résumé

Les systèmes fortement corrélés présentent souvent des diagrammes de phase riches avec différentes phases ordonnées impliquant des degrés de liberté de spin, de charge, d'appariement ou d'orbite. La description théorique de la compétition entre les différentes instabilités dans les systèmes fortement corrélés, qui donne lieu à cette phénoménologie, reste l'un des Saint-Graal de la théorie moderne de la matière condensée. Elle pose un énorme défi de complexité à la fois conceptuelle et informatique, et l'interaction des fluctuations électroniques concurrentes constitue donc un obstacle à la compréhension des diagrammes de phase complexes d'une large gamme de matériaux quantiques corrélés. Cela motive la recherche de méthodes simplifiées pour étudier l'interaction des fluctuations collectives.

Nous présentons une extension multicanal de l'approche du champ fluctuant récemment développée pour les fluctuations collectives concurrentes dans les systèmes électroniques corrélés. La méthode est basée sur une optimisation variationnelle d'une action d'essai qui contient explicitement les paramètres d'ordre des principaux canaux de fluctuation. Elle donne un accès direct à l'énergie libre du système, facilitant la distinction entre les phases stables et métastables du système. Nous appliquons notre approche au modèle de Hubbard étendu, un modèle de réseau fermionique paradigmatique, qui occupe une place de choix dans la théorie de la matière condensée en raison de la pertinence potentielle de ses versions répulsives et attractives pour les matériaux électroniques et les systèmes artificiels. En utilisant notre technique pour étudier le régime de couplage faible à intermédiaire de l'interaction répulsive, nous constatons qu'elle capture l'interaction de compétition entre la fonction l'onde de densité de charge en compétition et des fluctuations antiferromagnétiques en accord qualitatif avec des méthodes plus coûteuses en termes de calcul. En outre, cette méthode permet d'accéder aux propriétés de l'état excité par le biais du spectre d'excitation d'une particule, et aux effets de corrélation à plusieurs corps, par le biais de l'auto-énergie, directement sur l'axe des fréquences réelles sans utiliser de techniques de continuation analytique numérique. L'approche du champ fluctuant multicanal offre donc une voie prometteuse pour un traitement numériquement peu coûteux de l'interaction entre les fluctuations collectives dans les systèmes de petite et grande taille.

En utilisant l'approche introduite du champ fluctuant multicanal, nous explorons le diagramme de phase du modèle de Hubbard étendu dans les régimes répulsif et attractif, en abordant l'interaction des fluctuations dans les canaux antiferromagnétiques, de l'onde de densité de charge, de l'onde s supraconductrice et de la séparation de phase. Bien que ce modèle ait été étudié de manière intensive depuis des décennies, notre nouvelle approche nous permet d'identifier une nouvelle phase caractérisée par la coexistence de fluctuations collectives de l'onde s supraconductrice et de la séparation de phase. Ces résultats sont en accord avec les observations précédentes de phases supraconductrices et de séparation de phases dans les systèmes électroniques, notamment

dans les supraconducteurs à haute température. En outre, la méthode des champs fluctuants multicanaux permet de mettre en évidence la quintessence du modèle de Hubbard étendu grâce à la grande variété de types de compétitions qui émergent de l'interaction des différentes instabilités. La nature générale de la théorie proposée, qui permet d'incorporer une grande variété de modes collectifs, en fait un outil prometteur pour l'étude de l'interaction des fluctuations collectives dans les systèmes fermioniques fortement corrélés.

Contents

Chapter 1

Introduction

"... in science, we often have predecessors much further back in time than we think a priori." - L. Néel [1]

Significant changes in civilisation have been accomplished through the discovery of materials and their application in the development of tools. While the stone age was defined by wide usage of stone tools, the advancement of metallurgy in the bronze and iron ages allowed for the development of intricate tools based on copper alloys and carbon steel, respectively. An aspect such materials have in common are their *functionality* leading to them display a wide range of different applications. The importance of *functional materials* is truly displayed in the multiple periods of human civilisation being named after them. Even our own era of semiconductor electronics is defined by a functional material: highly-purified silicon. It has contributed to immense societal changes under only a few decades, through the application of semiconductor electronics in information technology. The key properties of functional materials are their complexity, associated with a large number of degrees of freedom, and the possibility of controlling their emerging properties.

Flexibility in the control of the properties of functional materials such as, e.g., structural, electronic, spectral and transport properties, motivate their usage. For example, semiconductors, a *quantum material*, are characterised by their unique transport properties emerging from the quantum nature of the electrons within the system. Semiconductors are characterised by the existence of a sufficiently small band gap, between the highest occupied electronic states (valence states) and the lowest unoccupied electronic states (conduction states), to allow for thermal population of the conduction states. This allows for direct thermal control of the conducting behaviours of semiconductors. In addition, another important external control parameter is realised by the controlled introduction of external impurities (doping), which determines the conducting properties of semiconductors. An important class of properties in quantum materials, emerging due to the quantum nature of electrons and the correlation between them, are ones linked to collective phenomena. Due to their importance, significant amount of research aims to understand and exploit the rich phase diagrams of correlated quantum materials. An exemplary phase diagram is due to the compound V_2O_3 under varying temperature, pressure and doping, see Fig. 1.1. It exhibits two paramagnetic (PM) phases connected by a metal-to-insulator transition and an antiferromagnetic (AFM) insulating phase [2–9]. In the metallic PM phase, while the electrons are *dressed* (renormalised) by their interaction, they remain well-described as weakly interacting quasi-particles dominated by their kinetic contribution. Cross-

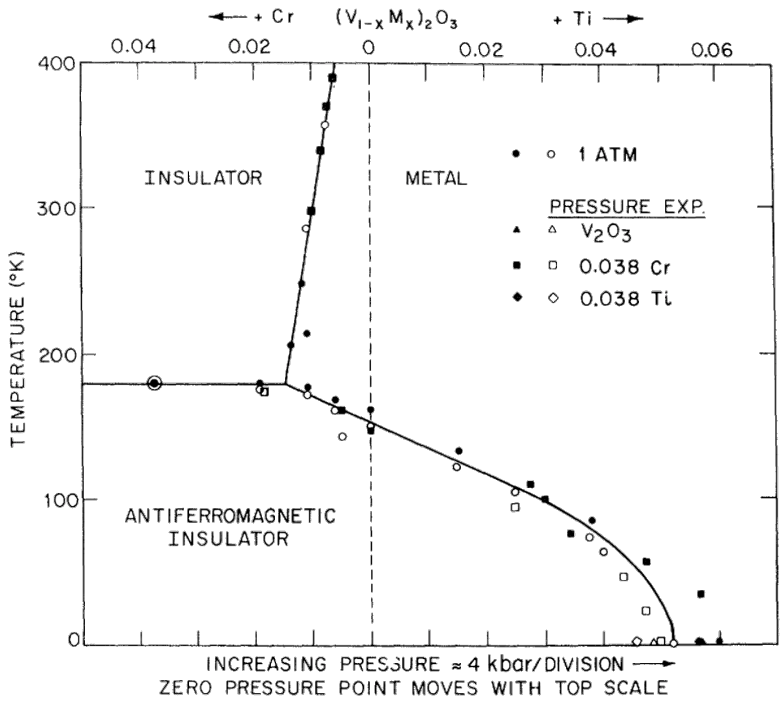

Figure 1.1: Phase diagram of V_2O_3 for varying temperature, pressure and chemical substitution of vanadium (V) by chromium (Cr) or titanium (Ti), which act as a chemical pressure. Three phases are displayed: a paramagnetic metal, a paramagnetic insulator and an antiferromagnetic insulator. Image taken from Ref. [6].

ing through the metal-to-insulator transition, the correlation drives the system into an insulating phase which is drastically different from the behaviour of the independent electrons. An intuitive view of a metal-to-insulator transition as a collective phenomenon follows from considering the dynamics of crowds of pedestrians. Consider a crowd of walking pedestrians which respect a certain distance of social distancing. An analogue of a metallic and insulating system may thus be considered a system with a short and large social distance, respectively. Moving through a crowd with a short-distance of social distancing is a simple process (metal), associated with nearly free-moving pedestrians. In contrast, obeying strict social distancing rules significantly constrains the movement of pedestrians (insulator). For a single pedestrian to move in the insulating state, the nearest-neighbouring pedestrian is required to move, and so forth, thus requiring a collective of pedestrians to move whenever a single pedestrian wishes to move. This exemplifies collective phenomena to be a general feature of complex systems with relevance in, e.g., social and biological systems, in addition to correlated quantum materials. Furthermore, the rigidity associated with the difficulty of a collective movement of pedestrians in the insulating state is an intuitive example of the rigidity, and thus stability, displayed by collective phenomena in general [10].

As for functional materials, the discovery of collective ordering phenomena and their applications have been fundamental in the progression of our understanding of nature. The importance of the discovery of magnetism, i.e. collective spin ordering, in ancient history was truly realised by the later invention of the compass and its application for navigation of naval vessels [11]. In 1620, F. Bacon expressed concisely the historical significance of magnetism: *"...printing, gunpowder, and the magnet. For these three have*

changed the whole state of things throughout the world; the first in literature, the second in warfare, the third in navigation; ..." [12]. The theoretical unification of magnetism and electricity, two and a half centuries later, led to a significant milestone in the field of physics through the development of Maxwell's equations and the classical theory of electrodynamics [13]. The formulation of classical electrodynamics contributed to significant advancements in the theoretical understanding of nature: *special relativity*, as a theoretical description unifying space and time [14], *quantum electrodynamics*, as a quantum and relativistic theoretical description of the interaction between light and matter [15, 16], and *electroweak theory*, as unification of quantum electrodynamics and weak interaction [17–19].

The discovery of superconductivity, i.e. collective pair ordering, in 1911 is in relation to magnetism a recent discovery [20]. Similar to magnetism, superconductivity displays significant functionality, e.g. through its application in superconducting magnets employed in nuclear magnetic resonance [21] and its medical counterpart, magnetic resonance imaging. Furthermore, superconductivity has induced major theoretical developments, e.g. the triumphant Bardeen-Cooper-Schrieffer theory as a microscopic theory of the emergence of superconductivity [22, 23]. In addition, following the initial discovery of high-temperature superconductivity in copper oxides in 1986 [24], significant research into strongly correlated materials has been spurred on by the search for the basic mechanism of high-temperature superconductivity [25–27]. Unlike magnetism and superconductivity, the formation of collective ordering of charges in materials, i.e. charge density waves, was initially a theoretical prediction by R. Peierls in the 1930s [28]. The formation of charge density waves allows for stabilisation or destabilisation of other phases, such as various unconventional superconducting and magnetic states. This signals the occurrence of an interplay between different ordering phenomena. In fact, a hallmark of correlated quantum materials is their typically extremely rich phase diagrams, exhibiting various kinds of ordering phenomena involving, e.g., charge, spin, orbital or pairing fluctuations, which are in competition. Through only small changes in external control parameters, correlated materials may display drastic changes by crossing from one phase to another. This motivates correlated quantum systems as a platform for functional materials, which thus necessitates a deep understanding of their phase diagrams.

Collective behaviour in materials emerges from the complexity generated by the macroscopic number of constituent electrons and ions obeying the well-known microscopic laws of nature, thus defining an interacting many-body system. Due to the interaction introducing correlations between all constituents, the general problem is untractable and requires intelligently designed approximate techniques. Nearly a century ago, P. A. M. Dirac comprehensively and accurately posed the guiding principle of the field: *"The underlying physical laws necessary for the mathematical theory of a large part of physics ... are thus completely known, and the difficulty is only that the exact application of these laws leads to equations much too complicated to be soluble. It therefore becomes desirable that approximate practical methods of applying quantum mechanics should be developed, which can lead to an explanation of the main features ... without too much computation."* [29]. Since then, progress in theoretical techniques has allowed for the successful description of correlated quantum materials. A revolution in the understanding of materials was born from the development of density functional theory (DFT) [30, 31], which allows for a description of material ground-state properties from first principles, i.e. from only the knowledge of the constituent atoms and

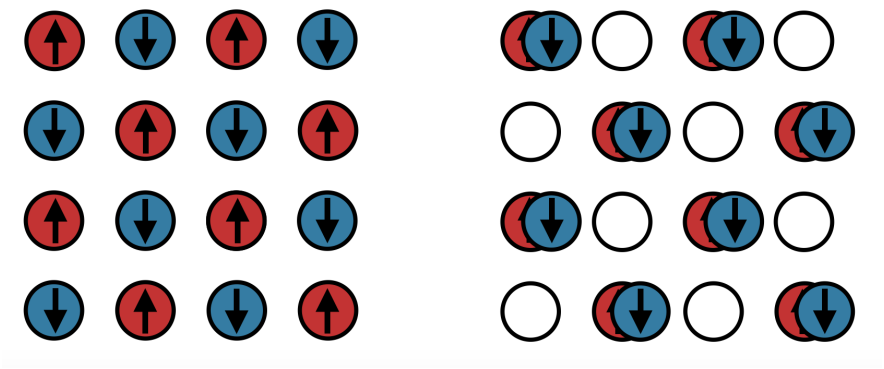

Figure 1.2: Sketch of the collective ordering in an antiferromagnetic (AFM) phase (left) and a checker-board pattern charge density wave (CDW) (right) phase, with coloured circle denoting electrons with a spin-polarisation denoted by the up and down arrows.

their arrangement. However, the description of excited state properties and many-body effects within correlated materials is more naturally framed with many-body techniques. For weakly to moderately correlated systems, perturbative techniques, such as the GW method [32], allow for a description of correlation effects and the excitation spectrum of materials by utilizing DFT as a perturbation theory starting point. For strongly correlated systems, non-perturbative techniques are required, such as dynamical mean-field theory (DMFT) [33–36]. These methods are only applicable to low-energy models, modelling the low-energy physics of the materials. However, many material properties of interest are primarily determined by the low-energy physics, thus motivating the usage of low-energy models. The strategy of modelling the low-energy physics and collective phenomena have been a successful approach in giving an intuitive understanding of the underlying physics. For sufficiently accurate downfolding to the low-energy models, quantitative descriptions of many-body effects in material properties are a possibility.

The theoretical description of competing collective phenomena in systems with correlated fermions remains one of the holy grails of modern condensed matter physics. It remains a challenging issue of computational complexity [37–39] as well as conceptual difficulty, e.g. requiring the enforcement of explicit breaking of symmetries within methods [40,41]. In this sense, the interplay of competing electronic fluctuations constitutes a roadblock to the understanding of the complex phase diagrams of a wide range of material systems. Constructing simplified methods to study interplaying collective fluctuations is thus of crucial importance. Among the fermionic lattice models used to model the interplay of collective fluctuations, the *extended Hubbard model* [42–45] occupies a prime place due to the potential relevance of its repulsive and attractive versions for both electronic materials and artificial systems. Motivated by the limitations in current approaches for quantum lattice systems capturing competing collective fluctuations, we seek in this thesis to make progress on the development of computationally efficient methods with the potential of broad and general usage for the study of interplaying collective instabilities.

The outline of the thesis is as follows: In chapter 2, we review the full many-body problem of correlated quantum materials and its reduction to low-energy quantum lattice models. Particular attention is given to reviewing the paradigmatic Hubbard

and extended Hubbard models, acting as starting point for the discussion of collective behaviours and their interplay. In chapter 3, we review a selection of numerical many-body techniques developed for quantum lattice systems. In chapter 4, we propose a theoretical technique inspired by the recently introduced fluctuating local field (FLF) theory for the study of collective magnetic fluctuations. We introduce the multi-channel fluctuating field (MCFF) theory as a multi-channel generalisation of the fluctuating field theory, based on the variational optimisation of a trial action incorporating the main leading collective modes. Through our generalisation, we construct an efficient approach to collective instabilities in the charge, spin and pairing channels. In chapter 5, we utilise the derived MCFF method to investigate the competing charge and spin degrees of freedom within the single-orbital extended Hubbard model on a square lattice at half-filling. Previous extensive research on the phase diagram of the model allows us to conduct a benchmarking of the strengths and weaknesses of our proposed theory. We observe the method to efficiently capture qualitative features of the phase diagram, with some quantitative agreement with numerically more expensive methods, without any explicit symmetry breaking enforced. In chapter 6, we explore the phase diagram of the single-orbital extended Hubbard model at half-filling for both repulsive and attractive interactions by MCFF theory. We explore the interplay between the charge, spin and s-wave pairing instabilities. Our investigation allows us to display the quintessential nature of the extended Hubbard model for competing collective ordering, with the phase diagram displaying multiple exemplary forms of competing behaviours. Importantly, our novel approach allows us to identify a novel phase that is characterised by the coexistence of s-wave superconductivity and phase separation fluctuations. The thesis concludes with chapter 7 which gives a summary of our work, and an outlook on interesting problems to apply the MCFF theory and viable paths to extend the theory further.

Chapter 2

Collective phenomena in correlated quantum systems

> *"The progress of science requires the growth of understanding in both directions, downward from the whole to the parts and upward from the parts to the whole."* - F. Dyson [46]

Collective phenomena are of fundamental importance within the field of condensed matter theory. It naturally connects with the aim of the field, to describe macroscopic (and mesoscopic) properties of matter originating from the well-known microscopic laws determining the behaviour of its microscopic constituents. In correlated quantum systems, the intertwined effects of interaction and quantum statistics of the microscopic constituents is the driving force behind the formation of collective phenomena. Of particular importance is the correlated quantum system composed of interacting electron system within solids, which describes the electronic properties of quantum materials. In this thesis, we seek to study the interplay between different collective phenomena in correlated quantum systems, specifically in quantum lattice models composed of electrons. We are interested in investigating the competition between a wide range of different collective fluctuations, e.g., magnetism, superconductivity and charge ordering, which determine the electronic properties.

In this chapter, we review correlation and collective phenomena in the context of correlated electronic systems in solids. To facilitate our discussion of collective phenomena, the chapter begins with a brief review on the general description of collective phenomena within Landau theory. It is followed by a section on electronic systems in solids and a motivation for utilising low-energy quantum lattice models for describing their low-energy collective behaviour. The chapter concludes with a review of the properties of two paradigmatic quantum lattice models: the Hubbard and extended Hubbard model.

2.1 Collective behaviour and Landau theory

A system may display a variety of different phases distinguished by their unique properties, i.e. the distinct features of the collective phenomena of each phase. The phases are connected through phase transitions, determined by the competition between their respective collective phenomena. A phase transition can be conveniently classified based on their behaviour into two classes: first-order (discontinuous) and second-order

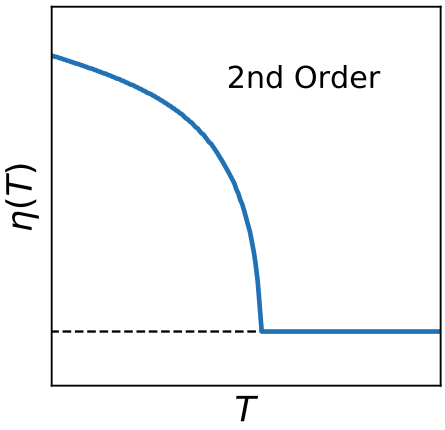

Figure 2.1: Sketch of the behaviour of the order parameter $\eta(T)$ as a function of the temperature T for a continuous phase transition.

(continuous) phase transitions. For the description of second-order phase transitions, the order parameter η associated to a phase is a standard concept, acting as a measure for the different phases. Nevertheless, the concept of an order parameter has usage for the description of first-order phase transitions as well. By definition, the order parameter η is a function of the parameter space defining a phase diagram, with the value of the function being non-zero only in its associate phase, and zero otherwise. At a second-order phase transition, limiting to only systems in which the temperature T is a tunable parameter, the transition is associated with an order parameter which is a continuous function of the temperature T, see Fig. 2.1. Together with the concept of an order parameter, an exceptionally useful framework for the description of phase transitions is Landau theory. Landau theory has its origin from a work of L. Landau in 1937 [47], seeking to formulate a general theory for second-order phase transitions. It allows for an intuitive and quantitative characterisation of both second- and first-order phase transitions through the construction of the free energy of the system. Since the original development of Landau theory, significant progress in the description of phase transitions has occurred due to renormalisation group and scaling theory ideas [48]. Nevertheless, Landau theory remains a useful framework for the description of phase transitions. In particular, the theoretical description of interplaying collective fluctuations to be developed in this thesis takes partial inspiration from the Landau theory perspective on phase transitions.

Landau theory is a broad framework with applicability to both classical and quantum systems. The theory lies on two assumptions regarding the behaviour of the free energy of the system: it is assumed to be an analytic function of the order parameter and its gradients, and to respect the symmetries of the system Hamiltonian. Consider a Hamiltonian with a symmetry which is spontaneously broken below a critical temperature, leading to the development of a phase characterised by the order parameter η. Within Landau theory, a phenomenological expression for the free energy can be constructed as a Taylor series in the order parameter,

$$\mathcal{F}[\eta, T] = \mathcal{F}_0[T] + a(T)\eta^2 + b(T)\eta^4 + \dots \,. \tag{2.1}$$

Only even terms in the order parameter are kept, on the assumption that the symmetry which is obeyed enforces an invariance of the physical properties under the transfor-

mation $\eta \to -\eta$. For a general system, odd terms in the order parameter may appear, however, such symmetries will not appear in this thesis. Stability of the system requires the existence of a global minimum of the free energy, in turn requiring that the coefficient for the highest order term in the series expansion is positive for all values of T. Limiting our considerations up to fourth-order in η, the normal (symmetry-conserving) state is associated with a positive $a(T)$ and the phase transition then occurs as $a(T)$ becomes negative, see Fig. 2.2(a), due to the development of a global minimum at $\eta \neq 0$. Note the continuous connection between the global minima at $\eta = 0$, in the normal state, and at $\eta \neq 0$, in the symmetry-broken state, signalling a second-order phase transition.

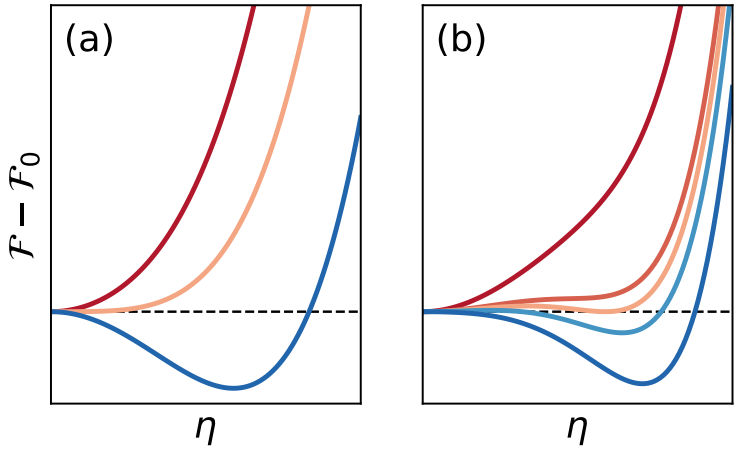

Figure 2.2: Sketch of the behaviour of the shifted free energy $\mathcal{F} - \mathcal{F}_0$ as a function of the parameter η at different temperatures T for a continuous (a) and discontinuous (b) phase transition. Note the existence of a local minimum at $\eta \neq 0$ in (b) associated with a metastable state as a precursor to the first-order phase transition.

To describe a first-order phase transition within Landau theory, one is required to at least keep terms up to the sixth-order in the Taylor expansion in η in the construction of the phenomenological expression for the free energy:

$$\mathcal{F}[\eta, T] = \mathcal{F}_0[T] + a(T)\eta^2 + b(T)\eta^4 + c(T)\eta^6 \ldots \,. \tag{2.2}$$

Limiting our considerations up to sixth-order in η, the stability of the system requires the coefficient $c(T)$ to be positive for all values of T. A simple description of a first-order phase transition occurs for strictly negative $b(T)$ coefficient. If $a(T)$ is negative, the global minimum occurs at $\eta \neq 0$. In contrast, if $a(T)$ is positive, multiple types of scenarios are allowed, see Fig. 2.2(b). For large positive values of $a(T)$, the only global minimum is displayed at $\eta = 0$. As the positive value of $a(T)$ decreases with lowering temperature, a local minimum forms at $\eta \neq 0$ which continuously develops into a global minimum at sufficiently small positive value of $a(T)$. However, the global minimum $\eta = 0$ cannot be continuously developed into the global minima at $\eta \neq 0$ due to the free energy barrier between them. This discontinuity signals the existence of a first-order phase transition. In addition, a metastable state associated with the local minima of the free energy is formed as a precursor to the symmetry-broken phase in the vicinity of the phase transition. Through only essential symmetry arguments, Landau theory allows for a general framework to describe both continuous and discontinuous

phase transitions in an intuitive way. Note that no reference has been made to the underlying system or the specific type of collective phenomena, which will now be the topic of the remainder of this chapter.

2.2 From solids to quantum lattice models

A diversity of solids appear in nature. Their properties are determined by the constituent atoms from the periodic table of elements and their structural arrangement. For crystalline solids, the atoms have a periodic arrangement associated with a discrete translational symmetry, with a plethora of allowed symmetries given by the table of space groups. For example, through only the arrangement of carbon atoms, a grand assortment of structures are possible such as, e.g., diamond, graphite, graphene [49,50], twisted bilayer graphene [51], buckminsterfullerenes [52], see Fig. 2.3. These different arrangements display various fascinating electronic properties [53–56]. The stability of a crystal is determined by the energetics associated with the arrangement of the atoms, determined by the Coulombic interaction between the ions and electrons. As the electrons propagate through the solids, they observe a potential environment defined by the underlying geometry of the arrangement of ions and the other electrons. Simultaneously, the ions experience the potential environment of the electrons and the other ions. Thus, the microscopic laws obeyed by the solids are known: the Coulomb interaction, describing the interaction between the particles, and quantum mechanics, describing the quantum statistical properties of the particles.

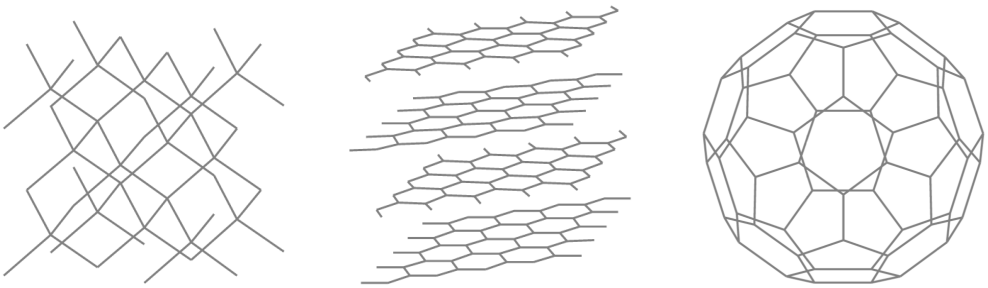

Figure 2.3: Some forms of carbon appearing in nature: diamond (left), graphite (middle) and buckminsterfullerenes (right). Graphene corresponds to a single-layer of graphite, while twisted bilayer graphene consists of two stacked layers of graphene with a relative twist angle. Images taken from Ref. [57].

2.2.1 Quantum many-body problem

As a crystalline solid is a quantum mechanical system composed of quantum particles, assumed non-relativistic (which often is a suitable approximation), the system is determined by the (time-dependent) Schrödinger equation [58]:

$$i\hbar\frac{d}{dt}\Psi(t) = \hat{H}\Psi(t). \tag{2.3}$$

All information of the system, as determined by the Hamiltonian $\hat{H}$, is thus accessible through the wavefunction $\Psi(t)$ solving the Schrödinger equation. With the microscopic

laws of the constituents being known, the Hamiltonian for the interacting many-body problem in a solid is given by:

$$\hat{H} = \sum_i \left(-\frac{\hbar^2 \nabla_i^2}{2m} \right) - \sum_{i,\alpha} \frac{Z_\alpha e^2}{|\mathbf{r}_i - \mathbf{R}_\alpha|} + \frac{1}{2} \sum_{i \neq j} \frac{e^2}{|\mathbf{r}_i - \mathbf{r}_j|} + \sum_\alpha \left(-\frac{\hbar^2 \nabla_\alpha^2}{2M_\alpha} \right) + \frac{1}{2} \sum_{\alpha \neq \beta} \frac{Z_\alpha Z_\beta e^2}{|\mathbf{R}_\alpha - \mathbf{R}_\beta|}. \tag{2.4}$$

Here $\mathbf{r}_i$ specifies the operator giving the location of electron i, with the electron mass m and the elementary charge e, while $\mathbf{R}_\alpha$ specifies the location of nucleus α with the nuclear mass M_α and the nuclear charge Z_α. The Hamiltonian incorporates the kinetic energy of the electrons (first term) and the nuclei (fourth term) in addition to the interaction terms: the electron-nuclei interaction (second term), the electron-electron interaction (third term) and the nuclei-nuclei interaction (fifth term). This complicated many-body Hamiltonian is the exact description of any solid without relativistic effects.

Due to the sheer difficulty of this interacting problem, approximations to simplify the Hamiltonian are desirable. Focusing on the electronic degrees of freedom, a standard approximation is the Born-Oppenheimer approximation which freeze the positions of the nuclei [59]. This approximation is based on the assumption that the energy scales associated with the electronic degrees of freedom and the phononic degrees of freedom, associated with lattice vibrations, are sufficiently separated, as is commonly applicable due to the heavier mass of the nuclei. Thus, this approximation is unsuitable for systems with strong electron-phonon coupling which require a more careful treatment of the phononic degrees of freedom. Freezing the positions of the nuclei, the remaining electronic degrees of freedom are then determined by the following Hamiltonian of N interacting electrons:

$$\hat{H} = \sum_{i=1}^{N} \left(-\frac{\hbar^2 \nabla_i^2}{2m} + V(\mathbf{r}_i, \{\mathbf{R}\}) \right) + \frac{1}{2} \sum_{i \neq j} \frac{e^2}{|\mathbf{r}_i - \mathbf{r}_j|}. \tag{2.5}$$

Here $V(\mathbf{r}_i, \{\mathbf{R}\})$ is an external potential generated by the nuclei of the solid through the electron-nuclei interaction. Given the knowledge of the nuclei and their positional arrangement, the external potential is fully known and thus the interacting many-electron problem is well-defined.

The wavefunction $\Psi(\mathbf{r}_1\sigma_1, ..., \mathbf{r}_N\sigma_N)$ solving the N interacting electron Hamiltonian Eq. (2.5), with $\sigma_i \in \{\uparrow, \downarrow\}$ denoting the spin projection of an electron in position $\mathbf{r}_i$, determines all the physics of the electronic system. However, when directly utilizing the Schrödinger equation in order to study the many-electron problem, in practice, one arrives at two fundamental issues:

1. In order to solve Eq. (2.3) for a general many-body problem, one is required to perform the diagonalization of a matrix of an inaccessibly large dimension due to an exponential scaling with respect to the system size. This limits application of exact diagonalization techniques, such as Lanczos algorithm [37], to only small systems.

2. Assuming one is able to solve Eq. (2.3) for a general many-body problem, one is still required to store the full wavefunction Ψ in the memory on a computer. However, the amount of memory required to store the full wavefunction of a general many-particle system is beyond the capability of any physical computer.

These two fundamental issues within the quantum many-body theory, among others, go under the name of "the quantum many-body problem". The source of the difficulty is the electron-electron interaction term. Due to the correlated behaviour of the interacting electrons, one cannot in the generic case, a priori, treat the electrons as independent particles. In order to make progress on the theoretical description of many-electron systems, an extensive selection of practical approximate and exact methods have been developed. These methods are based on the idea of evaluating objects which contain sufficient information about the physical systems, while remaining feasible to store in the memory on a computer. This follows from the majority of relevant physical observables not requiring the full information contained within the many-electron wavefunctions.

2.2.2 Solids in the occupation number representation

There are several different paths to treat an interacting electronic system, defined by the Hamiltonian Eq. (2.5). For many-body techniques, it is suitable to represent the expressed problem utilising the occupation number representation, i.e., the second quantisation representation. Within the occupation number representation, one promotes the bosonic and fermionic fields themselves to operators endowed with their respective quantum statistics, i.e., Fermi-Dirac statistics for fermions and Bose-Einstein statistics for bosons. Working in this representation, one introduces the fermionic or bosonic field creation $\hat{\phi}^{\dagger}_{\sigma}(\mathbf{r})$ and annihilation $\hat{\phi}_{\sigma}(\mathbf{r})$ operators, written in real-space, which create and annihilate a quantum particle at position $\mathbf{r}$ with spin-polarisation σ, respectively. In the occupation number representation, the fermionic and bosonic fields operate within Fock space, acting as a direct sum of Hilbert spaces associated with the particle numbers $\{0, 1, 2, ...\}$, in which states are indexed by the occupation number of each single-particle state. The fermionic field obey the Fermi-Dirac statistics by satisfying the following anti-commutation relations:

$$\{\hat{\phi}_{\sigma}(\mathbf{r}), \hat{\phi}^{\dagger}_{\sigma'}(\mathbf{r}')\} = \delta^{(3)}(\mathbf{r} - \mathbf{r}')\delta_{\sigma\sigma'}, \quad \{\hat{\phi}_{\sigma}(\mathbf{r}), \hat{\phi}_{\sigma'}(\mathbf{r}')\} = \{\hat{\phi}^{\dagger}_{\sigma}(\mathbf{r}), \hat{\phi}^{\dagger}_{\sigma'}(\mathbf{r}')\} = 0, \tag{2.6}$$

with the (three-dimensional) Dirac delta distribution $\delta^{(3)}(\mathbf{r} - \mathbf{r}')$ and the Kronecker delta function $\delta_{\sigma\sigma'}$. Equivalently, the bosonic fields obey the Bose-Einstein statistics by satisfying identical relations with the commutator employed instead of the anti-commutator. Following the introduction of the fermionic field operators, one may conveniently rewrite the Hamiltonian in the occupation number representation as:

$$\begin{aligned}\hat{H} = &\sum_{\sigma} \int d\mathbf{r} \hat{\phi}^{\dagger}_{\sigma}(\mathbf{r}) \left(-\frac{\hbar^2 \nabla^2_{\mathbf{r}}}{2m} + V(\mathbf{r}, \{\mathbf{R}\}) \right) \hat{\phi}_{\sigma}(\mathbf{r}) \\ &+ \frac{1}{2} \sum_{\sigma\sigma'} \int d\mathbf{r} d\mathbf{r}' \hat{\phi}^{\dagger}_{\sigma}(\mathbf{r}) \hat{\phi}^{\dagger}_{\sigma'}(\mathbf{r}') \frac{e^2}{|\mathbf{r} - \mathbf{r}'|} \hat{\phi}_{\sigma'}(\mathbf{r}') \hat{\phi}_{\sigma}(\mathbf{r}).\end{aligned} \tag{2.7}$$

Note that the kinetic and potential terms are of a single-particle form, expressed as a single pair of creation and annihilation operators. In contrast, the Coulombic interaction is of a two-particle form, expressed as two pairs of creation and annihilation operators.

Within a solid, electrons may display both itinerant (delocalised) and localised behaviour. A natural basis for the localised behaviour of electrons is a basis localised on the atomic orbitals, e.g., a Gaussian basis or the linear combination of atomic

orbitals basis [60]. Expressing the localised basis centred on the atoms as $|jn\rangle$, with j specifying the atomic site located at $\mathbf{R}_j$ and n specifying the atomic orbital, one may write the field operators as:

$$\hat{\phi}_\sigma(\mathbf{r}) = \sum_{jn} \psi_{jn}(\mathbf{r})\hat{c}_{jn\sigma}, \quad \hat{\phi}^\dagger_\sigma(\mathbf{r}) = \sum_{jn} \psi^*_{jn}(\mathbf{r})\hat{c}^\dagger_{jn\sigma}. \tag{2.8}$$

Here, the orbital function $\psi_{jn}(\mathbf{r}) = \langle \mathbf{r}|jn\rangle$ is introduced, defining a transformation matrix between the two bases. In the localised basis, the fermionic creation and annihilation operators obey the following anti-commutation relations:

$$\{\hat{c}_{in\sigma}, \hat{c}^\dagger_{jm\sigma'}\} = \delta_{ij}\delta_{nm}\delta_{\sigma\sigma'}, \quad \{\hat{c}_{in\sigma}, \hat{c}_{jm\sigma'}\} = \{\hat{c}^\dagger_{in\sigma}, \hat{c}^\dagger_{jm\sigma'}\} = 0. \tag{2.9}$$

Utilising the localised basis, the many-electron Hamiltonian Eq. (2.7) may be written in the form:

$$\begin{aligned}\hat{H} = &- \sum_{\substack{\sigma,ij\\nm}} t^{nm}_{ij}\hat{c}^\dagger_{in\sigma}\hat{c}_{jm\sigma} + \sum_{\sigma,i,n} v^n_i \hat{c}^\dagger_{in\sigma}\hat{c}_{in\sigma} \\ &+ \frac{1}{2}\sum_{\substack{\sigma\sigma',iji'j'\\nmn'm'}} U^{nmn'm'}_{iji'j'}\hat{c}^\dagger_{in\sigma}\hat{c}^\dagger_{jm\sigma'}\hat{c}_{j'm'\sigma}\hat{c}_{i'n'\sigma}.\end{aligned} \tag{2.10}$$

Here, the hopping parameters t^{nm}_{ij}, potential parameters v^n_i and interaction parameters $U^{nmn'm'}_{iji'j'}$ have been introduced:

$$t^{nm}_{ij} \equiv \int d\mathbf{r}\psi^*_{in}(\mathbf{r})\frac{\hbar^2\nabla^2_{\mathbf{r}}}{2m}\psi_{jm}(\mathbf{r}), \tag{2.11}$$

$$v^n_i \equiv \int d\mathbf{r}\psi^*_{in}(\mathbf{r})V(\mathbf{r},\{\mathbf{R}\})\psi_{in}(\mathbf{r}), \tag{2.12}$$

$$U^{nmn'm'}_{iji'j'} \equiv \int d\mathbf{r}d\mathbf{r}'\psi^*_{in}(\mathbf{r})\psi^*_{jm}(\mathbf{r}')\frac{e^2}{|\mathbf{r}-\mathbf{r}'|}\psi_{j'm'}(\mathbf{r}')\psi_{i'n'}(\mathbf{r}). \tag{2.13}$$

The hopping parameters describe the kinetic energy of the system, and act as the probability amplitude of an electron to hop between different sites and orbitals. The on-site potential determine the single-particle occupation energy for an electron to occupy a certain site and orbital. Neglecting the interaction term, the hopping and on-site potential terms define a tight-binding model. Given that the localised basis is complete and spans the full single-particle Hilbert space, the many-electron Hamiltonian Eq. (2.10) is an explicit rewriting of the many-electron problem in solids.

For the itinerant behaviour of electrons, it is convenient to work in the momentum basis instead of the real-space basis. Limiting our considerations to crystalline solids, the quasi-momentum basis allows together with Bloch's theorem to naturally exploit the regular and periodic nature of the underlying crystalline lattice. Bloch's theorem was originally formulated by F. Bloch in 1928 [61], seeking to describe the conduction of electrons in crystalline solids, i.e., electrons with itinerant behaviour. The theorem states that the solution to the single-particle Schrödinger equation for a periodic potential can be expressed in the form of the wavefunction:

$$\psi_{n\mathbf{k}}(\mathbf{r}) = e^{i\mathbf{k}\cdot\mathbf{r}}u_{n\mathbf{k}}(\mathbf{r}), \tag{2.14}$$

with the quasi-momentum vector $\mathbf{k}$, which is a conserved ("good") quantum number associated with the discrete translation symmetry of the system, as follows from Noether's theorem [62]. In Bloch's theorem, the wavefunction is factorised into a plane-wave $e^{i\mathbf{k}\cdot\mathbf{r}}$ and a Bloch function $u_{n\mathbf{k}}(\mathbf{r})$, which displays an identical periodicity to the lattice. Following from Bloch's theorem, one defines, by a discrete Fourier transformation, the Wannier function as a localised basis in real space [63–65]:

$$\psi_{nj}(\mathbf{r}) \equiv \frac{1}{N}\sum_{\mathbf{k}} e^{-i\mathbf{k}\cdot\mathbf{R}_j}\psi_{n\mathbf{k}}(\mathbf{r}), \tag{2.15}$$

where $\mathbf{R}_j$ are the Bravais lattice vectors defining the discrete points generated by the translational symmetry of the periodic lattice, and N is the number of primitive cells in the crystal. The sum over $\mathbf{k}$ is restricted to the first Brillouin zone, i.e., the primitive cell in reciprocal (quasi-momentum) space as determined by the geometry of the lattice. By the inverse Fourier transform, one may similarly relate the Bloch and Wannier functions by

$$\psi_{n\mathbf{k}}(\mathbf{r}) = \sum_{j} e^{i\mathbf{k}\cdot\mathbf{R}_j}\psi_{nj}(\mathbf{r}). \tag{2.16}$$

The localised Wannier basis allows to incorporate the periodic symmetry of the underlying crystalline lattice, and thus permits to connect to the quasi-momentum space. In addition, the local nature of the Wannier function gives an insightful view of electronic properties due to, e.g., chemical bonding as they act as the solid-state equivalent to localised molecular orbitals in chemistry [66]. Note that the Bloch functions are only defined up to an overall phase $\theta_{\mathbf{k}}$, however, without any consequence on the properties of the Bloch states. In contrast, the freedom of choice for the global phase $\theta_{\mathbf{k}}$ may drastically change the Wannier functions [66]. Exploiting the phase freedom in order to construct the most convenient Wanner basis is therefore standard, such as in the construction of, e.g., the maximally-localised Wannier functions [66, 67].

Utilising the Fourier transform, the electron creation and annihilation operators in quasi-momentum space are defined as,

$$\hat{c}_{\mathbf{k}n} \equiv \sum_{j} e^{-i\mathbf{k}\cdot\mathbf{R}_j}\hat{c}_{jn}, \quad \hat{c}_{jn} \equiv \frac{1}{N}\sum_{\mathbf{k}} e^{i\mathbf{k}\cdot\mathbf{R}_j}\hat{c}_{n\mathbf{k}}. \tag{2.17}$$

This allows to rewrite the many-electron Hamiltonian Eq. (2.10) in the quasi-momentum basis as

$$\begin{aligned}\hat{H} = &\frac{1}{N}\sum_{\substack{\sigma,\mathbf{k}\\ nm}} \left(\epsilon^{nm}_{\mathbf{k}} + v^{n}_{\mathbf{k}}\delta_{nm}\right)\hat{c}^{\dagger}_{\mathbf{k}n\sigma}\hat{c}_{\mathbf{k}m\sigma} \\ &+ \frac{1}{2}\sum_{\substack{\sigma\sigma',\mathbf{k}\mathbf{k}'\mathbf{q}\\ nmn'm'}} U^{nmn'm'}_{\mathbf{q}}\hat{c}^{\dagger}_{\mathbf{k}n\sigma}\hat{c}^{\dagger}_{\mathbf{q}-\mathbf{k},m\sigma'}\hat{c}_{\mathbf{q}-\mathbf{k}',m'\sigma}\hat{c}_{\mathbf{k}'n'\sigma}.\end{aligned} \tag{2.18}$$

In quasi-momentum space, the Fourier transform leads to the introduction of the bare dispersion $\epsilon^{nm}_{\mathbf{k}}$, defined by:

$$\epsilon^{nm}_{\mathbf{k}} \equiv -\sum_{i,j} t^{nm}_{ij} e^{-i\mathbf{k}\cdot(\mathbf{R}_i-\mathbf{R}_j)}. \tag{2.19}$$

Similarly, the quasi-momentum forms of the potential $v^n_{\mathbf{k}}$ and interaction parameters $U^{nmn'm'}_{\mathbf{q}}$ may be introduced. Note that the bare dispersion is written here in a generic basis which may display off-diagonal elements in orbital space.

The importance of exploiting symmetries such as, e.g., periodicity and the space group of crystalline solids is apparent. It allows to account for the symmetries which restricts the number of degrees of freedom of the many-electron problem in solids. However, it is worth emphasizing that the many-electron problem defined by the Hamiltonian Eq. (2.18) remains beyond the scope of any direct exact treatment. Thus, approximate methods allowing to calculate electronic properties of solids remain desirable.

2.2.3 From band theory to density functional theory

Through the application of Bloch's theorem, F. Bloch pioneered *band structure theory* within the field of solid-state physics. The theory seeks to describe a range of different physical properties of solids within an effective single-particle system, i.e., a noninteracting picture. For itinerant electrons, the nearly free electron (NFE) approximation, associated with neglecting the interaction parameters $U^{nmn'm'}_{\mathbf{q}}$, appears as a reasonable approximation to the description of electronic properties given that the electron-electron interaction is sufficiently screened. Within the NFE approximation, the single-electron eigenenergies of the noninteracting Hamiltonian, defined by the bare dispersion $\epsilon^{nm}_{\mathbf{k}}$ and potential $v^n_{\mathbf{k}}$, allows to generate well-defined energy bands spanning the Brillouin zone. The set of energy bands describe the, so called, electronic structure of the solids, and allow to computed a selection of different physical observables. Despite band theory being based on the NFE approximation, or similar single-particle constructions, the theory has been impressively successful in qualitatively describing many properties of solids. For example, it allows for a simple and intuitive understanding of the characteristic transport properties of large selection of quantum materials: From metals and semimetals, associated with partially filled bands, to semiconductors and band insulators, associated with filled bands. In fact, the theoretical basis of all solid-state devices employed in contemporary information technology originates from conventional band theory.

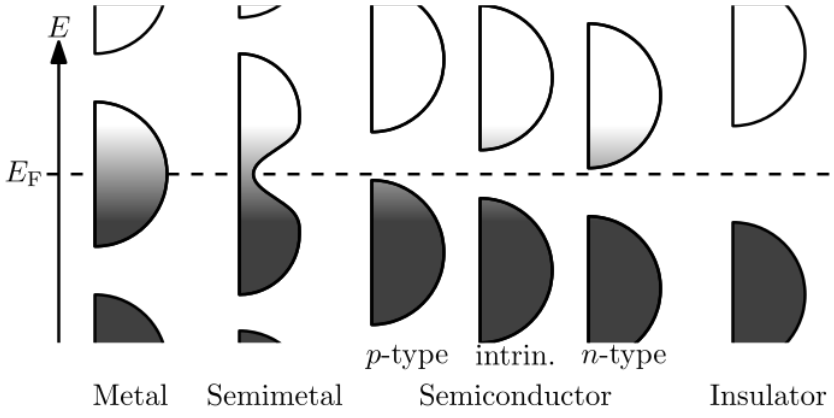

Figure 2.4: Sketch of the density of electronic states at equilibrium within a metal, semimetal, semiconductor and insulator, as a function of band filling or location of the Fermi energy E_F. Image taken from Ref. [68].

A particularly appropriate description of metals is given by NFE approximation, due to the strong screening of the electron-electron interactions within conventional metals. Nevertheless, incorporating effects of the interaction on the single-particle level is necessary for improving the description of the electronic structure of quantum materials. The majority of all electronic structure calculations are today calculated within density functional theory (DFT) [30,31], which allows to incorporate interaction effects within a single-particle description. The theory is distinct from mean-field theory (MFT), e.g., the Hartree-Fock approximation, which also allows to include interaction effects in the band structure description through the construction of an effective single-particle system. The foundation of DFT is based two guiding ideas: The Hohenberg-Kohn theorem [30] and the Kohn-Sham system [31]. The Hohenberg-Kohn theorem states that the external potential $V(\mathbf{r}, \{\mathbf{R}\})$ is an unique functional of the ground-state electron density [30, 69, 70]. As the form of the kinetic energy and Coulombic interaction is fixed by nature, all many-electron observables are thus determined by the external potential $V(\mathbf{r}, \{\mathbf{R}\})$ and therefore the ground-state electron density. Unlike the full wavefunction, the ground-state electron density of a many-electron system is easily storable in the memory of a computer. Thus, the Hohenberg-Kohn theorem shows a path to tackle the quantum many-body problem. However, the existence theorem does not itself provide a way to calculate the observables of a many-electron system from the ground-state density. To make progress, one maps the many-electron system to a fictitious single-particle system, the Kohn-Sham system, constrained to display the same ground-state density as the original many-electron system [31]. This allows to construct a self-consistent description of the fictitious single-particle system obeying the, so called, Kohn-Sham equations. While the mapping is exact in theory, it depends on an exchange-correlation functional, which is only known for a few special cases, such as, e.g., for the free-electron problem [71] and the Hooke's atom [72]. Thus, in practice, the exchange-correlation functional is required to be approximated for modelling of ground-state quantum materials. A wide range of different approximations of the exchange-correlation functional have been developed, e.g., local density approximation (LDA) [31, 71], generalised gradient approximation (GGA) [73], and hybrid functionals [74,75], in ascending accuracy and complexity [76].

The first-principle description of quantum materials has significantly progressed due to the development of DFT. For example, it reproduces surprisingly well the experimentally measured form of the single-particle excitation spectrum as measured in, e.g., angle-resolved photoemission spectroscopy (ARPES). In the ARPES experiment technique, to be expanded upon in the next chapter, a monochromatic beam of photons with frequency $\hbar\omega$ is aimed at the surface of a material, leading to the photo-ejection of electrons. The photo-emitted electrons are then collected, allowing for a measurement of the probability distribution with a resolution of the kinetic energy $E_{\mathbf{k}}$ and momentum $\mathbf{k}$. It follows that the experimental band structure associated with the single-particle excitations are accessible with the ARPES technique below the Fermi energy E_F. Impressive agreement between the experimental band structure and the theoretical Kohn-Sham band structure may occur as exemplified in Fig. 2.5, where an excellent agreement for the electronic structure of $1\mathrm{T}-\mathrm{VSe}_2$ is obtained between the experimental measurement, obtained by soft X-ray ARPES, and the theoretical prediction, obtained within GGA [77]. While interpreting the Kohn-Sham eigenenergies, which define the electronic structure, as the physical band structure has proven

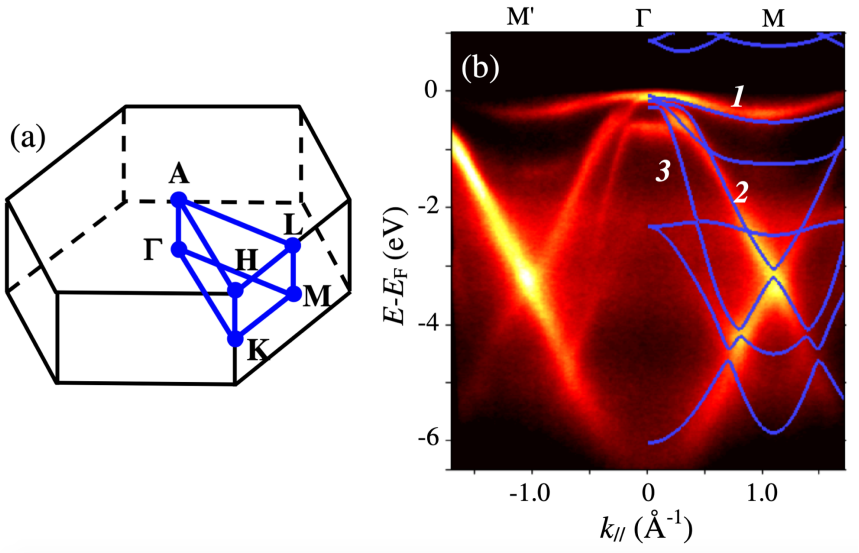

Figure 2.5: (a) Sketch of the Brillouin zone of a hexagonal lattice, with high-symmetry points denoted. (b) Experimental soft X-ray angle-resolved photoemission spectroscopy (ARPES) intensity is plotted as a colour map along the $\mathbf{M}' - \mathbf{\Gamma} - \mathbf{M}$ high-symmetry path for the hexagonal 1T$-VSe_2$ compound. As comparison, the theoretical prediction of the electronic structure calculated within GGA is included as blue lines. Image taken from Ref. [77], with modifications.

immensely useful, strictly speaking, the Kohn-Sham eigenenergies have no physical interpretation.

Despite the success of DFT, due to the single-particle nature of the technique, it is inadequate to give a theoretical description of many-body effects in strongly correlated quantum materials. Limitations of band theory are perhaps most clearly displayed in the Mott insulator [78–81]. Within band theory, insulators are only associated with fully filled bands, and thus the interaction-driven Mott insulator associated with partially filled bands cannot be captured. A description of correlation effects requires the utilisation of many-body techniques. These techniques treat the interaction in a more explicit fashion in exchange for a higher computational effort. Many-body perturbation theory techniques, such as the GW method [32], utilizing DFT as a perturbation theory starting point allows for significant improvements in weakly to moderately correlated quantum materials by the inclusion of correlation effects. For strongly correlated quantum materials, correlation effects associated with collective phenomena are difficult to capture within perturbation theory due to the breakdown of the assumption of an adiabatic connection of the groundstate between the exact solution and the perturbation theory starting point. Thus, non-perturbative techniques, such as DMFT [33–36], are required. Due to the computational effort, the applicability of techniques for strongly correlated systems are limited to "simple" systems with fewer degrees of freedom which describe the low-energy observables of the system.

2.2.4 Downfolding to low-energy degrees of freedom

Condensed matter theory seeks to describe the fundamental physics in the limit of many degrees of freedom. This limit may be compared to the fundamental physics

associated with the two infinities, i.e. the limit of the smallest and largest scales, which high-energy particle physics seeks to describe. The interacting electron problem in correlated quantum materials contains an immense number of degrees of freedom, however, a large selection of electronic properties of interest are low-energy observables. This motivates the construction of low-energy model systems describing the low-energy physics of system. Quantum lattice models are a common class of low-energy models for correlated quantum materials, allowing to, e.g., describe the low-energy collective phenomena and their interplay.

The degrees of freedom of interacting many-electron systems of solids may be divided into low- and high-energy degrees of freedom. An explicit connection between high-energy degrees of freedom to the low-energy ones is enabled by the renormalisation group technique. It corresponds to the machinery of iteratively integrating out the high-energy degrees of freedom, defining a flow in parameter space determining the low-energy model. The parameters flow towards fixed points, which define the form of the low-energy models. Fixed points of such a flow in parameter space are, e.g., the Landau Fermi liquid and the Mott insulator. In particular, within the Landau Fermi liquid theory, the low-energy physics is described by weakly interacting quasiparticles [82], which motivates the usage of the NFE approximation. In practice, while exact, the renormalisation group treatment is unfeasible to implement for the general interacting electron problem in solids, and thus approximations are used. A commonly employed approximation for downfolding is the constrained random phase approximation (cRPA) [83]. Within cRPA, a low-energy model is constructed by allowing the high-energy degrees of freedom to screen the low-energy interaction parameters, connecting a many-electron system to the low-energy quantum lattice models. This concludes a long journey, from the full description of the many-body problem of quantum materials, on the basis of only the microscopic laws obeyed by its constituents, to the modelling of the low-energy observables by downfolding to quantum lattice models.

2.3 Strong correlation and quantum lattice models

Strong correlation in quantum materials originates due to the localised nature of the electrons, unlike delocalised electrons which experience significant screening of the Coulombic interaction. A prevalent group of strongly correlated quantum materials in nature are the transition metal oxides, with partially filled d- or f-shells of the transition metals. Due to the localised nature of d- and f-orbitals, relative to the more extended s- and p-orbitals, strong correlation emerges. The most prominent strongly correlated quantum materials are probably the high-temperature superconductors, e.g., existing within three main families of compounds: the copper-oxide compounds (cuprates) discovered in 1986 [24], iron-based superconductors (pnictides) discovered in 2008 [84,85], and nickel-oxides compounds (nickelates) discovered in 2019 [86]. Here, the copper- and nickel-oxide compounds together with select iron-based superconductors belong to the broad class of transition metal oxides. However, a plethora of strongly correlated systems exists in nature beyond the high-temperature superconductors such as, e.g., heavy fermion systems [87–90] and multiferroics [91–95]. Nevertheless, high-temperature superconducting systems have all experienced extensive experimental and theoretical research since their discoveries. Important aims has been the fundamental understanding of the underlying mechanism behind the superconductivity and the search for quantum materials displaying room-temperature superconductivity at ambient pressures, which

remain topics under heavy investigation since the initial discovery of the copper-oxide materials nearly four decades ago. This has motivated significant theoretical effort in giving a theoretical description of the superconducting pairing mechanism within different low-energy models. Of particular importance are the quantum lattice models.

Quantum lattice models have their origin in the single-orbital Hubbard model, independently proposed and studied by J. Hubbard, M. C. Gutzwiller and J. Kanamori in 1963 [42–44]. It acts as paradigmatic model of a strongly correlated system in condensed matter theory, as the Drosophila melanogaster (a species of fruitfly) acts as a model organism in genetics or the Ising model acts as a paradigmatic model for phase transitions in statistical mechanics. In the Hubbard model, the electrons may occupy sites on a lattice described by a tight-binding model. The Coulomb interaction is modelled by a local interaction term, which penalises two electrons occupying the same site. The physics of the model is thus determined by the "simple" competition between the kinetic energy and the local interaction term. Due to its simplicity, it allows for a controlled investigation of fundamental many-body physics. However, the simplicity should be contrasted with the inherent difficulty of actual computing its solutions in practice. In fact the model is only analytically solvable in zero, one [96], and infinite dimensions [33], and numerically exact calculations are restricted in their applicability. This illustrates the complexity of strongly correlated systems, as even the paradigmatic single-orbital Hubbard model, remains a hard problem.

The single-orbital Hubbard model is commonly believed to be sufficient to model the low-energy physics of the CuO_2-layers of the copper oxides [25, 26] and is commonly utilised to model the low-energy physics of the NiO_2-layers of the infinite-layer nickel oxides [97, 98]. However, the extensions of the Hubbard model are important to give a more quantitative description, and to take into account effects not captured within the single-orbital Hubbard model. In fact, non-local interactions in the single-orbital Hubbard model are commonly implemented in the theoretical description of the low-energy physics of copper oxide compounds, as they are thought to be important [99–103]. The extended Hubbard model [45], which includes local and non-local interaction parameters, were implicitly considered already in the initial work of J. Hubbard [42]. The single-orbital representation is not sufficient for describing the low-energy physics of iron-based superconductors, and possible indications for underlying multi-orbital physics in copper- and nickel-oxide compounds exist [27, 104–106]. Multi-orbital physics are incorporated in the Kanamori-Hubbard model studied by J. Kanamori [44]. Extensions of the Hubbard model, allows for the exploration of a large parameter space associated with a wide range of different collective phenomena and their interplay. Within this thesis, our considerations will be limited to two single-orbital models: the Hubbard and extended Hubbard model. Thus, we seek in the current section to give a broad overview of these two models.

2.3.1 Hubbard model

The Hubbard model is a single-orbital model defined by the following Hamiltonian

$$\hat{H} = -\sum_{ij,\sigma} t_{ij}\hat{c}^{\dagger}_{i\sigma}\hat{c}_{j\sigma} + U\sum_{i}\hat{n}_{i\uparrow}\hat{n}_{i\downarrow} - \mu\sum_{i,\sigma}\hat{n}_{i\sigma}. \tag{2.20}$$

In this expression, $\hat{c}^{(\dagger)}_{i\sigma}$ operators correspond to the annihilation (creation) of electrons, where the subscripts denote the position i and spin projection $\sigma \in \{\uparrow, \downarrow\}$. Within

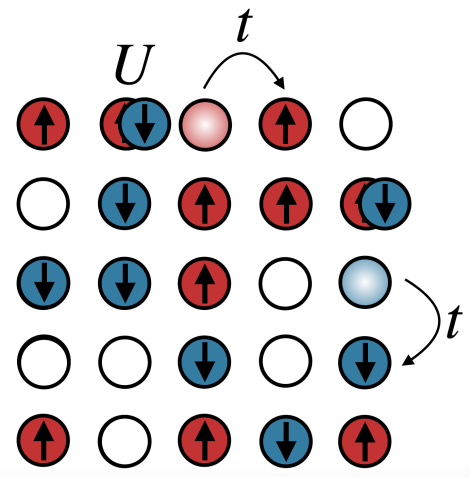

Figure 2.6: Sketch of the Hubbard model on a two-dimensional square lattice, with the coloured circles denoting electrons with a spin-polarisation denoted by the up and down arrows. Note that the hopping parameter t is associated with the probability of jumping between nearest-neighbour sites and the local U is associated with an energetic penalty of double-occupation of sites.

Eq. (2.20), the hopping t_{ij} is between the lattice sites i and j, and μ is the chemical potential determining the filling of the system. The Coulomb interaction between electronic densities $\hat{n}_{i\sigma} = \hat{c}^{\dagger}_{i\sigma}\hat{c}_{i\sigma}$ is modelled by an on-site interaction parameter U. Thus, the physics of this model is determined by the competition between the hopping t_{ij} and the local U interaction, for a given lattice geometry and filling of the system, see Fig. 2.6 for a sketch of the model. We note that it is standard to constrain the hopping parameter up to nearest- or next-nearest-neighbour hopping, as the longer-range hopping terms are expected to be subleading. However, long-range hopping terms t_{ij} are required for a realistic description of the band structure in quantum materials.

Repulsive U Hubbard model

Extensive studies have been conducted on the single-orbital Hubbard model at half-filling with a d-dimensional hypercubic lattice and nearest-neighbour hopping. Following convention, the hopping parameter between the nearest-neighbour sites $\langle i, j\rangle$ is denoted as t. Constrained to a paramagnetic (PM) state, the Hubbard model exhibits a correlation-driven first-order quantum phase transition without any symmetry-breaking from a metallic state to a Mott insulating state at an intermediate value of U and zero temperature [36, 107, 108]. The Mott insulator is characterised by the repulsive U forbidding transport of the electrons due to the penalty associated with two charges occupying the same site, thus freezing the charge degrees of freedom. An exception is the Hubbard model on a one-dimensional chain, which lacks a Mott insulating phase [96]. The metal-to-insulator transition originated due to two underlying mechanisms: the Mott-Hubbard transition [107,108], describing the opening of a gap at the Fermi energy due to formation of the incoherent upper and lower Hubbard bands, and the Brinkman-Rice transition [108, 109], describing suppression of spectral weight of a quasiparticle peak at the Fermi energy. The zero-temperature metal-to-insulator transition connects to a finite coexistence region of the metallic and insulating phases at finite temperatures, enclosed between lower $U_{c1}(T)$ and higher $U_{c2}(T)$ critical inter-

actions [110]. This behaviour continues up to a critical point [110], where above the coexistence region a supercritical Widom line emerges continuously from the thermodynamic metal-to-insulator transition line $U_c(T)$ within the coexistence region [110–115], see Fig. 2.7 for a sketch of the phase diagram. Furthermore, in the PM phase diagram, at low- to intermediate values of U, a coherent quasiparticle peak form at the low temperatures, associated with the formation of a Landau Fermi liquid (FL). However, as the temperature is increased, the Hubbard model enters an incoherent region without a well-defined quasiparticle peak at high-temperature.

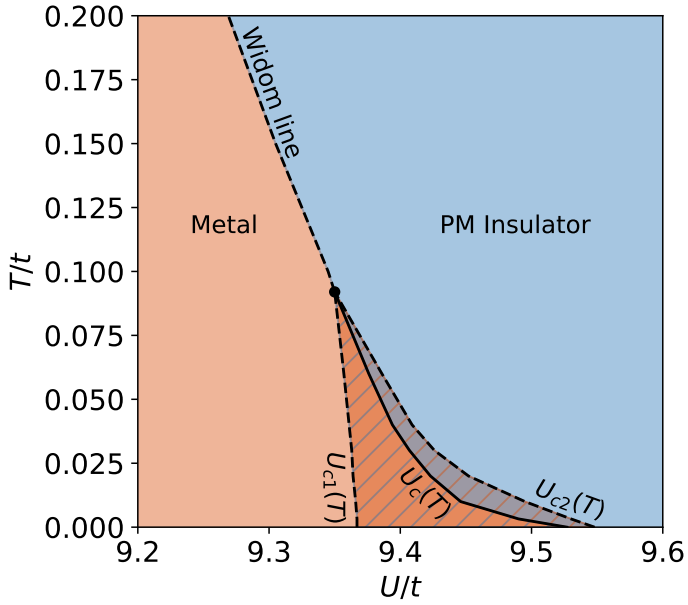

Figure 2.7: A sketch of the phase diagram of the half-filled Hubbard model for repulsive U, near the Mott-Hubbard metal-to-insulator transition within the single-site DMFT approximation restricted to the PM phase. An orange and blue region denote a metallic and insulating state. In the vicinity of the thermodynamic first-order phase boundary $U_c(T)$ between the metal and insulator, a coexistence region emerges denoted by two regions with hatched patterns. It is enclosed by $U_{c1}(T)$ and $U_{c2}(T)$, and is associated with the occurrence of an insulating or metallic metastable state in addition to the stable metallic or insulating state, respectively. The coexistence regions ends at a critical point, followed by a supercritical Widom line signaling the smooth crossover between the metallic and insulating solutions. All values are given by single-site DMFT constrained to a PM solution on a two-dimensional square lattice, with values calculated in Ref. [110].

Besides the local dynamics driving the Mott physics, the repulsive U stabilises collective spin fluctuations which emerges as the formation of an AFM phase [116]. The AFM phase is associated with a long-range and regular pattern of spin with opposite alignment between nearest-neighbour sites [117,118]. These collective spin fluctuations are associated with the spin density,

$$\hat{n}^s_{\mathbf{Q}} = \frac{1}{N} \sum_{\mathbf{k},\sigma\sigma'} \hat{c}^\dagger_{\mathbf{k}+\mathbf{Q}\sigma} \sigma^s_{\sigma\sigma'} \hat{c}_{\mathbf{k}\sigma'}, \tag{2.21}$$

with the ordering vector $\mathbf{Q} = (\pi, \pi)$ for the AFM state, here written for a two-dimensional square lattice, and where σ^s are the Pauli spin matrices. As for the spin density, the

charge density is defined as:

$$\hat{n}^c_{\mathbf{Q}} = \frac{1}{N} \sum_{\mathbf{k},\sigma\sigma'} \hat{c}^\dagger_{\mathbf{k}+\mathbf{Q}\sigma} \sigma^c_{\sigma\sigma'} \hat{c}_{\mathbf{k}\sigma'}, \tag{2.22}$$

where σ^c is the identity, i.e., the Kronecker delta function. While the AFM phase is associated with an instability in the spin channel and a partial translation symmetry breaking, the Mott phase is in contrast associated with a charge instability and does not break any translation symmetries. In the weak-coupling limit, the underlying mechanism of the AFM state is the Fermi surface nesting, thus leading to a Slater-type AFM insulator [119, 120] associated with long-range spin fluctuations. In contrast, in the strong-coupling limit, the half-filled Hubbard model reduces to an effective Heisenberg model [120, 121] which forms localised moments, leading to a Heisenberg-type AFM associated with short-range spin fluctuations. Due to the Mermin-Wagner theorem [122–124], the stability of the AFM state is dependent on the dimensionality. The theorem states that the magnetic ordering at finite temperature is excluded in a broad class of one- and two-dimensional systems, including the Hubbard model, due to the continuous nature of the underlying SU(2) symmetry. Therefore, the Hubbard model in a one- or two-dimensional lacks an AFM phase at finite-temperature. However, a true AFM phase emerges at zero temperature within the two-dimensional Hubbard model [120]. In vicinity of the AFM phase, a region emerges as precursor to AFM ordering denoted as the pseudogap (PG) state [125–137]. This region is distinguished by the existence of a partial gap, due to the formation of a gap in the Fermi surface occurring at different temperatures for different quasi-momentum $\mathbf{k}$. Similarly, the formation of the FL with a coherent quasiparticle peak at low-temperatures occurs at different temperatures for different quasi-momentum $\mathbf{k}$ [137]. Collectively, these two intermediate regions in the vicinity of the AFM phase and the incoherent region display non-Fermi liquid behaviour (NFL) [136]. As summary, a sketch of the AFM phase diagram is displayed in Fig. 2.8.

At half-filling, the single-orbital Hubbard model displays a varied phase diagram due to only two tunable parameters: the local interaction U/t and the temperature T/t. By doping the Hubbard model away from half-filling, the complexity of the phase diagram increases. Mobile charge carriers are introduced into the Mott insulator by doping, leading to the formation of a correlated metal replacing the Mott insulator [36]. In addition, a first-order metal-to-metal transition between the weakly correlated metal and the correlated metal develops [112,139] A PG phase emerges in the PM solution of the doped Hubbard model in a low-doped region below the correlated metal at larger doping, with the underlying mechanism being due to spin fluctuations [140]. As the temperature is lowered, this regime connects to a phase characterised by the formation of a stripe-ordered ground-state associated with intertwined spin- and charge ordering at zero temperature [140–143]. Due to reshaping of the Fermi surface as function of the filling, the nesting may promote incommensurate spin density waves with ordering vector depending on the filling.

As doping introduces a third tunable parameter, turning on the next-nearest neighbour hopping t' between the next-nearest-neighbour sites $\langle\langle i, j\rangle\rangle$ introduces an additional level of complexity. It breaks the particle-hole symmetry of the Hubbard model. Significant work have focused on the $t-t'$ Hubbard model on a two-dimensional square lattice, due to its relevance for the description of the low-energy physics of the high-temperature copper-oxide superconductors. A non-zero t'-hopping permits the develop-

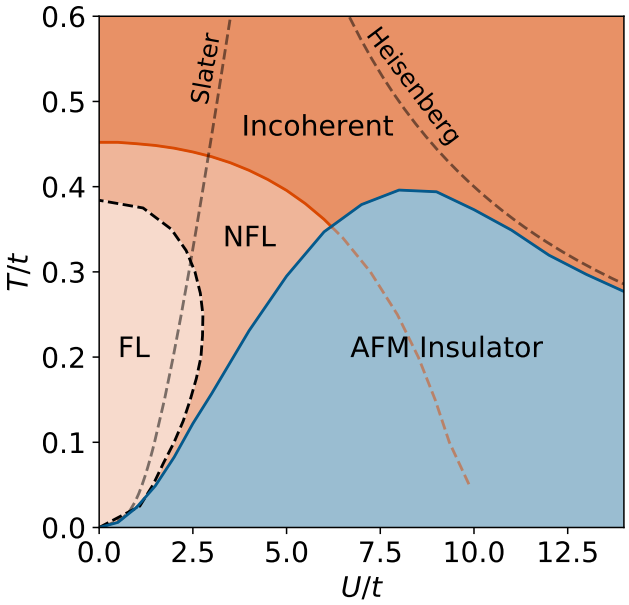

Figure 2.8: A sketch of the phase diagram of the half-filled Hubbard model for repulsive U allowing for AFM ordering. The blue, light-orange and dark-orange regions denotes the AFM insulator, the FL metal with coherent quasiparticles, and the incoherent region without quasiparticles, respectively. In addition, an intermediate region emerges, characterised by NFL behaviour. For comparison, the Slater estimate at weak-U and the Heisenberg estimate at strong-U for AFM are included. Values for the AFM phase boundary and incoherent region are given by the single-site DMFT for a two-dimensional square lattice, with values calculated in Ref. [138] for the AFM phase boundary and in Ref. [137] for the incoherent region. Values for the NFL region are qualitative, and take inspiration from the work of Refs. [136, 137] calculated for the half-filled Hubbard model on a two-dimensional square lattice with nearest-neighbour hopping. Note, Mott physics is not indicated within the phase diagram for convenience.

ment of various collective behaviour: the development of d-wave superconductivity at finite-doping and temperature [144–146], the formation of a stripe-ordered phase [147], and strange metallic transport associated with linear-T resistivity [148]. The d-wave superconducting state, the stripe-ordered state and the strange metal are topics of relevance in the copper-oxide compounds. This brief review has focused on a d-dimensional cubic lattice, however, the Hubbard model on other lattice geometries allows for the introduction of additional collective phenomena due to, e.g., frustration. An underlying lattice geometry of particular attention currently is the triangular Hubbard model which can be simulated using the low-energy degrees of freedom of the Moiré physics in twisted bilayer systems [149].

Attractive U Hubbard model

In contrast with the repulsive U regime, less attention has been paid to the regime of attractive U, dominated by charge and s-wave superconducting (s-SC) fluctuations rather than spin fluctuations [133, 150–173]. The reason is due to the repulsive nature the Coulomb interaction between electrons. Nevertheless, it is known that coupling

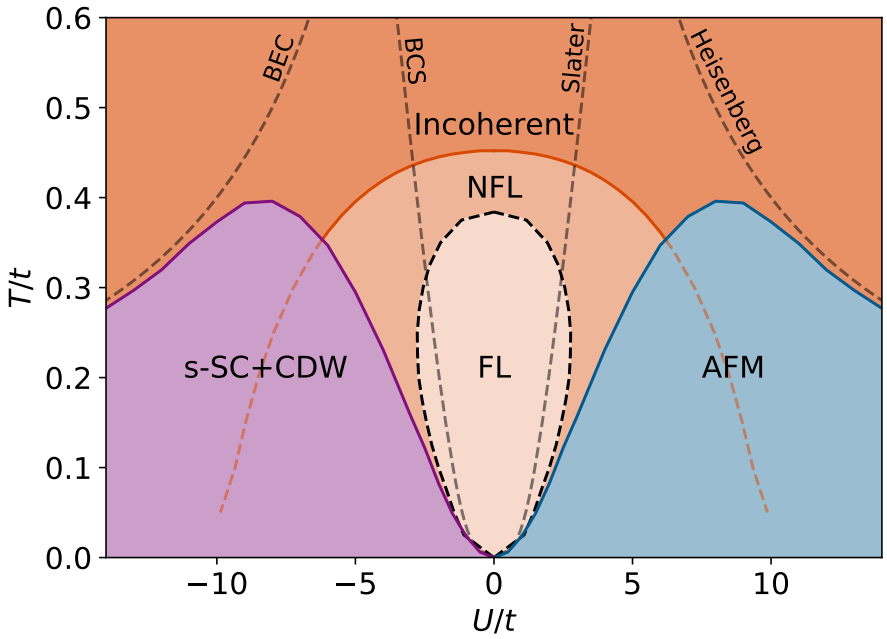

Figure 2.9: A sketch of the phase diagram of the half-filled Hubbard model for repulsive and attractive U allowing for both AFM and s-SC+CDW ordering. The blue, purple, light-orange and dark-orange regions denotes the AFM ordering, s-SC+CDW ordering, the FL metal with coherent quasiparticles, and the incoherent region without quasiparticles, respectively. In addition, an intermediate region emerges, characterised by NFL behaviour. In weak-coupling regime, the AFM Slater and BCS estimates are included in the repulsive and attractive U regimes, respectively, for comparison. In the strong-coupling regime, the AFM Heisenberg and BEC estimates are included in the repulsive and attractive U regimes, respectively, for comparison. Values for the AFM phase boundary and incoherent region in the repulsive U regime are given by the single-site DMFT for a two-dimensional square lattice, with values calculated in Ref. [138] for the AFM phase boundary and in Ref. [137] for the incoherent region. Values for the NFL region in the repulsive U regime are qualitative, and take inspiration from the work of Refs. [136, 137] evaluated on a two-dimensional square lattice with only nearest-neighbour hopping. Exploiting the staggered particle-hole symmetry allows to construct the s-SC+CDW phase boundary, the incoherent region and the NFL region in the attractive U regime. Note, Mott physics is not indicated within the phase diagram for convenience.

electrons to external degrees of freedom, e.g., phonons, may lead to an effective low-energy electronic system with attractive interactions. Specific examples are doped fullerenes [174] and one-dimensional copper oxide chains [175], $Ba_{1-x}K_xBiO_3$ [176,177], $LaAlO_3/SrTiO_3$ interfaces [178–181], and selected d- and f- transition metals [182,183]. In addition, fermionic systems with attractive local interactions are realizable in cold atom experiments [173,184–186]. This gives physical motivation to treat the attractive regime, beyond that of a purely theoretical interest.

For the single-orbital Hubbard model on a bipartite lattice with particle-hole symmetry, e.g., with d-dimensional cubic lattice geometry with a nearest-neighbour hopping, a staggered particle-hole symmetry connects the repulsive and attractive U regimes [158,159]. The staggered particle-hole symmetry of the Hubbard model is asso-

ciated with η-pairing [158,159]. It displays an underlying SU(2) pseudo-spin symmetry of the half-filled Hubbard model, combining the s-wave pairing and charge degrees of freedom in a single Nambu spinor [158, 159]. The Nambu basis, a useful representation for a unified description of the s-wave pairing in the particle-particle channel and charge fluctuations in the particle-hole channel, is conveniently written in real-space as:

$$\hat{\psi}_{j\uparrow} = \hat{c}_{j\uparrow} \quad \hat{\psi}_{j\downarrow} = (-1)^j \hat{c}^\dagger_{j\downarrow} \quad \hat{\psi}^\dagger_{j\uparrow} = \hat{c}^\dagger_{j\uparrow} \quad \hat{\psi}^\dagger_{j\downarrow} = (-1)^j \hat{c}_{j\downarrow}. \tag{2.23}$$

Equivalently, the Nambu spinors may be written in the quasi-momentum basis:

$$\hat{\psi}_{\mathbf{k}\uparrow} = \hat{c}_{\mathbf{k}\uparrow} \quad \hat{\psi}_{\mathbf{k}\downarrow} = \hat{c}^\dagger_{-\mathbf{k}+\mathbf{M},\downarrow} \quad \hat{\psi}^\dagger_{\mathbf{k}\uparrow} = \hat{c}^\dagger_{\mathbf{k}\uparrow} \quad \hat{\psi}^\dagger_{\mathbf{k}\downarrow} = \hat{c}_{-\mathbf{k}+\mathbf{M},\downarrow} \tag{2.24}$$

where $\mathbf{M} \equiv (\pi, \pi)$. Analogously to the collective spin fluctuations, the collective pseudo-spin fluctuations are associated with the pseudo-spin density,

$$\hat{n}^{s_p}_{\mathbf{Q}} \equiv \frac{1}{N} \sum_{\mathbf{k},\sigma\sigma'} \hat{\psi}^\dagger_{\mathbf{k}+\mathbf{Q},\sigma} \sigma^{s_p}_{\sigma\sigma'} \hat{\psi}_{\mathbf{k}\sigma'}. \tag{2.25}$$

Hence, $\hat{n}^{s_p}_{\mathbf{Q}}$ refers to the s-wave pairing ($s_p \in \{x, y\}$) and the charge fluctuations ($s_p \in \{z\}$).

The attractive U stabilizes collective pseudo-spin fluctuations, leading to the development of a combined s-wave superconducting (s-SC) and charge-density wave (CDW) phase (denoted as "s-SC + CDW") as an analogue of the AFM phase[1]. The s-SC and CDW phases are associated with long-range and regular patterns, with the s-SC phase being associated with formation of Cooper pairs and with the CDW phase being associated with charges distributed in a checker-board-like pattern. In the weak-coupling limit, the Cooper pairs in the s-SC + CDW phase form a Bardeen–Cooper–Schrieffer (BCS) theory-like state [154, 156, 162, 165, 187], with delocalised Cooper pairs [22, 23], analogously to the Slater-type AFM state. In the strong-coupling limit, the underlying mechanism of the the s-SC + CDW phase is the formation of localised Cooper pairs in the vein of a Bose-Einstein condensate (BEC) [152,162,163,166,171,187,188], as an analogue of the Heisenberg-type AFM state. At intermediate interaction strength, a superfluid (SF) region emerges in the crossover between the BCS and BEC physics [166,171]. By exploiting the staggered particle-hole symmetry, we expect at low-temperatures the emergence of a FL in the weak-coupling limit, which develops into a NFL as a precursor to the s-SC + CDW and the incoherent regions. As summary, a sketch of the repulsive and attractive U phase diagram is displayed in Fig. 2.9.

Constraining the phase diagram to the pseudo-spin analogue of the PM state, an analogue of the Mott-Hubbard first-order metal-to-insulator transition appears as a transition from a weakly correlated metal to an insulator characterised by local pairs (LP) [164, 173]. By analogy, as the Mott insulator forms due to freezing of the charge degrees of freedom, the LP insulator forms due to freezing of the spin$-z$ degrees of freedom. Alike the Mott insulator, the LP insulator forbid the transport of Cooper pairs, due to the effective penalty associated with a spin-up electron and spin-down hole, or a spin-down electron and spin-up hole, occupying the same site. By the symmetry considerations, we expect a finite coexistence region at finite-temperatures ending at a critical points, above which a supercritical Widom line appears. We note

[1] A common misconception is that the attractive U regime is only composed of s-wave pairing degrees of freedom or the charge degrees of freedom.

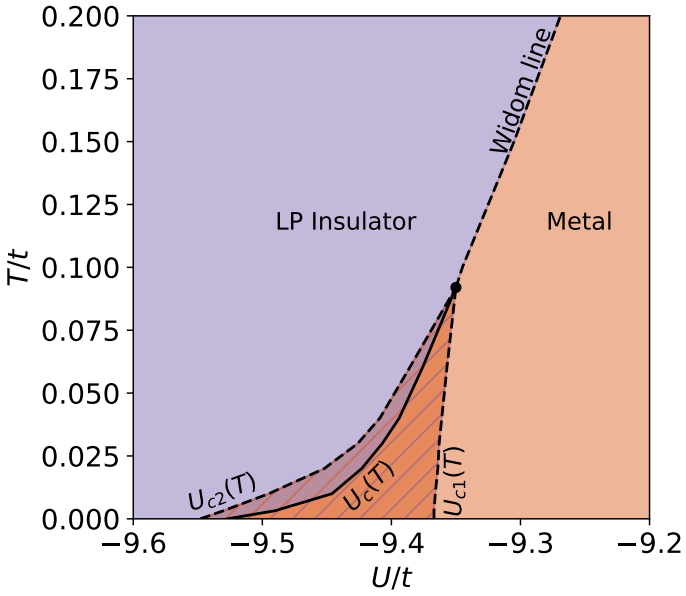

Figure 2.10: A sketch of the phase diagram of the half-filled Hubbard model for attractive U within the single-site DMFT approximation to the LP phase, acting as an analogue of the Mott-Hubbard metal-to-insulator transition displayed in Fig. 2.7. An orange and purple region denote a metallic and insulating state. In the vicinity of the thermodynamic first-order phase boundary $U_c(T)$ between the metal and insulator, a coexistence region emerges denoted by two regions with hatched patterns. It is enclosed by $U_{c1}(T)$ and $U_{c2}(T)$, and is associated with the occurrence of an insulating or metallic metastable state in addition to the stable metallic or insulating state, respectively. The coexistence regions ends at a critical point, followed by a supercritical Widom line signaling the smooth crossover between the metallic and insulating solutions. Exploiting the staggered particle-hole symmetry, all values are given by single-site DMFT constrained to a PM solution on a two-dimensional square lattice with a repulsive U, with values calculated in Ref. [110].

that the observed SF region seems to be located in the vicinity of the supercritical Widom-line.

Doping the attractive Hubbard model away from half-filling breaks the SU(2) pseudo-spin symmetry, decoupling the s-wave pairing and charge degrees of freedom. This leads to the promotion of the s-wave pairing degrees of freedom to the detriment of the charge degrees of freedom, which become less stable [153, 172]. While the SU(2) pseudo-spin symmetry is broken, the connection between the attractive and repulsive Hubbard model remains, with the staggered particle-hole transformation of the doped attractive Hubbard model being analogous to the half-filled repulsive Hubbard model with an external Zeeman field [189].

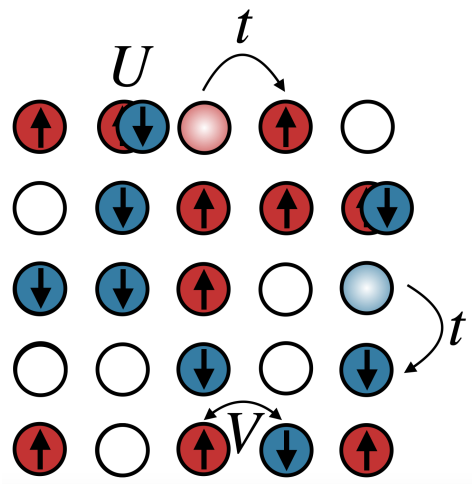

Figure 2.11: Sketch of the extended Hubbard model on a two-dimensional square lattice, with the coloured circles denoting electrons with a spin-polarisation denoted by the up and down arrows. Note the hopping parameter t is associated with the probability of jumping between nearest-neighbour sites, the local U is associated with double-occupied sites and the non-local V is associated with electrons occupying nearest-neighbour sites.

2.3.2 Extended Hubbard model

The single-orbital extended Hubbard model extends the single-orbital Hubbard model through the introduction of a nonlocal interaction V, with the Hamiltonian defined as

$$\hat{H} = -\sum_{\langle i,j\rangle,\sigma} t_{ij}\hat{c}^{\dagger}_{i\sigma}\hat{c}_{j\sigma} + U\sum_{i}\hat{n}_{i\uparrow}\hat{n}_{i\downarrow} + \frac{1}{2}\sum_{\langle i,j\rangle,\sigma\sigma'} V_{ij}\hat{n}_{i\sigma}\hat{n}_{j\sigma'} - \mu\sum_{i,\sigma}\hat{n}_{i\sigma}. \tag{2.26}$$

Thus, the Coulomb interaction between electronic densities $\hat{n}_{i\sigma} = \hat{c}^{\dagger}_{i\sigma}\hat{c}_{i\sigma}$ is modelled by an on-site U interaction and a nonlocal V_{ij} interaction. Our considerations, as commonly is the case, will be restricted to a nonlocal interaction between nearest-neighbour sites only, denoted as V. For a given lattice geometry and filling, the physics of this model is thus determined by the competition between two tunable parameters: U/t and V/t.

Repulsive U, V extended Hubbard model

Considerable insight has been acquired for the repulsive extended Hubbard model, elucidating the interplay between collective charge and spin fluctuations [150, 190–202] and between collective charge fluctuations and Mott physics [203–207]. In particular, significant focus has been given to the extended Hubbard model at half-filling with nearest-neighbour interaction V on a one-dimension (1D) chain [45, 150, 190, 192, 193, 208–210] and on a two-dimensional square lattice [103, 194–200, 203, 205, 211–217]. The earliest considerations of the extended Hubbard model were already implicit in the initial work of J. Hubbard in 1963 [42]. However, the first studies of the model occurred in the 1970's, with studies of the strong [45, 150] and weak coupling limits of the half-filled 1D chain [190, 208]. Together with an access to the intermediate coupling regime by early numerical exact diagonalisation and lattice Monte Carlo calculations [192, 193], the phase diagram of the 1D extended Hubbard model was predicted to be composed of

regions of strong charge density wave (CDW) and AFM fluctuations, with a CDW-AFM transition occurring in the vicinity of $U = 2V$. The transition was later discovered to be modified in the weak coupling limit by an intermediate bond-order wave (BOW) state [209, 210].

The extended Hubbard model on a two-dimensional square lattice has been found to display a phase diagram similar to the 1D counterpart, besides the apparent lack of an intermediate BOW phase. The repulsive U stabilises collective spin fluctuations [116], which may compete with charge fluctuations driven by a strong repulsive V [45, 218]. In particular, the system reveals a checkerboard CDW pattern, which interplays with strong AFM fluctuations in the vicinity of a CDW-AFM transition line $U = 4V$ [194, 195, 219]. Furthermore, the competition induces a coexistence region of charge- and spin-ordered states in the vicinity of the first-order CDW-AFM transition line [199]. In the weak-coupling limit of U and V, the collective orderings give way for a metallic phase. Depending on the value of temperature and interaction strength, the nature of the metal is FL- or NFL-like, as discussed for the Hubbard model. Within the weak-coupling regime, the metallic phase is connected to the regions of strong collective CDW and AFM fluctuations through second-order phase transitions. The CDW phase boundary occurs along $V = U/8 + \text{cst}$ at weak coupling [213], while the AFM phase boundary starts at a critical U, which extends to the $V = U/4$ phase boundary at intermediate coupling [199]. The behaviour at intermediate coupling is followed by $V \sim U + \text{cst}$ in the strong coupling limit [203, 204, 214, 216, 220, 221]. We include a sketch summarising the interplaying collective CDW and AFM fluctuations in the finite temperature U, V phase diagram of the half-filled extended Hubbard model on the two-dimensional square lattice in Fig. 2.12.

The extended Hubbard model Eq. (2.26) displays two symmetries of importance in the repulsive U, V region: the continuous SU(2) symmetry associated with the spin degrees of freedom and the discrete particle-hole symmetry related to the charge degrees of freedom. By the Mermin-Wagner theorem [122–124], the AFM ordering is excluded in two-dimensional extended Hubbard model on a square lattice, due to the continuous nature of the underlying symmetry. Thus, the regime of strong collective AFM fluctuations is, strictly speaking, not a phase. However, in this thesis the AFM phase will refer to a slightly broader definition of short-range AFM ordering, which transforms to a true phase for a quasi-two-dimensional system. In contrast, due to the discrete symmetry nature of the charge degrees of freedom, the CDW phase is not forbidden by the Mermin-Wagner theorem.

Constraining to a PM solution, the Mott insulating phase is stable with respect to the nonlocal V interaction. However, the width of the coexistence region associated with the first-order Mott-Hubbard metal-to-insulator transition decreases with increasing nonlocal V interaction [203, 204]. At sufficiently large V, an interplay between the Mott state and the CDW phase emerges [203, 204]. This leads to the emergence of a transition between the CDW and the Mott insulator, in addition, to the first-order Mott-Hubbard metal-to-insulator transition previously reviewed.

In comparison to the half-filled Hubbard model with repulsive interaction U, intricate details of the half-filled extended Hubbard model have not been studied as extensively. This is even more pronounced in the doped and $t - t'$ extended Hubbard models, which is counter to the importance of the doped $t-t'$ extended Hubbard model as one of the simplest low-energy models for the correlation effects in the CuO_2 layers of the copper-oxides compounds [99–102]. By doping the extended Hubbard model away

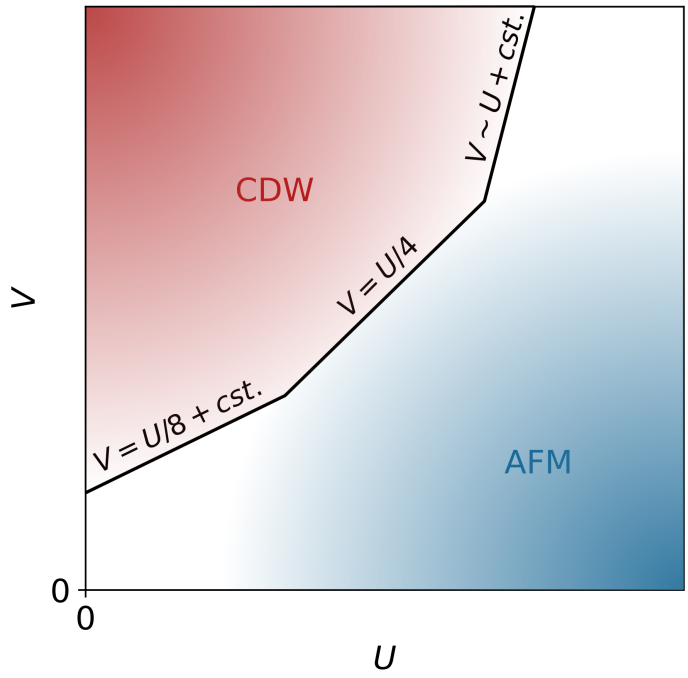

Figure 2.12: A sketch of the phase diagram of the quasi-two-dimensional half-filled extended Hubbard model with repulsive interactions U and V at sufficiently low, but finite, temperature, allowing for antiferromagnetic (AFM) and charge density wave (CDW) fluctuations. Beyond a critical local interaction, a regime of dominant AFM fluctuations is expected, while strong nonlocal interactions drive the system into a CDW phase. At low U, V the orderings give way for a normal metal phase. The schematic phase boundaries of the CDW phase are determined by the asymptotic expressions $V = U/8 + \text{cst}$ at weak coupling [213], $V = U/4$ at intermediate coupling [194, 195, 219], and $V \simeq U + \text{cst}$ at strong coupling [203, 204, 214, 216, 220, 221]. At weak to intermediate coupling, the AFM regime extrapolates from a critical U at vanishing V to the $V = U/4$ phase boundary [199].

from half-filling, the collective charge and spin fluctuations weaken and may develop incommensurate ordering.

Partially and fully attractive U, V extended Hubbard model

In comparison to the repulsive U, V extended Hubbard model, less research has been aimed at the interaction regimes with a partially or fully attractive interaction [198, 212, 222–228]. Nevertheless, the regime gives a suitable framework for the investigation of interplaying charge and pairing degrees of freedom. In addition to the attractive U driving collective pseudo-spin fluctuations, attractive V stabilises collective phase separation (PS) fluctuations in the charge channel [225]. Simultaneously, collective p-wave and d-wave superconducting fluctuations may form in the regime of attractive V [227,228]. At half-filling, the PS state is associated with the ordering vector $\mathbf{Q} \to \mathbf{\Gamma}$, with $\Gamma = \mathbf{0}$, and corresponds to the formation of broad puddles with uniform filling larger or smaller than the average filling of the system. In the absence of a nonlocal interaction, the SU(2) pseudo-spin symmetry of the half-filled attractive Hubbard model is conserved. By turning on the nonlocal interaction V, the "CDW + s-SC" coexis-

tence phase breaks down, with the system entering into a CDW and s-SC phase by the repulsive and attractive V, respectively. For a finite V, we note that the attractive U extended Hubbard model at half-filling is analogous, by the staggered particle-hole transformation, to the repulsive Hubbard model with an additional $V_{\mathbf{q}} n^{s,z}_{\mathbf{q}} n^{s,z}_{-\mathbf{q}}$ term describing a nearest-neighbour ferromagnetic (FM) or AFM exchange coupling in the spin-z direction.

Motivated by the well-controlled nature of the extended Hubbard model as a framework for studying the interplay of collective fluctuations in a strongly correlated system, this thesis seeks to conduct an exploration of the phase diagram. To evaluate the collective properties of the phase diagram, which have been reviewed throughout this section, many-body techniques are required. Connecting to the quantum lattice models introduced in the current chapter, the following chapter aims at reviewing the available many-body methods for describing competing collective fluctuations.

Chapter 3

Many-body techniques for describing collective phenomena

"Do to others what you want them to do to you." - Matthew 7:12

An extensive selection of many-body techniques have been developed to determine the properties of quantum lattice models. The methods range from approximate to exact techniques, with observables evaluated from different computational objects, e.g., the ground-state density, the many-body Green's function, or the ground-state wavefunction. These methods involve different strengths and weaknesses related to their, e.g., accuracy, convergence within the parameter space, and possibility to resolve different collective phenomena. Throughout this chapter, we seek to give a broad overview on the available theoretical techniques utilised to study interplaying collective fluctuations in quantum lattice models. Most introduced techniques will be directly relevant for the theoretical developments in this thesis. However, a few techniques will be briefly discussed only for completeness.

The chapter begins with a general review on the many-body Green's function, and the related susceptibilities, used within many-body approach. It is followed by a section reviewing mean-field theory, with focus on techniques relevant for the current thesis, and a section reviewing dynamical mean-field theory and its extensions. The chapter concludes with a brief review on numerically exact techniques for quantum lattice systems based on exact diagonalisation, quantum Monte Carlo and tensor network techniques.

3.1 Many-body Green's function

Two fundamental issues composes the quantum many-body problem, discussed in the previous chapter. It is associated with the unfeasible nature of both computing and storing the exact wavefunction of a general many-electron problem. However, in the large majority of experimental and theoretical studies, one is not concerned with the exact form of the wavefunction. One is rather concerned with a selection of observables associated with single-particle or two-particle operators. In fact, the evaluation of few-particle observables does not necessitate the full knowledge of the wavefunction, as it contains significant redundancies. Thus, it becomes desirable to work with computational objects which allows for the evaluation of only few-particle observables, avoiding the utilisation of the full wavefunction.

3.1.1 Observables and correlation functions

From the theoretical perspective, an observable is equivalent to the average value (expectation value) of its corresponding operator $\hat{O}$, defined by:

$$\langle \hat{O} \rangle = \mathrm{Tr}\left[\hat{O}\hat{\rho}\right] \tag{3.1}$$

expressed within the density matrix formalism pioneered by von Neumann. Here Tr denotes a trace with respect to the states $\{|\Psi_n\rangle,\ n = 1, 2, ...\}$ spanning the configuration space of the quantum system:

$$\mathrm{Tr}[\hat{A}] \equiv \sum_n \langle \Psi_n | \hat{A} | \Psi_n \rangle. \tag{3.2}$$

The density matrix $\hat{\rho}$ describes the uncertainty of the state occupied by the system, and is determined by the probabilities λ_n of the system occupying the different states:

$$\hat{\rho} \equiv \sum_n \lambda_n |\Psi_n\rangle\langle\Psi_n|, \quad \text{with} \quad \sum_n \lambda_n = 1 \quad \text{and} \quad 0 \leq \lambda_n \leq 1. \tag{3.3}$$

Potential sources of the uncertainty of the state of the system may be due to, e.g., uncertainty in the preparation of the state, or the statistical nature of a system at thermal equilibrium with a finite temperature.

For a system at thermal equilibrium, the statistical distribution of probabilities is determined in the grand-canonical ensemble by the Boltzmann probability distribution:

$$\lambda_n = \frac{1}{\mathcal{Z}} e^{-\beta(E_n - \mu)}, \quad \text{with} \quad \mathcal{Z} = \sum_n e^{-\beta(E_n - \mu)}, \tag{3.4}$$

where E_n are the eigenenergies for each state $|\Psi_n\rangle$, $\beta = 1/k_B T$ is the inverse temperature and k_B is Boltzmann's constant. Governing the thermal properties of the system is the partition function $\mathcal{Z}$, which is directly connected to the free energy of the system:

$$\mathcal{F} = -k_B T \ln \mathcal{Z}. \tag{3.5}$$

For a quantum system at finite temperature, an explicit rewriting of Eq. (3.1) gives for any thermally-averaged observable:

$$\langle \hat{O} \rangle = \frac{\mathrm{Tr}\left[e^{-\beta(\hat{H} - \mu\hat{N})}\hat{O}\right]}{\mathrm{Tr}\left[e^{-\beta(\hat{H} - \mu\hat{N})}\right]}, \tag{3.6}$$

where the Hamiltonian $\hat{H}$ is employed to rewrite the form of the density matrix $\hat{\rho}$, through the introduction of the particle-number operator $\hat{N}$.

A class of convenient functions for calculating any n-particle observable are the n-particle correlation functions,

$$\langle \hat{c}^\dagger_{\alpha_1} \hat{c}^\dagger_{\alpha_2} ... \hat{c}_{\alpha'_{n-1}} \hat{c}_{\alpha'_n} \rangle, \tag{3.7}$$

defined as the expectation value of $2n$ number of creation and annihilation operators. Importantly, computational techniques exist for the direct evaluation of classes of correlation functions, avoiding the construction of the more complex wavefunction. A class of correlation functions of fundamental importance within the field of condensed matter theory are the many-body Green's functions. In particular, central to the many-body Green's function techniques is the single-particle Green's function, a single-particle correlation function.

3.1.2 Retarded Green's function

The retarded Green's function is a particular single-particle correlation function:

$$G_{ij}(t-t') = -i\theta(t-t')\left\langle\left\{\hat{c}_i(t), \hat{c}_j^\dagger(t')\right\}\right\rangle. \tag{3.8}$$

Its time-dependence enters through the time-dependence of the creation and annihilation operators:

$$\hat{c}_j(t) \equiv \hat{U}(-t)\hat{c}_j\hat{U}(t), \quad \hat{c}_j^\dagger(t) \equiv \hat{U}(-t)\hat{c}_j^\dagger\hat{U}(t) \tag{3.9}$$

in which the time-evolution operator $\hat{U}(t)$ has been introduced:

$$\hat{U}(t) \equiv e^{-i(\hat{H}-\mu\hat{N})t}. \tag{3.10}$$

In particular, the function is denoted as the *retarded* one-particle Green's function due to causality being enforced through the Heaviside function $\theta(t-t')$. Note that the Green's function is formulate within the Heisenberg picture, in which the time-dependence is incorporated within the operators, while the states are time-independent. A physically equivalent formulation is the Schrödinger picture, in which the time-dependence is rather incorporated within the states, while the operators are time-independent.

Computational techniques exists for the evaluation of the retarded Green's function, motivating its usage. However, the utility of the retarded one-particle Green's function originates in the information of the system it contains:

- Any thermally-averaged single-particle observable is directly accessible by the retarded one-particle Green's function.

- By the Galitskii-Migdal formula, the thermally-averaged energy, as determined by the Hamiltonian, i.e. a two-particle observable, is accessible.

A particularly important single-particle observable accessible by the Green's function is the single-particle excitation spectrum. It allows to give an intuitive view of the physical interpretation of the Green's function. The Green's function describes the probability amplitude of the creation (or annihilation) of an electron in the position j at an earlier time t', which propagates and is subsequently annihilated (or created) at the position i at the later time t. Therefore, the function captures single-particle excitations associated with the creation of an electron or hole, and their propagation. Furthermore, this allows for a natural connection to photoemission spectroscopy (PES) and inverse photoemission spectroscopy (IPES) techniques, see Fig. 3.1 for a sketch of an ARPES experiment. The creation of a hole and its subsequent propagation describes the underlying mechanism of a PES experiment, associated with the photoemission of electrons through the photoelectric effect, describing the occupied density of states. Similarly, the IPES experiment measuring the unoccupied density of states, based on the inverse photoelectric effect by the emission of light by incident electrons, is described by the underlying mechanism of the creation of an electron and its subsequent propagation.

Limiting our considerations to a periodic lattice structure and equilibrium for a system determined by a time-independent Hamiltonian, one may express the retarded

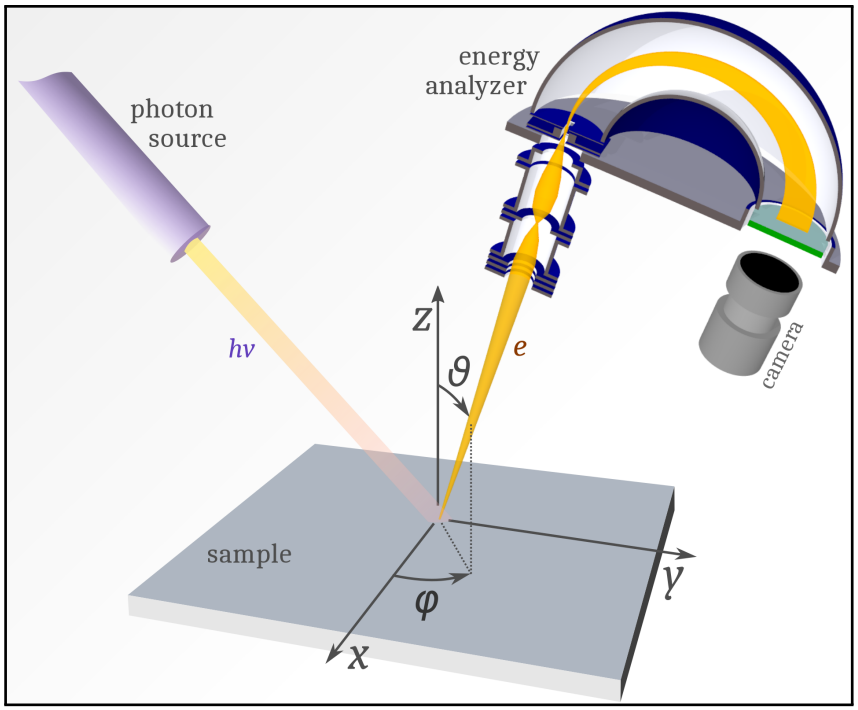

Figure 3.1: Sketch of the experimental setup of an ARPES experiment. The surface of material is irradiate with a monochromatic source of photons with the energy $h\nu$, leading to the emission of electrons through the photoelectric effect. Photoemitted electrons escaping the surface of the materials are then captured by an energy analyser oriented at a certain angle θ, which measures their kinetic energy $E_{\mathbf{k}}$. This permits to evaluate the intensity of electrons in momentum and frequency space. Image taken from Ref. [229].

Green's function in quasi-momentum and frequency space by application of the Fourier transform:

$$G_{\mathbf{k},\omega} = \sum_{\mathbf{r}_{ij}} \int d\tau \;\; e^{-i\mathbf{k}\cdot\mathbf{r}_{ij}+i\omega\tau} G_{\mathbf{r}_{ij}}(\tau), \;\; \text{with} \;\; \mathbf{r}_{ij} \equiv \mathbf{R}_i - \mathbf{R}_j \;\; \text{and} \;\; \tau = t - t'. \tag{3.11}$$

Here, one exploits that the spatial and temporal dependency of the retarded Green's function only enters through the differences $\mathbf{r}_{ij}$ and τ. Assuming only one-photon processes, the measured intensity of an ARPES experiment is directly proportional to the spectral function, in turn related to the retarded Green's function:

$$A(\mathbf{k},\omega) = -\frac{1}{\pi}\mathrm{Im}[G_{\mathbf{k},\omega}]. \tag{3.12}$$

The spectral function describes the single-particle excitation spectrum, as the function describes the probability of a single-particle excitation occurring at a certain momentum $\mathbf{k}$ and frequency ω.

The retarded Green's function contains information of the physical system, however computing the function directly is inconvenient. For example, the evaluation of the retarded Green's function at zero-temperature is conventionally performed through the calculation of time-ordered Green's function, which allows for an easier evaluation. While the time-ordered Green's function is easier to evaluate, it retains sufficient information for the construction of the retarded Green's function. The time-ordered Green's

function is a single-particle correlation function defined as

$$G_{ij}^{T}(t-t') = -i\left\langle \mathcal{T}\left(\hat{c}_i(t)\hat{c}_j^{\dagger}(t')\right)\right\rangle, \tag{3.13}$$

where $\mathcal{T}$ is the time-ordering operator, ordering the creation and annihilation operators from left to right with decreasing time coordinate, with a sign change under interchange of fermions. A favourable aspect of the time-ordered G^T is that it allows for a construction through perturbation theory. This motivates employing the time-ordered G^T. In perturbation theory, the Hamiltonian $\hat{H}$ is separated in a noninteracting $\hat{H}_0$ and interaction term $\hat{V}$, i.e. $\hat{H} = \hat{H}_0 + \hat{V}$. A diagrammatic construction of the interacting time-ordered G^T then follows from a series expansion in the interacting term $\hat{V}$ and the noninteracting G_0^T, defined by $\hat{H}_0$ and analytically solvable. In contrast, for a system at finite temperature, the time-ordered G^T becomes inconvenient due to the emergence of difficulties in its construction by a diagrammatic expansion. The origin of the problem is due to the time-evolution and the density matrix requiring two separate series expansions, which leads to the introduction of the *Matsubara* Green's function.

3.1.3 Matsubara Green's function

For a system at thermal equilibrium, it is convenient to work on the imaginary-time $\tau = it$ axis, as it allows to exploit the similarity of the density matrix operator and the time-evolution operator,

$$\hat{U}(\tau) \equiv e^{-(\hat{H}-\mu\hat{N})\tau}. \tag{3.14}$$

Working on the imaginary time axis, one introduces the Matsubara Green's function $\mathcal{G}$, a single-particle correlation function defined as:

$$\mathcal{G}_{ij}(\tau-\tau') = -\left\langle \mathcal{T}\left(\hat{c}_i(\tau)\hat{c}_j^{\dagger}(\tau')\right)\right\rangle. \tag{3.15}$$

Here, using the time-evolution operator on the imaginary-time axis, the creation and annihilation operators are written in the modified Heisenberg picture,

$$\hat{c}_j(\tau) \equiv \hat{U}(-\tau)\hat{c}_\tau\hat{U}(\tau), \quad \hat{c}_j^{\dagger}(\tau) \equiv \hat{U}(-\tau)\hat{c}_j^{\dagger}\hat{U}(\tau). \tag{3.16}$$

Note the particular property $[\hat{c}_j(\tau)]^{\dagger} \neq \hat{c}_j^{\dagger}(\tau)$ along the imaginary-time axis. Acting identically to its counterpart on the real-time axis, introduced above, $\mathcal{T}$ is the imaginary time-ordering operator. Due to the identical form of the density matrix operator and the time-evolution operator, the Matsubara Green's function can be evaluated as a well-defined series expansion, allowing for an intuitive diagrammatic description.

The Matsubara Green's function contains several distinct properties. It is a 2β-periodic function and is an odd (even) function in τ for fermions (bosons). This leads to $\mathcal{G}(\tau) = \pm\mathcal{G}(\tau-\beta)$, with a negative (positive) sign for fermions (bosons). The periodicity in imaginary time τ allows to express the Matsubara Green's function as a Fourier series in odd (even) terms for fermions (bosons):

$$\mathcal{G}_{ij}(\tau-\tau') = \frac{1}{\beta}\sum_{n=-\infty}^{\infty} e^{-i\omega_n(\tau-\tau')}\mathcal{G}_{ij,\omega_n}. \tag{3.17}$$

Here $\mathcal{G}_{ij,\omega_n}$ are the coefficients of the Fourier series, with the introduction of the bosonic ω_n and fermionic ν_n Matsubara frequencies:

$$\omega_n = 2n\pi/\beta, \qquad \text{for bosons,} \tag{3.18}$$

$$\nu_n = (2n+1)\pi/\beta, \quad \text{for fermions.} \tag{3.19}$$

In order to avoid confusion, we will in this thesis employ ω_n and ν_n to specify bosonic and fermionic Matsubata frequencies, respectively. As for the retarded Green's function on the real-time axis, one may further exploit the existence of the underlying periodic lattice structures to Fourier transform from real space to quasi-momentum space.

Diagonalisation of the noninteracting Hamiltonian allows for the construction of the noninteracting Matsubara Green's function:

$$\mathcal{G}^0_{\mathbf{k},\nu_n} = \frac{1}{i\nu_n + \mu - \epsilon_{\mathbf{k}}}, \tag{3.20}$$

for convenience, written for a single-orbital Hamiltonian with a bare dispersion $\epsilon_{\mathbf{k}}$. However, diagonalisation techniques are heavily constrained in their treatment of the interacting Hamiltonian, motivating the usage of many-body techniques such as, e.g., diagrammatic techniques in order to develop the interacting Matsubara Green's function. A useful function capturing many-body correlation effects is the self-energy $\Sigma_{\mathbf{k},\nu_n}$, defined by the Dyson equation

$$\Sigma_{\mathbf{k},\nu_n} = \left[\mathcal{G}^0_{\mathbf{k},\nu_n}\right]^{-1} - \left[\mathcal{G}_{\mathbf{k},\nu_n}\right]^{-1}, \tag{3.21}$$

allowing for an explicit connection between the noninteracting and interacting Matsubara Green's function. Furthermore, it permits for a concise expression of the interacting Matsubara Green's function

$$\mathcal{G}_{\mathbf{k},\nu_n} = \frac{1}{i\nu_n + \mu - \epsilon_{\mathbf{k}} - \Sigma_{\mathbf{k},\nu_n}}. \tag{3.22}$$

Evaluation of the self-energy itself is conducted within a wide range of different many-body techniques (diagrammatic or nonperturbative techniques), in turn determining the interacting Matsubara Green's function through the Dyson equation (3.21).

Physical properties of a system is contained within the Matsubara Green's function directly and indirectly. Any thermally-averaged single-particle static observable is directly accessible, however, dynamical observables are only indirectly accessible, requiring full knowledge of the retarded Green's function on the real frequency axis. For example, the spectral function and its description of the single-particle excitation spectrum associated with removal or addition of electrons relevant for PES and IPES experiments are not directly accessible from the Matsubara Green's function. A Wick's rotation from the Matsubara Green's function to the retarded Green's function is required, associated with an analytic continuation from the real axis to the complex plane. To illustrate the analytic continuation, we consider the noninteracting Matsubara and retarded Green's functions,

$$\mathcal{G}^0_{\mathbf{k},\nu_n} = \frac{1}{i\nu_n + \mu - \epsilon_{\mathbf{k}}} \quad \text{and} \quad G^0_{\mathbf{k},\omega} = \frac{1}{\omega + \mu - \epsilon_{\mathbf{k}} + i\eta}, \tag{3.23}$$

with an infinitesimal $\eta \to 0^+$ for the retarded Green's function, associated with the physical properties being contained within the upper complex plane. The analytic

continuation from the imaginary frequency $i\nu_n$ to the real frequency ω is identified to be associated with a simple replacement $i\nu_n = \omega + i\eta$, which furthermore holds for their interacting representatives. In practice, however, the analytic form is often not accessible, thus requiring the usage of numerical procedures to estimate the analytic continuation. The problem of numerically estimating the analytic continuation is a difficult one [230–239], and numerical procedures are in general afflicted with an ill-defined nature.

3.1.4 Susceptibilities

Not all physical properties of a system are described by single-particle observables. The description above for the single-particle Green's function can be generalised to the n-particle Green's function, which contains information for computing any n-particle observables. However, in general, the computational complexity in computing n-particle Green's function grows significantly with increasing n. However, full knowledge of the two-particle Green's function is often not required for the evaluation of two-particle observables. We limit our considerations to an important class of two-particle observables: susceptibilities, which governs the response of a system to an external perturbation.

A natural description of the response of a system to small external perturbations is given by linear response theory. Consider the response/deviation of an observable, associated with the operator $\hat{O}_1(t)$, due to a small external perturbation $\theta(t)\hat{O}_2(t)\delta h(t)$, where $\theta(t)$ enforces causality. The response of $\hat{O}_1(t)$ due to the small external field $\delta h(t)$ is given by the Kubo formula:

$$\delta\langle\hat{O}_1(t)\rangle = \langle\hat{O}_1(t)\rangle - \langle\hat{O}_1(t)\rangle_0 \approx -\frac{i}{\hbar}\int_0^t dt'\langle[\hat{O}_1(t), \hat{O}_2(t')]\rangle\delta h(t), \tag{3.24}$$

where the expectation values $\langle ...\rangle$ and $\langle ...\rangle_0$ refer to the system Hamiltonian with and without the perturbative field, respectively, and where higher-order terms in $\delta h(t)$ are neglected. Applying the Kubo formula to describe the response of the charge density $\hat{n}^c_j(t)$ of a single-orbital system, given by

$$\hat{n}^c_j(t) = \sum_\sigma \hat{c}^\dagger_{j,\sigma}(t)\hat{c}_{j,\sigma}(t), \tag{3.25}$$

with respect to a small external field coupling to the charge density, leads to the following linear response:

$$\frac{\delta\langle\hat{n}^c_i(t)\rangle}{\delta h_j(t)} = -\frac{i}{\hbar}\int_0^t dt'\langle[\hat{n}^c_i(t), \hat{n}^c_j(t')]\rangle. \tag{3.26}$$

The linear response of the system is connected to its charge susceptibility χ^c, defined as

$$\chi^c_{ij}(t-t') = \langle\hat{n}^c_i(t)\hat{n}^c_j(t')\rangle. \tag{3.27}$$

Furthermore, for a system at thermal equilibrium with an underlying periodic lattice, it is convenient to express the charge susceptibility using the imaginary Matsubara frequencies and the quasi-momentum:

$$\chi^c_{\mathbf{q},\omega_n} = \langle\hat{n}^c_{\mathbf{q},\omega_n}\hat{n}^c_{-\mathbf{q},-\omega_n}\rangle. \tag{3.28}$$

Here, the charge density is written in Fourier space as:

$$\hat{n}^c_{\mathbf{q},\omega_n} = \frac{1}{\beta N} \sum_{\mathbf{k},\nu_n,\sigma} \hat{c}^\dagger_{\mathbf{k}+\mathbf{q},\nu_n+\omega_n,\sigma} \hat{c}_{\mathbf{k},\nu_n,\sigma}. \tag{3.29}$$

An important property of the charge susceptibility is the absences of the commutativity of the limits $\mathbf{q} \to \mathbf{0}$ and $\nu_n \to 0$, which is of fundamental importance in our later treatment of phase separation fluctuations.

The charge susceptibility quantifies the correlation between the charge density at two coordinates. It allows to define a correlation length, expressing an characteristic length scale of the correlation within a system. At a second-order phase transition, associate with a charge instability, the charge susceptibility diverges as the correlation length becomes infinite following from the formation of long-range ordering. Thus, there is a close connection between collective phenomena, associated with symmetry breaking, and the susceptibilities.

The concept of a susceptibility is not limited to the charge channel. Equivalently, the spin susceptibility χ^s describing the response of the spin dynamics with respect to an external field coupling to the spin degrees of freedom can be defined:

$$\chi^s_{\mathbf{q},\omega_n} = \langle \hat{n}^s_{\mathbf{q},\omega_n} \hat{n}^s_{-\mathbf{q},-\omega_n} \rangle. \tag{3.30}$$

Here, the spin component is denoted by $s \in \{x, y, z\}$ and the spin density is written in Fourier space:

$$\hat{n}^s_{\mathbf{q},\omega_n} = \frac{1}{\beta N} \sum_{\mathbf{k},\nu_n,\sigma\sigma'} \hat{c}^\dagger_{\mathbf{k}+\mathbf{q},\nu_n+\omega_n,\sigma} \sigma^s_{\sigma\sigma'} \hat{c}_{\mathbf{k},\nu_n,\sigma'}. \tag{3.31}$$

Constructions of the susceptibility of single-particle observables associated with other degrees of freedom can be formulated equivalently. Thus, the fundamental concept of the susceptibility is important for the theoretical theoretical description of collective phenomena.

3.2 Mean-field theory

Seeking to develop a theoretical description of the formation of ferromagnetism, P. Curie [240] and P. Weiss [241] pioneered the development of mean-field theory (MFT). It is of conceptual importance within the fields of condensed matter theory and statistical mechanics, corresponding to a mapping of the many-body problem to an effective one-body problem, through the replacement of the interaction of the many-body problem with an effective external field of a one-body form. This effective external field is sometimes denotes as the Weiss (molecular) field, and is determined through a self-consistent procedure. In the current section, we seek to give a review of a selection of different MFTs, which are unified in their static (time-independent) form of the effective external field.

3.2.1 Weiss molecular field theory

The paradigmatic Ising model is a suitable model for the introduction of the concept of a MFT. It is a classical spin model, defined by the Hamiltonian

$$H(\sigma) = -\sum_{\langle i,j \rangle} J\sigma_i\sigma_j - \sum_j h\sigma_j, \tag{3.32}$$

describing the dynamics of classical spins $\sigma_j \in \{-1, 1\}$ with two possible orientations. The first term in Eq.(3.32) is a two-particle interaction term, determined by a nearest-neighbour nonlocal interaction J, which determines the magnetic ordering of the system. A parameter $J > 0$ ($J < 0$) corresponds to a FM (AFM) interaction, with parallel (antiparallel) orientation of adjacent spins being energetically favoured by the interaction. For the special case of $J = 0$, the model reduces to a noninteracting Ising model. In particular, the current considerations will be limited to a FM interaction with $J > 0$. The second term in Eq.(3.32) is a one-particle term, describing a uniform external field h coupled to the spins, which promotes spins to orient parallel with respect to the field.

An intuitive application of MFT to the FM Ising model is due to the Weiss molecular field theory, in which the spin terms are rewrites as,

$$\sigma_j \equiv \langle \sigma_j \rangle + \delta\sigma_j, \tag{3.33}$$

into an average spin $\langle \sigma_j \rangle \equiv m_j$ and a fluctuation $\delta\sigma_j$ around the average. By separating the spin term into an average term and a fluctuations term, one may rewrite the FM Ising model Eq.(3.32) as

$$H(\sigma) = -J \sum_{\langle i,j \rangle} [m_i m_j + m_i \delta\sigma_j + \delta\sigma_i m_j + \delta\sigma_i \delta\sigma_j] - h \sum_j \sigma_j. \tag{3.34}$$

The principle idea of MFT corresponds to neglecting the second-order term in the fluctuations, allowing for the mapping of the many-body system to an effective single-body system, determined by the Hamiltonian

$$H^{\mathrm{MF}}(\sigma) = -J \sum_{\langle i,j \rangle} [m_j \sigma_i + m_i \sigma_j - m_i m_j] - h \sum_j \sigma_j. \tag{3.35}$$

Assuming the average spin m_j is site-independent, with the uniform average spin denoted as m, allows to rewrite the Hamiltonian of the effective single-body system as noninteracting Ising model with an effective external field:

$$H^{\mathrm{MF}}(\sigma) = \frac{Jm^2 Nz}{2} - h_{\mathrm{eff}} \sum_j \sigma_j, \quad \text{with} \quad h_{\mathrm{eff}} = h + mJz, \tag{3.36}$$

where N is the number of spins and z is the coordination number. The self-consistent nature of MFT is displayed by the effective external field h_{eff} being dependent on the uniform average spin m, itself determined by the system. The fluctuations neglected within Weiss molecular field theory become suppressed for systems with a large dimension d (or large coordination number z), allowing for increasingly accurate theoretical description for increasing d. In fact, in the limit of $d \to \infty$, the Weiss molecular field theory gives an exact description of the Ising model. For low-dimensional systems, however, the fluctuations become more dominant, weakening the predictive power of the theory.

Formalistion of MFT, extending its applicability beyond the intuitive application above for the FM Ising model, is based on the Bogoliubov inequality, allowing for a formulation of MFT through a variational principle. Consider a many-body system determined by a Hamiltonian $\hat{H}$. Its free energy $\mathcal{F}$ obeys the Bogoliubov inequality,

$$\mathcal{F} \leq \mathcal{F}_0 + \langle \hat{H} - \hat{H}_0 \rangle_0, \tag{3.37}$$

which gives an upper bound on the free energy $\mathcal{F}$, with the Hamiltonian $\hat{H}_0$ defining a trial system. A mean-field approximation then corresponds to the choice of an uncorrelated trial system, which is variationally optimised with respect to the many-body system governed by $\hat{H}$ by minimisation of the upper bound in the Bogoliubov inequality. Formulating the MFT mapping of the many-body system to an effective one-body system on the rigorous grounds of the variational principle and the Bogoliubov inequality allows for a wide applicability of the MFT concepts.

3.2.2 Hartree-Fock approximation

The Hartree-Fock (HF) approximation, and its associate HF method, was developed in a series of works of D.R. Hartree [242, 243], J.C Slater [244–246], J.A. Gaunt [247] and V.A. Fock [248, 249] in the early years following the discovery of the Schrödinger equation, with aim of allowing for an ab-initio solution to the many-body time-independent Schrödinger equation. Within the HF approximation, the many-electron wavefunction of the time-independent Schrödinger equation is approximated as a Slater determinant, defined as a determinant of single-electron wavefunctions which enforces the antisymmetry of the wavefunction. It is a MFT formulated through the variational principle, based on the minimisation of the energy of the HF wavefunction, leading to a coupled set of equations to determine the uncorrelated effective single-electron system.

We exemplify the HF approximation by applying it to the single-orbital extended Hubbard model Eq.(2.26), with the interaction parametrised by a local and nearest-neighbour nonlocal interaction. Within the HF approximation, the local interaction term is approximated by the average Hartree and Fock exchange terms, allowing it to be expressed as

$$\hat{n}_{i\uparrow}\hat{n}_{i\downarrow} \approx \frac{1}{4}\hat{n}_i^c\langle\hat{n}_i^c\rangle - \frac{1}{4}\hat{\vec{n}}_i^s \cdot \langle\hat{\vec{n}}_i^s\rangle, \tag{3.38}$$

which decouples the local interaction into the charge and spin channels. In contrast, application of the HF approximation to the nonlocal interaction term,

$$\hat{n}_i^c\hat{n}_j^c \approx \frac{1}{2}\hat{n}_i^c\langle\hat{n}_j^c\rangle + \frac{1}{2}\hat{n}_j^c\langle\hat{n}_i^c\rangle, \tag{3.39}$$

only displays a contribution in the charge channel. This defines an effective single-body system, with the local and nonlocal interactions replaced by an external field determined through a self-consistent procedure. Here, we limited our considerations to the charge and spin channels, however, the Cooper pair channel may similarly be treated within the HF approximation.

Symmetry-broken solutions associated with collective ordering are accessible within the HF framework, similar to the treatment of magnetic ordering in the Ising model. Collective ordering described by the mean-field Hamiltonian require an explicit symmetry-breaking through the introduction of a small perturbative field, which allows for a simplistic description of formation of collective ordering associated to an extensive selections of different orderings. A beneficial aspect of the HF theory is that it avoids the Fierz ambiguity in the decoupling of the on-site Coulomb interaction U between the different collective channels [250–252], which appears, e.g., in MFTs constructed as the saddle-point approximation of the *Hubbard-Stratonovich transformation*.

3.2.3 Hubbard-Stratonovich transformation and decoupling

The Hubbard-Stratonovich transformation [253, 254] allows for an exact rewriting of an interacting fermion system as a noninteracting fermion system coupled to additional auxiliary bosonic degrees of freedom. It is convenient to express the Hubbard-Stratonovich transformation within the path integral formulation of quantum mechanics, rather than the equivalent operator formulation (described above). To facilitate the introduction of the Hubbard-Stratonovich transformation, we will begin by giving a brief reminder on the path integral formalism.

The role of the Hamiltonian $\hat{H}$ in determining the physics of a system in the operator formulation, is within the path integral formulation replaced by the action $\mathcal{S}$, expressed as a functional of complex numbers rather than operators. Importantly, fermionic and bosonic particles, represented as creation and annihilation operators endowed with their respective quantum statistics in the operator formalism, are instead represented by complex numbers. Bosons are represented by complex variables, naturally obeying the commutation relations, and fermions are represented by complex Grassmann variables, which are anticommuting variables. Observables as expressed by the expectation value of associate operators, are governed by the action of the system:

$$\langle \hat{O}[\hat{c}^\dagger, \hat{c}] \rangle = \frac{1}{\mathcal{Z}} \int D[c^*, c] O[c^*, c] e^{-\mathcal{S}[c^*, c]}, \quad \text{with} \quad \mathcal{Z} = \int D[c^*, c] e^{-\mathcal{S}[c^*, c]}, \tag{3.40}$$

with the Grassmann variables $c^{(*)}$ corresponding to the annihilation (creation) of electrons employed. An apparent feature of the path integral formulation of quantum mechanics, is the exhibition of a deeper connection between quantum mechanics and statistical mechanics, a distinguishing feature relative the operator formulation.

We exemplify the path integral formalism by considering the single-orbital Hubbard model, defined by the following action:

$$\mathcal{S} = -\frac{1}{\beta N} \sum_{\mathbf{k}, \nu_n, \sigma} c^*_{\mathbf{k}\nu_n\sigma} \mathcal{G}^{-1}_{\mathbf{k}\nu_n} c_{\mathbf{k}\nu_n\sigma} + \frac{U}{\beta N} \sum_{\mathbf{q}, \omega_n} n_{\mathbf{q}\omega_n\uparrow} n_{-\mathbf{q}, -\omega_n\downarrow}, \tag{3.41}$$

with the inverse temperature β and number of sites N. The inverse of the bare Green's function is denoted by $\mathcal{G}^{-1}_{\mathbf{k}\nu_n} = i\nu_n + \mu - \epsilon_k$, where μ is the chemical potential and $\epsilon_{\mathbf{k}}$ is the bare dispersion. The local interaction is expressed by the composite variable

$$n_{\mathbf{q}\omega_n\sigma} = \frac{1}{\beta N} \sum_{\mathbf{k}, \nu_n, \sigma} c^*_{\mathbf{k}+\mathbf{q}, \nu_\mathbf{n}\sigma} c_{\mathbf{k}\nu_n\sigma}, \tag{3.42}$$

expressing the (spin-resolved) density. As expected, the quartic term is the source of the difficulty of solving the interacting fermionic system.

The Hubbard-Stratonovich transformation allows for an explicit rewriting of the quartic term of a fermionic action, through the introduction of an auxiliary bosonic field. Consider a generic interacting fermionic system, determined by the action

$$\mathcal{S}[c^*, c] = -\frac{1}{\beta N} \sum_{\mathbf{k}, \nu_n, \sigma} c^*_{\mathbf{k}\nu_n\sigma} \mathcal{G}^{-1}_{\mathbf{k}\nu_n} c_{\mathbf{k}\nu_n\sigma} + \frac{1}{2\beta N} \sum_{\mathbf{q}, \omega_n} n^\varsigma_{\mathbf{q}\omega_n} V^\varsigma_{\mathbf{q}\omega_n} n^\varsigma_{-\mathbf{q}, -\omega_n}, \tag{3.43}$$

with the interaction $V^{\varsigma\omega}_{\mathbf{q}}$ described by the composite single-particle variables $n^\varsigma_{\mathbf{q}\omega}$ with the channel denoted by ς. In essence, the Hubbard-Stratonovich transformation follows directly from the Gaussian integral identity in its functional form:

$$e^{-\mathcal{S}[c^*, c]} = \frac{1}{\mathcal{N}} \int D[\varphi] e^{-\mathcal{S}[c^*, c, \varphi]}, \tag{3.44}$$

with a normalisation $\mathcal{N}$, and with the introduction of the Hubbard-Stratonovich action:

$$\mathcal{S}[c^*, c, \varphi] = -\frac{1}{\beta N}\sum_{\mathbf{k},\nu_n,\sigma} c^*_{\mathbf{k}\nu_n\sigma}\mathcal{G}^{-1}_{\mathbf{k}\nu_n} c_{\mathbf{k}\nu_n\sigma} + \frac{1}{\beta N}\sum_{\mathbf{q},\omega}\left[n^{\varsigma}_{\mathbf{q}\omega_n}\varphi^{\varsigma}_{-\mathbf{q},-\omega_n}, -\frac{1}{2}\varphi^{\varsigma}_{\mathbf{q}\omega_n}\left[V^{\varsigma}_{\mathbf{q}\omega_n}\right]^{-1}\varphi^{\varsigma}_{-\mathbf{q},-\omega_n}\right]. \tag{3.45}$$

The quartic term of the fermionic action Eq.(3.43) is recast by the Hubbard-Stratonovich transformation as a Gaussian fermionic term, coupled the auxiliary bosonic degrees of freedom.

Applying the saddle-point approximation to the Hubbard-Stratonovich action, associated with fixing the bosonic variable to the value φ^{MF} which minimises the action, allows to define a MFT system:

$$\mathcal{S}^{\mathrm{MF}}[c^*, c] = \mathcal{S}[c^*, c, \varphi \to \varphi^{\mathrm{MF}}]. \tag{3.46}$$

A particularity emerges for the mean-field treatment of the local interaction U. The local term can be decoupled between the charge, spin and Cooper pairing channels in a infinite assortment of way, all associated with different Hubbard-Stratonovich actions. Each Hubbard-Stratonovich action is an exact reformulations of the true many-fermion system, however, any approximation of the Hubbard-Stratonovich actions are at risk of introducing different predictions and thus ambiguities. A well-known example is the saddle-point approximation being associated with such ambiguity [255], allowing for an infinite selection of different MFTs, clearly demonstrating the Fierz ambiguity.

3.2.4 Random phase and fluctuating exchange approximations

A common strategy to evaluate the susceptibilities is by a summation of relevant diagrammatic contributions in the series expansion of the interacting susceptibility in terms of the interaction $V_{\mathbf{q},\omega}$ and noninteracting susceptibilities. An important approximation within this class of strategies is the random phase approximation (RPA), allowing for a MFT estimate of the charge susceptibility χ^c. It approximates the charge susceptibility χ^c as an infinite sum of bubble diagrams composed of the noninteracting charge susceptibility Π^c and the interaction V^c in the charge channel:

$$\chi^c_{\mathbf{q},\omega_n} = \Pi^c_{\mathbf{q},\omega_n} + \Pi^c_{\mathbf{q},\omega_n} V^c_{\mathbf{q},\omega_n}\chi^c_{\mathbf{q},\omega} \tag{3.47}$$

$$= \frac{\Pi^c_{\mathbf{q},\omega_n}}{1 - \Pi^c_{\mathbf{q},\omega_n} V^c_{\mathbf{q},\omega_n}}. \tag{3.48}$$

The noninteracting system allows for an analytic evaluation of its charge susceptibility Π^c, demonstrating a form of the Lindhard function varity:

$$\Pi^c_{\mathbf{q},\omega_n} = -2\sum_{\mathbf{k},\nu_n}\frac{n_F(\epsilon_{\mathbf{k}+\mathbf{q}}) - n_F(\epsilon_{\mathbf{k}})}{\epsilon_{\mathbf{k}+\mathbf{q}} - \epsilon_{\mathbf{k}} - i\omega_n}. \tag{3.49}$$

The factor 2 arises due to spin-degeneracy and $\epsilon_{\mathbf{k}}$ denotes the bare dispersion of the noninteracting system. With full knowledge of the form of the noninteracting susceptibility Π^c, RPA theory allows for an approximate estimate of the interacting susceptibility χ^c.

With access to the charge susceptibility χ^c within RPA theory, the formation of charge instabilities associated with the development of divergences in the static ($\omega = 0$)

charge susceptibility can be identified. Divergences in the charge susceptibility for a given ordering vector $\mathbf{q}$ are demonstrated within RPA theory if the following equation holds:

$$1 - \Pi^{c}_{\mathbf{q},0} V^{c}_{\mathbf{q},0} = 0. \tag{3.50}$$

Thus, RPA theory allows to predict collective charge instabilities associated with the formation of CDWs with certain ordering vectors $\mathbf{q}$. Importance of the RPA method is further demonstrated by its fundamental importance for GW theory, allowing to compute the screen interaction in weakly correlated systems, and the cRPA approach, utilised for the approximate downfolding to low-energy models.

A limitation in RPA theory is its restriction to the charge channel. This constrains its applicability for collective instabilities occurring in any other channel such, e.g., collective magnetic and Cooper pairing fluctuations. An extension of the main ideas of RPA theory incorporating the magnetic and Cooper pair channels is the fluctuating exchange (FLEX) approximation. Given a decoupling of the interaction in different channels ς, the FLEX approximations allows to express the susceptibilities in each channel as a sum of an infinite series of diagrams in the vein of RPA

$$\chi^{\varsigma}_{\mathbf{q},\omega_n} = \Pi^{\varsigma}_{\mathbf{q},\omega_n} + \Pi^{\varsigma}_{\mathbf{q},\omega_n} V^{\varsigma}_{\mathbf{q},\omega_n} \chi^{\varsigma}_{\mathbf{q},\omega_n} \tag{3.51}$$

$$= \frac{\Pi^{\varsigma}_{\mathbf{q},\omega_n}}{1 - \Pi^{\varsigma}_{\mathbf{q},\omega_n} V^{\varsigma}_{\mathbf{q},\omega_n}}. \tag{3.52}$$

In FLEX theory, a choice of decoupling of the local interaction U is required, as discussed in the context of the Fierz ambiguity previously. The conventional choice of decoupling in the charge and spin channels is within FLEX theory a local charge interaction given by $U^{\mathrm{c}} = U/2$ and a local spin interaction given by $U^{\mathrm{s}} = -U/2$, which is a decoupling choice motivated by its agreement with the results of HF theory, devoid of the Fierz ambiguity.

3.3 Dynamical mean-field theory

Quantum lattice models are within MFT described utilising effective single-electron systems, without inclusion of correlation effects. For a theoretical description of the many-body correlation effects in strongly correlated systems, a natural framework are the many-body techniques, incorporating an explicitly many-body character. Dynamical mean-field theory (DMFT) is a many-body approach allowing for a non-perturbative description of local dynamics in quantum lattice models [33–36], acting as quantum generalisation of the Weiss molecular field theory reviewed above [241]. It corresponds to a mapping of the paradigmatic single-orbital Hubbard model to an effective Anderson impurity model, composed of a single site coupled to an effective bath, which is solved self-consistently. In fact, the role of the paradigmatic single-orbital Hubbard model for DMFT, is analogous to the role of the paradigmatic Ising model for the Weiss molecular field theory.

3.3.1 Hubbard model in the infinite-dimensional limit

Making an analogy with the Weiss molecular field theory, which emerges as an exact description of the Ising model in the infinite dimensional limit, we seek to give a brief

review of the solution of the infinite-dimensional Hubbard model [33]. Working in the path integral formalism, the single-orbital Hubbard model action is defined as

$$\mathcal{S} = \int_0^\beta d\tau \left[\sum_{i,\sigma} c^*_{i\tau\sigma} \left(\frac{\partial}{\partial \tau} - \mu \right) c_{i\tau\sigma} + \sum_{ij,\sigma} c^*_{i\tau\sigma} t_{ij} c_{j\tau\sigma} + U \sum_i c^*_{i\tau\uparrow} c_{i\tau\uparrow} c^*_{i\tau\downarrow} c_{i\tau\downarrow} \right], \quad (3.53)$$

written in real space and imaginary time. Consider a d-dimensional hypercubic lattice restricted to a nearest-neighbour hopping t, with the number of nearest-neighbours given by the coordination number $z = 2d$. Taking the limit of $d \to \infty$ requires subtlety, which is apparent in the density of states (DOS) for the bare dispersion:

$$D(\omega) = \frac{1}{\sqrt{2\pi} t \sqrt{z}} e^{-\frac{1}{2}\left(\frac{\omega}{t\sqrt{z}}\right)}, \quad (3.54)$$

derived through the application of the central limit theorem in the limit of $d \to \infty$. The variance of the Gaussian form of $D(\omega)$ is given by $\sigma = t\sqrt{z}$, thus requiring a rescaling of the hopping parameter to ensure that the nontrivial competition between the kinetic and interaction terms of the Hubbard model survives in the limit $d \to \infty$. The choice of rescaling of t can be divided into three different categories:

- The variance $\sigma \to 0$ for $d \to \infty$, leading to the physics being trivially dominated by the interaction term.
- The variance $\sigma \to \infty$ for $d \to \infty$, leading to the physics being trivially dominated by the kinetic term.
- A nontrivial interplay between the interaction and kinetic terms survives if the variance σ remains finite for $d \to \infty$, which is accomplished by the rescaling, e.g., $t \to t/\sqrt{z}$.

The choice of a nontrivial limit of the infinite dimensional limit leads to significant simplification of the description of many-body correlation effects of the Hubbard model. By scaling arguments, only the local component of the self-energy gives a contribution to the self-energy in the limit of $d \to \infty$:

$$\Sigma_{ij,\tau} = \delta_{ij} \Sigma^{\text{loc}}_{i,\tau}, \quad (3.55)$$

with higher-order diagrams giving a vanishing contribution. It follows by the translation invariance of the system, that a site-independent self-energy is a natural assumption. Thus, the self-energy of the Hubbard model in the infinite dimensional limit is momentum-independent:

$$\Sigma_{\mathbf{k},\nu_n} = \Sigma^{\text{loc}}_{\nu_n}, \quad (3.56)$$

however, with an explicit frequency-dependence governing the local dynamics. Despite the local nature of the self-energy, the Matsubara Green's function retains a nonlocal contribution due to the hopping parameter:

$$\mathcal{G}_{\mathbf{k},\nu_n} = \frac{1}{i\nu_n + \mu - \epsilon_{\mathbf{k}} - \Sigma^{\text{loc}}_{\nu_n}}. \quad (3.57)$$

which follows from the Dyson equation Eq.(3.21). Due to the importance of the local dynamics, it is convenient to introduce the local Matsubara Green's function,

$$\mathcal{G}^{\text{loc}}_{\nu_n} = \frac{1}{N} \sum_{\mathbf{k}} \mathcal{G}_{\mathbf{k},\nu_n}, \quad (3.58)$$

which is of importance in the construction of the self-consistent DMFT equations, through the mapping of the lattice model to the Anderson impurity model.

3.3.2 Mapping to Anderson impurity model

To allow for a tractable numerically exact description of the local correlations of the model, an exact mapping between the Hubbard model and the Anderson impurity model in the $d \to \infty$ limit is exploited [34–36]. The Anderson impurity model can be defined by the effective impurity action:

$$\mathcal{S}^{\text{imp}} = -\int_0^\beta d\tau_1 \int_0^\beta d\tau_2 \sum_\sigma c^*_{\tau_1\sigma} \left[\mathrm{G}^0_{\sigma,\tau_1-\tau_2}\right]^{-1} c_{\tau_2\sigma} + U\int_0^\beta d\tau c^*_{\tau\uparrow}c_{\tau\uparrow}c^*_{\tau\downarrow}c_{\tau\downarrow}, \tag{3.59}$$

describing an interacting impurity coupled to a noninteracting bath, which is integrated out. The bare propagator $\mathrm{G}^0_{\sigma,\nu_n}$ denotes the, so called, Weiss field

$$\mathrm{G}^0_{\sigma,\nu_n} = i\nu_n + \mu - \Delta_{\sigma,\nu_n} \tag{3.60}$$

describing the propagation of the impurity electrons coupled to an effective bath through the hybridisation function Δ_{σ,ν_n}. The benefit of mapping the Hubbard model onto the Anderson impurity model is the existence of a large selection of numerically powerful techniques for solving the impurity problem. Impurity solvers have been developed based on, e.g., quantum Monte Carlo [256–260], exact diagonalisation [261, 262], renormalisation group [263], and tensor networks [264–267]. A few of these numerical techniques acting as the basis for the impurity solvers will be briefly reviewed later in this chapter.

Solving the Anderson impurity model gives access to the local impurity Green's function $\mathrm{G}_{\sigma,\nu_n}$, which coincides with the local lattice Green's function $\mathcal{G}^{\text{loc}}_{\nu_n}$ in the limit of $d \to \infty$. The equivalence of the local impurity Green's function $\mathrm{G}_{\sigma,\nu_n}$ and the local lattice Green's function $\mathcal{G}^{\text{loc}}_{\nu_n}$ constitutes the self-consistency condition for DMFT, based on following self-consistency equations:

1. Given an initial guess for the local lattice self-energy $\Sigma^{\text{loc}}_{\nu_n}$, the Weiss field $\mathrm{G}^0_{\sigma,\nu_n}$ (and the associated hybridisation function Δ_{σ,ν_n}) is accessible by

$$\left[\mathrm{G}^0_{\sigma,\nu_n}\right]^{-1} = \Sigma^{\text{loc}}_{\sigma,\nu_n} + \frac{1}{N}\sum_{\mathbf{k}} \frac{1}{i\nu_n + \mu - \epsilon_{\mathbf{k}} - \Sigma^{\text{loc}}_{\nu_n}}. \tag{3.61}$$

2. Solving the effective impurity problem, allows access to the local impurity Green's function $\mathrm{G}_{\sigma,\nu_n}$, giving the local lattice Green's function by:

$$\mathcal{G}^{\text{loc}}_{\nu_n} = \mathrm{G}_{\sigma,\nu_n}. \tag{3.62}$$

3. With knowledge of the local lattice Green's function $\mathcal{G}^{\text{loc}}_{\nu_n}$ and the Weiss field $\mathrm{G}^0_{\sigma,\nu_n}$, an update guess of the local self-energy is generated by the Dyson equation:

$$\Sigma^{\text{loc}}_{\sigma,\nu_n} = \left[\mathrm{G}^0_{\sigma,\nu_n}\right]^{-1} - \left[\mathcal{G}^{\text{loc}}_{\nu_n}\right]^{-1}. \tag{3.63}$$

4. With an updated guess for the local self-energy $\Sigma^{\text{loc}}_{\nu_n}$, the self-consistent procedure is iterated from step 1 until converges.

The self-consistent equations from DMFT can be derived by a selection of different methods such as, e.g., the cavity method [35, 36] or from the Baym–Kadanoff functional [268, 269]. They allows for an exact solution of the Hubbard model in infinite dimensional limit, and for an approximate nonperturbative solution for the d-dimensional

Hubbard model, in which the spatial fluctuations of lattice self-energy are neglected. The breakthrough of DMFT is that it allows for a nonperturbative treatment of the local dynamics, from the nearly-free electron limit to the atomic limit. An important success of DMFT is its PM solution capturing the Mott-Hubbard metal-to-insulator phase transition due to increase of local dynamical correlation as the local interaction U increases.

3.3.3 Extensions of DMFT to nonlocal correlation

A plethora of extensions of DMFT have extended the applicability of the formalism, allowing for the treatment of multi-orbital physics [36, 270], nonlocal interactions [271–277], and out-of-equilibrium physics [278–280]. For the study of quantum materials, DMFT in combination with DFT [36, 270] or GW [281–284] allows for an evaluation of the electronic structure in the regime of strong correlation from first principles. Nevertheless, an apparent issue of DMFT is the restriction to local correlation, with nonlocal correlation being neglected. As the formation of collective phenomena are heavily dependent on the existence of short- and long-range collective fluctuations, the incorporation of these effects beyond DMFT are of crucial importance. Two main categories of systematic extensions of DMFT exists for the inclusion of nonlocal correlations: cluster and diagrammatic extensions.

The principle idea behind the cluster extensions of DMFT, such as, e.g., cellular DMFT [129, 269, 285–288] and dynamical cluster approximation (DCA) [289–291], is the mapping of the Hubbard model on to a cluster impurity embedded in a dynamical bath. For a given choice of cluster, the cluster extensions of DMFT allow for a systematic and unbiased inclusion of any correlation considered "local" with respect to the cluster. There is significant flexibility in the choice for the structure of the cluster, regarding the number of sites incorporated and its geometric shape. In the limit of a cluster composed of a single-site, the conventional DMFT problem is recovered, while in the opposite limit of an infinite cluster spanning the full lattice, the cluster extensions of DMFT become an exact treatment of the Hubbard model. In practice, however, due to heavy numerical cost associated with solving the cluster impurity problem for large clusters, computations are restricted to small clusters and thus short-range correlations. While any short-range collective fluctuation within the cluster may be treated accurately, allowing for unambiguous theoretical description of their interplay within strongly correlated systems [199, 205], the approach is inherently restricted to small system sizes and thus cannot address long-range collective fluctuations. Thus, if the correlation length ξ associated with a certain collective fluctuation which extends beyond the size of the cluster, the cluster extensions are unable to accurately describe such a mode.

Advanced diagrammatic extensions of DMFT [292] are able to describe long-range fluctuations simultaneously in different instability channels. While the principle idea behind diagrammatic extensions of DMFT is the inclusion of nonlocal correlation through the summation of Feynman diagrams, their formulations differ significantly. A class of the diagrammatic extensions of DMFT are approaches based on continuing in the spirit of DMFT by applying the idea of "locality" to the vertex functions [293–299]. Within the dynamical vertex approximation (DΓA), the irreducible two-particle vertex is treated as local with full inclusion of dynamical correlation [293–297], while in the triply irreducible local expansion (TRILEX), a local approximation of the fermion-

boson vertex is employed [298, 299]. From the quantum impurity models, the local vertices can be extracted, allowing for a theoretical description of nonlocal correlation. Another class of the diagrammatic extensions of DMFT are the dual approaches, including the dual fermion (DF) [300–305], dual boson (DB) [204, 214, 306–308] and dual TRILEX (D-TRILEX) [201, 202, 309–313] theories. Their construction is based on integrating out the single-impurity DMFT problem, allowing for a diagrammatic expansion in the propagators dressed by the DMFT self-energy, leading to the inclusion of nonlocal correlations. In the presence of the nonlocal interaction V, long-range fluctuations in multiple instability channels can be treated within the DB theory [204, 214, 216, 307, 308], the DΓA [295, 296], the TRILEX method [314], or the D-TRILEX approach [202,312,313]. However, these fluctuations are usually treated in a ladder-like approximation, where different instability channels affect each other only indirectly via self-consistent renormalization of single- and two-particle quantities.

3.4 Numerically exact techniques

A selection of computationally powerful methods allows for an explicit treatment of interplaying collective fluctuations, however, all accompanied with their respective limitations. Exact diagonalisation (ED) due to the Lanczos algorithm [37] allows to evaluate a set of the lowest/highest eigenstates of a $N \times N$ Hermitian matrix, allowing to decompose a Hamiltonian into the most "important" states. However, ED scales unfavourably with system size, thus restricting it to small system sizes which cannot address long-range collective fluctuations, similar to the problem inherent to the cluster extensions of DMFT. The same problem is intrinsic to lattice Monte Carlo [38], associated with the evaluation of observables through a random sampling of configurations of the lattice, restricting its applicability to small plaquettes. However, due to their unbiased treatment, both ED and lattice Monte Carlo have been applied to small plaquettes of the single-orbital extended Hubbard model, which allowed for the earliest numerical investigations in to the study of the interplay between U and V [192–195].

Limited to one-dimensional systems, tensor network (TN) techniques [315] such as, e.g., density matrix renormalisation group (DMRG) [39, 316, 317], allows for an highly efficient and accurate description of ground-state, thermodynamic and low-energy excited-state properties. TN methods are based on an efficient representation of quantum states utilising the dominant contributions of a decomposition, commonly the singular-value decomposition (SVD). While it allows for a very accurate treatment of one-dimensional systems, the computational cost for TNs for higher-dimensional systems grows unfavourably with system size. Thus, for two-dimensional systems, the techniques are restricted to small to intermediate size clusters. Nevertheless, the intermediate cluster sizes accessible by TN techniques are sufficiently large to allow for the theoretical description of, e.g., stripe-order in the Hubbard model [141–143].

The generality of the stochastic sampling of configuration of the Monte Carlo method allows grand flexibility in its design. Its application within quantum theory is denoted as quantum Monte Carlo (QMC), encompassing a diverse and large family of different methods unified by their stochastic nature. Included within this family are, e.g., the variational Monte Carlo (VMC) methods [318,319], the auxiliary-field QMC (AF-QMC) methods [320,321], continuous-time QMC (CT-QMC) methods [258–260,321–323] and diagrammatic Monte Carlo (DiagMC) [324–327]. VMC methods are based on the variational method, seeking to minimise the ground-state energy, allowing

access to zero-temperature ground-state properties. At finite-temperature, AF-QMC methods, based on an importance sampling of the auxiliary bosonic field introduced through the Hubbard-Stratonovich transformation, and CT-QMC, based on a sampling of diagrammatic contributions, allows for the evaluation of properties of quantum lattice models. An unifying problem of the QMC techniques for fermionic systems is the numerical sign problem, which restricts the applicability of the technique from accessing the full parameter space. For example, the nonlocal interaction V is required to be sufficiently small within the half-filled single-orbital extended Hubbard model for convergence [227]. Of particular importance for benchmarking of the current work are three QMC techniques: AF-QMC, determinant Monte Carlo (DQMC) (within the family of CT-QMC methods) and diagrammatic Monte Carlo (DiagMC). While both AF-QMC and DQMC methods are restricted to small system sizes, allowing for an unbiased treatment of competing of short-range collective fluctuations, DiagMC work directly in the thermodynamic limit [326], allowing for an accurate treatment of long-range magnetic fluctuations [136].

Chapter 4

Fluctuating field theory for competing collective fluctuations

> "... the art of choosing a suitable approximation, of checking its consistency and finding at least intuitive reasons for expecting the approximation to be satisfactory, is much more subtle than that of solving an equation exactly." - R. Peierls [328]

The tremendous challenges remaining in the theoretical description of interplaying collective fluctuations, motivates searches for constructing simplified methods for studying interplaying collective instabilities. Progressing on the development of such theoretical tools is the main aim of the current chapter and thesis. In this chapter, we introduce a theoretical approach based on the recently developed fluctuating local field (FLF) approach, originally introduced for the study of collective magnetic fluctuations in the Ising and Heisenberg models [329, 330] as well as the Hubbard model [331–333]. The proposed theoretical approach corresponds to a multi-channel generalisation of the FLF theory, which we call the multi-channel fluctuating field (MCFF) approach. The aim of the MCFF approach is the study of competing collective fluctuations in quantum lattice systems. In order to contrast our generalised theory with the prior theory, we denote the FLF approach as the single-channel fluctuating field (SCFF) approach applied to the magnetic channel. This chapter follows closely the work in Ref. [334, 335] by the author of this thesis and collaborators.

4.1 Multi-channel fluctuating field theory

The principle idea behind the SCFF theory is a variational mapping of an initial complex system to a simpler trial system which only incorporates the main leading magnetic fluctuations. For example, in Ref. [331–333] the variational mapping corresponded to mapping the Hubbard model action on a simplified trial action including only a single or a few magnetic modes. The simplicity of the trial action permits a numerically exact treatment, which allows for inclusion of non-perturbative effects without any explicit symmetry breaking. In fact, due to the limited number of degrees of freedom in the SCFF trial action, this numerically exact treatment may performed in a very efficient manner. However, the SCFF approach is limited to only magnetic fluctuations. Thus,

the applicability of the approach for systems which are dominated by other fluctuation channels is limited.

Figure 4.1: Schematic view summarizing the guiding idea behind the MCFF theory.

Taking inspiration of the principle idea of the SCFF approach, our work generalises the approach to the competition between any arbitrary channels described by order parameters associated with single-particle composite operators. For convenience, we limit our considerations in the current chapter to the single-orbital extended Hubbard model [42–45, 336]. The model provides a suitable framework for investigating the interplay between collective electronic fluctuations in the spin, charge and pairing channels. However, we note that our approach can be straightforwardly generalised to more complex single- and multi-band quantum lattice systems. To summarize, the proposed MCFF theory is a variational mapping of an initial complicated quantum lattice system to a simpler trial system, allowing to incorporate the main leading collective instabilities.

4.1.1 Variational mapping of charge and spin fluctuations

We restrict our initial introduction of the MCFF theory to interplaying collective charge and spin fluctuations following Ref. [334]. Throughout the chapter, the MCFF theory will be further generalised through the inclusion of a growing number of collective fluctuations. However, in order to keep the structure clear and transparent, we opt for slowly complexifying the approach.

We seek to considered the MCFF theory in the context of the single-orbital extended Hubbard model, defined by the following action:

$$\mathcal{S} = -\frac{1}{\beta N}\sum_{\mathbf{k},\nu,\sigma} c^{*}_{\mathbf{k}\nu\sigma}\mathcal{G}^{-1}_{\mathbf{k}\nu}c_{\mathbf{k}\nu\sigma} + \frac{U}{\beta N}\sum_{\mathbf{q},\omega}\rho_{\mathbf{q}\omega\uparrow}\rho_{-\mathbf{q},-\omega\downarrow} + \frac{1}{2\beta N}\sum_{\mathbf{q},\omega,\sigma\sigma'} V_{\mathbf{q}}\rho_{\mathbf{q}\omega\sigma}\rho_{-\mathbf{q},-\omega\sigma'}. \tag{4.1}$$

Here, the inverse of the bare Green's function is defined as $\mathcal{G}^{-1}_{\mathbf{k}\nu} = i\nu + \mu - \epsilon_k$, where μ is the chemical potential and $\epsilon_{\mathbf{k}} = -2t(\cos k_x + \cos k_y)$ is the dispersion relation as parametrised by the nearest-neighbour hopping t on a two-dimensional square lattice. For notational simplicity, we will without loss of generality set $t = 1$ as an unit of energy. As argued for later in the derivations to follow, it is convenient to write the interaction parts of the action (4.1) using the shifted densities $\rho_{\mathbf{q}\omega\sigma} = n_{\mathbf{q}\omega\sigma} - \langle n_{\mathbf{q}\omega\sigma}\rangle\delta_{\mathbf{q},\mathbf{0}}\delta_{\omega,0}$. In addition, the non-local interaction is limited to only the nearest-neighbour term, leading to the momentum-space representation for the non-local interaction following $V_{\mathbf{q}} = 2V(\cos q_x + \cos q_y)$. Note that previous applications of the FLF theory to quantum lattice systems only considered the Hubbard model, i.e. a vanishing non-local interaction $V = 0$. Thus, the non-local electronic interaction considered in the current work is an additional novelty within the proposed approach to be derived.

Trial action

The basis of the fluctuating field theory is the variational mapping of the complicated system on to a simplified trial system. Within the MCFF theory, the variational mapping is based on the MCFF trial action, which we define as:

$$\mathcal{S}^* = -\frac{1}{\beta N}\sum_{\mathbf{k},\nu,\sigma} c^*_{\mathbf{k}\nu\sigma}\mathcal{G}^{-1}_{\mathbf{k}\nu}c_{\mathbf{k}\nu\sigma} + \sum_{\mathbf{Q},\varsigma}\left[\phi^\varsigma_{\mathbf{Q}}\rho^\varsigma_{-\mathbf{Q}} - \frac{1}{2}\frac{\beta N}{J^\varsigma_{\mathbf{Q}}}\phi^\varsigma_{\mathbf{Q}}\phi^\varsigma_{-\mathbf{Q}}\right]. \tag{4.2}$$

Within the trial action, collective fluctuations are explicitly incorporated through the scalar ($\varsigma = c$) and vector ($\varsigma = s \in \{x, y, z\}$) fields $\phi^\varsigma_{\mathbf{Q}}$ coupled to the composite variables $\rho^\varsigma_{\mathbf{Q}}$, defined by:

$$\rho^\varsigma_{\mathbf{Q}} = n^\varsigma_{\mathbf{Q}} - \langle n^\varsigma_{\mathbf{Q}}\rangle\delta_{\mathbf{Q},\mathbf{0}}. \tag{4.3}$$

These composite variables are associated with static ($\omega = 0$) order parameters of interest, which we initially limit to the charge ($\varsigma = c$) and spin ($\varsigma = s$) densities:

$$n^\varsigma_{\mathbf{Q}} = \frac{1}{\beta N}\sum_{\mathbf{k},\nu,\sigma\sigma'} c^*_{\mathbf{k}+\mathbf{Q},\nu\sigma}\sigma^\varsigma_{\sigma\sigma'}c_{\mathbf{k}\nu\sigma'}, \tag{4.4}$$

where $\mathbf{Q}$ is the ordering wave vector, σ^c is the identity and σ^s is the Pauli spin matrices. To retrieve the initial FLF trial action for the magnetic fluctuations, one restricts the action to only the fields associated with the spin degrees of freedom. By definition, the bare terms of the original action (4.1) and trial action (4.2) are identical. The distinguishing feature of the trial action (4.2) is the modelling of the interaction term which describes the competition of the collective fluctuations through the classical fields $\phi^\varsigma_{\mathbf{Q}}$ associated with the main leading instabilities of the system. Determining the form of the interaction part is a set of stiffness constants $J^\varsigma_{\mathbf{Q}}$ associated to each classical field $\phi^\varsigma_{\mathbf{Q}}$. The set of stiffness constants $J^\varsigma_{\mathbf{Q}}$ are unknown a priori and will be determined through a variational principle.

Motivating the form of the MCFF trial action (4.2) is that the structure is identical to the Hubbard-Stratonovich action with a decoupling of the local interaction in the charge and spin channels. As the Hubbard-Stratonovich transformation is an exact rewriting of the fermionic action through the introduction of additional auxiliary bosonic degrees of freedom, the MCFF theory would be exact if all modes in quasi-momentum and frequency space are treated explicitly. The Hubbard-Stratonovich action contains bosonic fields coupled to the leading and sub-leading collective modes. Instead, in practice, the MCFF theory is restricted to only the main leading instabilities of the system, allowing for a numerically low-cost treatment. Limited to only a few modes, the MCFF theory will appear to converge in the thermodynamic limit to a symmetry-conserving sum over symmetry-broken solutions of mean-field theory. However, for any finite system, the MCFF theory will introduce important corrections beyond mean-field theory. Furthermore, our choice to keep only the main $\mathbf{Q}$ mode for each fluctuation is motivated by the observation that the momentum-space representation for the static lattice susceptibility $X^\varsigma(\mathbf{q}, \omega = 0)$ at the transition point between the normal and the ordered phases usually has the form of a delta-function-like Bragg peak located at the ordering vectors $X^\varsigma(\mathbf{q}, \omega = 0) \sim \delta_{\mathbf{q},\mathbf{Q}}$ (see, e.g. Refs. [201, 202]). Thus, we argue that considering only the leading $\mathbf{Q}$-mode is sufficient for predicting phase boundaries in the case of strong competing fluctuations.

By construction, the trial action (4.2) is Gaussian with respect to both the Grassmann variables $c^{(*)}$ and classical fields ϕ^{ς}. It follows that an effective action for either the fermionic or classical degrees of freedom may be generated by analytically integrating out the other degrees of freedom. Integrating out the fermionic degrees of freedom, the effective action for the classical fields becomes:

$$\mathcal{S}_{\phi} = -\operatorname{Tr}\ln\left[\mathcal{G}^{-1}_{\mathbf{k}\nu}\delta_{\mathbf{Q},0}\delta_{\sigma,\sigma'} - \sum_{\varsigma}\phi^{\varsigma}_{\mathbf{Q}}\sigma^{\varsigma}_{\sigma\sigma'}\right] - \frac{1}{2}\sum_{\mathbf{Q},\varsigma}\frac{\beta N}{J^{\varsigma}_{\mathbf{Q}}}\phi^{\varsigma}_{\mathbf{Q}}\phi^{\varsigma}_{-\mathbf{Q}}. \tag{4.5}$$

Here, the trace is taken over the momenta $\mathbf{k}, \mathbf{Q}$, frequency ν, and spin σ, σ' indices. The effective action (4.5) depends on a small number of classical fields $\phi^{\varsigma}_{\mathbf{Q}}$ which describes the collective fluctuations and their interplay. In addition, one may construct an effective fermionic action $\mathcal{S}_c$, corresponding to the trial action (4.2) with the classical fields $\phi^{\varsigma}_{\mathbf{Q}}$ being integrated out. This effective fermionic action $\mathcal{S}_c$ is of the following form:

$$\mathcal{S}_c = -\frac{1}{\beta N}\sum_{\mathbf{k},\nu,\sigma} c^{*}_{\mathbf{k}\nu\sigma}\mathcal{G}^{-1}_{\mathbf{k}\nu}c_{\mathbf{k}\nu\sigma} + \frac{1}{2}\sum_{\mathbf{Q},\varsigma}\frac{J^{\varsigma}_{\mathbf{Q}}}{\beta N}\rho^{\varsigma}_{\mathbf{Q}}\rho^{\varsigma}_{-\mathbf{Q}}. \tag{4.6}$$

Within our derivation, the action $\mathcal{S}_c$ will be suitable to utilize within the variational principle, as the starting point of the variational mapping is the fermionic action of the quantum lattice system, i.e. the single-orbital extended Hubbard model action.

Variational principle

Taking inspiration from the FLF theory [331], we use the Peierls-Feynman-Bogoliubov variational principle [337–339] in order to determine the stiffness parameters $J^{\varsigma}_{\mathbf{Q}}$. This allows for a unique and unambiguous construction of the set of stiffness parameters $J^{\varsigma}_{\mathbf{Q}}$, through the minimization of the functional:

$$\mathcal{F}(J^{\varsigma}_{\mathbf{Q}}) = \mathcal{F}_c(J^{\varsigma}_{\mathbf{Q}}) + \frac{1}{\beta N}\left\langle \mathcal{S} - \mathcal{S}_c\right\rangle_{\mathcal{S}_c}. \tag{4.7}$$

Minimization of the functional with respect to variation of $J^{\varsigma}_{\mathbf{Q}}$, corresponds to calculating:

$$\partial\mathcal{F}/\partial J^{\varsigma}_{\mathbf{Q}} = 0. \tag{4.8}$$

Within the functional, the partition function $\mathcal{Z}_c$ of the action $\mathcal{S}_c$ (4.6) is introduced in order to define the free energy $\mathcal{F}_c(J^{\varsigma}_{\mathbf{Q}}) = -\ln(\mathcal{Z}_c)/\beta N$. Our earlier choice of writing the interaction terms of the initial (4.1) and the trial (4.2) actions using the shifted densities ρ^{ς}, allows us now to simplify the variational treatment. The simplification arises through the bare Green's function $\mathcal{G}_{\mathbf{k}\nu}$ being of an identical form in both actions, meaning a shift in the chemical potential is not necessary. Another choice of variables would have necessitated a shift in the chemical potential in the trial action $\mathcal{S}^{*}$ relative to the initial action $\mathcal{S}$. This treatment allows to generalize the derivation of the FLF theory, which is implicitly defined at half-filling, to any doping.

Evaluating the functional (4.7) corresponds to evaluating the expectation value $\langle\mathcal{S}-\mathcal{S}_c\rangle_{\mathcal{S}_c}$ appearing within the functional. A convenient way to evaluate the expectation value is by an explicit rewriting of the expectation value. The expectation value of the form $\langle\ldots\rangle_{\mathcal{S}_c}$, with the interior being a generic composite fermionic operator, can be explicitly rewrite as (see Ref. [331] for details):

$$\langle ...\rangle_{\mathcal{S}_c} = \langle\langle ...\rangle_{\mathcal{S}_e}\rangle_{\mathcal{S}_{\phi}}, \tag{4.9}$$

with an exterior expectation value taken with respect to the classical field action $\mathcal{S}_\phi$ (4.5) and an interior expectation value taken with respect to an action of the form:

$$\mathcal{S}_e = -\frac{1}{\beta N}\sum_{\mathbf{k},\nu,\sigma} c^*_{\mathbf{k}\nu\sigma}\mathcal{G}^{-1}_{\mathbf{k}\nu}c_{\mathbf{k}\nu\sigma} + \sum_{\mathbf{Q},\varsigma}\phi^\varsigma_{\mathbf{Q}}\rho^\varsigma_{-\mathbf{Q}}. \tag{4.10}$$

The action $\mathcal{S}_e$ corresponds to the single-particle terms in the MCFF trial action $\mathcal{S}^*$ (4.2), and is thus Gaussian with respect to the fermionic degrees of freedom with an effective field depending on the classical fields $\phi^\varsigma_{\mathbf{Q}}$. By separating $\langle\ldots\rangle_{\mathcal{S}_c}$ into an exterior and interior expectation value, we may exploit the Gaussian nature of the action $\mathcal{S}_e$ with respect to the fermions through the application of Wick's theorem in the inner expectation value. In addition, it allows for an intuitive view of the MCFF approach. Any non-zero value of the classical field $\phi^\varsigma_{\mathbf{Q}}$ in the term $\phi^\varsigma_{\mathbf{Q}}\rho^\varsigma_{-\mathbf{Q}}$ in the action (4.10) acts like an effective field which breaks the associate symmetries in the $\mathcal{S}_e$ sub-system. However, by taking the exterior expectation value $\langle\ldots\rangle_{\mathcal{S}_\phi}$, the original symmetries of the full system $\mathcal{S}_c$ are retained. Therefore, the effective classical field action $\mathcal{S}_\phi$ controls the distribution of the ensemble of classical fields breaking the associate symmetries in the $\mathcal{S}_e$ sub-systems. While mean-field approaches require the introduction of an explicit symmetry breaking in the system to enter ordered phases, the fluctuating field approach allows the system to fluctuate in any ordering channel without any explicit symmetry breaking.

The expectation value appearing in the functional $\mathcal{F}(J^\varsigma_{\mathbf{Q}})$ (4.7) may now be explicitly written as:

$$\begin{aligned}\langle\mathcal{S}-\mathcal{S}_c\rangle_{\mathcal{S}_c} = &\frac{U}{\beta N}\sum_{\mathbf{q},\omega}\langle\rho_{\mathbf{q}\omega\uparrow}\rho_{-\mathbf{q},-\omega\downarrow}\rangle_{\mathcal{S}_c} + \frac{1}{2}\sum_{\mathbf{q},\omega}\frac{V_{\mathbf{q}}}{\beta N}\langle\rho_{\mathbf{q}\omega}\rho_{-\mathbf{q},-\omega}\rangle_{\mathcal{S}_c}\\ &-\sum_{\mathbf{Q},\varsigma}\frac{1}{2}\frac{J^\varsigma_{\mathbf{Q}}}{\beta N}\left\langle\rho^\varsigma_{\mathbf{Q}}\rho^\varsigma_{-\mathbf{Q}}\right\rangle_{\mathcal{S}_c}.\end{aligned} \tag{4.11}$$

Exploiting the relationship (4.9), we may rewrite the local interaction term explicitly using Wick's theorem as:

$$U\langle n_{j\tau\uparrow}n_{j\tau\downarrow}\rangle_{\mathcal{S}_c} = \frac{U}{4}\left\langle\langle n^c_{j\tau}\rangle^2_{\mathcal{S}_e} - \langle\vec{n}^s_{j\tau}\rangle^2_{\mathcal{S}_e}\right\rangle_{\mathcal{S}_\phi}, \tag{4.12}$$

where for convenience we have employed a real-space representation for the interaction term. Rewriting the term in the Fourier basis, we arrive at:

$$\sum_{j,\tau}U\langle\rho_{j\tau\uparrow}\rho_{j\tau\downarrow}\rangle_{\mathcal{S}_c} = \frac{1}{\beta N}\sum_{\mathbf{q},\omega}\frac{U}{4}\left\langle\left|\left\langle\rho^c_{\mathbf{q}\omega}\right\rangle_{\mathcal{S}_e}\right|^2 - \left|\left\langle\vec{\rho}^{\,s}_{\mathbf{q}\omega}\right\rangle_{\mathcal{S}_e}\right|^2\right\rangle_{\mathcal{S}_\phi}. \tag{4.13}$$

A similar procedure allows us to rewrite the non-local interaction term approximately using Wick's theorem as:

$$\begin{aligned}\frac{1}{2}V_{ij}\langle n_{i\tau}n_{j\tau}\rangle_{\mathcal{S}_c} &= \frac{1}{2}V_{ij}\sum_{\sigma\sigma'}\left\langle\left\langle c^\dagger_{i\tau\sigma}c_{i\tau\sigma}\right\rangle_{\mathcal{S}_e}\left\langle c^\dagger_{j\tau\sigma'}c_{j\tau\sigma'}\right\rangle_{\mathcal{S}_e} - \left\langle c^\dagger_{i\tau\sigma}c_{j\tau\sigma'}\right\rangle_{\mathcal{S}_e}\left\langle c^\dagger_{j\tau\sigma'}c_{i\tau\sigma}\right\rangle_{\mathcal{S}_e}\right\rangle_{\mathcal{S}_\phi}\\ &\approx \frac{1}{2}V_{ij}\left\langle\langle n^c_{i\tau}\rangle_{\mathcal{S}_e}\langle n^c_{j\tau}\rangle_{\mathcal{S}_e}\right\rangle_{\mathcal{S}_\phi},\end{aligned} \tag{4.14}$$

with $i \neq j$, and where we have dropped the non-local expectation values which are sub-leading with the scaling $1/N$, see Ref. [331]. Same as for the local interaction term, rewriting the non-local interaction term in the Fourier basis, we arrive at:

$$\frac{1}{2}\sum_{ij,\tau} V_{ij} \langle \rho_{i\tau}\rho_{j\tau}\rangle_{\mathcal{S}_c} \approx \frac{1}{2\beta N}\sum_{\mathbf{q},\omega} V_{\mathbf{q}} \left\langle \left| \langle \rho^c_{\mathbf{q}\omega}\rangle_{\mathcal{S}_e} \right|^2 \right\rangle_{\mathcal{S}_\phi} . \tag{4.15}$$

Finally, the procedure may be employed to approximately evaluate the expectation value of the interaction term in the MCFF action as:

$$\frac{1}{2}\frac{J^\varsigma_{\mathbf{Q}}}{\beta N} \langle \rho^\varsigma_{\mathbf{Q}}\rho^\varsigma_{-\mathbf{Q}}\rangle_{\mathcal{S}_c} \approx \frac{1}{2}\frac{J^\varsigma_{\mathbf{Q}}}{\beta N} \left\langle \left| \langle \rho^\varsigma_{\mathbf{Q}}\rangle_{\mathcal{S}_e} \right|^2 \right\rangle_{\mathcal{S}_\phi} , \tag{4.16}$$

in which sub-leading corrections scaling as $1/N$ have been dropped.

Due to the form of the MCFF trial action $\mathcal{S}_e$ (4.10), only certain quasi-momentum and frequency modes of the local and non-local interaction terms (4.13, 4.15) contribute to the functional (4.7). Specifically, only the static ($\omega = 0$) components with the momenta $\mathbf{q} = \mathbf{Q}$ contributes to the average of the shifted density: $\langle \rho^\varsigma_{\mathbf{q}\omega}\rangle_{\mathcal{S}_c} = \langle \rho^\varsigma_{\mathbf{Q}}\rangle_{\mathcal{S}_c}$. Therefore, by combining Eqs. (4.13, 4.15, 4.16), we may approximately rewrite the functional (4.7) as:

$$\begin{aligned}\mathcal{F}(J^\varsigma_{\mathbf{Q}}) \approx \mathcal{F}_c(J^\varsigma_{\mathbf{Q}}) &+ \frac{1}{(\beta N)^2}\sum_{\mathbf{Q}} \left(\frac{U}{4} + \frac{V_{\mathbf{Q}}}{2} - \frac{J^c_{\mathbf{Q}}}{2}\right) \left\langle \left| \langle \rho^c_{\mathbf{Q}}\rangle_{\mathcal{S}_e} \right|^2 \right\rangle_{\mathcal{S}_\phi} \\ &- \frac{1}{(\beta N)^2}\sum_{\mathbf{Q}} \left(\frac{U}{4} + \frac{J^s_{\mathbf{Q}}}{2}\right) \left\langle \left| \langle \vec{\rho}^{\,s}_{\mathbf{Q}}\rangle_{\mathcal{S}_e} \right|^2 \right\rangle_{\mathcal{S}_\phi} .\end{aligned} \tag{4.17}$$

Identification of the stiffness parameters $J^\varsigma_{\mathbf{Q}}$ through the Peierls-Feynman-Bogoliubov variational principle are now simple to obtain through the minimization of the functional (4.7). We determine the stiffness in the spin channel as $J^s_{\mathbf{Q}} = -\frac{U}{2}$, in agreement with previous considerations for the Hubbard model in Ref. [331], while the stiffness in the charge channel is identified as $J^c_{\mathbf{Q}} = \frac{U}{2} + V_{\mathbf{Q}}$. Limiting our considerations to the half-filled extended Hubbard model with repulsive U, V interactions, the leading collective modes are the AFM and CDW fluctuations. Both modes display an ordering vector $\mathbf{Q} = \mathbf{M}$. This gives us the stiffness parameters $J^s_{\mathbf{M}} = -U/2$ and $J^c_{\mathbf{M}} = U/2 - 4V$ for the collective AFM and CDW fluctuations, respectively. By restricting ourselves to the AFM and CDW fluctuations, the MCFF theory describes the collective AFM and CDW states and their interplay.

An important property of the variational approach is the lack of a hidden Fierz ambiguity in the decoupling of the on-site Coulomb interaction U between the different fluctuating channels [250–252]. The obtained values of the stiffness constants $J^\varsigma_{\mathbf{Q}}$ are identical to the form of the bare interaction in HF theory, which avoid the Fierz ambiguity problem [219,340], in the fluctuating exchange (FLEX) approximation [341,342], and in the diagrammatic D-TRILEX approach, which resolves the Fierz ambiguity problem in a completely different way [309,310,313]. At the current stage, the MCFF trial action (4.2) is fully defined which allows for study of competing collective fluctuations.

Free energy

With the MCFF trial action determined through the variational principle, the aim is to employ the simplified system to compute relevant observables associated with

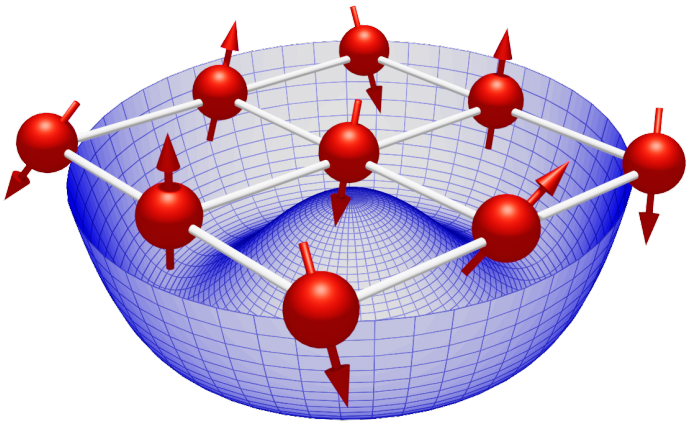

Figure 4.2: Schematic view of magnetic fluctuations in a Hubbard plaquette in an effective Mexican-hat potential. Image taken from Ref. [331].

collective fluctuations and their interplay. Interplay between collective fluctuations in the extended Hubbard model can be studied through a free energy construction based on the effective classical field action $\mathcal{S}_\phi$ (4.5). We introduce a single-channel free energy $\mathcal{F}(\phi^a)$ for a single field of interest ϕ^a, which fully accounts for the influence of the collective fluctuations in the other channels ϕ^b which are integrated out. The single-channel free energy is defined as:

$$\mathcal{F}(\phi^a) \equiv -\frac{1}{\beta N} \ln \left[\int d\phi^b \, \exp\left\{ -\mathcal{S}_\phi[\phi^b] \right\} \right], \tag{4.18}$$

where all classical fields ϕ^b, except for a single field of interest ϕ^a, are integrated out numerically exactly. For a few collective modes, as holds in the current work, the numerical integration over the fields ϕ^b may be performed by the trapezoidal rule over a sufficiently dense grid. By performing the integration exactly, the approach permits to respect the underlying symmetries of the system and to incorporate non-Gaussian fluctuations non-perturbatively. For example, the phase transitions can be determined based on the free energy $\mathcal{F}(\phi^a)$ of the effective MCFF action (4.5), allowing us to avoid computing the more complex susceptibilities in the instability channels. Fluctuations of the relevant order parameters ρ^a are non-perturbatively incorporated in $\mathcal{F}(\phi^a)$ by allowing the development of a global minimum of $\mathcal{F}(\phi^a)$ to shift away from $\phi^a = 0$ in the vein of the development of an effective Mexican-hat potential. Thus a global minimum of $\mathcal{F}(\phi^a)$ lying at $\phi^a \neq 0$ signals the formation of an ordered phase in the phase diagram. Besides the global minimum, the free energy may reveal local minima that indicates the presence of metastable phases.

An important property of the $\mathcal{F}(\phi^a)$ is the stability requirement $J^a < 0$. The requirement ensures that $\mathcal{F}(\phi^a)$ has a global minimum for each ϕ^a, i.e. the ϕ^a-mode is stable. In contrast, the effective fermionic action Eq. (4.6) for $J^a > 0$ is associated with an unstable collective mode, as ordering in the ρ^a-channel is energetically penalized. This requirement limits the regions in which the different collective fluctuations are incorporated within the MCFF scheme. For example, for the considered extended Hubbard model at half-filling, the stability requirement for the AFM and CDW fluctuations are $U > 0$ and $V > U/8$, respectively.

Free energy for interplaying collective CDW and AFM fluctuations

Focusing our attention on the interplay between collective CDW and AFM fluctuations in the extended Hubbard model, the effective classical field action (4.5) is by definition:

$$\mathcal{S}_\phi[\phi^c_{\mathbf{M}}, \phi^s_{\mathbf{M}}] = -\,\mathrm{Tr}\ln\left[\mathcal{G}^{-1}_{\mathbf{k}\nu}\delta_{\mathbf{M},0}\delta_{\sigma,\sigma'} - \sum_{\varsigma=c,s}\phi^\varsigma_{\mathbf{M}}\sigma^\varsigma_{\sigma\sigma'}\right] - \frac{1}{2}\sum_{\varsigma=c,s}\frac{\beta N}{J^\varsigma_{\mathbf{M}}}(\phi^\varsigma_{\mathbf{M}})^2. \tag{4.19}$$

Here, the effective action is rotational invariant with respect to $\phi^s_{\mathbf{M}}$, as required by the spin SU(2) symmetry of the extended Hubbard model. The effective action $\mathcal{S}_\phi[\phi^c_{\mathbf{M}}, \phi^s_{\mathbf{M}}]$ allows to introduce the free energy $\mathcal{F}(\phi^c_{\mathbf{M}})$ for the classical field $\phi^c_{\mathbf{M}}$ with the spin degrees of freedom $\phi^s_{\mathbf{M}}$ numerically exactly integrated out:

$$\mathcal{F}(\phi^c_{\mathbf{M}}) = -\frac{1}{\beta N}\ln\int D[\phi^s_{\mathbf{M}}]\,\exp\big\{-\mathcal{S}_\phi[\phi^c_{\mathbf{M}}, \phi^s_{\mathbf{M}}]\big\}. \tag{4.20}$$

Note, the free energy of the classical vector spin field $\phi^s_{\mathbf{M}}$ can be obtained equivalently by instead integrating out the $\phi^c_{\mathbf{M}}$ field. Within the logarithm in the free energy $\mathcal{F}(\phi^c_{\mathbf{M}})$, the numerical integration over $\phi^s_{\mathbf{M}}$ may be performed by the trapezoidal rule over a sufficiently dense grid. Here it is convenient to exploit the rotational invariance of the action $\mathcal{S}_\phi[\phi^c_{\mathbf{M}}, \phi^s_{\mathbf{M}}]$ with respect to $\phi^s_{\mathbf{M}}$.

In order to compute the free energy $\mathcal{F}(\phi^\varsigma_{\mathbf{M}})$, the action $\mathcal{S}_\phi[\phi^c_{\mathbf{M}}, \phi^s_{\mathbf{M}}]$ is required to be evaluated. An efficient evaluation of the first term in the action (4.5) may be obtained by rewriting the trace over all internal indices as a trace over $\mathbf{k}$ and ν indices over the logarithm of the determinant of a 4×4 matrix in a 2×2 momentum $(\mathbf{k}, \mathbf{k}+\mathbf{M})$ and 2×2 spin $(\uparrow,\downarrow)$ space:

$$\mathrm{Tr}_{\mathbf{k},\mathbf{M},\nu,\sigma}\ln[\ldots] = \mathrm{Tr}_{\mathbf{k},\nu}\ln\det_{\mathbf{Q},\sigma}[\ldots]. \tag{4.21}$$

Note, that within this rewriting $\mathrm{Tr}_{\mathbf{k}}$ is taken over the reduced (half) Brillouin zone. We may evaluate the logarithm of the determinant of the 4×4 matrix appearing in the action (4.5) at half-filling ($\mu = 0$) as:

$$\begin{aligned}\ln\det_{\mathbf{Q},\sigma}[\ldots] &= \ln\det\begin{pmatrix} i\nu-\epsilon_{\mathbf{k}} & 0 & -\phi^c_{\mathbf{M}}-\phi^{s,z}_{\mathbf{M}} & -\phi^{s,x}_{\mathbf{M}}+i\phi^{s,y}_{\mathbf{M}} \\ 0 & i\nu-\epsilon_{\mathbf{k}} & -\phi^{s,x}_{\mathbf{M}}-i\phi^{s,y}_{\mathbf{M}} & -\phi^c_{\mathbf{M}}+\phi^{s,z}_{\mathbf{M}} \\ -\phi^c_{\mathbf{M}}-\phi^{s,z}_{\mathbf{M}} & -\phi^{s,x}_{\mathbf{M}}+i\phi^{s,y}_{\mathbf{M}} & i\nu-\epsilon_{\mathbf{k}+\mathbf{M}} & 0 \\ -\phi^{s,x}_{\mathbf{M}}-i\phi^{s,y}_{\mathbf{M}} & -\phi^c_{\mathbf{M}}+\phi^{s,z}_{\mathbf{M}} & 0 & i\nu-\epsilon_{\mathbf{k}+\mathbf{M}}\end{pmatrix} \\ &= \ln\left[i\nu-\epsilon_{\mathbf{k},-}\right]+\ln\left[i\nu+\epsilon_{\mathbf{k},-}\right]+\ln\left[i\nu-\epsilon_{\mathbf{k},+}\right]+\ln\left[i\nu+\epsilon_{\mathbf{k},+}\right]\end{aligned} \tag{4.22}$$

where we have exploited $\epsilon_{\mathbf{k}+\mathbf{M}} = -\epsilon_{\mathbf{k}}$ and introduced the eigenvalues:

$$\epsilon_{\mathbf{k},\pm} = \sqrt{\epsilon^2_{\mathbf{k}} + (|\phi^c_{\mathbf{M}}| \pm |\vec{\phi}^{\,s}_{\mathbf{M}}|)^2}. \tag{4.23}$$

Note, that the determinant displays the expected rotational invariance of the action $\mathcal{S}_\phi[\phi^c_{\mathbf{M}}, \phi^s_{\mathbf{M}}]$ with respect to $\phi^s_{\mathbf{M}}$. The sum over the Matsubara frequencies ν may now be performed analytically,

$$\mathrm{Tr}_\nu\ln\det_{\mathbf{Q},\sigma}[\ldots] = \sum_{\alpha=\pm}\left[\ln(1+e^{\beta\epsilon_{\mathbf{k},\alpha}})+\ln(1+e^{-\beta\epsilon_{\mathbf{k},\alpha}})\right], \tag{4.24}$$

which allows rewrite the effective action $\mathcal{S}_\phi[\phi^c_{\mathbf{M}}, \phi^s_{\mathbf{M}}]$ as:

$$\mathcal{S}_\phi[\phi^c_{\mathbf{M}}, \phi^s_{\mathbf{M}}] = -\operatorname{Tr}_{\mathbf{k}}\left[\ln(1+e^{\beta\epsilon_{\mathbf{k},\alpha}}) + \ln(1+e^{-\beta\epsilon_{\mathbf{k},\alpha}})\right] - \frac{1}{2}\sum_{\varsigma=c,s}\frac{\beta N}{J^\varsigma_{\mathbf{M}}}(\phi^\varsigma_{\mathbf{M}})^2. \tag{4.25}$$

which leaves the reduced $\mathbf{k}$ summation and the integration over $\phi^s_{\mathbf{M}}$ to be performed numerically in the evaluation of the single-channel free energies $\mathcal{F}(\phi^\varsigma_{\mathbf{M}})$.

Limiting to collective CDW and AFM fluctuations in the extended Hubbard model without any interplay, i.e. the SCFF theory within the charge or spin channel, allows to further understand the fluctuating field theory. This regime is a valid approximation in the weak-coupling regime, where the competition between the two channels is not expected to be strong. For a single classical field, either in the CDW channel ($\phi^c_{\mathbf{M}}$) or in the AFM channel ($\phi^s_{\mathbf{M}}$), the effective $\mathcal{S}_\phi[\phi^\varsigma_{\mathbf{M}}]$ may be explicitly written in the following form:

$$\mathcal{S}_\phi[\phi^\varsigma_{\mathbf{M}}] = -\sum_k\left[\ln\left(1+e^{-\beta\epsilon_{\mathbf{k},+}}\right) + \ln\left(1+e^{-\beta\epsilon_{\mathbf{k},-}}\right)\right] - \frac{1}{2}\frac{\beta N}{J^\varsigma_{\mathbf{M}}}{\phi^\varsigma_{\mathbf{M}}}^2. \tag{4.26}$$

Here the $\mathbf{k}$ summation is the non-reduced one, and the parameters $\epsilon_{\mathbf{k},\pm}$ are the eigenvalues:

$$\epsilon_{\mathbf{k},\pm} = \frac{\epsilon_{\mathbf{k}} + \epsilon_{\mathbf{k}+\mathbf{M}}}{2} \pm \sqrt{\left(\frac{\epsilon_{\mathbf{k}} - \epsilon_{\mathbf{k}+\mathbf{M}}}{2}\right)^2 + {\phi^\varsigma_{\mathbf{M}}}^2}, \tag{4.27}$$

where we have chosen not to exploit $\epsilon_{\mathbf{k}+\mathbf{M}} = -\epsilon_{\mathbf{k}}$ in order to later connect to the charge and spin susceptibilies within RPA and FLEX theories. By performing a Taylor expansion in the first term of Eq. (4.26),

$$\mathcal{S}_\phi = \left\{\beta\sum_k\left[\frac{n_F(\epsilon_{\mathbf{k}}) - n_F(\epsilon_{\mathbf{k}+\mathbf{Q}})}{\epsilon_{\mathbf{k}} - \epsilon_{\mathbf{k}+\mathbf{Q}}}\right] - \frac{1}{2}\frac{\beta N}{J^\varsigma_{\mathbf{Q}}}\right\}{\phi^\varsigma_{\mathbf{Q}}}^2 + \mathcal{O}({\phi^\varsigma_{\mathbf{Q}}}^4), \tag{4.28}$$

one identifies the structure to be an effective free energy functional of the Landau theory form for a second-order transition. It follows, that the critical value of the stiffness parameter for a collective ordering may be identified as a change in the sign of the ${\phi^\varsigma_{\mathbf{Q}}}^2$ term. This leads to the critical stiffness parameters for both the CDW and AFM channels respecting the following analytic relationship:

$$J^\varsigma_{\mathbf{M}} = 1/\Pi_{\mathbf{M}}. \tag{4.29}$$

Here the (static) noninteracting polarisation $\Pi_{\mathbf{M}}$ for the momentum transfer $\mathbf{q} = \mathbf{M}$ is employed. By allowing for multiple channels in competition, the collective fluctuations describes by effective Mexican-hat potentials are mutually coupled through their coupling to the electronic degrees of freedom, i.e. through the $\operatorname{Tr}\ln[\ldots]$ term of the effective action (4.5). Thus, a simple analytic treatment performed here is in general unfeasible in the case of interplaying collective fluctuations.

Studying the SCFF estimates for the critical stiffness parameters allows to connect the approach to the charge and spin susceptibilies within RPA and FLEX theories. Within RPA theory, the critical non-local interaction $V^{\mathrm{CDW}}_{U=0}$ for the CDW phase boundary is identified by a divergence of the RPA charge susceptibility at the $\mathbf{M}$-point, leading to the estimate:

$$V_{\mathbf{Q}} = 1/\Pi_{\mathbf{Q}}. \tag{4.30}$$

Analogously, within FLEX theory, the critical local interaction $U^{\mathrm{AFM}}_{V=0}$ for the AFM phase boundary is identified by a divergence of the FLEX spin susceptibility at the **M**-point, which gives:

$$U^s = 1/\Pi_{\mathbf{Q}}. \tag{4.31}$$

Due to the choice of decoupling of the local interaction in the FLEX theory, the local spin interaction is given by $U^{\mathrm{s}} = -U/2$. Thus, we identify the SCFF theory to be in exact agreement with the $V^{\mathrm{CDW}}_{U=0}$ and $U^{\mathrm{AFM}}_{V=0}$ transition points of RPA and FLEX theory, respectively.

Order parameters and measure of collective fluctuations

Within our later numerical studies, it will be useful to quantify the strength of the collective fluctuations within the MCFF approach. Therefore, we introduce a measure $\langle|n^{\varsigma}_{\mathbf{Q}}|\rangle$ to quantify the fluctuations around the minimum of the free energy. The measure $\langle|n^{\varsigma}_{\mathbf{Q}}|\rangle$ is defined as the expectation value of $|n^{\varsigma}_{\mathbf{Q}}|$ in a channel of choice $n^{\varsigma}_{\mathbf{Q}}$ by performing a numerical integration over all other classical field degrees of freedom associated with the collective fluctuations. The numerical integration corresponds to the inclusion of fluctuations about the saddle-point known to be important, e.g. see work on the crossover from BCS theory to Bose-Einstein condensate [343, 344]. Our calculations of the measure $\langle|n^{\varsigma}_{\mathbf{Q}}|\rangle$ may be compared to the saddle-point estimate $\langle|n^{\varsigma}_{\mathbf{Q}}|\rangle_{\mathrm{MF}}$, i.e. the value at the minimum of the free energy, which is equivalent with a conventional mean-field theory estimate. Thus, the difference between the integrated and saddle-point measure of collective fluctuations allows to evaluate the differences between the fluctuating field and mean-field theories. Insight into the interplay between collective ordering is convenient to calculating through the saddle-point estimate, as it acts as a natural order parameter.

Interacting Green's function and self-energy

We seek now to evaluate the Matsubara Green's function of the fluctuating field theory. It is accessible by exploiting the explicit rewriting (4.9) of the expectation value, allowing to express the interacting Matsubara Green's function $\mathcal{G}_I$ as an integration over the bare Matsubara Green's functions $\mathcal{G}_e[\phi^{\varsigma}_{\mathbf{M}}]$ of the Gaussian action $\mathcal{S}_e$ Eq. (4.10):

$$\mathcal{G}_{I,\mathbf{k}\nu} = \frac{1}{Z_\phi}\int D[\phi^{\varsigma}_{\mathbf{M}}]\mathcal{G}_{e,\mathbf{k}\nu}[\phi^{\varsigma}_{\mathbf{M}}]\exp\{-S_\phi[\phi^{\varsigma}_{\mathbf{M}}]\}. \tag{4.32}$$

The interacting Matsubara Green's function $\mathcal{G}_I$ is thus an ensemble or multi-reference Green's function [345–347] corresponding to a weighted ensemble of symmetry-broken bare Matsubara Green's functions. Importantly, the exterior expectation value retains the translational and spin symmetries of the original system. To observe these properties, we write the symmetry-broken bare Matsubara Green's functions $\mathcal{G}_e[\phi^{\varsigma}_{\mathbf{Q}}]$ in the eigenbasis of the Gaussian action $\mathcal{S}_e$ Eq. (4.10) as

$$\mathcal{G}_{e,\alpha\nu} = \frac{1}{i\nu - \epsilon_\alpha[\phi^{\varsigma}_{\mathbf{M}}]}, \tag{4.33}$$

with the eigenvalues $\epsilon_\alpha[\phi^{\varsigma}_{\mathbf{M}}]$, associated with the 4×4 matrix in a 2×2 momentum $(\mathbf{k}, \mathbf{k}+\mathbf{M})$ and 2×2 spin $(\uparrow,\downarrow)$ space as employed in generating the free energy. To

retrieve the $\mathcal{G}_{e,\alpha\nu}$ in momentum and spin space, a transformation from the eigenbasis to the momentum and spin basis is required. Within the momentum and spin basis, the bare Matsubara Green's function $\mathcal{G}_e[\phi^{\varsigma}_{\mathbf{Q}}]$ becomes

$$\mathcal{G}_{e,\mathbf{k_1}\mathbf{k_2},\sigma_1\sigma_2,\nu} = \sum_{\alpha} \frac{\psi^*_{\alpha:\mathbf{k}_1,\sigma_1}\psi_{\alpha:\mathbf{k}_2,\sigma_2}}{i\nu - \epsilon_\alpha[\phi^{\varsigma}_{\mathbf{M}}]}, \tag{4.34}$$

where $\mathbf{k_1}, \mathbf{k_2} \in \{\mathbf{k}, \mathbf{k}+\mathbf{Q}\}$ and $\psi_{\alpha:\mathbf{k}_i,\sigma_i}$ are the coefficients of eigenfunctions in the momentum and spin basis. The bare Matsubara Green's functions are off-diagonal, however, by performing the exterior integration over the classical fields, the symmetries of the full system is enforced. This leads to a vanishing contribution of the off-diagonal terms to the interacting Matsubara Green's function $\mathcal{G}_I$.

An analytic dependency of the Matsubara frequency dependence in the interacting Matsubara Green's function $\mathcal{G}_I$ is observed. We may thus employ an analytic continuation $i\nu \to \omega + i0^+$ to rotate from the imaginary frequency axis to the real frequency axis, allowing us to calculate the physical retarded Green's function G_R. From the retarded Green's function G_R, we may calculate the spectral function,

$$A_{\mathbf{k},\omega} = -\frac{1}{\pi}\mathrm{Im}[G_{R,\mathbf{k},\omega}], \tag{4.35}$$

allowing access to spectral properties within the fluctuating field theory. By inverting the Dyson equation, we have access to the effective self-energy of the fluctuating field theory,

$$\Sigma_{\mathbf{k},\omega} = G^{-1}_{0,R,\mathbf{k},\omega} - G^{-1}_{R,\mathbf{k},\omega}, \tag{4.36}$$

where $G_{0,R,\mathbf{k},\omega}$ is the bare retarded Green's function. The spectral function and the self-energy allows for a convenient framework to discuss the many-body effects captured within the theory. With the methods for constructing the free energy, the measure of collective fluctuations, the spectral function and the self-energy within the MCFF theory, we are sufficiently ready to discuss results in the repulsive U, V phase diagram for the extended Hubbard model in Chapter 5.

4.1.2 Variational mapping of s-wave pairing fluctuations

By limiting our considerations to repulsive U, V interactions in the extended Hubbard model on a two-dimensional square lattice, the dominant collective fluctuations are entirely within the particle-hole channel, e.g. the charge and spin channels. However, by allowing for attractive U, V interactions in the system, dominant collective fluctuations in the particle-particle channel emerges, e.g. collective s-wave pairing fluctuations. In order to incorporate s-wave pairing channel, we now seek to generalise the MCFF theory to include collective fluctuations in the particle-particle channel following Ref. [335].

The main structures of the extended Hubbard action $\mathcal{S}$ and the MCFF trial action $\mathcal{S}^*$ remain unchanged with the inclusion s-wave pairing fluctuations. Besides a set of classical spin ($\varsigma = s \in \{x, y, z\}$) vector fields $\phi^s_{\mathbf{Q}}$, a novel feature in the trial action is the introduction of a new set of classical pseudo-spin ($\varsigma = s_p \in \{x, y, z\}$) vector fields $\phi^{s_p}_{\mathbf{Q}}$. These novel fields are coupled to the composite variables $\rho^{s_p}_{\mathbf{Q}}$, defined by the pseudo-spin density:

$$n^{s_p}_{\mathbf{Q}} = \frac{1}{\beta N}\sum_{\mathbf{k},\nu,\sigma\sigma'} \psi^*_{\mathbf{k}+\mathbf{Q},\nu\sigma}\sigma^{s_p}_{\sigma\sigma'}\psi_{\mathbf{k}\nu\sigma'}, \tag{4.37}$$

where the expression is written in the Nambu spinor basis introduced for the pseudo-spin symmetry in a previous chapter. The vector pseudo-spin field $\phi^{s_p}_{\mathbf{Q}}$ combines collective fluctuations in both the s-wave pairing channel ($s_p \in \{x, y\}$) and the charge channel ($s_p \in \{z\}$). As in the investigation of interplaying collective charge and spin fluctuations, a set of stiffness parameters $J^{\mathrm{s}}_{\mathbf{Q}}$ associated to each classical field $\phi^{\mathrm{s}}_{\mathbf{Q}}$ determine the form of their interplay. Analytic techniques developed to manipulate the MCFF trial action in the previous section are applicable for the current considerations as well, allowing to determine the stiffness parameters $J^{\mathrm{s}}_{\mathbf{Q}}$ through the variational principle.

Variational principle

Allowing for collective fluctuations in the s-wave pairing channel modifies the variational principle utilized in the determination of the stiffness parameters $J^{\mathrm{s}}_{\mathbf{Q}}$ by the introduction of additional terms in the functional (4.7). The additional terms enters only through the local interaction term in the expectation value $\langle \mathcal{S} - \mathcal{S}_c \rangle_{\mathcal{S}_c}$ appearing in the functional $\mathcal{F}(J^{\mathrm{s}}_{\mathbf{Q}})$ (4.7). Allowing for charge, spin and s-wave pairing fluctuations leads to the following local interaction term:

$$U \left\langle n_{j\tau\uparrow} n_{j\tau\downarrow} \right\rangle_{\mathcal{S}_c} = \frac{U}{4} \left\langle \left\langle \vec{n}^{s_p}_{j\tau} \right\rangle^2_{\mathcal{S}_e} - \left\langle \vec{n}^{s}_{j\tau} \right\rangle^2_{\mathcal{S}_e} \right\rangle_{\mathcal{S}_\phi}, \tag{4.38}$$

written in a real-space representation. By transforming to the Fourier basis, the generalised form of the local interaction term (4.13) is given by:

$$\sum_{j,\tau} U \left\langle \rho_{j\tau\uparrow} \rho_{j\tau\downarrow} \right\rangle_{\mathcal{S}_c} = \frac{1}{\beta N} \sum_{\mathbf{q},\omega} \frac{U}{4} \left\langle \left| \left\langle \vec{\rho}^{\,s_p}_{\mathbf{q}\omega} \right\rangle_{\mathcal{S}_e} \right|^2 - \left| \left\langle \vec{\rho}^{\,s}_{\mathbf{q}\omega} \right\rangle_{\mathcal{S}_e} \right|^2 \right\rangle_{\mathcal{S}_\phi}. \tag{4.39}$$

Remaining terms in the functional $\mathcal{F}(J^{\mathrm{s}}_{\mathbf{Q}})$ (4.7) are unchanged, under the approximation where all sub-leading terms scaling as $1/N$ are neglected. Thereby, we may approximately rewrite the functional $\mathcal{F}(J^{\mathrm{s}}_{\mathbf{Q}})$ (4.7) to obtain:

$$\begin{aligned}
(\beta N)^2 [\mathcal{F}(J^{\mathrm{s}}_{\mathbf{Q}}) - \mathcal{F}_c(J^{\mathrm{s}}_{\mathbf{Q}})] \approx & \sum_{\mathbf{Q}} \left(\frac{U}{4} + \frac{V_{\mathbf{Q}}}{2} - \frac{J^{s_p,z}_{\mathbf{Q}}}{2} \right) \left\langle \left| \left\langle \rho^{s_p,z}_{\mathbf{Q}} \right\rangle_{\mathcal{S}_e} \right|^2 \right\rangle_{\mathcal{S}_\phi} \\
& + \sum_{i=x,y} \sum_{\mathbf{Q}} \left(\frac{U}{4} - \frac{J^{s_p,i}_{\mathbf{Q}}}{2} \right) \left\langle \left| \left\langle \rho^{s_p,i}_{\mathbf{Q}} \right\rangle_{\mathcal{S}_e} \right|^2 \right\rangle_{\mathcal{S}_\phi} \\
& - \sum_{i=x,y,z} \sum_{\mathbf{Q}} \left(\frac{U}{4} + \frac{J^{s,i}_{\mathbf{Q}}}{2} \right) \left\langle \left| \left\langle \rho^{s,i}_{\mathbf{Q}} \right\rangle_{\mathcal{S}_e} \right|^2 \right\rangle_{\mathcal{S}_\phi}.
\end{aligned} \tag{4.40}$$

By symmetry, we observe the stiffness parameters are restricted to three independent channels: the spin channel with $J^{s}_{\mathbf{Q}} = J^{s,i}_{\mathbf{Q}}$ for $i \in \{x, y, z\}$, the charge channel with $J^{c}_{\mathbf{Q}} = J^{s_p,i}_{\mathbf{Q}}$ for $i \in \{z\}$ and the s-wave pairing channel with $J^{s-\mathrm{SC}}_{\mathbf{Q}} = J^{s_p,i}_{\mathbf{Q}}$ for $i \in \{x, y\}$. By the minimization of the functional (4.7) with respect to variation in the stiffness parameters $J^{\mathrm{s}}_{\mathbf{Q}}$, we identify the stiffness in the s-wave pairing channel as $J^{s-\mathrm{SC}}_{\mathbf{Q}} = \frac{U}{2}$. The stiffness parameters in the charge and spin channels are in agreement with our previous considerations. Note the equivalence $J^{c}_{\mathbf{Q}} = J^{s-\mathrm{SC}}_{\mathbf{Q}}$ for $V = 0$, which displays the emergence of the SU(2) pseudo-spin symmetry in the MCFF trial action for vanishing

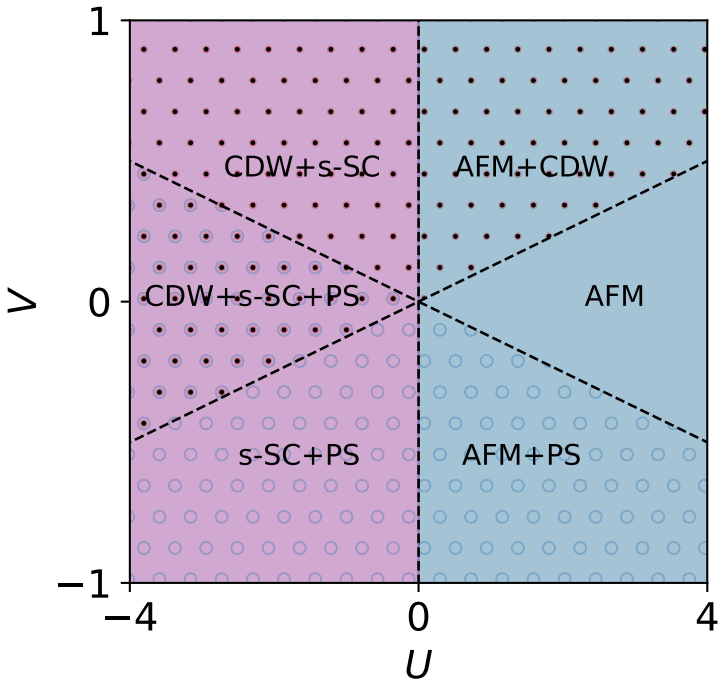

Figure 4.3: Regions associated with different stability requirement for the half-filled extended Hubbard model with both repulsive and attractive U, V interactions. Dashes lines separated the different regions, with blue (purple) background colour corresponding to the AFM (s-SC) channel and red (blue) coloured rings corresponding to the CDW (PS) channel.

non-local interaction. Through the generalisation of the MCFF theory in the current section, we observe the possibility of incorporating any competing order parameter expressable as a single-particle fermionic composite variable.

Limiting our considerations to the half-filled extended Hubbard model with both repulsive and attractive U, V interactions, the leading collective modes within the considered channels are the AFM, CDW and s-SC fluctuations with an ordering vector $\mathbf{Q} = \mathbf{M}$ and PS fluctuations with an ordering vector $\mathbf{Q} \to \mathbf{\Gamma}$. We wish to remind the reader that the PS state, i.e. phase separation, corresponds in our consideration to the formation of broad puddles with uniform filling larger or smaller than half-filling. This gives us $J^s_{\mathbf{M}} = -U/2$ for the AFM state, $J^c_{\mathbf{M}} = U/2 - 4V$ and $J^c_{\mathbf{\Gamma}} = U/2 + 4V$ for the CDW and PS states, respectively, and $J^{s-\mathrm{SC}}_{\mathbf{M}} = U/2$ for the s-SC state. Restricting ourselves to those four collective modes, the MCFF theory describes the collective fluctuations and their mutual interplay. However, due to the stability requirement $J^{\gamma}_{\mathbf{Q}} < 0$ for the collective modes, all four collective modes are not concurrently stable. Collective AFM (s-SC) fluctuations are restricted to the repulsive (attractive) U regime, leading to an absence of competing magnetic and s-wave pairing fluctuations. In the charge channel, collective CDW (PS) fluctuations are limited to the $U < 8V$ ($U < -8V$) regime. Therefore, within the MCFF theory, interplaying collective CDW and PS fluctuations may only occur at attractive U interactions. A beneficial aspect of the MCFF theory is the freedom related with the choice of the allowed ordering channels, permitting a careful study of the different contributions to the interplay between multiple modes.

Free energy for interplaying collective charge, spin and pairing fluctuations

We restrict our investigating to competition between collective CDW, AFM, s-SC and PS fluctuations through the free energy construction within the MCFF theory. The stability requirement leads to a natural division between the repulsive U regime with competing CDW, AFM and PS fluctuations, and the attractive U regime with competing CDW, s-SC and PS fluctuations. Thus, treating the repulsive U regime is conveniently done within the conventional spinor basis, while the attractive U regime is preferentially studied through the Nambu spinor basis. Extending the previous considerations to the collective modes with the ordering vector $\mathbf{Q} = \mathbf{M}$ is straightforward. However, incorporating the collective PS fluctuations with an ordering vector $\mathbf{Q} \to \mathbf{\Gamma}$ is a subtle point requiring additional considerations.

Working within the Nambu spinor basis, the interplaying CDW and s-SC modes are described by the effective classical field action (4.5) defined by:

$$\mathcal{S}_{\phi}[\phi^{s_p}_{\mathbf{M}}] = -\operatorname{Tr}\ln\left[\mathcal{G}^{-1}_{\mathbf{k}\nu}\delta_{\mathbf{M},0}\delta_{\sigma,\sigma'} - \sum_{\varsigma=s_p}\phi^{\varsigma}_{\mathbf{M}}\sigma^{\varsigma}_{\sigma\sigma'}\right] - \frac{1}{2}\sum_{\varsigma=s_p}\frac{\beta N}{J^{\varsigma}_{\mathbf{M}}}(\phi^{\varsigma}_{\mathbf{M}})^2. \tag{4.41}$$

It follows from our previous considerations for interplay CDW and AFM fluctuations, that it is convenient to rewrite the trace over all internal indices in the first term of the effective classical field action $\mathcal{S}_{\phi}$ (4.41) as a trace over $\mathbf{k}$ and ν indices over the logarithm of the determinant of a 4×4 matrix in a 2×2 momentum $(\mathbf{k}, \mathbf{k}+\mathbf{M})$ and 2×2 pseudo-spin $(\uparrow, \downarrow)$. For the system at half-filling ($\mu = 0$), the logarithm of the determinant may be evaluated as:

$$\begin{aligned}\ln\det_{\mathbf{Q},\sigma}[\ldots] &= \ln\det\begin{pmatrix} i\nu-\epsilon_{\mathbf{k}} & 0 & -\phi^{s_p,z}_{\mathbf{M}} & -\phi^{s_p,x}_{\mathbf{M}}+i\phi^{s_p,y}_{\mathbf{M}} \\ 0 & i\nu-\epsilon_{\mathbf{k}} & -\phi^{s_p,x}_{\mathbf{M}}-i\phi^{s_p,y}_{\mathbf{M}} & +\phi^{s_p,z}_{\mathbf{M}} \\ -\phi^{s_p,z}_{\mathbf{M}} & -\phi^{s_p,x}_{\mathbf{M}}+i\phi^{s_p,y}_{\mathbf{M}} & i\nu-\epsilon_{\mathbf{k}+\mathbf{M}} & 0 \\ -\phi^{s_p,x}_{\mathbf{M}}-i\phi^{s_p,y}_{\mathbf{M}} & +\phi^{s_p,z}_{\mathbf{M}} & 0 & i\nu-\epsilon_{\mathbf{k}+\mathbf{M}} \end{pmatrix} \\ &= 2\ln\left[i\nu-\epsilon_{0,\mathbf{k}}\right] + 2\ln\left[i\nu+\epsilon_{0,\mathbf{k}}\right], \end{aligned} \tag{4.42}$$

where we have exploited $\epsilon_{\mathbf{k}+\mathbf{M}} = -\epsilon_{\mathbf{k}}$ and introduced the eigenvalues:

$$\epsilon_{0,\mathbf{k}} = \sqrt{\epsilon^2_{\mathbf{k}} + [\vec{\phi}^{\,s_p}_{\mathbf{M}}]^2}. \tag{4.43}$$

As for the repulsive U, V case, the Matsubara summation Tr_{ν} may be performed analytically, and the remaining $\mathrm{Tr}_{\mathbf{k}}$ over the reduced (half) Brillouin zone is required to be taken numerically. Construction of the single-channel free energy (4.18) corresponds to a numerical integration over the charge or s-wave superconducting degrees of freedom. Note that the first term in $\mathcal{S}_{\phi}[\phi^{s_p}_{\mathbf{M}}]$ displays a rotational invariance with respect to $\phi^{s_p}_{\mathbf{M}}$, associated with the pseudo-spin SU(2) symmetry. In contrast, the second term in effective classical field action $\mathcal{S}_{\phi}[\phi^{s_p}_{\mathbf{M}}]$ (4.41) breaks the pseudo-spin symmetry for any value $V \neq 0$. Thus, the pseudo-spin SU(2) symmetry naturally emerges for vanishing non-local interaction as the model turns into the two-dimensional square lattice Hubbard model.

Focusing on the collective PS fluctuations, we expect difficulties to arise at $\mathbf{Q} \to \mathbf{\Gamma}$ for any static ($\omega = 0$) order parameter. The origin of the difficulty is the ill-defined nature of the susceptibility due to the limits $\omega \to 0$ and $\mathbf{q} \to 0$ being non-commuting. This leads to a certain ambiguity in the treatment of PS fluctuations. For example,

if one naively couples the classical PS field $\phi^z_{\mathbf{\Gamma}}$ to the corresponding charge density component:

$$n^c_{\mathbf{\Gamma}} \equiv \frac{1}{\beta N} \sum_{\mathbf{k},\nu,\sigma} c^*_{\mathbf{k}\nu\sigma} c_{\mathbf{k}\nu\sigma}, \tag{4.44}$$

the field $\phi^c_{\mathbf{\Gamma}}$ behaves as an effective chemical potential of the system. Evaluating the first term in the effective action $\mathcal{S}_\phi[\phi^c_{\mathbf{\Gamma}}]$, however, generates both odd and even terms in orders of $\phi^z_{\mathbf{\Gamma}}$. Odd terms are problematic, as their presences breaks the particle number conservation, because the system violates the invariance of $\mathcal{S}_\phi[\phi^c_{\mathbf{\Gamma}}]$ under a sign change of the field $\phi^c_{\mathbf{\Gamma}} \to -\phi^c_{\mathbf{\Gamma}}$. To overcome this problem, we couple the collective PS field $\phi^c_{\mathbf{\Gamma}}$ to the electronic density taken at $\mathbf{Q} \to \mathbf{\Gamma}$:

$$n^c_{\mathbf{\Gamma}} \equiv \frac{1}{2\beta N} \sum_{\mathbf{k},\nu,\sigma} \lim_{\mathbf{k}' \to \mathbf{k}} \left[c^*_{\mathbf{k}\nu\sigma} c_{\mathbf{k}'\nu\sigma} + \text{h.c.} \right] \tag{4.45}$$

and rewrite the bare term as:

$$-\frac{1}{\beta N} \sum_{\mathbf{k},\nu,\sigma} c^*_{\mathbf{k}\nu\sigma} \mathcal{G}^{-1}_{\mathbf{k}\nu} c_{\mathbf{k}\nu\sigma} = -\frac{1}{2\beta N} \sum_{\mathbf{k},\nu,\sigma} \lim_{\mathbf{k}' \to \mathbf{k}} \left[c^*_{\mathbf{k}\nu\sigma} \mathcal{G}^{-1}_{\mathbf{k}\nu} c_{\mathbf{k}\nu\sigma} + c^*_{\mathbf{k}'\nu\sigma} \mathcal{G}^{-1}_{\mathbf{k}'\nu} c_{\mathbf{k}'\nu\sigma} \right], \tag{4.46}$$

This procedure leads to an artificial enlargement of the quasi-momentum ($\mathbf{k}$) space to a 2×2 matrix form in the $(\mathbf{k}, \mathbf{k}')$ space for each momentum $\mathbf{k}$, which results in a "1/2" prefactor in front of the trace over momentum $\mathbf{k}$:

$$\mathrm{Tr}_{\mathbf{k},\nu,\sigma} \ln[\ldots] = \frac{1}{2} \mathrm{Tr}_{\mathbf{k},\nu,\sigma} \lim_{\mathbf{k}' \to \mathbf{k}} \ln \det_{(\mathbf{k},\mathbf{k}')} [\ldots]. \tag{4.47}$$

The logarithm of the determinant of the 2×2 matrix in the momentum $(\mathbf{k}, \mathbf{k}')$ space explicitly reads:

$$\ln \det \begin{pmatrix} i\nu - \epsilon_{\mathbf{k}} & -\phi^z_{\mathbf{\Gamma}} \\ -\phi^z_{\mathbf{\Gamma}} & i\nu - \epsilon_{\mathbf{k}'} \end{pmatrix} = \ln \left[i\nu - \epsilon_{\mathbf{k}} + \phi^z_{\mathbf{\Gamma}} \right] + \ln \left[i\nu - \epsilon_{\mathbf{k}'} - \phi^z_{\mathbf{\Gamma}} \right], \tag{4.48}$$

where the "1/2" prefactor in front of each element of the matrix is dropped out, as it only gives an irrelevant constant term in the effective action $\mathcal{S}_\phi[\phi^c_{\mathbf{\Gamma}}]$. Note, that the logarithm of the determinant is an even function with respect to the field $\phi^c_{\mathbf{\Gamma}}$. Thus, no problematic breaking of particle number conservation occurs in this treatment. Effectively, the enlargement of the momentum space contributes to the PS fluctuations capturing the formation of homogeneous regions of positive and negative shifts in the chemical potential, i.e. electronic puddles of lower and higher filling.

With the treatment of the collective PS mode defined, we may now allow it to compete with the collective AFM mode for repulsive U or the collective CDW and s-SC modes for attractive U. Due to the nearly identical procedure in both regimes, we limit our considerations to the repulsive U regime for convenience. By inclusion of PS modes, the effective classical field action (4.41) describing the interplaying CDW and AFM modes is enlarged:

$$\begin{aligned} \mathcal{S}_\phi[\phi^c_{\mathbf{M}}, \phi^s_{\mathbf{M}}, \phi^c_{\mathbf{\Gamma}}] = &- \mathrm{Tr} \ln \left[\mathcal{G}^{-1}_{\mathbf{k}\nu} \delta_{\mathbf{M},0} \delta_{\sigma,\sigma'} - \sum_{\varsigma=c,s} \phi^\varsigma_{\mathbf{M}} \sigma^\varsigma_{\sigma\sigma'} - \phi^c_{\mathbf{\Gamma}} \sigma^c_{\sigma\sigma'} \right] \\ &- \frac{1}{2} \sum_{\varsigma=c,s} \frac{\beta N}{J^\varsigma_{\mathbf{M}}} (\phi^\varsigma_{\mathbf{M}})^2 - \frac{1}{2} \frac{\beta N}{J^c_{\mathbf{\Gamma}}} (\phi^c_{\mathbf{\Gamma}})^2. \end{aligned} \tag{4.49}$$

In order to evaluate the first term of the effective classical field action $\mathcal{S}_\phi$ (4.49), we rewrite the trace over all internal indices as a trace over $\mathbf{k}$ and ν indices over the logarithm of the determinant of a 8×8 matrix in a 4×4 momentum $(\mathbf{k}, \mathbf{k}', \mathbf{k}+\mathbf{M}, \mathbf{k}'+\mathbf{M})$ and 2×2 spin $(\uparrow, \downarrow)$ spaces. The logarithm of the determinant of the enlarged 8×8 matrix size may be analytically evaluated as:

$$\begin{aligned}\frac{1}{2}\ln \det_{\mathbf{Q},(\mathbf{k},\mathbf{k}'),\sigma}[\ldots] &= \frac{1}{2}\ln\det\begin{pmatrix}\mathcal{A}_{\mathbf{k}}^{4\times4} & \mathcal{B}^{4\times4} \\ \mathcal{B}^{4\times4} & \mathcal{A}_{\mathbf{k}+\mathbf{M}}^{4\times4}\end{pmatrix} \\ &= \frac{1}{2}\sum_{\alpha=\pm}\left\{\ln\left[\left(i\nu-\epsilon_{\mathbf{k},\alpha}+\phi_{\mathbf{\Gamma}}^{c}\right)\left(i\nu-\epsilon_{\mathbf{k},\alpha}-\phi_{\mathbf{\Gamma}}^{c}\right)\right]\right. \\ &\left.+\ln\left[\left(i\nu+\epsilon_{\mathbf{k},\alpha}+\phi_{\mathbf{\Gamma}}^{c}\right)\left(i\nu+\epsilon_{\mathbf{k},\alpha}-\phi_{\mathbf{\Gamma}}^{c}\right)\right]\right\}, \end{aligned} \tag{4.50}$$

where the limit $\mathbf{k}' \to \mathbf{k}$ has been taken in the expression, and where we have introduced the 4×4 matrices:

$$\mathcal{A}_{\mathbf{k}}^{4\times4} = \begin{pmatrix} i\nu-\epsilon_{\mathbf{k}} & 0 & -\phi_{\mathbf{\Gamma}}^{c} & 0 \\ 0 & i\nu-\epsilon_{\mathbf{k}} & 0 & -\phi_{\mathbf{\Gamma}}^{c} \\ -\phi_{\mathbf{\Gamma}}^{c} & 0 & i\nu-\epsilon_{\mathbf{k}} & 0 \\ 0 & -\phi_{\mathbf{\Gamma}}^{c} & 0 & i\nu-\epsilon_{\mathbf{k}} \end{pmatrix}, \tag{4.51}$$

$$\mathcal{B}^{4\times4} = \begin{pmatrix} -\phi_{\mathbf{M}}^{s,z} & -\phi_{\mathbf{M}}^{s,x}+i\phi_{\mathbf{M}}^{s,y} & 0 & 0 \\ -\phi_{\mathbf{M}}^{s,x}-i\phi_{\mathbf{M}}^{s,y} & +\phi_{\mathbf{M}}^{s,z} & 0 & 0 \\ 0 & 0 & -\phi_{\mathbf{M}}^{s,z} & -\phi_{\mathbf{M}}^{s,x}+i\phi_{\mathbf{M}}^{s,y} \\ 0 & 0 & -\phi_{\mathbf{M}}^{s,x}-i\phi_{\mathbf{M}}^{s,y} & +\phi_{\mathbf{M}}^{s,z} \end{pmatrix}. \tag{4.52}$$

The case of competing interplaying CDW, s-SC and PS fluctuations is retrieved by the following replacement: $\phi_{\mathbf{M}}^{s} \to \phi_{\mathbf{M}}^{s_p}$ for the collective CDW and s-SC fluctuations and $\phi_{\mathbf{\Gamma}}^{c} \to \phi_{\mathbf{\Gamma}}^{s_p,z}$ for the collective PS fluctuations. This completes the evaluation of the effective classic field actions $\mathcal{S}_\phi$ (4.5) required for the computation of the single-channel free energies (4.18). With details regarding the implementation of collective PS fluctuations presented, the theoretical basis of the results in the repulsive and attractive U, V phase diagram for the extended Hubbard model in Chapter 6 has been introduced.

4.2 Summary and perspectives

We have introduced a multi-channel extension of the fluctuating field theory to address interplaying collective fluctuations for correlated electronic systems, based on a variational optimization of a trial action respecting the underlying symmetries of the system. Our work allows for the application of the fluctuating field theory to interplay of collective fluctuations associated with arbitrary one-particle composite operators in the particle-hole or particle-particle channels. In the chapter, we restricted our derivation to charge, spin and s-wave superconducting fluctuations which will allow us to extensively study the half-filled extended Hubbard model $U-V$ phase diagram in the two chapters to follow.

Chapter 5

Interplaying charge and spin order in the fluctuating field theory

> "If you know what to do, you should have done it yesterday." - A. I. Lichtenstein

The considerable insight existing for the extended Hubbard model on a 2D square lattice at half-filling with nearest-neighbour interaction V [194–200, 203, 205, 211–217], makes it an optimal framework for investigating the strengths and weaknesses of the introduced MCFF theory. In this chapter, we investigate the repulsive $U - V$ phase diagram of the extended Hubbard model on a two-dimensional square lattice using the free energy construction within the MCFF method. We give special attention to the evolution of the $U - V$ phase diagram from small finite systems to the thermodynamic limit. In addition, the introduced measure of collective fluctuations allow us to quantify the relevance of collective fluctuations around the saddle-point as a function of the interaction parameters U, V and the system size. This allows us to contrast the fluctuating field and mean-field theories. Throughout the chapter the MCFF approach will be compared to a representative selection of theoretical approaches: mean-field theories (Hartree-Fock, RPA and FLEX) and SCFF, in addition to comparisons to DCA, which incorporates local dynamical fluctuations, and the numerically exact DiagMC and QMC. This chapter follows closely the work in Ref. [334] by the author of this thesis and collaborators.

5.1 Phase diagram in thermodynamic limit

We construct using the MCFF theory the repulsive $U - V$ phase diagram of the half-filled extended Hubbard model on a square lattice from the free energies $\mathcal{F}(\phi^{\varsigma}_{\mathbf{M}})$ (4.20) of the CDW and AFM fluctuations. Here, we reminder the reader that for notational simplicity, we continue to set $t = 1$ as an unit of energy. The phase diagram is determined through the position of the global minimum of $\mathcal{F}(\phi^{\varsigma}_{\mathbf{M}})$. In the normal phase, the global minimum of $\mathcal{F}(\phi^{\varsigma}_{\mathbf{M}})$ lies at $\phi^{\varsigma}_{\mathbf{M}} = 0$. In contrast, the formation of the ordered phase is signaled by a shift of the global minimum to a $\phi^{\varsigma}_{\mathbf{M}} \neq 0$ point. Besides the global minimum, the free energy may reveal local minimum that indicates the presence of a metastable phase. Through this procedure, we perform calculations for a plaquette of 128×128 lattice sites with periodic boundary conditions. We argue that his may be considered as the thermodynamic limit, as we do not see any difference

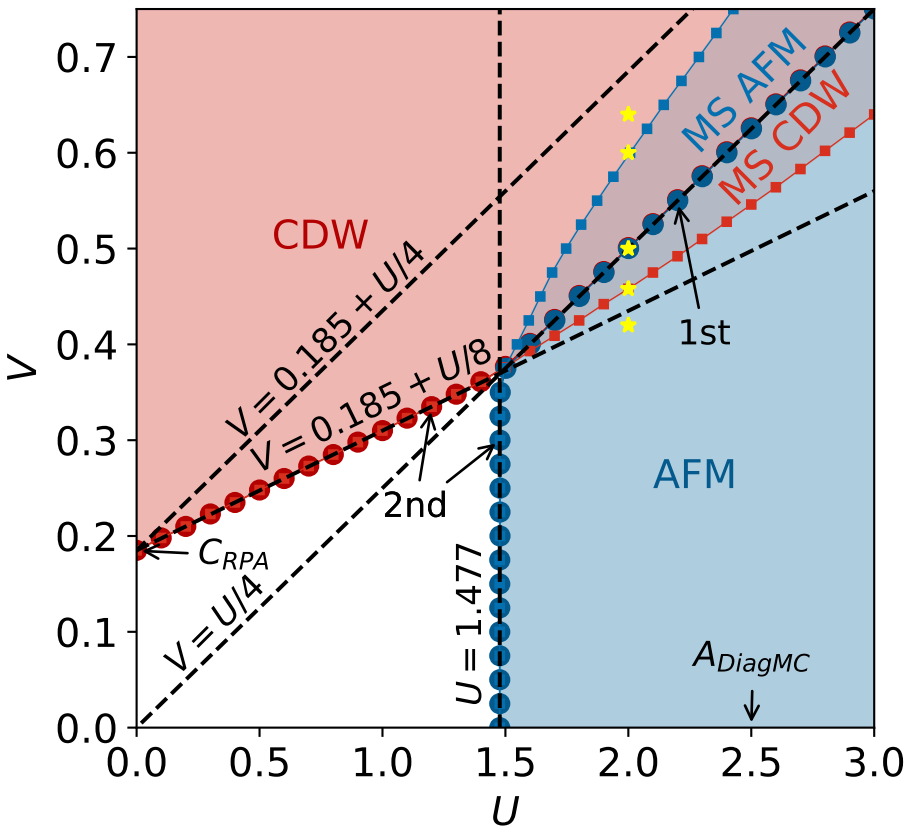

Figure 5.1: Phase diagram for the half-filled extended Hubbard model with repulsive U, V interactions as predicted by the MCFF approach. The result is obtained at $\beta = 10$ for a plaquette of 128×128 lattice sites. Red and blue areas depict the CDW and AFM phases, respectively. The corresponding phase boundaries are shown by coloured circles. Black dashed lines describe the asymptotic behaviour of the phase boundaries: $V = 0.185 + U/8$ for CDW, $U = 1.477$ for AFM, and $V = U/4$ for CDW-AFM transitions. The boundaries of metastable CDW and AFM phases are illustrated by lines with small square markers. Metastability displays the first-order nature of the CDW-AFM phase transition, to contrast with the second-order phase transitions occurring between the normal metal phase (white region) and the CDW and AFM phases. Yellow stars depict the points at which the free energies shown in Fig. 5.4 were calculated. For comparison, we add the RPA estimate $C_{\mathrm{RPA}} = 0.185$ for the CDW boundary in the $U \to 0$ limit, and the DiagMC estimate A_{DiagMC} for the AFM boundary in the limit of $V \to 0$ [136]. The RPA estimate $V = 0.185 + U/4$ for the CDW boundary is also shown.

in the results compared to the 256×256 case. Fig. 5.1 shows the phase diagram of the system obtained at $\beta = 10$. The choice of β is due to convenience in the comparison to earlier works, as the MCFF method can also be applied at both at much higher and lower temperatures.

Following the free energy construction, our calculations reveal three phases: a normal (white colour), a CDW (red colour), and an AFM (blue colour) phase. We find that in the weak coupling regime $U \leq 1.447$ the CDW phase boundary follows the $V = 0.185 + U/8$ line. This result is in the exact agreement with the perturbative estimation $V = C_{\mathrm{RPA}} + U/8$ [213], where the constant C_{RPA} corresponds to the critical

value of the non-local interaction for the CDW transition $V_{U=0}^{\mathrm{CDW}}$ obtained for $U = 0$ within RPA. The RPA estimate is determined by the critical $V_{U=0}^{\mathrm{CDW}}$ associate with a singularity in the RPA construction of the charge susceptibility at the **M**-point, or equivalently determined by a vanishing RPA dielectric function. For the considered system, $C_{\mathrm{RPA}} = 0.1847$, which confirms that the MCFF theory correctly captures the exact $U \to 0$ limit for the CDW phase boundary. The AFM phase boundary in the weak coupling regime lies along the $U = 1.477$ line in the exact agreement with the FLEX result obtained for $V = 0$: $A_{\mathrm{FLEX}} = U_{V=0}^{\mathrm{AFM}} = 8C_{\mathrm{RPA}}$. However, FLEX is known to underestimate the critical interaction for the AFM transition. For instance, in the thermodynamic limit the exact diagrammatic Monte Carlo (DiagMC) solution gives $A_{\mathrm{DiagMC}} \simeq 2.5$ for $\beta = 10$ [136]. Determination of $U_{V=0}^{\mathrm{AFM}}$ within FLEX is similar to the RPA estimate of the critical $V_{U=0}^{\mathrm{CDW}}$, associated instead with a divergence of the FLEX construction of the spin susceptibility at the **M**-point. We note, that in the weak-coupling regime close to the obtained phase boundaries either the CDW or AFM fluctuation is negligibly small. If one neglects one of these two modes within the MCFF method and applies a saddle-point approximation to the remaining mode, the theory reduces to a mean-field approach with the form of the bare local interactions $U^{\mathrm{c/s}} = \pm U/2$ used, e.g., in the FLEX approach. Furthermore, the exact agreement for the phase boundaries in the weak-coupling regime of the fluctuating field and mean-field theories were shown analytically in the previous chapter by considering the SCFF theory.

In the moderate interaction regime, where the competition between the CDW and AFM fluctuations is strong, one has to take both fluctuations into account. Indeed, if one considers fluctuations only in one channel and completely disregards the other channel, the SCFF method predicts the CDW and AFM phase boundary to follow exactly $V = C_{\mathrm{RPA}} + U/8$ and $U = 8C_{\mathrm{RPA}}$, respectively, as depicted by dashed lines in Fig. 5.1. The SCFF method thus predicts the weak interaction estimate to continue into the moderate interaction regime. If we now consider both fluctuations, the CDW and AFM phases are mutually exclusive, with the interplay leading to the system developing a CDW-AFM phase boundary at $V = U/4$ in agreement with numerically exact techniques [194, 195] and the mean-field Hartree-Fock estimate [219], and follows the mean-field RPA or GW [221] prediction $V = U/4 + \mathrm{cst.}$ (except for a constant shift). An explanation for the simple form of the CDW-AFM phase boundary is rather intuitive. Due to both fluctuations displaying identical ordering vector $\mathbf{Q} = \mathbf{M}$, their contributions to the first term of the effective action (4.5) are analogues. Thus, the strength of these fluctuations is dominantly determined by the stiffness parameters: $J_{\mathbf{M}}^{s} = -U/2$ and $J_{\mathbf{M}}^{c} = U/2 - 4V$. An equal value of the two stiffness parameters thus arises at $V = U/4$, i.e. along the CDW-AFM phase boundary. A more non-trivial competition arises for small system sizes as considered in the next section. In addition, non-trivial interplay may arise for competing modes characterized by different ordering vectors $\mathbf{Q}$, due to the coupling of modes through the first term of the effective action (4.5), as will be considered in the next chapter.

5.2 Free energy and metastability

Our investigation is based on the single-channel free energies $\mathcal{F}(\phi_{\mathbf{M}}^{\varsigma})$, and therefore we aim to elaborate on the structure of the free energy itself. Competition between the CDW and AFM modes are incorporated in the single-channel free energy $\mathcal{F}(\phi_{\mathbf{M}}^{\varsigma})$ by

performing a numerical integration over one of the fields of the free energy $\mathcal{F}(\phi^c_{\mathbf{M}}, \phi^s_{\mathbf{M}})$, defined by:

$$\mathcal{F}(\phi^c_{\mathbf{M}}, \phi^s_{\mathbf{M}}) = -\frac{1}{\beta N} \ln \exp\big\{ -\mathcal{S}_\phi[\phi^c_{\mathbf{M}}, \phi^s_{\mathbf{M}}]\big\}. \tag{5.1}$$

Here $\mathcal{F}(\phi^c_{\mathbf{M}}, \phi^s_{\mathbf{M}})$ depends only on the scalar field $\phi^c_{\mathbf{M}}$ and radial component of the vector field $\phi^s_{\mathbf{M}}$. We calculate the free energy $\mathcal{F}(\phi^c_{\mathbf{M}}, \phi^s_{\mathbf{M}})$ along three different cuts of the $U - V$ phase diagram for a 128×128-sized plaquette in Fig. 5.2. The three cuts of the $U - V$ phase diagram are given by: $V = U/4$ with $U \in [1.5, 2.5]$ (Cut 1), $V = 0.5$ with $U \in [1.5, 2.5]$ (Cut 2) and $U = 2.0$ with $V \in [0.475, 0.625]$ (Cut 3), see Fig. 5.3 for a graphical view of the cuts within the $U - V$ phase diagram. Along cut 1, i.e. the transition line, we observe a four-fold rotational symmetric $\mathcal{F}(\phi^c_{\mathbf{M}}, \phi^s_{\mathbf{M}})$ with a degeneracy of the scalar field $\phi^c_{\mathbf{M}}$ and radial vector field $\phi^s_{\mathbf{M}}$ components. Increasing interaction parameters leads to a distancing of the global minima relative origin as the collective fluctuations becomes stronger. Simultaneously, the stability of the collective fluctuations increases as the depth of $\mathcal{F}(\phi^c_{\mathbf{M}}, \phi^s_{\mathbf{M}})$ increase. The degeneracy is broken away from the transition line, e.g. along cuts 2 and 3, as a two-fold rotational symmetry develops. Along cut 2, we observe dominant CDW (AFM) fluctuations for $U < 2.0$ ($U > 2.0$), as the $\mathcal{F}(\phi^c_{\mathbf{M}}, \phi^s_{\mathbf{M}})$ displays global minima in the $\phi^c_{\mathbf{M}}$-channel ($\phi^s_{\mathbf{M}}$-channel). In addition, $\mathcal{F}(\phi^c_{\mathbf{M}}, \phi^s_{\mathbf{M}})$ is invariant under the transformation $U \to 4.0 - U$ together with the exchange of the scalar field $\phi^c_{\mathbf{M}}$ and radial vector field $\phi^s_{\mathbf{M}}$. The invariance arises due the stiffness parameters, which dominantly determine the strength of the collective fluctuations as described previously, are themselves invariant under the same transformation. As an example, the free energy $\mathcal{F}(\phi^c_{\mathbf{M}}, \phi^s_{\mathbf{M}})$ displays similar behaviour along cut 3 as cut 2, however there is no clear display along cut 3 of the invariance under the transformation.

Allowing for the CDW and AFM modes to compete, we retrieve the behaviour of the one channel in the environment of the remaining channel through numerical integration. A typical behaviour of the introduced free energy $\mathcal{F}(\phi^\varsigma_{\mathbf{M}})$ is illustrated in Fig. 5.4. In the normal phase, the global minimum of $\mathcal{F}(\phi^\varsigma_{\mathbf{M}})$ lies at $\phi^\varsigma_{\mathbf{M}} = 0$. The formation of the ordered phase is signaled by a shift of the global minimum to a $\phi^\varsigma_{\mathbf{M}} \neq 0$ point. In addition, the free energy may exhibit a local minimum associated with a metastable (MS) phase. Finally, we observe a non-analyticity appearing as a kink in the free energy $\mathcal{F}(\phi^\varsigma_{\mathbf{M}})$. It signals a change of behaviour of $\mathcal{F}(\phi^\varsigma_{\mathbf{M}})$ between the region in the vicinity of $\phi^\varsigma_{\mathbf{M}} = 0$, where the fluctuations in the integrated channel are strong, and the region of $\phi^\varsigma_{\mathbf{M}} \neq 0$, where the fluctuations in the considered channel are strong. Thus, the observed kink is inherently connected to the interplay between the collective CDW and AFM fluctuations.

We find that in the vicinity of the CDW-AFM phase boundary, some regions inside the CDW and AFM phases reveal local minima associated with the presence of metastable phases. The boundaries of the metastable phases are depicted in Fig. 5.1 by blue (MS AFM) and red (MS CDW) lines with small square markers. In particular, Fig. 5.4 illustrates an example of the free energy behaviour in the regime of strong competing CDW and AFM fluctuations. In the spin channel (Fig. 5.4 a)), as V is increased from deep within the AFM phase the global minimum at $\phi^s_{\mathbf{M}} \neq 0$ in the free energy $\mathcal{F}(\phi^s_{\mathbf{M}})$ turns into a local minimum above the CDW-AFM transition point $V = U/4$, where the CDW ordering becomes dominant. The local minimum disappears at the metastable AFM phase transition point, which for $U = 2$ corresponds to $V = 0.60$.

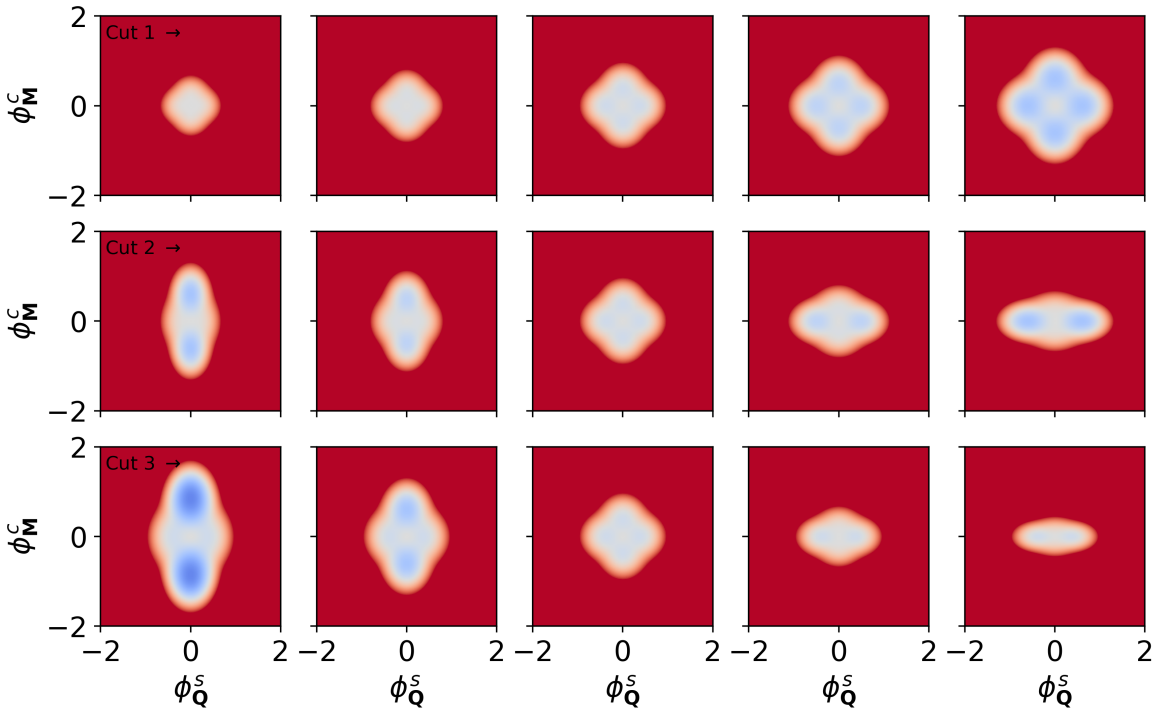

Figure 5.2: Free energy $\mathcal{F}(\phi^c_{\mathbf{M}}, \phi^s_{\mathbf{M}})$ as a function of the scalar field $\phi^c_{\mathbf{M}}$ and radial component of the vector field $\phi^s_{\mathbf{M}}$ is computed along three cuts of the repulsive U, V phase diagram, displayed in Fig. 5.3. Red (blue) values depict positive (negative) values of $\mathcal{F}(\phi^c_{\mathbf{M}}, \phi^s_{\mathbf{M}})$. Along the transition line $U = 4V$ (cut 1), we observe a four-fold rotational symmetry $\mathcal{F}(\phi^c_{\mathbf{M}}, \phi^s_{\mathbf{M}})$ associated with a degeneracy of the $\phi^c_{\mathbf{M}}$ and $\phi^s_{\mathbf{M}}$ modes. The degeneracy is broken away from the transition line (cut 2 and 3), with a two-fold rotational symmetry emerging. Depending on the interaction parameters, the global minima are positioned within the CDW or AFM channel.

Similar results can be found for the charge channel (Fig. 5.4 b)): as V decreases from deep within the CDW phase, the metastable CDW phase appears at the AFM-CDW transition point and vanishes at $U = 2$, $V = 0.46$.

We note that at the CDW-AFM transition the minima located at $\phi^{\varsigma}_{\mathbf{M}} = 0$ and $\phi^{\varsigma}_{\mathbf{M}} \neq 0$ points correspond to the same value of the free energy $\mathcal{F}(\phi^{\varsigma}_{\mathbf{M}})$. On the contrary, no metastable solution occurs in the vicinity of the phase boundaries that separate the normal phase from either the CDW or AFM phases. This result suggests that the transitions in the latter case are of second-order, while the transition between the competing CDW and AFM phases is of first-order. In addition, the degeneracy between the spin and charge channels ($\mathcal{F}(\phi^s_{\mathbf{M}}) = \mathcal{F}(\phi^c_{\mathbf{M}})$) we observe along the CDW-AFM transition line indicates that the two instabilities are mutually exclusive. If these free energies were not identical at the transition point, one channel would be energetically favourable. Fig. 5.5 shows the behaviour of the free energy $\mathcal{F}(\phi^{\varsigma}_{\mathbf{M}})$ at the CDW-AFM transition point $U = 2$, $V = 0.5$ for different temperatures. We observe that at high temperature corresponding to $\beta = 4$ the AFM and CDW fluctuations are suppressed, and the free energy has only one minimum at $\phi^{\varsigma}_{\mathbf{M}} = 0$: the normal phase. Upon lowering the temperature the second minima develops at $\phi^{\varsigma}_{\mathbf{M}} \neq 0$ and propagates to larger values of $\phi^{\varsigma}_{\mathbf{M}}$, corresponding to the increase of the strength of corresponding fluctuations. We also observe that the free energy barrier between the

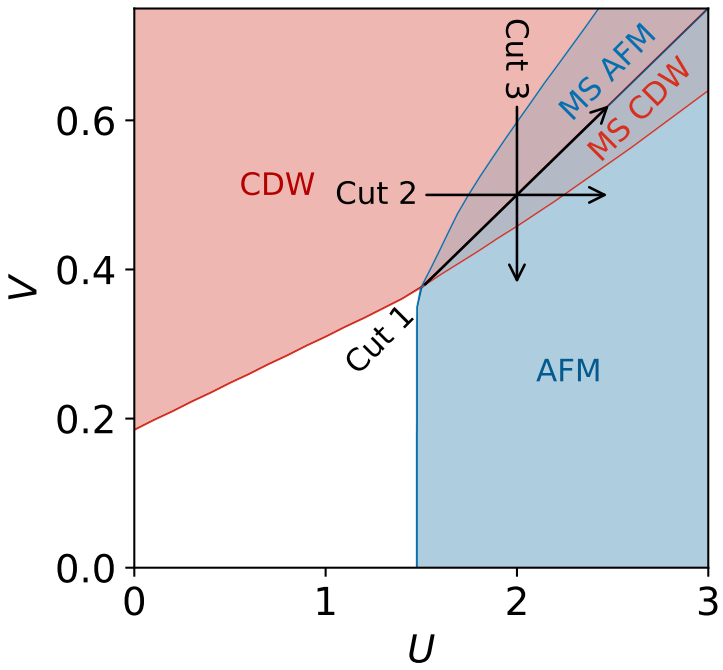

Figure 5.3: Phase diagram of the half-filled extended Hubbard model with repulsive U, V interaction is replotted from Fig. 5.1, with the inclusion of three cuts of the phase diagram being displayed: $V = U/4$ with $U \in [1.5, 2.5]$ (Cut 1), $V = 0.5$ with $U \in [1.5, 2.5]$ (Cut 2) and $U = 2.0$ with $V \in [0.475, 0.625]$ (Cut 3).

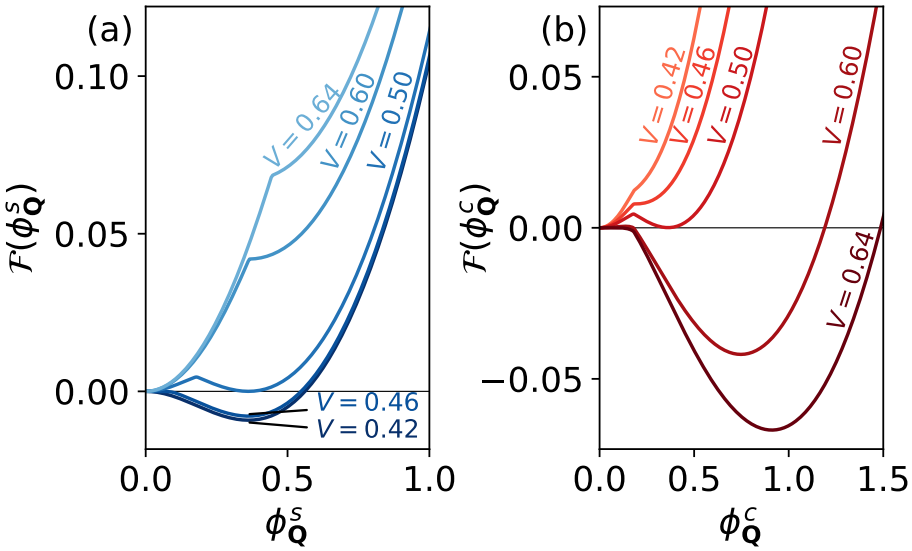

Figure 5.4: Free energy $\mathcal{F}(\phi^{\varsigma}_{\mathbf{M}})$ for the spin (a) and charge (b) channels. The results are obtained for the half-filled extended Hubbard model on a square lattice at $\beta = 10$ and $U = 2$ in the vicinity of the CDW-AFM transition point $V = U/4$, for a plaquette of 128×128 lattice sites. Choice of U, V are denoted as stars in Fig. 5.1.

two minima increases with decreasing temperature. A larger energy barrier allows for a more stable coexistence of the two phases associated with $\phi^{\varsigma}_{\mathbf{M}} = 0$ and $\phi^{\varsigma}_{\mathbf{M}} \neq 0$. It should be emphasized, however, that the two channels are degenerate and that the

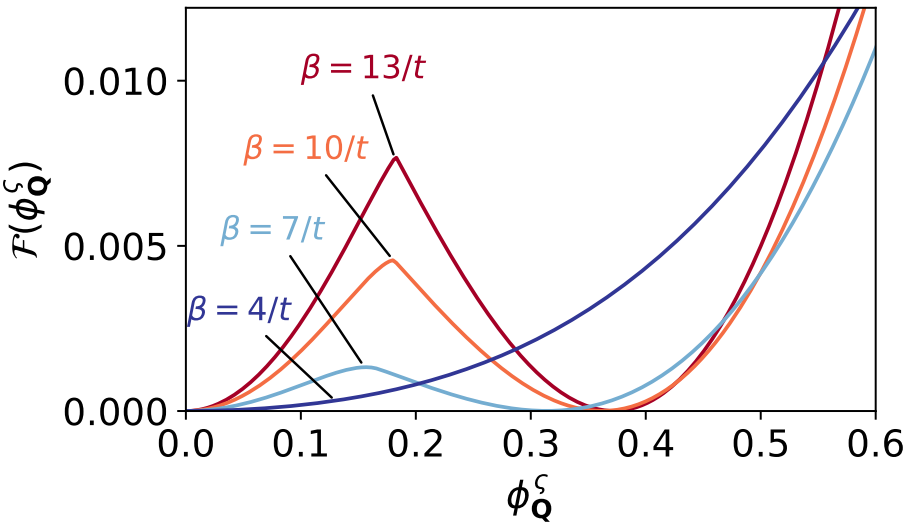

Figure 5.5: Free energy $\mathcal{F}(\phi^{c}_{\mathbf{M}}) = \mathcal{F}(\phi^{s}_{\mathbf{M}})$ calculated at the CDW-AFM transition point $U = 2$, $V = 0.5$ for a plaquette of 128×128 lattice sites, with different values of the inverse temperature β.

minima at $\phi^{\varsigma}_{\mathbf{M}} = 0$ and $\phi^{\varsigma}_{\mathbf{M}} \neq 0$ have the same energy only at the CDW-AFM transition point. Away from this point one of the two solutions becomes metastable, which means that one of the CDW or AFM phases always dominates. Distinguishing between stable and metastable solutions is not a trivial problem, and even the more elaborate DCA method in the regime of strong competing CDW and AFM fluctuations predicts a coexistence between these two mutually exclusive phases [199]. Thus, the ability to distinguish between the stable and the metastable phases is an advantage of the MCFF method.

5.3 Phase diagram evolving with the system size

The MCFF approach can also be applied to small systems, where it is expected to perform significantly better than the conventional mean-field theory [329, 331]. For small system sizes, the result of the MCFF method can be compared to the exact Monte Carlo calculations. Fig. 5.6 displays the stable (a) and metastable (b) ordering boundaries for AFM and CDW phases for 4×4, 6×6 and 8×8 plaquettes, in addition to the previously considered 128×128 plaquette near the thermodynamic limit. For all system sizes the MCFF approach extrapolates the AFM and CDW ordering boundaries between weak coupling results obtained respectively on the basis of FLEX calculations and perturbative estimations, and the asymptotic behaviour of the CDW-AFM phase boundary at intermediate coupling predicted by mean-field theories. A region of coexisting stable and metastable ordering is observed for all system sizes. Phase boundaries of the coexistence region appears converged for the 128×128 plaquette, indicating its stability in the thermodynamic limit. Importantly, we observe for small systems a more significant modification of the weak coupling CDW and AFM phase boundaries as predicted by the MCFF approach, due to the interplay of collective fluctuation. The modification displays itself by a bending of the phase boundaries not only in the vicinity of $V = U/4$, a distinct effect beyond conventional mean-field theory estimates.

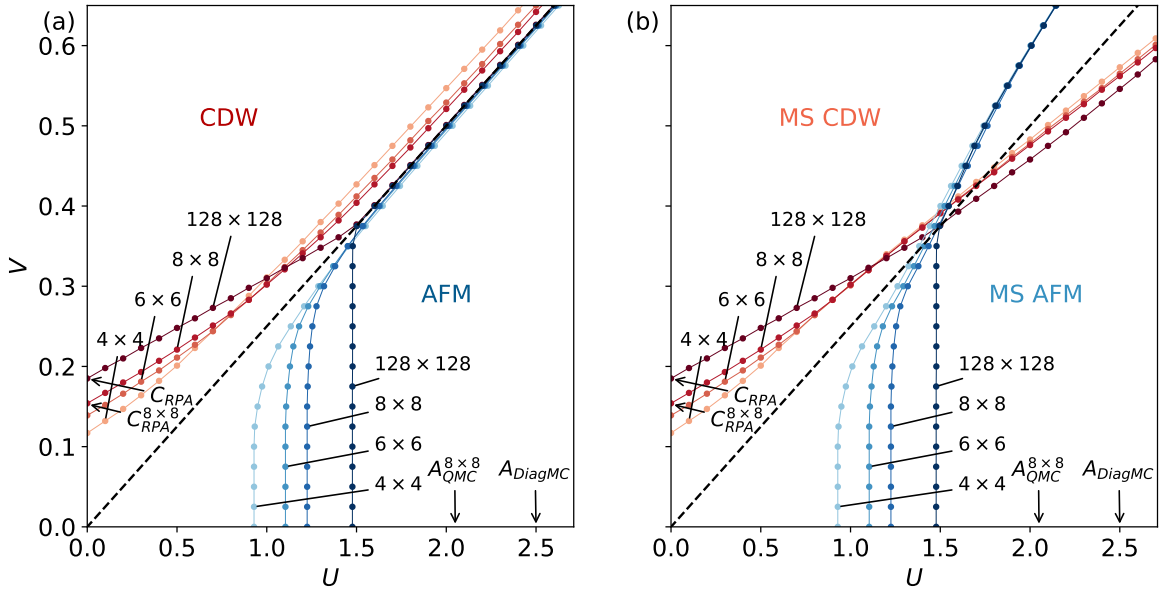

Figure 5.6: Stable (a) and metastable (b) AFM (blue) and CDW (red) ordering boundaries predicted by the MCFF approach for the half-filled extended Hubbard model on 4×4, 6×6, 8×8, and 128×128 plaquettes at $\beta = 10$. The dashed line specifies the mean-field estimate for the CDW-AFM phase boundary $V = U/4$. For comparison, the RPA estimates C_{RPA} and $C_{\mathrm{RPA}}^{8\times8}$ for the CDW boundary in the $U \to 0$ in the thermodynamic limit and for a 8×8 plaquette, respectively, are included. In addition, the DiagMC estimate A_{DiagMC}, taken from Ref. [136], and the QMC estimate $A_{\mathrm{QMC}}^{8\times8}$ for the AFM boundary in the limit of $V \to 0$ are included in the thermodynamic limit and for a 8×8 plaquette, respectively, are included.

In order to gain insight into the performance of the MCFF approach with inclusion of collective AFM and CDW fluctuations, we now perform a comparison with respect to numerically exact QMC simulations. For a 8×8 plaquette, QMC simulations give us $A_{\mathrm{QMC}}^{8\times8} = 2.05 \pm 0.05$ for $\beta = 10$. By a comparison to the MCFF prediction of $U_{V=0}^{\mathrm{AFM}} = 1.225$, we find a significant underestimation of the critical interaction U for the AFM phase boundary. This observation is consistent with our result for the 128×128 plaquette and can be related to dynamical correlation effects that are not incorporated within the approach. In contrast, the MCFF method accurately determines the CDW phase boundary at small U, with the MCFF prediction for the critical interaction $V_{U=0}^{\mathrm{CDW}}$ coinciding with the RPA result C_{RPA} for all plaquettes sizes.

5.4 Measure of collective fluctuations

In order to quantify the strength of the collective fluctuations in the MCFF approach around the minimum of the free energy, we introduce $\langle |n_{\mathbf{Q}}^{\varsigma}| \rangle$ as a measure. The measure $\langle |n_{\mathbf{Q}}^{\varsigma}| \rangle$ is computed by taking the expectation value of $|n_{\mathbf{Q}}^{\varsigma}|$ in the respective channel, i.e. performing a numerical integration over all classical field degrees of freedom associated with the collective fluctuations. The numerical integration corresponds to the inclusion of fluctuations about the saddle-point known to be important, e.g. see work on the crossover from BCS theory to Bose-Einstein condensate [343, 344]. Our calculations of the measure $\langle |n_{\mathbf{Q}}^{\varsigma}| \rangle$ are compared to the saddle-point estimate $\langle |n_{\mathbf{Q}}^{\varsigma}| \rangle_{\mathrm{MF}}$, i.e. the value

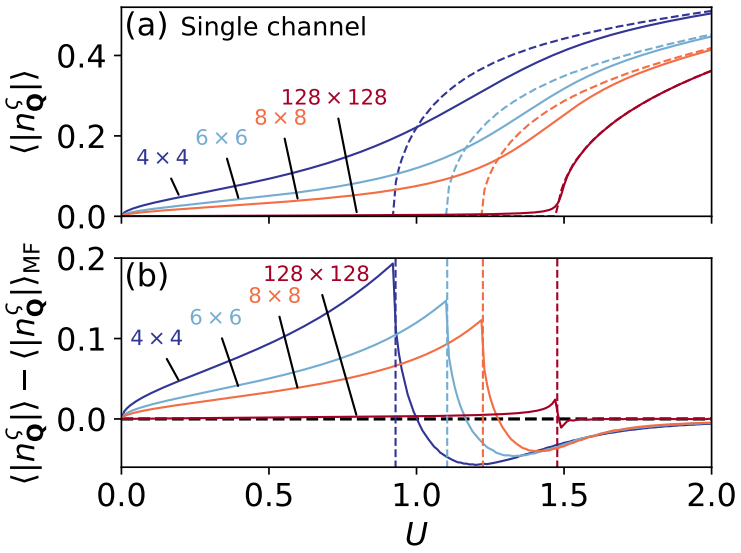

Figure 5.7: The measure $\langle|n^{\varsigma}_{\mathbf{Q}}|\rangle$ of collective fluctuations is calculated along $V = U/4$ in the phase diagram for 4×4, 6×6, 8×8, and 128×128 plaquettes at $\beta = 10$ in (a). Dashed line in (a) denote the saddle-point (mean-field) measure $\langle|n^{\varsigma}_{\mathbf{Q}}|\rangle_{\mathrm{MF}}$. In (b), the difference $\langle|n^{\varsigma}_{\mathbf{Q}}|\rangle - \langle|n^{\varsigma}_{\mathbf{Q}}|\rangle_{\mathrm{MF}}$ is plotted. Dashed line in (b) denote the saddle-point estimate of the phase transition boundaries. Without interplay, the two modes $\varsigma = c, s$ are degenerate along $V = U/4$.

at the minimum of the free energy, which is equivalent with a conventional mean-field theory estimate. Thus, we seek to evaluate the differences between the fluctuating field and mean-field theories.

Figs. 5.7, 5.8 displays the calculated integrated measure $\langle|n^{\varsigma}_{\mathbf{M}}|\rangle$ and the saddle-point measure $\langle|n^{\varsigma}_{\mathbf{M}}|\rangle_{\mathrm{MF}}$, in addition to their difference $\langle|n^{\varsigma}_{\mathbf{M}}|\rangle - \langle|n^{\varsigma}_{\mathbf{M}}|\rangle_{\mathrm{MF}}$, at $\beta = 10$ for plaquettes of the size 4×4, 6×6, 8×8, and 128×128 along $V = U/4$. Specifically, within Fig. 5.7 a, b the measures and their difference is calculated within the single-channel fluctuating field theory, namely without considering the interplay between the fluctuations in the competing channel. Note that along $V = U/4$ the non-interplaying collective CDW and AFM fluctuations are degenerate. We observe $\langle|n^{\varsigma}_{\mathbf{M}}|\rangle$, displayed as a solid line in Fig. 5.7 a, to be monotonically increasing function of U. The measure $\langle|n^{\varsigma}_{\mathbf{M}}|\rangle$ vanishes in the limit of $U \to 0$ and saturates to the mean-field theory estimate $\langle|n^{\varsigma}_{\mathbf{M}}|\rangle_{\mathrm{MF}}$ in the limit of large U, displayed as a dashed line in Fig. 5.7 a. We observe in Fig. 5.7 b the deviation of the measure relative to the saddle-point estimate is positive and monotonically increasing function of U below the phase boundaries evaluated within mean-field theory. A sharp decrease in the deviation follows above the phase boundaries, until a maximal negative deviation is reached in turn followed by a saturation to zero deviation at large U. The collective fluctuations around the minimum of the free energy are most relevant in the vicinity of the phase transition, and especially for small systems. We observe the difference $\langle|n^{\varsigma}_{\mathbf{M}}|\rangle_{\mathrm{MF}}$ to be suppressed with increasing the systems size. However, we note that for a plaquette of the size 128×128 deviations with respect to mean-field theory remain small but non-negligible close to the phase boundary.

We now consider the measures for interplaying collective CDW and AFM fluctuations within the introduced MCFF theory, displayed in Fig. 5.8. Due to degeneracy of

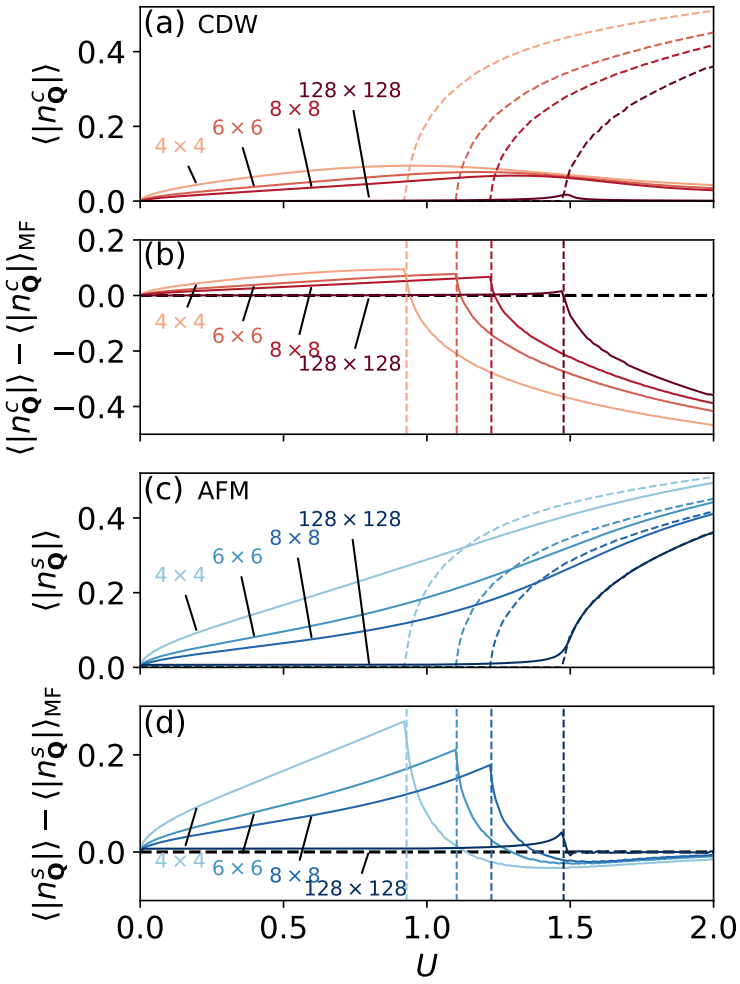

Figure 5.8: The measure $\langle |n^{\varsigma}_{\mathbf{Q}}| \rangle$ of collective fluctuations is calculated along $V = U/4$ in the phase diagram for 4×4, 6×6, 8×8, and 128×128 plaquettes at $\beta = 10$ in (a, c). Dashed lines in (a, c) denote the saddle-point (mean-field) measure $\langle |n^{\varsigma}_{\mathbf{Q}}| \rangle_{\mathrm{MF}}$. In (b, d), the difference $\langle |n^{\varsigma}_{\mathbf{Q}}| \rangle - \langle |n^{\varsigma}_{\mathbf{Q}}| \rangle_{\mathrm{MF}}$ is plotted. Dashed lines in (b, d) denote the saddle-point estimate of the phase transition boundaries. With interplay, displayed in (a, b) for the CDW mode and (c, d) for the AFM mode, the degeneracy displayed by the non-competing case is broken. However, due to the degeneracy of the saddle-point minima of the channels two choices of $\langle |n^{\varsigma}_{\mathbf{Q}}| \rangle_{\mathrm{MF}}$ exists: zero or non-zero.

the saddle-point minima of the CDW and AFM channels along $V = U/4$, two choices of $\langle |n^{\varsigma}_{\mathbf{M}}| \rangle_{\mathrm{MF}}$ exist. Either $\langle |n^{c}_{\mathbf{M}}| \rangle_{\mathrm{MF}}$ is non-zero for vanishing $\langle |n^{s}_{\mathbf{M}}| \rangle_{\mathrm{MF}}$, or vice versa. We observe that the collective AFM fluctuations (Fig. 5.8 c) dominate over the collective CDW fluctuations (Fig. 5.8 a) in the regime of study. This naturally follows from the larger number of degrees of freedom of the AFM mode relative the CDW mode. A behaviour similar to the single-channel results is observed in the measure $\langle |n^{s}_{\mathbf{M}}| \rangle$, displayed as a solid line in Fig. 5.8 c. However, within the multi-channel results the measure $\langle |n^{s}_{\mathbf{M}}| \rangle$ is larger for the interplaying treatment due to the additional channel of fluctuation. In contrast, the measure $\langle |n^{c}_{\mathbf{M}}| \rangle$ behaves dissimilar to the single-channel results. We observe the measure $\langle |n^{c}_{\mathbf{M}}| \rangle$ to display a non-monotonic behaviour: increasing as function of U at small U and decreasing as a function of U at large U. In fact, the measure $\langle |n^{c}_{\mathbf{M}}| \rangle$ vanishes in both limits of small and large U. As noted previously,

the largest deviation with respect to mean-field theory occur in the vicinity of the phase transition and for small system sizes. In the thermodynamic limit, the collective CDW and AFM fluctuations appear to saturate to the mean-field theory following the saddle-point choice associate with a non-zero $\langle |n^s_{\mathbf{M}}| \rangle_{\mathrm{MF}}$ and vanishing $\langle |n^c_{\mathbf{M}}| \rangle_{\mathrm{MF}}$. The main message remains from the single-channel considerations, contributions from collective fluctuations around the minimum of the free energy are of largest importance near the phase boundaries evaluated within mean-field theory, with most significant contributions for small system sizes.

5.5 Excited-state properties and correlation effects

An investigation of many-body correlation effects are naturally expressed using the spectral function $\mathcal{A}_{\mathbf{k},\omega}$, describing the single-particle excitation spectrum, and the self-energy $\Sigma_{\mathbf{k},\omega}$, encoding the connection between the noninteracting and interacting systems. Due to the analytic structure of their dependency of the Matsubara frequency within our implementation of the MCFF approach, analytic continuation allows for a direct computation on the real frequency axis. Thus, we have access to the physical spectral function $\mathcal{A}_{\mathbf{k},\omega}$ and self-energy $\Sigma_{\mathbf{k},\omega}$. Through their computation, we seek to evaluate by which means the excited-state properties and correlation effects emerges within the MCFF theory.

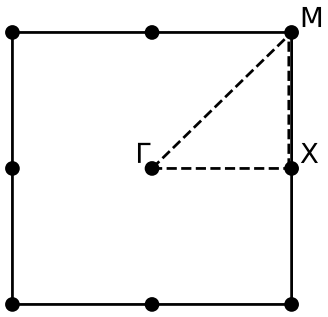

Figure 5.9: Sketch of the first Brillouin zone of the square lattice, with the high-symmetry points denoted: $\mathbf{\Gamma} = (0,0)$, $\mathbf{X} = \{(\pi,0),(\pi,0)\}$ and $\mathbf{M} = (\pi,\pi)$. The high-symmetry path ΓXMΓ is indicated by the dashed lines.

5.5.1 Many-body effects within the single-channel FF theory

Our investigation focuses initially on the SCFF theory for a single collective mode, i.e., without any interplay between modes. As a representation of the behaviour of the collective CDW and AFM fluctuations, we restrict the ourselves along $V = U/4$ in the $U - V$ phase diagram, associated with degenerate stiffness parameters $J^c_{\mathbf{M}}$, $J^s_{\mathbf{M}}$. In fact, our calculations of the spectral function $\mathcal{A}_{\mathbf{k},\omega}$ and self-energy $\Sigma_{\mathbf{k},\omega}$ for the CDW and AFM modes gives largely indistinguishable results for the parameters employed, and for convenience we will mostly limit ourselves to the displayed computations for the collective CDW fluctuations as a representation for the SCFF theory. However, we will give clear comment where the results for the CDW and AFM channels differentiate themselves.

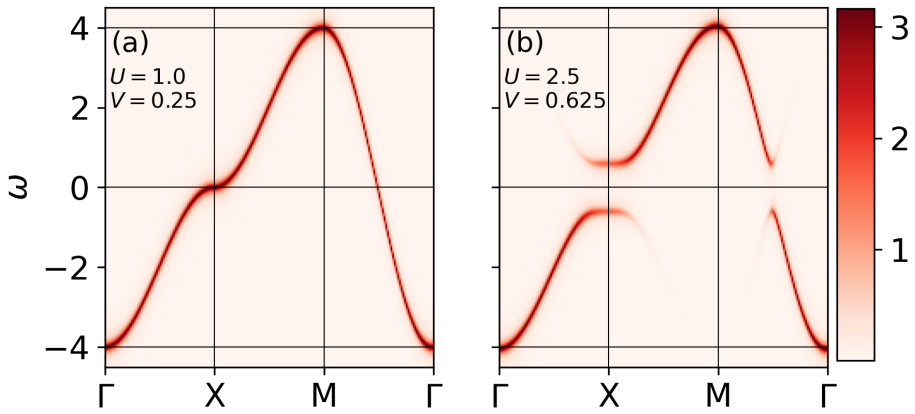

Figure 5.10: Spectral function $\mathcal{A}_{\mathbf{k},\omega}$ of half-filled extended Hubbard model, with $\beta = 10$ and system size 128×128, as predicted by the SCFF theory. Calculations are performed along a high-symmetry path, sketched in Fig. 5.9, for representative values of the interaction parameters: (a) $U = 1.0$, $V = 0.25$ (normal phase), and (b) $U = 2.5$, $V = 0.625$ (symmetry-broken phase). In the normal phase, the spectral function demonstrates spectral weight at the Fermi energy, which is suppressed by the formation of a gap in the symmetry-broken phase. As the interaction increases, the gap widens simultaneously as the spectral weight is transferred to a "mirrored" band.

We perform calculations of the spectral function $\mathcal{A}_{\mathbf{k},\omega}$, with a peak broadening $\eta = 0.1$, for a plaquette of 128×128 lattice sites and inverse temperature $\beta = 10$. Fig. 5.10ab shows the spectral function $\mathcal{A}_{\mathbf{k},\omega}$ calculated along the high-symmetry path $\Gamma\mathrm{X}\mathrm{M}\Gamma$ for varying $U \in \{1.0, 2.5\}$, see sketch of the first Brillouin zone in Fig. 5.9. Within the normal metal phase, represented in Fig. 5.10a, the spectral function $\mathcal{A}_{\mathbf{k},\omega}$ is largely unchanged from its form in the noninteracting limit. It displays a metallic behaviour, with spectral weight at the Fermi energy $\omega = 0$ displayed at both the nodal (N) and antinodal (AN) points along the high-symmetry path, with the nodal point located at $\mathbf{Q} = (\frac{\pi}{2}, \frac{\pi}{2})$ and the antinodal point located at $\mathbf{Q} = \mathbf{X}$. Transitioning into the symmetry-broken phase, represented in Fig. 5.10b, a gap Δ centred $\omega = 0$ emerges at the N and AN points. Its underlying mechanism can be identified as avoided crossing of the $\epsilon_{\mathbf{k}}$ and $\epsilon_{\mathbf{k}+\mathbf{M}}$ bands due their mixing associated with the field $\phi^{\mathrm{s}}_{\mathbf{M}}$ within the SCFF method. As the nonlocal interaction increases, we observe the gap $\Delta^{CDW/AFM}$ to widen simultaneously as the spectral weight is transferred to a "mirrored" band. The "mirrored" band originates from band-folding due to the underlying 2×2 structure in the momentum space, associated with the $\mathbf{M}$-ordering of the $\phi^{\mathrm{s}}_{\mathbf{M}}$ field coupling the $\epsilon_{\mathbf{k}}$ and $\epsilon_{\mathbf{k}+\mathbf{M}}$ bands. Nevertheless, we emphasis that no translational symmetry breaking is enforced and that the spectral function $\mathcal{A}_{\mathbf{k},\omega}$ is calculated within the non-reduced Brillouin zone.

To visualise the opening of the gap, we evaluated the Fermi surface for two representative values, one within the normal metal ($U = 1.0$) and the other within the symmetry-broken phase ($U = 2.0$), displayed in Fig. 5.11ab. We observe the gap to open through a substantial decrease of the spectral weight. It appears to open uniformly in momentum space, without any distinguishing differences between the N and AN points. This indicates the MCFF theory restricted to the main leading collective modes with ordering vector $\mathbf{Q} = \mathbf{M}$ is not sufficent to describe the formation of a partial gap, associated with NFL and PG physics.

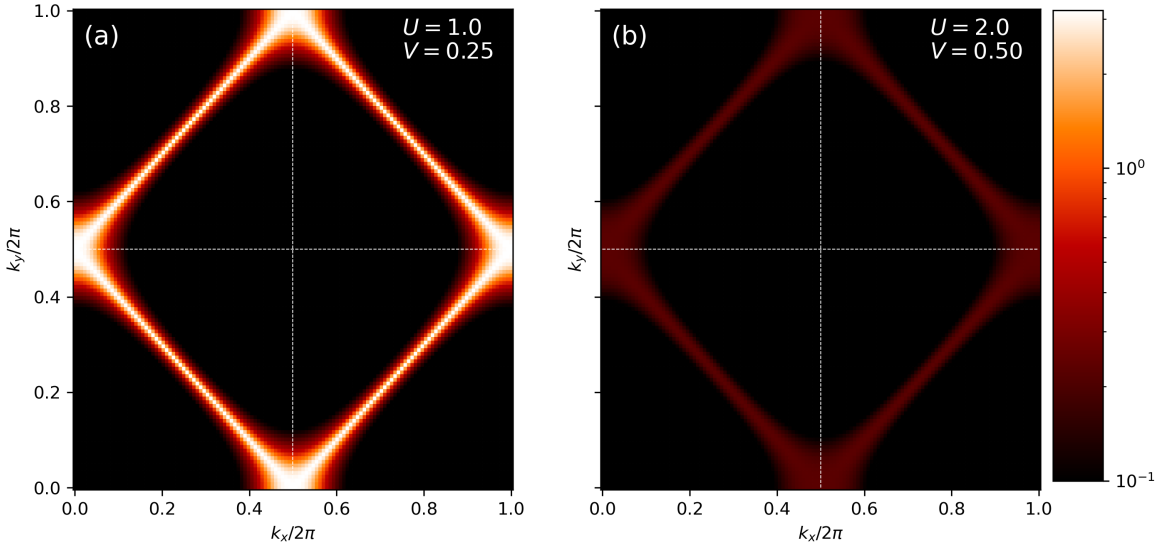

Figure 5.11: Fermi surface of the half-filled extended Hubbard model, with $\beta = 10$ and system size 128×128, predicted by the SCFF theory for a single fluctuating field $\phi^{\mathrm{S}}_{\mathbf{M}}$, for two representative values of the interaction parameters: (a) $U = 1.0$, $V = 0.25$ (normal phase) and (b) $U = 2.0$, $V = 0.50$ (symmetry-broken phase). In the normal phase, the Fermi surfaces is largely independent of the interaction. However, in the symmetry-broken phase (CDW and AFM), the spectral weight at the Fermi surface uniformly decreases as the interaction increases, signaling the formation of the gap as observed in the spectral function (see Fig. 5.10).

In Fig. 5.12, we include the local spectral function $\mathcal{A}^{\mathrm{loc}}_{\omega}$ (Fig. 5.12a) and the spectral function $\mathcal{A}_{\mathbf{k},\omega}$ at the high-symmetry point $\mathbf{X}$ (Fig. 5.12b). In particular, these components of the spectral function are calculated for select values of interaction parameters along $V = U/4$, with $U \in \{0.5, 1.0, 1.5, 2.0\}$. Universal in both representations of the spectral function is its near invariance of the interaction parameters within the normal phase, in agreement with the previous discussion. Entering into the symmetry-broken phase, all components of the spectral function are renormalised through the interaction. We observe the local spectral function $\mathcal{A}^{\mathrm{loc}}_{\omega}$ to display the noninteracting local DOS (LDOS) of a two-dimensional square lattice in the normal phase, with a broad distribution of states within the bandwidth $\omega \in [-4, 4]$ with a peak at $\omega = 0$ associated with a van Hove singularity. In the symmetry-broken phase, the appearance of a gap is visible in the local spectral function $\mathcal{A}^{\mathrm{loc}}_{\omega}$, associated with a reduction of the spectral weight in the vicinity of $\omega = 0$, and the formation of a two-peak structure. The dramatic changes are concentrated in the vicinity of the Fermi energy, with little change of $\mathcal{A}^{\mathrm{loc}}_{\omega}$ far from the Fermi energy. These observations concur with $\mathcal{A}_{\mathbf{k},\omega}$ at the high-symmetry points. The spectral function $\mathcal{A}_{\mathbf{k},\omega}$ at the high-symmetry point $\mathbf{X}$ is in the noninteracting limit composed of a single peak, centred at $\omega = 0$. As the collective fluctuations strengthen, the component develop a two-peak structure with two equally weighted peaks positioned symmetrically around $\omega = 0$.

Making a connection to our previous investigation of the evolution of the FF theory with system size, we calculate the local spectral function $\mathcal{A}^{\mathrm{loc}}_{\omega}$ for different plaquette sizes differentiating the CDW and AFM modes. In Fig. 5.13, the local spectral function $\mathcal{A}^{\mathrm{loc}}_{\omega}$ for 4×4, 6×6 and 8×8 plaquettes for select values of interaction parameters

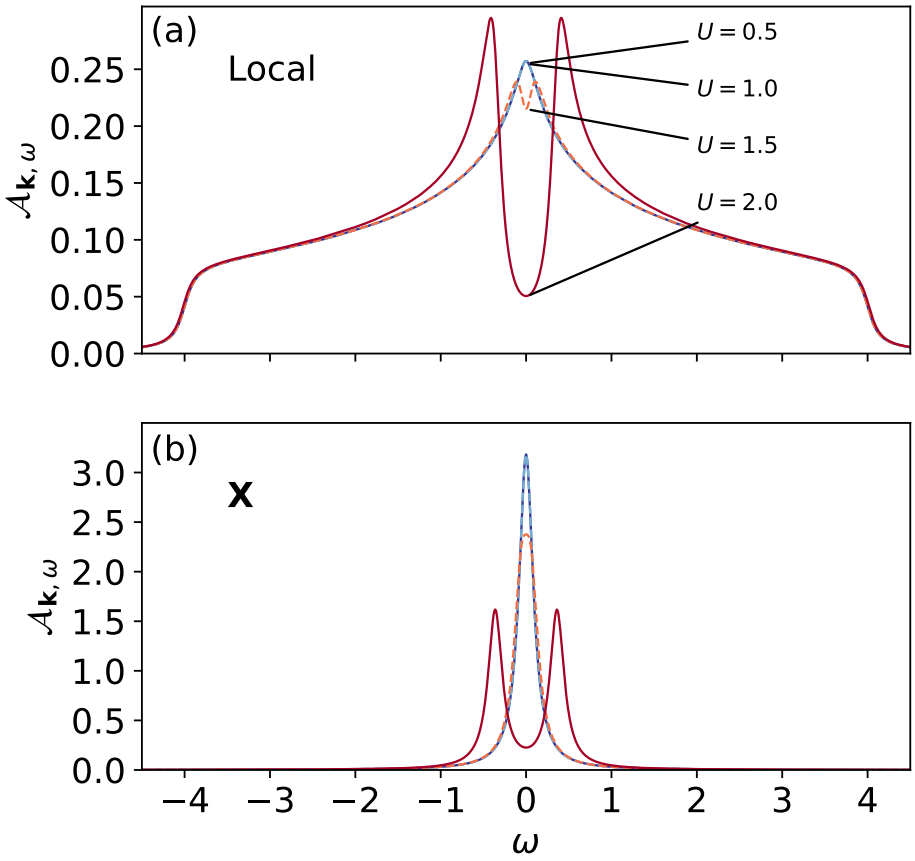

Figure 5.12: Spectral function $\mathcal{A}_{\mathbf{k},\omega}$ of the half-filled extended Hubbard model is displayed for a collection of points along $V = U/4$, with $U \in \{0.5, 1.0, 1.5, 2.0\}$, as caclulated by the SCFF theory for a single fluctuating field $\phi^{\text{S}}_{\mathbf{M}}$. To represent the spectral function $\mathcal{A}_{\mathbf{k},\omega}$, the local (a) and $\mathbf{X}$-point (b) components of the spectral function are displayed. Note, the near identical value for the calculated value of $\mathcal{A}_{\mathbf{k},\omega}$ for $U = 0.5$, denoted by a solid dark blue line, and $U = 1.0$, denoted by a dashed light blue line.

along $V = U/4$, with $U \in \{0.5, 1.0, 1.5, 2.0\}$, is shown for both the collective CDW and AFM fluctuations. We observe in the metallic phase, a collection of peaks associated with the bare dispersion $\epsilon_{\mathbf{k}}$. In contrast to the calculations performed for the plaquette of 128×128, acting as the thermodynamic limit, the central peak is noticably affected by the collective fluctuations within the normal phase. For small plaquettes, the collective AFM fluctuations in the normal phase visibly suppresses the spectral weight to a larger degree than the collective CDW fluctuations, due to the larger number of degrees of freedom of the AFM mode. Passing the critical interaction associated with the symmetry-broken phase, we observe the central peak at $\omega = 0$ to separate into a two-peak structure. For the 4×4 plaquette, associate with well-separated peaks, the collective CDW fluctuations mainly modify the central peak. However, with increasing plaquette size the number of peaks in the vicinity of the Fermi energy increases. We observe the peaks surrounding the central peak to shift away from the Fermi energy with increasing strength of the collective fluctuations. Note the convergence of the local spectral function $\mathcal{A}^{\text{loc}}_{\omega}$ for the CDW and AFM modes as functions of their respective stiffness parameter $J^{\text{S}}_{\mathbf{M}}$ with increasing system size.

Through the inversion of the Dyson equation, we have access to the self-energy,

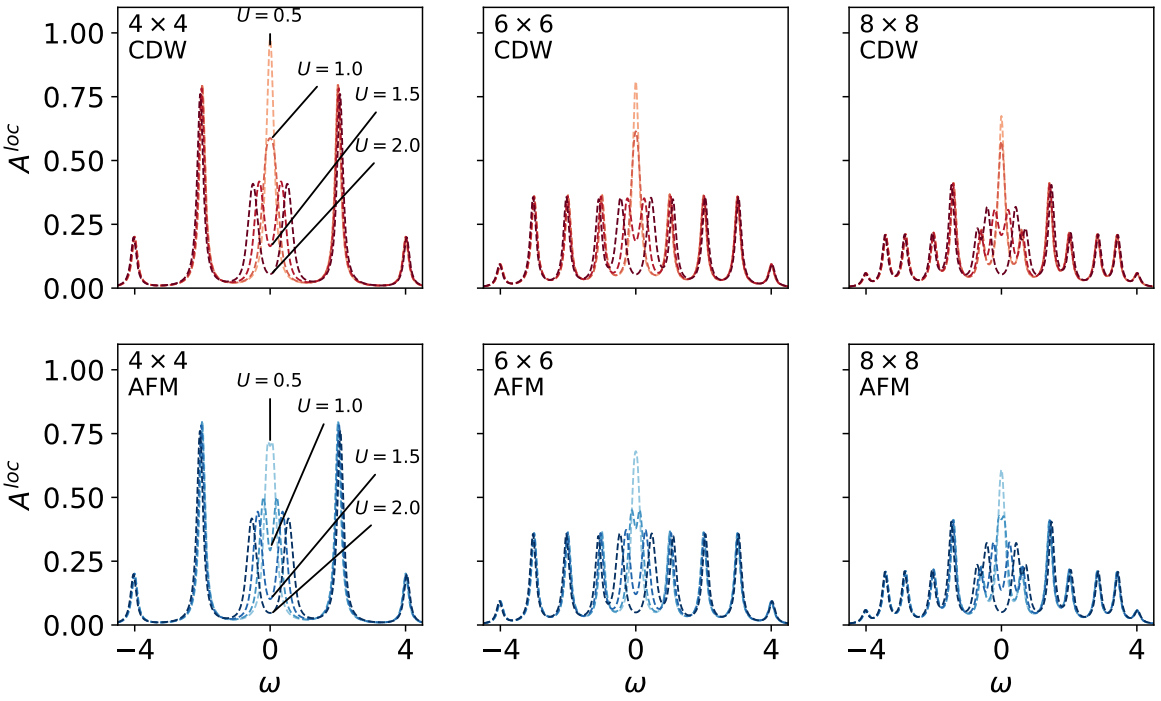

Figure 5.13: The local spectral function $\mathcal{A}_{\omega}^{\text{loc}}$ calculated along $V = U/4$ in the $U - V$ phase diagram for varying plaquette size of 4×4, 6×6, and 8×8 as predicted by the SCFF theory for the CDW and AFM modes respectively.

allowing for a useful description of the correlation effects of the FF theory. For a plaquette of 128×128 lattice sites and inverse temperature $\beta = 10$, we perform calculations of the self-energy $\Sigma_{\mathbf{k},\omega}$ along the high-symmetry path $\Gamma\text{X}\text{M}\Gamma$, with the peak broadening set to $\eta = 0.1$. Fig. 5.14 displays the real and imaginary components of the self-energy $\Sigma_{\mathbf{k},\omega}$ for a value of interaction parameters along $V = U/4$ representing the self-energy in the symmetry-broken phase. The main features of the self-energy is observed along $\omega = -\epsilon_{\mathbf{k}}$ for all consider values of the interaction parameters, associated with a line singularity in the self-energy and a strong momentum-dependence. The line singularity displays itself within the real part of the self-energy $\Sigma_{\mathbf{k},\omega}$ by the function switching sign, and within the imaginary part of the self-energy $\Sigma_{\mathbf{k},\omega}$ as the emergence of a peak structure. The main effect of the value of the stiffness parameter $J_{\mathbf{M}}^{\text{S}}$ is determining the magnitude of the self-energy, with an increasing $J_{\mathbf{M}}^{\text{S}}$ enhancing its magnitude. In contrast, no modification of the location of the line singularity is observed within our calculations. To further investigate the correlation effects incorporated in FF theory, we plot the self-energy $\Sigma_{\mathbf{k},\omega}$ at the Fermi energy along the high-symmetry path $\Gamma\text{X}\text{M}\Gamma$, see Fig. 5.15. The underlying mechanism of the gap opening, as encoded in the self-energy, is due to the opposite sign of the real component of the self-energy $\text{Re}\Sigma_{\mathbf{k},\omega=0}$ at the Fermi surfaces. Positive values of $\text{Re}\Sigma_{\mathbf{k},\omega=0}$ shift the electronic structure in the direction towards higher energies, and reversibly negative values shift the electronic structure towards lower energies. This is accompanied with the emergence of a finite peak width in the spectral function due to the enhanced imaginary self-energy $\text{Im}\Sigma_{\mathbf{k},\omega=0}$, a clear signature of a correlation effect.

Completing our investigation of the correlation effects captured within the SCFF theory, we perform a scaling analysis by computing the real and imaginary parts of

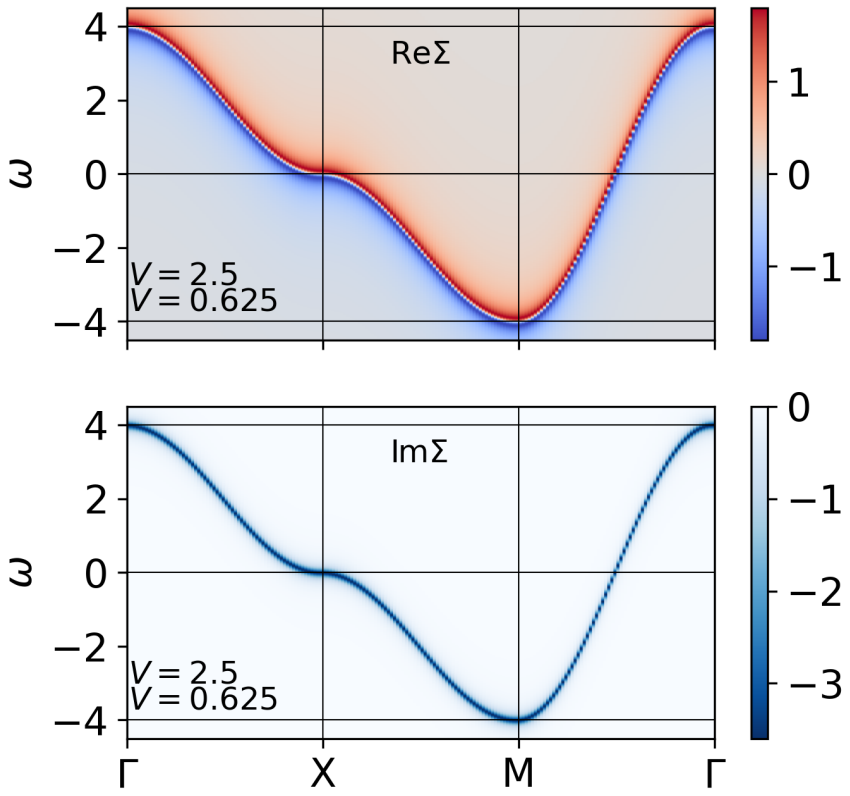

Figure 5.14: The self-energy $\Sigma_{\mathbf{k},\omega}$ of half-filled extended Hubbard model, with $\beta = 10$ and system size 128×128, as predicted by the SCFF theory, with the real and imaginary parts displayed separately. Red and blue colour denotes positive and negative values, respectively. Calculations are performed along a high-symmetry path, sketched in Fig. 5.9, for a representative value of the interaction parameters in the symmetry-broken phase $U = 2.5$, $V = 0.625$. The form of the self-energy is remains the same for any value of the stiffness parameter $J^{\varsigma}_{\mathbf{M}}$, however, it demonstrates a substantial enhancement of its magnitude with an increasing $J^{\varsigma}_{\mathbf{M}}$.

the local self-energy $\Sigma^{\mathrm{loc}}_{\omega}$ for plaquettes of the system size 4×4, 6×6, 8×8 and 128×128. In Fig. 5.16, the local self-energy $\Sigma^{\mathrm{loc}}_{\omega}$ is shown along the $V = U/4$ line, which for convenience is restricted to the CDW mode as a representation of the general behaviour of the SCFF theory with increasing system size. For small systems, we observe a saw-like structure in the real local self-energy $\Sigma^{\mathrm{loc}}_{\omega}$, with a repeated switching of signs. However, as system become larger, the saw-like structure is slowly smoothed out, eventually leading to a broad structure accompanied with a single change of sign at the Fermi energy. We observe the imaginary local self-energy $\Sigma^{\mathrm{loc}}_{\omega}$ to display a peak structure reminiscent of the spectral function at any plaquette size.

5.5.2 Many-body effects within the multi-channel FF theory

Following the investigation of the excited-state properties and correlation effects incorporated within the FF theory, we now consider the prediction of the interplay between collective CDW and AFM fluctuations. In particular, we calculate the local spectral function $\mathcal{A}^{\mathrm{loc}}$ for a plaquette of 128×128 lattice sites, an inverse temperature $\beta = 10$ and a peak broadening of $\eta = 0.1$, see Figs. 5.17a-c. Fig. 5.17a displays the local

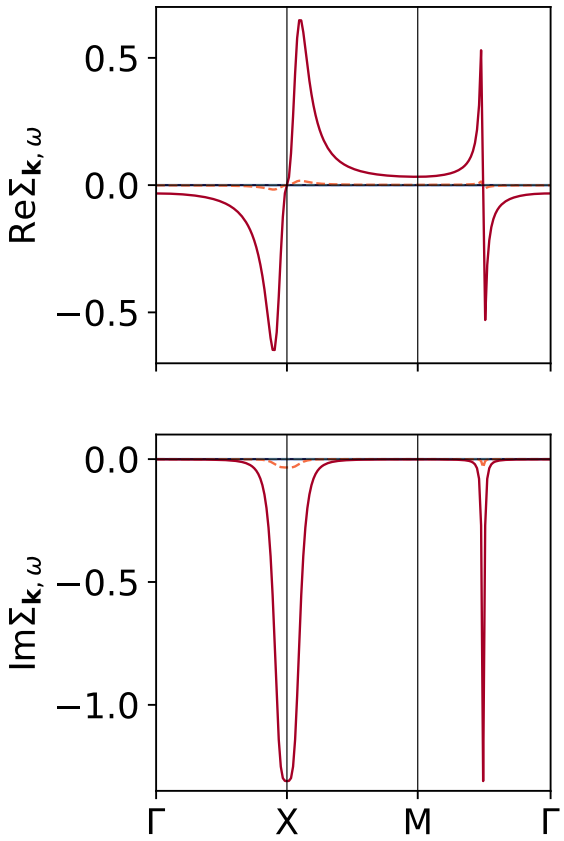

Figure 5.15: Real and imaginary self-energy $\Sigma_{\mathbf{k},\omega}$ along the high-symmetry path ΓXMΓ at the Fermi energy calculated utilising the SCFF theory. The components are evaluated along $V = U/4$ in the $U - V$ phase diagram, with a selection of values of the interaction parameters, denoted by their colours in Fig. 5.12. Note, only the self-energies associated with $U \in \{1.5, 2.0\}$ are sufficiently large to be observed.

spectral function $\mathcal{A}^{\mathrm{loc}}$ along $V = U/4$ in the $U - V$ phase diagram, demonstrating both the behaviour of the one-particle excitation spectrum in the normal phase, and on the first-order CDW-AFM phase boundary. In agreement with our previous investigation, the spectral function shows a clear independence of the interaction parameters within the metallic phase. At the CDW-AFM phase boundary, shown previously to display significant collective fluctuations, the emergence of a gap is visible in the local spectral function. Therefore, we are able to observe that the main behaviour of the spectral function follows closely those considered in the SCFF theory. For completeness, in Fig. 5.17bc the local spectral function $\mathcal{A}^{\mathrm{loc}}$ calculated at two representative points of the CDW and AFM phases within the $U - V$ phase diagram are displayed.

5.6 Summary and perspectives

Exploiting the numerically low-cost MCFF method, we are able to study competing CDW and AFM fluctuations in the half-filled extended Hubbard model from small to large plaquettes. The MCFF method predicts a repulsive U-V phase diagram in qualitative agreement with more costly methods. Our approach correctly captures the $U \to 0$ limit for the CDW phase boundary, which is a non-trivial problem for com-

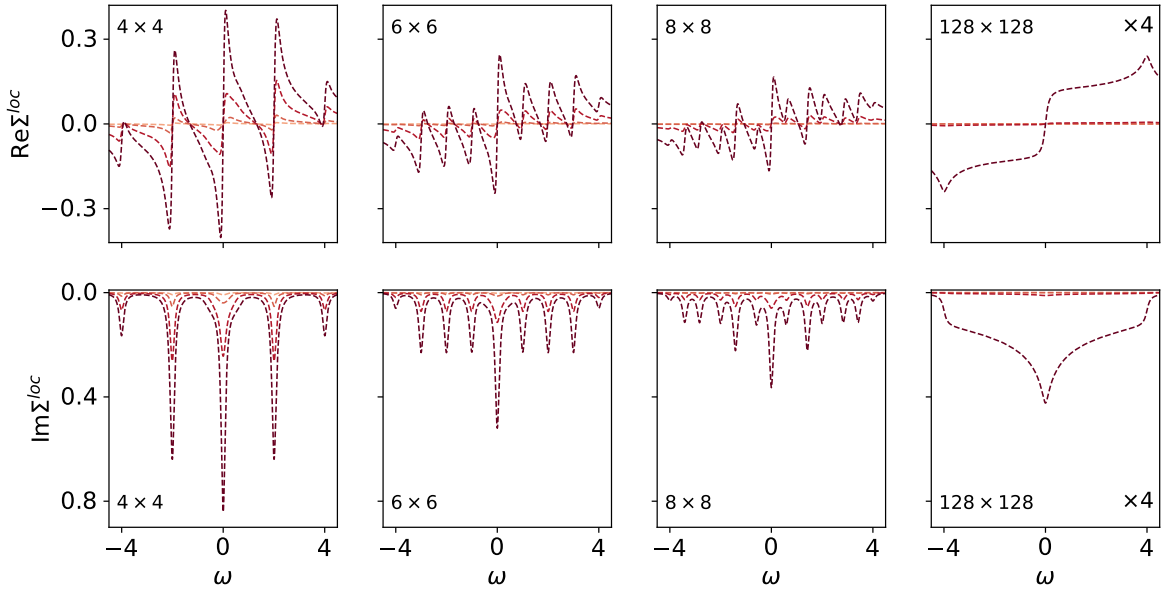

Figure 5.16: The local self-energy $\Sigma_\omega^{\text{loc}}$ calculated along $V = U/4$ in the $U - V$ phase diagram for a varying plaquette size of 4×4, 6×6, 8×8, and 128×128, as predicted by the SCFF theory for CDW mode. The values of the interaction parameters are denoted by their respective colours, as defined in Fig. 5.13. Note the local self-energy $\Sigma_\omega^{\text{loc}}$ on the 128×128 plaquette is re-scaled by a multiplicative factor of 4 for the purpose of easier visibility.

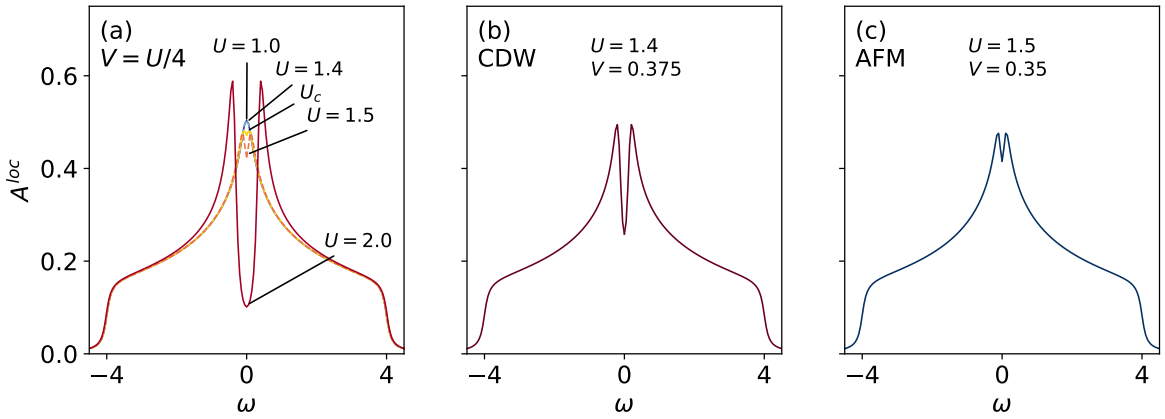

Figure 5.17: The local spectral function $\mathcal{A}^{\text{loc}}$ of the half-filled extended Hubbard model, with a plaquette size of 128×128 lattice sites and an inverse temperature $\beta = 10$, evaluated utilising the MCFF theory with interplaying CDW and AFM modes for a selection of interaction parameters. (a) $\mathcal{A}^{\text{loc}}$ is calculated for a collection of points along the $V = U/4$ line, representing the normal phase for $U < U_c$ and the first-order CDW-AFM phase boundary for $U > U_c$. (b) $\mathcal{A}^{\text{loc}}$ is calculated for a $U = 1.4$, $V = 0.375$ as a representative point of the CDW phase near its phase boundary. (c) Similarly, $\mathcal{A}^{\text{loc}}$ is evaluated at $U = 1.5$, $V = 0.35$ as a characterisation of the AFM phase near its phase boundary.

putationally heavy cluster-based DMFT techniques due to the cluster size limitations. In addition, at intermediate interactions a first-order CDW-AFM transition $U = 4V$

is captured in agreement with numerically exact methods. A quantitative agreement is observed with respect to DCA simulations [199], with both approaches observing a coexistence region of collective AFM and CDW fluctuations. The coexistence region display a strength of the MCFF approach, as it allows direct access to distinguishing between the stable and metastable phases. Studying the evolution of interplaying collective fluctuations, we observe MCFF theory to incorporate effects beyond mean-field theory which are exceptionally important for treatment in the vicinity of the phase boundaries for small plaquettes. The chapter concluded with an investigation focusing on the excited-state properties and correlation effects incorporated within the FF theory. We observed that FF theory allows for a symmetry-conserving construction of observables such as, e.g., the spectral function and self-energy with translational and spin symmetries respected.

Chapter 6

Coexisting s-wave superconductivity and phase separation

> "It is only slightly overstating the case to say that physics is the study of symmetry." - P. W. Andersson [10]

The regime of attractive U, V interactions in the extended Hubbard model promotes charge fluctuations and superconductivity, allowing the extended Hubbard model to be a suitable framework for a well-controlled investigation of competing charge, spin and pairing instabilities. In this chapter, using the introduced MCFF approach, we seek to address the interplay of charge density wave, s-wave superconductivity, antiferromagnetic and phase separation fluctuations in the attractive extended Hubbard model. Despite the fact that this model has been intensively studied for decades, our novel approach will allows us to identify a novel phase that is characterised by the coexistence of s-wave superconductivity and phase separation fluctuations. Importantly, we will comment on the relevance of the novel phase in correlated quantum materials and discuss the experimental realisability of the phase. This chapter follows closely the work in Ref. [335] by the author of this thesis and collaborators.

6.1 Competing order with repulsive U interaction

In the previous chapter, we investigated the repulsive $U-V$ phase diagram of the extended Hubbard model on a two-dimensional square lattice using the MCFF theory. In this regime, the collective AFM fluctuations driven by the repulsive local U interaction compete with the CDW stabilised by the repulsive nearest-neighbour V interaction. Extending our previous work to attractive nearest-neighbour V interaction, we seek to study the regime of interplaying AFM and PS fluctuations.

6.1.1 Interplay of collective AFM and PS fluctuations

Using the MCFF theory, following chapter 3, we construct the repulsive U and attractive V phase diagram of the half-filled extended Hubbard model on a square lattice from the free energies $\mathcal{F}(\phi^{\varsigma}_{\mathbf{M}})$ (4.20) of the AFM and PS fluctuations. In order to connect with the results of the previous chapter, we perform the calculations for a

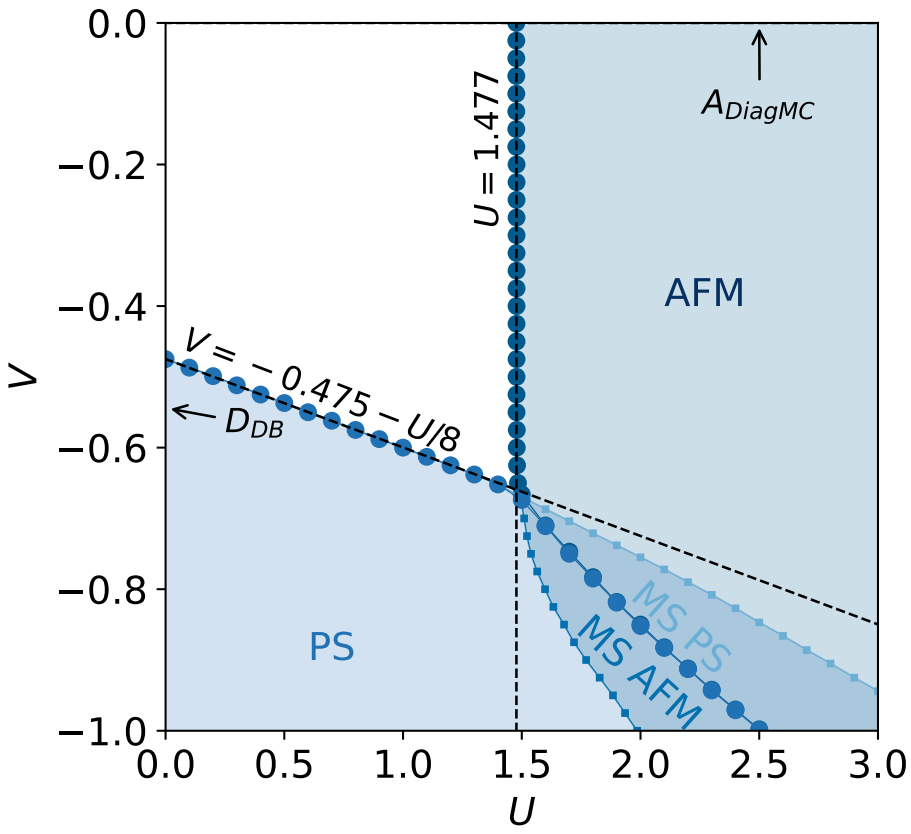

Figure 6.1: Phase diagram for the half-filled extended Hubbard model with repulsive U and attractive V interactions as predicted by the MCFF approach. The result is obtained at $\beta = 10$ for a plaquette of 128×128 lattice sites. Blue and light blue areas depict the AFM and PS phases, respectively. The corresponding phase boundaries are shown by coloured circles. Black dashed lines describe the asymptotic behaviour of the phase boundaries: $U = 1.477$ for AFM and $V = -0.475 - U/8$ for PS. The boundaries of metastable AFM and PS phases are illustrated by lines with small square markers. Metastability displays the first-order nature of the AFM-PS phase transition, to contrast with the second-order phase transitions occurring between the normal metal phase (white region) and the AFM and PS phases. For comparison, we add the DB estimate $D_{\mathrm{DB}} \simeq -0.54$ for the PS boundary in the $U \to 0$ limit [212], and the DiagMC estimate $A_{\mathrm{DiagMC}} \sim 2.5$ for the AFM boundary in the limit of $V \to 0$ [136].

plaquette of 128×128 lattice sites with periodic boundary conditions and inverse temperature $\beta = 10$. Unless the contrary is stated, throughout the chapter we will restrict our considerations to the 128×128 plaquette at inverse temperature $\beta = 10$. Fig. 6.1 shows the computed phase diagram of the system.

Our MCFF calculations reveal three phases: a normal (white colour), an AFM (blue colour), and a PS (light blue colour) phase. In the weak coupling regime $U \leq 1.447$ we find the PS phase boundary to follow the $V = -0.475 - U/8$ line. This result follows $V = D_{\mathrm{RPA}} - U/8$ in the weak coupling limit, where the constant D_{RPA} corresponds to the critical value of the non-local interaction for the PS transition $V^{\mathrm{PS}}_{U=0}$ obtained within RPA for $U = 0$. The RPA estimate is determined by the critical $V^{\mathrm{PS}}_{U=0}$ associate with a singularity in the RPA construction of the charge susceptibility in the limit of

the ordering vector $\mathbf{Q} \to \mathbf{\Gamma}$. Keep in mind the order of limits $\mathbf{Q} \to \mathbf{\Gamma}$ and $\omega \to 0$ is crucial due to their non-commuting nature. For the considered system, $D_{\text{RPA}} = -0.475$ is a slightly overestimation of the PS stability, as an extrapolated $U \to 0$ DB result for the PS transition point gives $V^{\text{PS}}_{U=0} \simeq -0.54$ [212]. Thus, while the $U \to 0$ limit of the CDW phase boundary is exactly captured, the MCFF theory underestimates the $U \to 0$ limit for the PS phase boundary. As the predicted PS phase boundary of EDMFT and DB theory are in agreement [212], our expectation is the origin of the slight mismatch is due to missing dynamical correlation effects. In the weak coupling regime, the AFM phase boundary follows the behaviour observed in the repulsive V regime, i.e. the observed $U = 1.477$ line is in exact agreement with the FLEX result obtained for $V = 0$: $A_{\text{FLEX}} = U^{\text{AFM}}_{V=0} = 8C_{\text{RPA}}$.

Progressing into the intermediate coupling regime, both AFM and PS fluctuations are required to be accounted for due to their significant interplay. Akin to the interplay between the CDW and AFM phases in the repulsive regime, the AFM and PS states are mutually exclusive with a first-order AFM-PS phase transition. Their mutually exclusive behaviour is accompanied by a region of metastability in the vicinity of the phase transition. Unlike the simple form of the $V = U/4$ CDW-AFM phase boundary, a non-trivial bending of the AFM-PS phase boundary occurs. The origin of the non-trivial behaviour is due to the competing modes being characterised by different ordering vectors $\mathbf{Q}$, unlike our prior considerations. Near the critical value $U = 1.477$, the AFM-PS phase boundary follows $V \propto -U$, which transform to $V \propto -xU$ with $x \sim 0.25 - 0.30$ in the vicinity of $U = 2.5$. Therefore, we observe the phase boundary to not follow a simple behavior defined by the line where $J^s_{\mathbf{M}} = -U/2$ and $J^c_{\mathbf{\Gamma}} = U/2 + 4V$ are equivalent, i.e. $V \propto -U/4$.

6.2 Competing order with attractive U interaction

Our studies of the $U - V$ phase diagram of the extended Hubbard model for repulsive U interaction is, within the MCFF theory, limited to interplay between charge and spin degrees of freedom. Seeking to study the attractive U regime, our aim is to now investigate the interaction between the charge and s-wave pairing degrees of freedom.

6.2.1 Interplay of collective CDW and PS fluctuations

Initially neglecting the collective s-SC fluctuations, we construct the attractive U and repulsive/attractive V phase diagram of the half-filled extended Hubbard model on a square lattice from the free energies $\mathcal{F}(\phi^{\varsigma}_{\mathbf{M}})$ (4.20) of the CDW and PS fluctuations. Fig. 6.2 shows the computed phase diagram of the system. Our MCFF method predict the occurrence of three phases: a normal (white colour), a CDW (red colour), and a PS (light blue colour) phase. In the weak coupling regime, both the CDW and PS phase boundaries continue their behaviour observed in the repulsive U regime: with $V = 0.185 + U/8$ for CDW and $V = -0.475 - U/8$ for PS.

In the intermediate regime, the CDW and PS fluctuations interact mutually exclusively, leading to the formation of a first-order CDW-PS phase transition surrounded by a region of metastability. Alike the non-trivial AFM-PS phase boundary observed previously, we observe the CDW-PS phase boundary is not uniquely determined by the degeneracy line of the stiffness parameters $J^c_{\mathbf{M}} = U/2 - 4V$ and $J^c_{\mathbf{\Gamma}} = U/2 + 4V$. Thus, we observe a general trend within the MCFF theory with competing collective

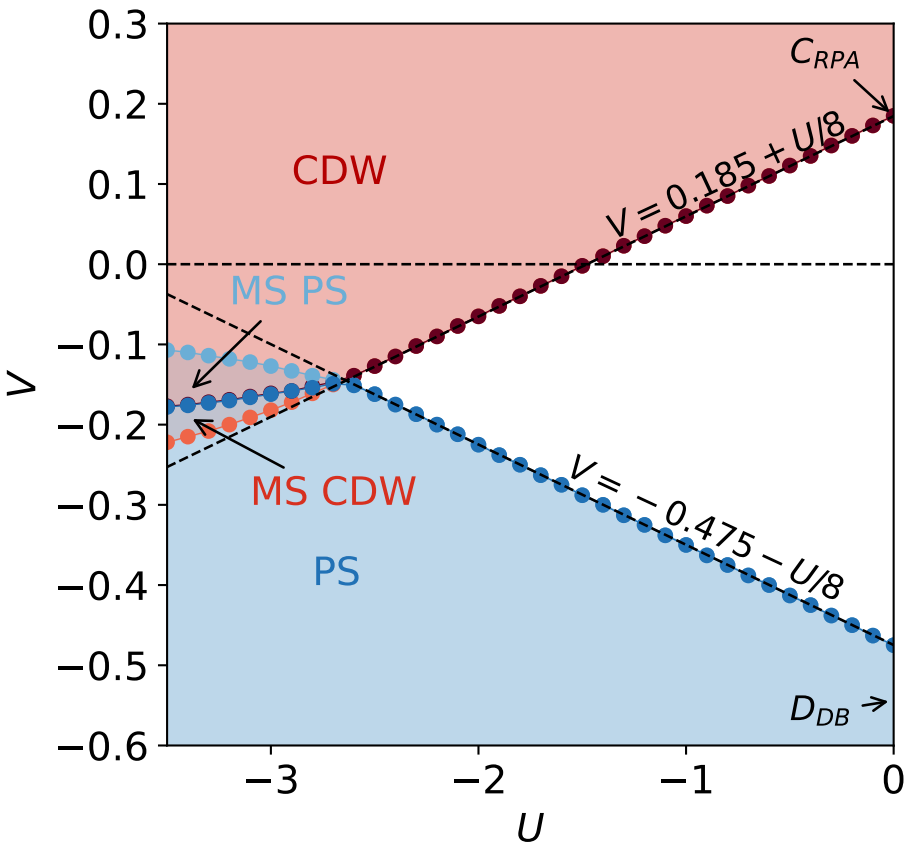

Figure 6.2: Phase diagram for the half-filled extended Hubbard model with attractive U and repulsive/attractive V interactions as predicted by the MCFF approach. The result is obtained at $\beta = 10$ for a plaquette of 128×128 lattice sites. Red and light blue areas depict the CDW and PS phases, respectively. The corresponding phase boundaries are shown by coloured circles. Black dashed lines describe the asymptotic behaviour of the phase boundaries: $V = 0.185 + U/8$ for CDW and $V = -0.475 - U/8$ for PS. The boundaries of metastable CDW and PS phases are illustrated by lines with small square markers. Metastability displays the first-order nature of the CDW-PS phase transition, to contrast with the second-order phase transitions occurring between the normal metal phase (white region) and the CDW and PS phases. For comparison, we add the RPA estimate $C_{\mathrm{RPA}} = 0.185$ for the CDW boundary in the $U \to 0$ limit, and the DB estimate $D_{\mathrm{DB}} \simeq -0.54$ for the PS boundary in the $U \to 0$ limit [212].

modes associated with different ordering vector $\mathbf{Q}$ leading to non-trivial structures of their intermediate phase boundaries. In addition, we may compare our MCFF calculations to the DB theory applied to the regime of interplaying collective CDW and PS fluctuations as computed in Ref. [212]. Within Ref. [212], DB theory is shown to predicts significant bending of both the CDW and PS phase boundaries as attractive U increases. Furthermore, by exploiting the staggered particle-hole symmetry of the Hubbard model relating the spin and pseudo-spin degrees of freedom [158, 159], the exact DiagMC solution gives $U_{V=0}^{\mathrm{DiagMC}} \simeq -2.5$ value at $\beta = 10$ for the CDW phase boundary at $V \to 0$ [136], which displays a significant shift relative the MCFF estimate of $U_{V=0}^{\mathrm{CDW}} = 1.447$. Thus, we expect the inclusion of local dynamics to weaken the interplay between collective CDW and PS fluctuation relative to the MCFF predictions.

6.2.2 Interplay of collective CDW and s-SC fluctuations

Within the half-filled extended Hubbard model on a square lattice, the collective s-SC fluctuations dominate in the region between the collective CDW and PS fluctuations. Limiting our investigation to the CDW and s-SC modes, we construct the attractive U and repulsive/attractive V phase diagram of the half-filled extended Hubbard model. Fig. 6.3 shows the resulting U-V phase diagram.

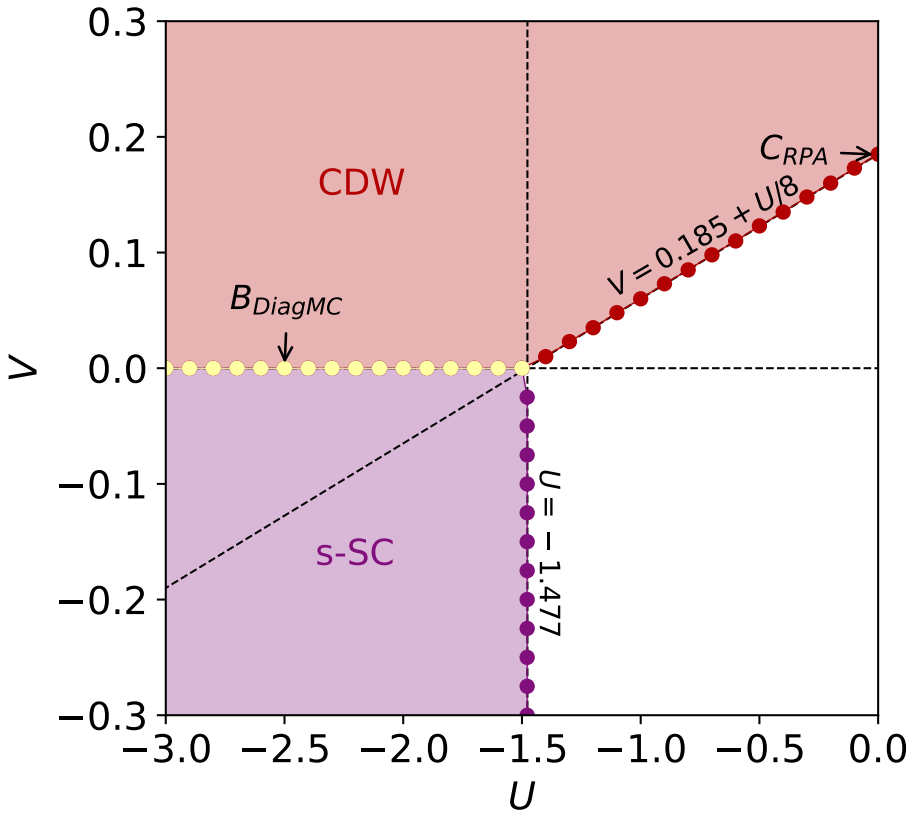

Figure 6.3: Phase diagram for the half-filled extended Hubbard model with attractive U and repulsive/attractive V interactions as predicted by the MCFF approach. The result is obtained at $\beta = 10$ for a plaquette of 128×128 lattice sites. Red and purple areas depict the CDW and s-SC phases, respectively. The corresponding phase boundaries are shown by coloured circles. Black dashed lines describe the asymptotic behaviour of the phase boundaries: $V = 0.185 + U/8$ for CDW and $U = -1.478$ for s-SC. The yellow line specifies the CDW and s-SC coexistence in the attractive Hubbard model ($V = 0$). For comparison, we add the RPA estimate $C_{\mathrm{RPA}} = 0.185$ for the CDW boundary in the $U \to 0$ limit. In addition, exploiting the staggered particle-hole symmetry of the Hubbard model, in the thermodynamic limit the exact DiagMC estimate gives $U_{V=0}^{\mathrm{DiagMC}} \simeq -2.5$ value at $\beta = 10$ for the CDW and s-SC coexistence transition point [136].

It consists of four phases: normal metal (white), CDW (red), s-SC (purple), and one phase where s-SC coexists with CDW ordering (yellow). At weak coupling ($|U| \lesssim 1.5$), the CDW phase boundary follow the $V = 0.185 + U/8$ line as observed previously. In agreement with the fluctuating exchange (FLEX) result obtained for $V = 0$, the MCFF s-SC phase boundary in the weak coupling regime follows the $U_{V=0}^{s-\mathrm{SC}} = -1.477$

line. FLEX is known to overestimate the strength of antiferromagnetic (AFM) fluctuations at $V = 0$. Therefore, by the staggered particle-hole symmetry of the Hubbard model relating the spin and pseudo-spin degrees of freedom [158, 159], FLEX is also expected to overestimate the strength of the coexisting CDW and s-SC fluctuations at $V = 0$. Exploiting this symmetry, as performed for the CDW phase above, in the thermodynamic limit the exact DiagMC solution gives $U_{V=0}^{\mathrm{DiagMC}} \simeq -2.5$ value at $\beta = 10$ for this transition point [136].

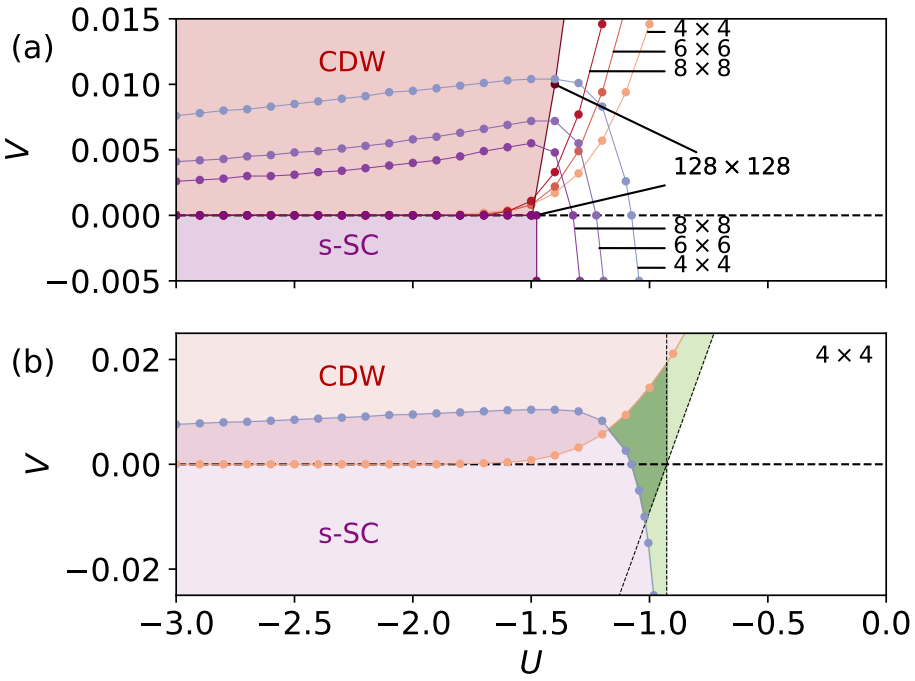

Figure 6.4: CDW (red) and s-SC (purple) ordering boundaries predicted by the MCFF approach for the half-filled extended Hubbard model obtained for $\beta = 10$: (a) for 4×4, 6×6, 8×8, and 128×128 plaquettes. (b) for a 4×4 plaquette with the green region enclosed by the thin black dashed lines that depict asymptotics for the non-interplaying CDW and s-SC instabilities, displaying the region, where the CDW and s-SC orderings stabilise without interplay. Dark green denotes the region where stabilisation of either the CDW or s-SC phase destroys the other ordering.

Turning to the intermediate coupling regime, the CDW and s-SC fluctuations develop a coexisting phase along the $V = 0$ line displayed in yellow colour in Fig. 6.3. This coexistence is associated with the emergent pseudo-spin symmetry between CDW and s-SC order parameters. Beyond this line the finite non-local interaction V favours the formation of either the CDW ($V > 0$) or s-SC ($V < 0$) phase. Remarkably, we find that at $V \neq 0$ the CDW and s-SC phases are mutually exclusive only in the thermodynamic limit. For small-size plaquettes of 4×4, 6×6, and 8×8 lattice sites we find that the CDW and s-SC orderings can coexist also in the vicinity of $V = 0$, and the coexistence region decreases with increasing the size of the system (Fig. 6.4 a). This convergence check allows us to identify that the coexistence region in the vicinity of $V = 0$ converges towards a single transition line occurring along $V = 0$ for $U \leq -1.447$ in the thermodynamic limit. Thus, the transition between the CDW and s-SC phases appearing as a direct first-order phase transition is composed of two first-order phase transitions passing through the intermediate coexistence phase constrained by the pseudo-spin SU(2)

symmetry [150].

Another interesting effect can be found in the region of the phase diagram depicted in Fig. 6.4 b by green colour. It displays a region where CDW or s-SC orderings are separately stable without interplay between the modes. The dark green area denotes the overlap region of the non-competing CDW and s-SC orderings. In the MCFF method, the CDW phase transition in the presence of the s-SC fluctuations is studied by integrating out the s-SC modes and investigating the behaviour of the free energy $\mathcal{F}(\phi^{\varsigma}_{\mathbf{M}})$ for the remaining CDW mode, and *vice versa*. In the region where the integrated s-SC mode is ordered, the MCFF analysis of the CDW transition corresponds to the investigation of the stability of the CDW ordering in the presence of the s-SC phase. In this regard, the integration of an ordered mode can be seen as an observation/measurement of this ordering in the system. We note that green regions in Fig. 6.4 b lie outside the CDW and s-SC phases that are obtained considering the interplay between the two fluctuations. Therefore, our results suggest that stabilising one of the two orderings in the dark green region immediately destroys the other one, which can be seen as a destruction of a quantum superposition of the two orderings by an observer. Remarkably, we find that no such non-trivial "green" phases exist in the thermodynamic limit, where quantum effects are suppressed. Note the generality of the discuss, as an analogous discuss may be performed for the study of other interplaying modes. For example, the finite-size scaling of the competing CDW and AFM modes studied prior may be viewed from an identical perspective.

6.2.3 Interplay of collective s-SC v PS fluctuations

We complete our investigation of the half-filled extended Hubbard model on a square lattice in the attractive $U-V$ phase diagram by limiting our considerations to interplaying s-SC and PS fluctuations. Within MCFF theory, we compute the $U-V$ phase diagram displayed in Fig. 6.5. The phase diagram is composed of four phases: normal metal (white), s-SC (purple), PS (light blue) and one phase where s-SC coexists with PS ordering (labelled "PS + s-SC"). At weak coupling, the s-SC and PS phase boundaries follow their behaviour observed above, i.e. $U=-1.477$ for the s-SC mode and $V=-0.475-U/8$ for the PS mode. Therefore the properties of the weak coupling behaviour of the two phases discussed above holds. However, in the intermediate coupling range, we observe the emergence of a novel phase that comprises coexisting PS and s-SC orderings, sketched in Fig. 6.6.

The PS+s-SC coexistence phase can be found in the regime of intermediate couplings of the attractive U,V extended Hubbard model (Fig. 6.5). In contrast to the previously considered coexisting CDW and s-SC orderings, the novel coexistence phase does not collapse to a single transition line in the thermodynamic limit, thus acquiring a finite width in V for a given U. We observe the width to be a non-monotonic function of U, with a maximal width occurring near $U=-3$. To obtain insight into the interplay between PS and s-SC ordering, in Fig. 6.7 a we show the normalised CDW, s-SC, and PS order parameters $\langle n^{\varsigma}_{\mathbf{Q}}\rangle$ that are computed for $U\in\{-2,-3,-4\}$ over a range of V. We observe a suppression of PS fluctuations in the weak coupling regime $V\gtrsim -0.3$ due to s-SC fluctuations, and *vice versa* at strong V. The competition between these two modes originates from the fact that the PS ordering on a lattice corresponds to the formation of broad puddles with uniform filling larger or smaller than the average filling of the system. Instead, the pairing process of s-SC fluctuations is energetically most

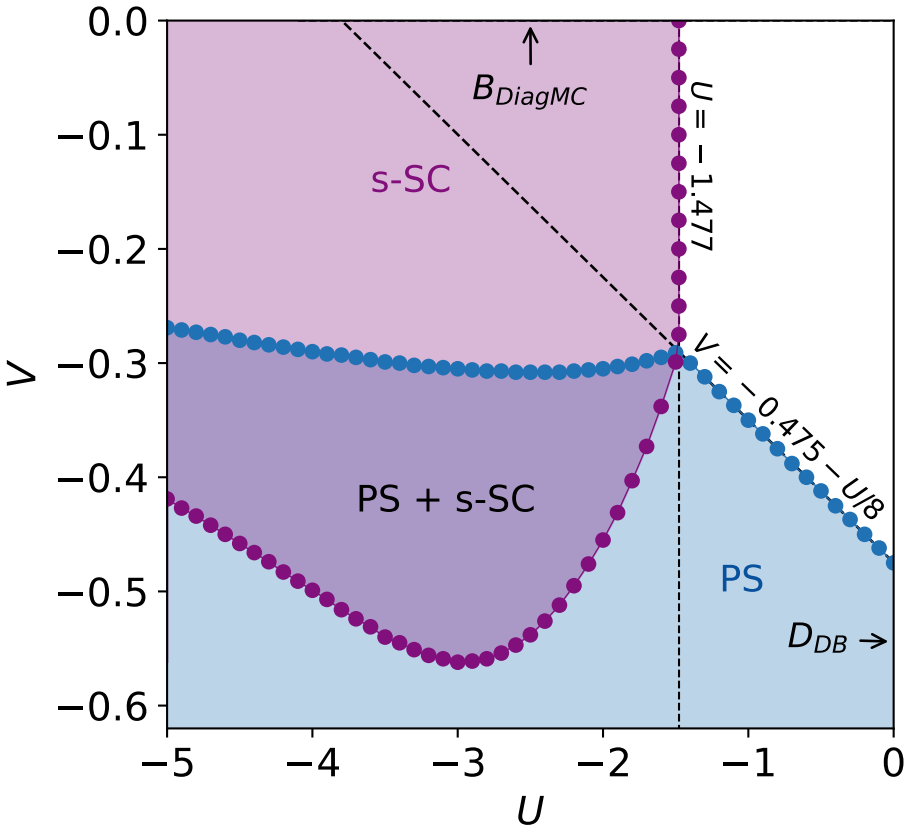

Figure 6.5: Phase diagram of the half-filled extended Hubbard model for attractive $U - V$. It is obtained from the MCFF method for a 128×128 square lattice with periodic boundary conditions at inverse temperature $\beta = 10$. This shows the existence of a novel phase "PS + s-SC" where PS and s-SC coexist, in addition to the conventional s-SC (purple) and PS (light blue) phases. For comparison, the DB theory estimate $D_{\mathrm{DB}} \simeq -0.54$ for the PS boundary in the $U \to 0$ limit is included [212]. In addition, we include the thermodynamic limit of the exact DiagMC estimate gives $U_{V=0}^{\mathrm{DiagMC}} \simeq -2.5$ value at $\beta = 10$ for the CDW and s-SC coexistence transition point [136].

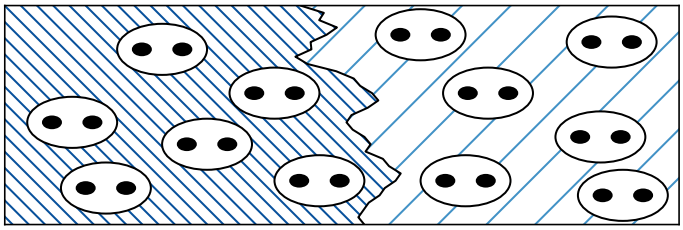

Figure 6.6: Cartoon picture of the novel phase characterised by the coexistence of PS and s-SC fluctuations. Within the phase, the collective s-SC fluctuations (Cooper pairs depicted by black dots) are sufficiently strong to stabilise the superconducting ordering within the PS puddles with uniform filling larger (left) or smaller (right) than half-filling, and *vice versa*.

favourable at half-filling. Due to the stability of the s-SC fluctuations for a relatively large range of fillings [153,172], the s-SC ordering can be formed inside the PS puddles,

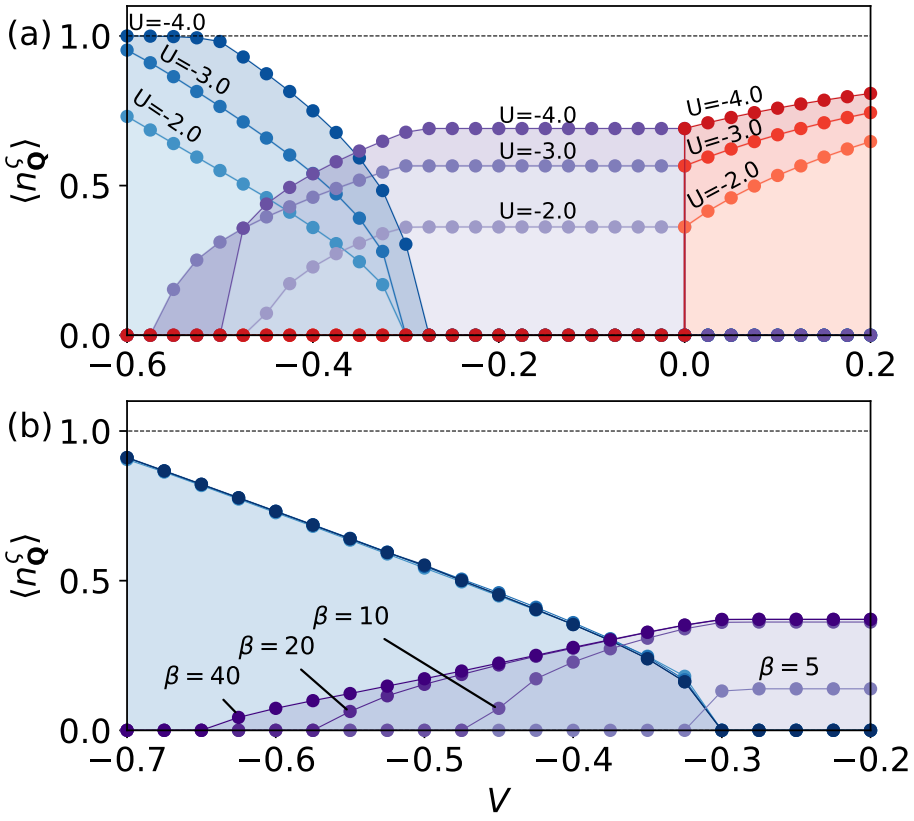

Figure 6.7: Normalised order parameters $\langle n^{\varsigma}_{\mathbf{Q}} \rangle$ computed for the half-filled 128×128 system using the MCFF approach. (a) CDW (red), s-SC (purple), and PS (blue) order parameters are calculated at $\beta = 10$ for $U \in \{-2, -3, -4\}$ for a range of V. (b) s-SC (purple) and PS (blue) order parameters calculated at $\beta \in \{5, 10, 20, 40\}$ at $U = -2$ for a range of V.

which results in a novel coexistence phase. Within the phase, the weights of the PS and s-SC modes vary with U, V. Thus, the phase is characterised by the PS and s-SC orderings being mutually compatible, i.e. collective s-SC fluctuations are stable in the environment of PS ordering and *vice versa*. As U increases, the region of s-SC fluctuations becomes more stable with respect to stronger PS fluctuations, leading to an increasing width of the coexistence region. However, the opposite trend occurs above a critical U as strong PS fluctuations leaves the system effectively in an empty or fully-filled sites configuration with $\langle n_{\mathrm{PS}} \rangle = 1$, completely suppressing any s-SC fluctuations. Note, that the CDW ordering on a square lattice corresponds to a checkerboard pattern of alternating lattice sites with higher and lower electronic densities. This does not allow for the formation of the s-SC ordering inside the CDW phase due to the strong inhomogeneity of the filling, except along the degenerate $V = 0$ line due to symmetry constraints.

We may connect our results to a recent determinant quantum Monte Carlo (DQMC) study of the zero-temperature U-V phase diagram of the half-filled extended Hubbard model [227]. In this work, few points of coexisting PS and s-SC orderings were identified evidencing our observations. However, due to the sparsity of the grid in the U-V space, the DQMC results do not allow one to make a definite statement on the presence of the coexistence phase in the system. In fact, the authors of this work

interpret this coexistence as a signature of a first-order transition between the s-SC and PS phases. Indeed, first-order transitions are usually accompanied by regions of metastable collective fluctuations appearing as coexistence regions [334]. However, in the current work we do not observe metastable collective fluctuations associated with any first-order transition, although the MCFF method allows for their detection in other contexts [334], as observed, e.g., in our study of interplaying CDW and AFM modes in the prior chapter. This fact allows us to argue for a true coexistence phase stable in the thermodynamic limit enclosed by two apparent second-order transition lines. An order parameter for this novel phase may be defined as the product of the s-SC and PS order parameters. To further connect our finite-temperature calculations to the zero-temperature DQMC results, we compute the s-SC and PS order parameters $\langle n^{\zeta}_{\mathbf{Q}} \rangle$ for $U = -2$ over a range of V at different inverse temperatures $\beta \in \{5, 10, 20, 40\}$. Figure 6.7 b display the increasing stabilisation of the s-SC fluctuations with decreasing temperature, as PS fluctuations remain nearly independent of the temperature. Thus, we expect the novel phase of coexisting PS and s-SC ordering to remain stable at zero temperature and to connect to the results observed in Ref. [227].

6.3 Experimental realizability of novel phase

Interplay between SC and PS fluctuations has been observed in high-temperature superconducting materials, such as copper oxides [24, 348–358] and iron-based superconductors [84, 359–363], but the microscopic mechanisms of the observed phenomena remain elusive. In doped copper oxides, it has been argued early on [350, 352] that dilute holes in an antiferromagnet have a strong tendency to phase-separate. Experimentally, interfaces of $La_{2-x}Sr_xCuO_4$-La_2CuO_4 [357] display an intriguing insensitivity of the critical temperature of the SC phase over an extended range of doping. These findings have been rationalised by invoking interlayer phase separation [358]. Thus, our findings of coexisting SC and PS at half-filling give yet another indication hinting at the possibly very fundamental role of phase separation in the physics of superconducting correlated fermionic systems.

Exploring the predicted phase diagram experimentally and switching between the different phases in realistic materials could be performed, e.g., by applying an external laser field. In the high-frequency regime of the driving, the applied laser field effectively decreases the hopping amplitude t of electrons [364–370], which effectively enhances the interactions U and V. In the low-frequency regime, driving phonon degrees of freedom may enhance the electron-phonon coupling [371], which would increase the strength of effective attractive electronic interactions [372–374]. This can potentially allow one to propagate within the U-V phase diagram and access the novel "PS + s-SC" coexistence phase.

6.4 Summary and perspectives

Through our investigation of the repulsive and attractive $U - V$ phase diagram of the half-filled extended Hubbard model on a square lattice in the last two chapters, we are permitted to summarise the phase diagram of interplaying CDW, AFM, s-SC and PS modes. The combined $U - V$ phase diagram is displayed in Fig. 6.8.

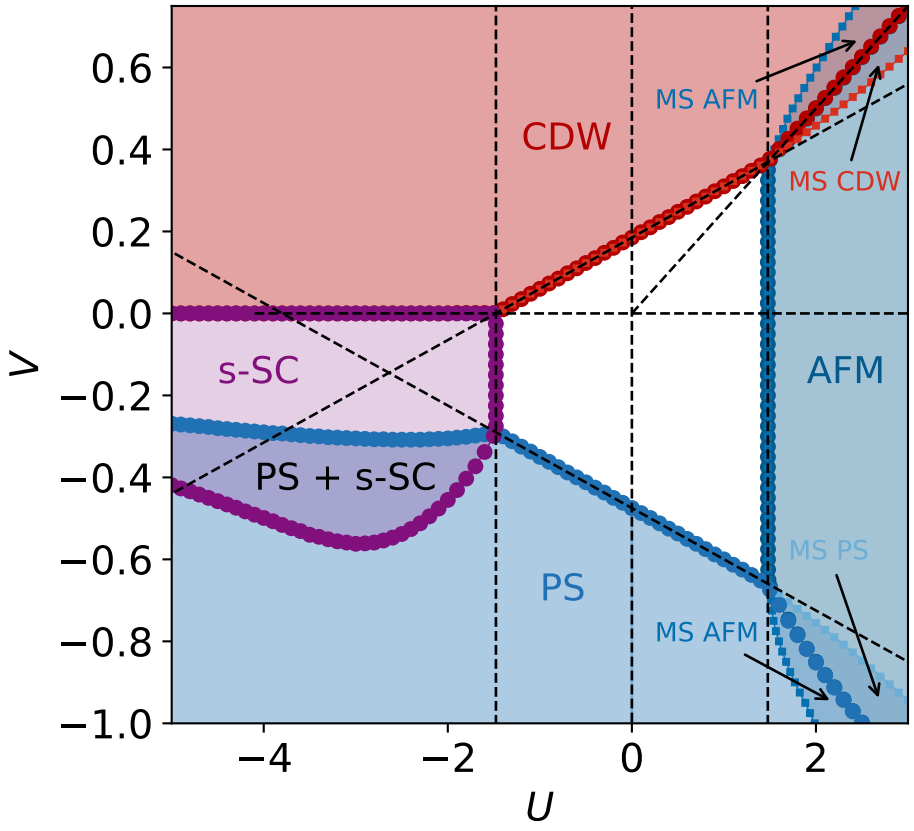

Figure 6.8: Phase diagram for the half-filled extended Hubbard model with repulsive and attractive U, V interactions as predicted by the MCFF approach. The result is obtained at $\beta = 10$ for a plaquette of 128×128 lattice sites. Red, blue, purple and light blue areas depict the CDW, AFM, s-SC and PS phases, respectively. The corresponding phase boundaries are shown by coloured circles. Black dashed lines describe the asymptotic behaviour of the phase boundaries: $V = 0.185 + U/8$ for CDW, $U = 1.477$ for AFM, $U = -1.477$ for s-SC and $V = -0.475 - U/8$ for PS. The boundaries of metastable CDW, AFM and PS phases are illustrated by lines with small square markers.

Determined by only two parameters, the local U and non-local V interactions between electrons, a complex phase diagram is observed to emerges with interplaying charge, spin and pairing degrees of freedom. Even restricting our considerations to the leading CDW, AFM, s-SC and PS modes, we observe the extended Hubbard model to be a quintessential model for investigating competing instabilities. A mutual exclusive nature of the collective AFM fluctuations is observed in their interplay with collective CDW and PS fluctuations. This may be contrasted with the mutually stable nature of the s-SC state with both CDW and PS fluctuations, leading to the emergence of coexistence phases: "CDW + s-SC" and "PS + s-SC". Furthermore, the origin of the coexistence phases are distinct. One one hand, the "CDW + s-SC" phase is associated with the emergent SU(2) pseudo-spin symmetry, and appears as a one-dimensional transition-line in the thermodynamic limit connected to the CDW and s-SC phases with corresponding first-order phase transitions. On the other hand, the "PS + s-SC" phase is not associated with any apparent underlying stabilising symmetry, and appears as a two-dimensional coexistence region in the thermodynamic limit connected

to the s-SC and PS phases through second-order phase transitions. Thus, a surprisingly complex energy landscape arises due to interplay of only two parameters in a simple parameter range of the extended Hubbard model. Of an even greater surprise, despite an extensive effort have been conducted into the study of the model, the novel "PS + s-SC" coexistence phase has not been reported previously.

Chapter 7

Conclusions and perspectives

"Goodbye to the Holy Mountain. Real life awaits us." - A. Jodorowsky [375]

Motivated by the search for novel theoretical tools for the description of collective phenomena and their interplay within strongly correlated quantum systems, we developed in this thesis the multi-channel fluctuating field (MCFF) theory [334, 335]. The basis for the proposed theory is a multi-channel generalisation of the recently introduced fluctuating local field (FLF) theory, utilised for a numerically low-cost description of magnetic fluctuations in the Ising, Heisenberg and Hubbard models [329–333]. Within the MCFF theory, we allow for any collective instabilities which may be formulated as the fluctuations of a single-particle composite variable, such as, e.g., the charge or spin densities. The guiding idea behind the MCFF approach is a variational mapping of the complicated action of a quantum lattice model on to a simplified trial action including classical fields associated with the main leading collective modes. By limiting to a few modes, the method allows for a numerically low-cost treatment of interplaying collective fluctuations without the enforcement of any explicit symmetry breaking. It naturally allows for the study of the phase transition associate with the collective instabilities through a free energy construction inspired by Landau theory. Through the free energies of the classical fields, stable and metastable state are distinguished, permitting a clear signature of the continuous or discrete nature of a phase transition. In addition, due to the analytic structure of the MCFF theory, observables can be directly evaluated on the real-frequency axis without utilisation of numerical analytic continuation. In particular, the spectral function, which describes the single-particle excitation spectrum, and the self-energy, which encodes the many-body correlation effects of the method, are accessible in forms respecting the underlying translational and spin symmetries of the original system.

Utilising the MCFF theory, we initial focused our attention on competing collective spin and charge fluctuations in the half-filled single-orbital extended Hubbard model with a repulsive Coulombic interaction. The interaction was modelled by a conventional choice: a local interaction U and a nearest-neighbour nonlocal interaction V, allowing for a significant benchmarking of the strengths and weaknesses of the MCFF method. A qualitative agreement with more computationally heavy methods is found for the repulsive U-V phase diagram. MCFF theory captures the $U \to 0$ limit for the CDW phase boundary, which is a nontrivial problem for many-body techniques with significant size limitations. However, the stability of the $V \to 0$ limit for the AFM phase boundary is observed to be significantly overestimated, due to the local

correlation missing within our implementation of the MCFF theory. At intermediate interactions, a first-order CDW-AFM transition $U = 4V$ is captured with an accompanying coexistence region of metastable AFM and CDW states, as observed in recent DCA calculations [199]. Through an investigation of the phase diagram and a measure of collective fluctuations as a function of the plaquette size, we observe MCFF theory to converge to a symmetry-conserving summation of MFTs in the thermodynamic limit. Nevertheless, important effects beyond MFT are incorporated within MCFF theory for small plaquettes, in particular in the vicinity of the phase boundaries, where nontrivial modification of the AFM and CDW phase boundaries are observed due to their mutual interplay. The first-particle excitation spectrum as predicted by the MCFF theory, displays the emergence of a gap in the spectral function centred at the Fermi energy due to the influence of the fluctuations of the static CDW and AFM orderings. With the current implementation of MCFF theory, with two FF fields $\phi^c_{\mathbf{M}}$, $\phi^s_{\mathbf{M}}$ associated with the ordering vector $\mathbf{M}$, the gap is observed to develop uniformly in momentum-space. Correlation effects encoded in the self-energy are observed to be dominant in the vicinity of the frequency $\omega = -\epsilon_{\mathbf{k}}$, with $\epsilon_{\mathbf{k}}$ denoting the bare dispersion, leading to a dominant contribution at Fermi energy. A clear signature of correlation effects, furthermore, appears in the imaginary self-energy, signalling the formation of a finite peak width in the spectral function.

Extending the MCFF theory to collective s-wave pairing fluctuations, we expanded our scope by investigating the competing collective spin, charge and s-wave pairing fluctuations in the half-filled single-orbital extended Hubbard model with both repulsive and attractive U and V interaction parameters. We limited our considerations to competing CDW, PS, AFM and s-SC ordering, allowing us to express a multitude of types of competing behaviours, displaying the quintessential nature of the extended Hubbard model in studying interplaying collective fluctuations. The mutual exclusive interplay of collective CDW and AFM modes, associated with a first-order phase transition, is observed in the regime of repulsive U and V. A similar behaviour is observed in the regime of repulsive U and attractive V, with competing PS and AFM modes, and in the regime of attractive U and V, with competing PS and CDW modes with the collective s-SC fluctuations suppressed. In contrast to the trivial competition between the collective CDW and AFM modes, both examples display a nontrivial bending of the phase boundary due to the difference in ordering vectors $\mathbf{Q}$.

By allowing for collective s-SC fluctuations, driven by the attractive U, the competition of the CDW and PS fluctuations is hidden under the s-SC phase. Its introduction leads to the emergence of two coexistence phases: "CDW + s-SC" and "PS + s-SC". The "CDW + s-SC" coexistence phase is connected to the emergent SU(2) pseudo-spin symmetry of the Hubbard model, and is limited to a one-dimensional transition line at $V = 0$ in the thermodynamic limit, acting as an intermediate phase between the competing CDW and s-SC phases. The "PS + s-SC" coexistence phase forms in the attractive U, V interaction regime. Unlike the "CDW + s-SC" phase originating due to an underlying symmetry, the "PS + s-SC" phase is not associated to an apparent emergent symmetry. Rather, the underlying mechanism of the "PS + s-SC" coexistence phase is the mutual stability of the s-SC modes with respect to the effective fillings of puddles of the PS fluctuations and, conversely, the stability of the PS fluctuations with respect to the formation of Cooper pairs. In addition, in the thermodynamic limit, the novel phase spans a two-dimensional region with a finite width. To the knowledge of the authors, a "PS + s-SC" coexistence phase has not been reported previously in

the literature, despite a significant effort in the investigation of the extended Hubbard model over the course of many decades.

As advertised within this thesis, the principle idea of the FF theory is quite general and thus allows for a broad selection of possible future applications and directions of progress. Our considerations have been restricted to the half-filled extended Hubbard model with leading commensurate modes. However, in fact the generality of MCFF theory allows for the treatment of collective fluctuations associated with incommensurate ordering vectors emerging away from half-filling. Inclusion of more interplaying collective fields associated with different quasi-momentum modes is further relevant for the physics underlying the Mermin-Wagner theorem, with the leading $\mathbf{M}$ being destroyed by the subleading quasimomentum modes in the one- and two-dimensional system. Incorporating subleading modes might further allow for the formation of a partial gap in the vein of NFL physics. In the same vein, by inclusion of more subleading Matsubara frequency modes beyond the static one, would allow for treating dynamical correlations. Another direction of pursuit is the inclusion of nonlocal order parameters, allowing for, e.g., the stabilisation of BOW and dimerisation. All these examples are directly applicable to the proposed form of the MCFF theory. It displays the general applicability of MCFF theory to a wide range of different quantum lattice models and the theoretical description of the interplay between a selection of different collective instabilities.

Within the current form of the MCFF theory, inclusion of instabilities without the existence of a natural order parameter, such as the Mott insulator, remains difficult. A solution would be to extended the MCFF theory by allowing for a dressing of the bare Green's function by the self-energy of DMFT in the spirit of Ref. [331], which naturally allows for a description of Mott physics. Inclusion of local correlation is further expected to improve upon the overestimation of the AFM phase boundary. Ultimately, the general nature of the MCFF theory makes it a promising tool for studying the interplay of collective fluctuations in strongly correlated fermionic systems.

Bibliography

[1] L. Néel. Banquet speech. *Nobel Prize*, 1970.

[2] D. B. McWhan and T. M. Rice. Critical Pressure for the Metal-Semiconductor Transition in V_2O_3. *Phys. Rev. Lett.*, 22:887–890, 1969.

[3] D. B. McWhan, T. M. Rice, and J. P. Remeika. Mott Transition in Cr-Doped V_2O_3. *Phys. Rev. Lett.*, 23:1384–1387, 1969.

[4] D. B. McWhan and J. P. Remeika. Metal-Insulator Transition in $(V_{1-x}Cr_x)_2O_3$. *Phys. Rev. B*, 2:3734–3750, 1970.

[5] P. D. Dernier and M. Marezio. Crystal Structure of the Low-Temperature Antiferromagnetic Phase of V_2O_3. *Phys. Rev. B*, 2:3771–3776, 1970.

[6] D. B. McWhan, J. P. Remeika, T. M. Rice, W. F. Brinkman, J. P. Maita, and A. Menth. Electronic Specific Heat of Metallic Ti-Doped V_2O_3. *Phys. Rev. Lett.*, 27:941–943, 1971.

[7] D. B. McWhan, A. Menth, J. P. Remeika, W. F. Brinkman, and T. M. Rice. Metal-insulator transitions in pure and doped v_2o_3. *Phys. Rev. B*, 7:1920–1931, 1973.

[8] H. Kuwamoto, J. M. Honig, and J. Appel. Electrical properties of the $(V_{1-x}Cr_x)_2O_3$ system. *Phys. Rev. B*, 22:2626–2636, 1980.

[9] G. A. Thomas, D. H. Rapkine, S. A. Carter, A. J. Millis, T. F. Rosenbaum, P. Metcalf, and J. M. Honig. Observation of the Gap and Kinetic Energy in a Correlated Insulator. *Phys. Rev. Lett.*, 73:1529–1532, 1994.

[10] P. W. Anderson. More is different: Broken symmetry and the nature of the hierarchical structure of science. *Science*, 177(4047):393–396, 1972.

[11] P. de Maricourt. *Epistola de magnete.* 1269.

[12] F. Bacon. *Novum Organum Scientiarum.* 1620.

[13] J. C. Maxwell. *A Treatise on Electricity and Magnetism.* Oxford University Press, 1873.

[14] A. Einstein. Zur Elektrodynamik bewegter Körper. *Annalen der Physik*, 322:891–921, 1905.

[15] P. A. M. Dirac. The quantum theory of the emission and absorption of radiation. *Proc. R. Soc. Lond. A*, 114:243–265, 1927.

[16] E. Fermi. Quantum Theory of Radiation. *Rev. Mod. Phys.*, 4:87–132, 1932.

[17] S. L. Glashow. The renormalizability of vector meson interactions. *Nuclear Physics*, 10:107–117, 1959.

[18] A. Salam and J. C. Ward. Weak and electromagnetic interactions. *Il Nuovo Cimento*, 11:568–577, 1959.

[19] S. Weinberg. A model of leptons. *Phys. Rev. Lett.*, 19:1264–1266, 1967.

[20] H. Kamerlingh Onnes. Further experiments with liquid helium. C. On the change of electric resistance of pure metals at very low temperatures etc. IV. The resistance of pure mercury at helium temperatures. *Proceedings of the Section of Sciences.*, 13:1274–1276, 1911.

[21] I. I. Rabi, J. R. Zacharias, S. Millman, and P. Kusch. A New Method of Measuring Nuclear Magnetic Moment. *Phys. Rev.*, 53:318–318, 1938.

[22] J. Bardeen, L. N. Cooper, and J. R. Schrieffer. Microscopic Theory of Superconductivity. *Phys. Rev.*, 106:162–164, 1957.

[23] J. Bardeen, L. N. Cooper, and J. R. Schrieffer. Theory of Superconductivity. *Phys. Rev.*, 108:1175–1204, 1957.

[24] J. G. Bednorz and K. A. Müller. Possible high T_c superconductivity in the Ba-La-Cu-O system. *Z. Phys. B Condens. Matter*, 64:189–193, 1986.

[25] P. W. Anderson. The Resonating Valence Bond State in La_2CuO_4 and Superconductivity. *Science*, 235:1196–1198, 1987.

[26] F. C. Zhang and T. M. Rice. Effective Hamiltonian for the superconducting Cu oxides. *Phys. Rev. B*, 37:3759–3761, 1988.

[27] V. J. Emery. Theory of high-T_c superconductivity in oxides. *Phys. Rev. Lett.*, 58:2794–2797, 1987.

[28] R. Peierls. *Quantum Theory of Solids*. Oxford Univ Press, New York, 1955.

[29] P. A. M. Dirac. Quantum mechanics of many-electron systems. *Proc. R. Soc. Lond. A*, 123:714–733, 1929.

[30] P. Hohenberg and W. Kohn. Inhomogeneous Electron Gas. *Phys. Rev.*, 136:B864–B871, 1964.

[31] W. Kohn and L. J. Sham. Self-Consistent Equations Including Exchange and Correlation Effects. *Phys. Rev.*, 140:A1133–A1138, 1965.

[32] L. Hedin. New Method for Calculating the One-Particle Green's Function with Application to the Electron-Gas Problem. *Phys. Rev.*, 139:A796–A823, 1965.

[33] W. Metzner and D. Vollhardt. Correlated Lattice Fermions in $d = \infty$ Dimensions. *Phys. Rev. Lett.*, 62:324–327, 1989.

[34] F. J. Ohkawa. Electron correlation in the Hubbard model in $d = \infty$ dimension. *J. Phys. Soc. Jpn.*, 60:3218–3221, 1991.

[35] A. Georges and G. Kotliar. Hubbard model in infinite dimensions. *Phys. Rev. B*, 45:6479–6483, 1992.

[36] A. Georges, G. Kotliar, W. Krauth, and M. J. Rozenberg. Dynamical mean-field theory of strongly correlated fermion systems and the limit of infinite dimensions. *Rev. Mod. Phys.*, 68:13–125, 1996.

[37] C. Lanczos. An Iteration Method for the Solution of the Eigenvalue Problem of Linear Differential and Integral Operators. *Journal of Research of the National Bureau of Standards*, 45:255–282, 1950.

[38] J. E. Hirsch and R. M. Fye. Monte Carlo Method for Magnetic Impurities in Metals. *Phys. Rev. Lett.*, 56:2521–2524, 1986.

[39] S. R. White. Density matrix formulation for quantum renormalization groups. *Phys. Rev. Lett.*, 69:2863–2866, 1992.

[40] M. Salmhofer, C. Honerkamp, W. Metzner, and O. Lauscher. Renormalization Group Flows into Phases with Broken Symmetry. *Progress of Theoretical Physics*, 112(6):943–970, 2004.

[41] P. Lykos and G. W. Pratt. Discussion on The Hartree-Fock Approximation. *Rev. Mod. Phys.*, 35:496–501, 1963.

[42] J. Hubbard. Electron correlations in narrow energy bands. *Proc. R. Soc. Lond. A*, 276:238–257, 1963.

[43] M. C. Gutzwiller. Effect of Correlation on the Ferromagnetism of Transition Metals. *Phys. Rev. Lett.*, 10:159–162, 1963.

[44] J. Kanamori. Electron Correlation and Ferromagnetism of Transition Metals. *Prog. Theor. Phys.*, 30(3):275–289, 1963.

[45] R. A. Bari. Effects of Short-Range Interactions on Electron-Charge Ordering and Lattice Distortions in the Localized State. *Phys. Rev. B*, 3:2662–2670, 1971.

[46] F. Dyson. *The Scientist as Rebel*. New York Review Books, 2006.

[47] L. Landau. On the Theory of Phase Transitions. *Zh. Eksp. Teor. Fiz.*, 7:19–32, 1937.

[48] K. G. Wilson. The renormalization group: Critical phenomena and the Kondo problem. *Rev. Mod. Phys.*, 47:773–840, 1975.

[49] K. S. Novoselov, A. K. Geim, S. V. Morozov, D. Jiang, Y. Zhang, S. V. Dubonos, I. V. Grigorieva, and A. A. Firsov. Electric Field Effect in Atomically Thin Carbon Films. *Science*, 306(5696):666–669, 2004.

[50] K. S. Novoselov, A. K. Geim, S. V. Morozov, D. Jiang, M. I. Katnelson, I. V. Grigorieva, S. V. Dubonos, and A. A. Firsov. Two-dimensional gas of massless Dirac fermions in graphene. *Nature*, 438:197–200, 2005.

[51] Y. Cao, V. Fatemi, A. Demir, S. Fang, S. L. Tomarken, J. Y. Luo, J. D. Sanchez-Yamagishi, K. Watanabe, T. Taniguchi, E. Kaxiras, R. C. Ashoori, and P. Jarillo-Herrero. Correlated insulator behaviour at half-filling in magic-angle graphene superlattices. *Nature*, 556:80–84, 2018.

[52] H. W. Kroto, J. R. Heath, S. C. O'Brien, R. F. Curl, and R. E. Smalley. C60: Buckminsterfullerene. *Nature*, 318:162–163, 1985.

[53] G. W. Semenoff. Condensed-Matter Simulation of a Three-Dimensional Anomaly. *Phys. Rev. Lett.*, 53:2449–2452, 1984.

[54] D. P. DiVincenzo and E. J. Mele. Self-consistent effective-mass theory for intralayer screening in graphite intercalation compounds. *Phys. Rev. B*, 29:1685–1694, 1984.

[55] J. J. Su and A. MacDonald. How to make a bilayer exciton condensate flow. *Nature Phys*, 4:799–802, 2008.

[56] A. F. Hebard, M. J. Rosseinsky, R. C. Haddon, D. W. Murphy, S. H. Glarum, T. T. M. Palstra, A. P. Ramirez, and A. R. Kortan. Superconductivity at 18 K in potassium-doped C_{60}. *Nature*, 350:600–601, 1991.

[57] Andel. Eight Allotropes of Carbon. *Wikimedia Commons*, 2019.

[58] E. Schrödinger. An Undulatory Theory of the Mechanics of Atoms and Molecules. *Phys. Rev.*, 28:1049–1070, 1926.

[59] M. Born and J.R. Oppenheimer. On the Quantum Theory of Molecules. *Ann. d. Phys*, 389:457–484, 1927.

[60] J. E. Lennard-Jones. The electronic structure of some diatomic molecules. *Trans. Faraday Soc.*, 25:668–686, 1929.

[61] F. Bloch. Über die Quantenmechanik der Elektronen in Kristallgittern. *Z. Physik*, 52:555–600, 1929.

[62] E. Noether. Invariante Variationsprobleme. *Nachrichten von der Gesellschaft der Wissenschaften zu Göttingen, Mathematisch-Physikalische Klasse*, 235–257, 1918.

[63] G. H. Wannier. The Structure of Electronic Excitation Levels in Insulating Crystals. *Phys. Rev.*, 52:191–197, 1937.

[64] W. Kohn. Analytic Properties of Bloch Waves and Wannier Functions. *Phys. Rev.*, 115:809–821, 1959.

[65] J. D. Cloizeaux. Orthogonal Orbitals and Generalized Wannier Functions. *Phys. Rev.*, 129:554–566, 1963.

[66] N. Marzari, A. A. Mostofi, J. R. Yates, I. Souza, and D. Vanderbilt. Maximally localized Wannier functions: Theory and applications. *Rev. Mod. Phys.*, 84:1419–1475, 2012.

[67] N. Marzari and D. Vanderbilt. Maximally localized generalized Wannier functions for composite energy bands. *Phys. Rev. B*, 56:12847–12865, 1997.

[68] Nanite. Band filling diagram. *Wikimedia Commons*, 2013.

[69] M. Levy. Universal variational functionals of electron densities, first-order density matrices, and natural spin-orbitals and solution of the v-representability problem. *PNAS*, 76 (12):6062–6065, 1979.

[70] E.H. Lieb. Density functionals for coulomb systems. *Int. J. Quantum Chem.*, 24:243–277, 1983.

[71] J. P. Perdew and Y. Wang. Accurate and simple analytic representation of the electron-gas correlation energy. *Phys. Rev. B*, 45:13244–13249, 1992.

[72] M. Taut. Two electrons in an external oscillator potential: Particular analytic solutions of a Coulomb correlation problem. *Phys. Rev. A*, 48:3561–3566, 1993.

[73] J. P. Perdew, K. Burke, and M. Ernzerhof. Generalized Gradient Approximation Made Simple. *Phys. Rev. Lett.*, 77:3865–3868, 1996.

[74] A. D. Becke. A new mixing of Hartree–Fock and local density-functional theories. *J. Chem. Phys.*, 98:1372–1377, 1993.

[75] J. Heyd, G. E. Scuseria, and M. Ernzerhof. Hybrid functionals based on a screened Coulomb potential. *J. Chem. Phys.*, 118:8207–8215, 2003.

[76] J. P. Perdew and K. Schmidt. Jacob's ladder of density functional approximations for the exchange-correlation energy. *AIP Conference Proceedings*, 577:1–20, 2001.

[77] V. N. Strocov, M. Shi, M. Kobayashi, C. Monney, X. Wang, J. Krempasky, T. Schmitt, L. Patthey, H. Berger, and P. Blaha. Three-Dimensional Electron Realm in VSe_2 by Soft-X-Ray Photoelectron Spectroscopy: Origin of Charge-Density Waves. *Phys. Rev. Lett.*, 109:086401, 2012.

[78] J. H. de Boer and E. J. W. Verwey. Semi-conductors with partially and with completely filled 3d-lattice bands. *Proc. Phys. Soc.*, 49:59, 1937.

[79] N. F. Mott and R. Peierls. Discussion of the paper by de Boer and Verwey. *Proc. Phys. Soc.*, 49:72, 1937.

[80] N. F. Mott. The Basis of the Electron Theory of Metals, with Special Reference to the Transition Metals. *Proc. Phys. Soc. A*, 62(7):416–422, 1949.

[81] N. F. Mott. The transition to the metallic state. *Phil. Mag.*, 6:287, 1961.

[82] A. A. Abrikosov, L. P. Gorkov, and I. E. Dzyaloshinski. *Methods of Quantum Field Theory in Statistical Physics*. Dover Publications, 2012.

[83] F. Aryasetiawan, M. Imada, A. Georges, G. Kotliar, S. Biermann, and A. I. Lichtenstein. Frequency-dependent local interactions and low-energy effective models from electronic structure calculations. *Phys. Rev. B*, 70:195104, 2004.

[84] Y. Kamihara, H. Hiramatsu, M. Hirano, R. Kawamura, H. Yanagi, T. Kamiya, and H. Hosono. Iron-Based Layered Superconductor: LaOFeP. *J. Am. Chem. Soc.*, 128(31):10012–10013, 2006.

[85] H. Takahashi, K. Igawa, K. Arii, Y. Kamihara, M. Hirano, and H. Hosono. Superconductivity at 43 K in an iron-based layered compound $LaO_{1-x}F_xFeAs$. *Nature*, 453:376–378, 2008.

[86] D. Li, K. Lee, B.Y. Wang, M. Osada, S. Crossley, H. R. Lee, Yi. Cui, Y. Hikita, and H. Y. Hwang. Superconductivity in an infinite-layer nickelate. *Nature*, 572:624–627, 2019.

[87] K. Andres, J. E. Graebner, and H. R. Ott. $4f$-Virtual-Bound-State Formation in $CeAl_3$ at Low Temperatures. *Phys. Rev. Lett.*, 35:1779–1782, 1975.

[88] F. Steglich, J. Aarts, C. D. Bredl, W. Lieke, D. Meschede, W. Franz, and H. Schäfer. Superconductivity in the Presence of Strong Pauli Paramagnetism: $CeCu_2Si_2$. *Phys. Rev. Lett.*, 43:1892–1896, 1979.

[89] H. v. Löhneysen, T. Pietrus, G. Portisch, H. G. Schlager, A. Schröder, M. Sieck, and T. Trappmann. Non-Fermi-liquid behavior in a heavy-fermion alloy at a magnetic instability. *Phys. Rev. Lett.*, 72:3262–3265, 1994.

[90] N. D. Mathur, F. M. Grosche, S. R. Julian, I. R. Walker, D. M. Freye, R. K. W. Haselwimmer, and G. G. Lonzarich. Magnetically mediated superconductivity in heavy fermion compounds. *Nature*, 394:39–43, 1998.

[91] N. A. Hill. Why are there so few magnetic ferroelectrics? *J. Phys. Chem. B*, 104 (29):6694–6709, 2000.

[92] J. Wang, J. B. Neaton, H. Zheng, V. Nagarajan, S. B. Ogale, B. Liu, D. Viehland, V. Vaithyanathan, D. G. Schlom, U. V. Waghmare, N. A. Spaldin, K. M. Rabe, M. Wuttig, and R. Ramesh. Epitaxial $BiFeO_3$ multiferroic thin film heterostructures. *Science*, 299:719–1722, 2003.

[93] T. Kimura, T. Goto, H. Shintani, K. Ishizaka, T. Arima, and Y. Tokura. Magnetic control of ferroelectric polarization. *Nature*, 426:55–58, 2003.

[94] N. Hur, S. Park, P. Sharma, J. S. Ahn, S. Guha, and S-W. Cheong. Electric polarization reversal and memory in a multiferroic material induced by magnetic fields. *Nature*, 429:392–395, 2004.

[95] B. Van Aken, T. Palstra, A. Filippetti, and N. A. Spaldin. Electric polarization reversal and memory in a multiferroic material induced by magnetic fields. *Nature Materials*, 3:164–170, 2004.

[96] E. H. Lieb and F. Y. Wu. Absence of Mott Transition in an Exact Solution of the Short-Range, One-Band Model in One Dimension. *Phys. Rev. Lett.*, 20:1445–1448, 1968.

[97] Y. Nomura, M. Hirayama, T. Tadano, Y. Yoshimoto, K. Nakamura, and R. Arita. Formation of a two-dimensional single-component correlated electron system and band engineering in the nickelate superconductor $NdNiO_2$. *Phys. Rev. B*, 100:205138, 2019.

[98] M. Kitatani, L. Si, O. Janson, R. Arita, Z. Zhong, and K. Held. Nickelate superconductors—a renaissance of the one-band Hubbard model. *npj Quantum Mater.*, 5:59, 2020.

[99] O.K. Andersen, A.I. Lichtenstein, O. Jepsen, and F. Paulsen. LDA energy bands, low-energy hamiltonians, t', t'', $t_\perp$ (k), and $J_\perp$. *Journal of Physics and Chemistry of Solids*, 56(12):1573–1591, 1995. Proceedings of the Conference on Spectroscopies in Novel Superconductors.

[100] L. F. Feiner, J. H. Jefferson, and R. Raimondi. Effective single-band models for the high-T_c cuprates. I. Coulomb interactions. *Phys. Rev. B*, 53:8751–8773, 1996.

[101] V. V. Mazurenko, I. V. Solovyev, and A. A. Tsirlin. Covalency effects reflected in the magnetic form factor of low-dimensional cuprates. *Phys. Rev. B*, 92:245113, 2015.

[102] E.A. Stepanov, L. Peters, I.S. Krivenko, A.I. Lichtenstein, M.I. Katsnelson, and A.N. Rubtsov. Quantum spin fluctuations and evolution of electronic structure in cuprates. *npj Quant Mater*, 3:54, 2018.

[103] D. Riegler, J. Seufert, E. H. da Silva Neto, P. Wölfle, R. Thomale, and M. Klett. Interplay of spin and charge order in the electron-doped cuprates. page arXiv:2305.08900, 2023.

[104] L.-H. Hu and C. Wu. Two-band model for magnetism and superconductivity in nickelates. *Phys. Rev. Res.*, 1:032046, 2019.

[105] P. Werner and S. Hoshino. Nickelate superconductors: Multiorbital nature and spin freezing. *Phys. Rev. B*, 101:041104, 2020.

[106] F. Lechermann. Multiorbital processes rule the $\mathrm{nd}_{1-x}\mathrm{sr}_x\mathrm{nio}_2$ normal state. *Phys. Rev. X*, 10:041002, 2020.

[107] A. Georges and W. Krauth. Numerical solution of the d=∞ Hubbard model: Evidence for a Mott transition. *Phys. Rev. Lett.*, 69:1240–1243, 1992.

[108] X. Y. Zhang, M. J. Rozenberg, and G. Kotliar. Mott transition in the d=∞ Hubbard model at zero temperature. *Phys. Rev. Lett.*, 70:1666–1669, 1993.

[109] W. F. Brinkman and T. M. Rice. Application of Gutzwiller's Variational Method to the Metal-Insulator Transition. *Phys. Rev. B*, 2:4302–4304, 1970.

[110] H. Park, K. Haule, and G. Kotliar. Cluster Dynamical Mean Field Theory of the Mott Transition. *Phys. Rev. Lett.*, 101:186403, 2008.

[111] L. Xu, P. Kumar, S. V. Buldyrev, S.-H. Chen, P. H. Poole, F. Sciortino, and H. E. Stanley. Relation between the Widom line and the dynamic crossover in systems with a liquid–liquid phase transition. *PNAS*, 102 (46):16558–16562, 2005.

[112] G. Sordi, K. Haule, and A.-M. S. Tremblay. Mott physics and first-order transition between two metals in the normal-state phase diagram of the two-dimensional Hubbard model. *Phys. Rev. B*, 84:075161, 2011.

[113] G. Sordi, P. Sémon, K. Haule, and A.-M. S. Tremblay. Pseudogap temperature as a Widom line in doped Mott insulators. *Sci Rep*, 2:547, 2012.

[114] G. Sordi, P. Sémon, K. Haule, and A.-M. S. Tremblay. *c*-axis resistivity, pseudogap, superconductivity, and Widom line in doped Mott insulators. *Phys. Rev. B*, 87:041101, 2013.

[115] L. Fratino, P. Sémon, M. Charlebois, G. Sordi, and A.-M. S. Tremblay. Signatures of the Mott transition in the antiferromagnetic state of the two-dimensional Hubbard model. *Phys. Rev. B*, 95:235109, 2017.

[116] A. B. Harris and R. V. Lange. Single-Particle Excitations in Narrow Energy Bands. *Phys. Rev.*, 157:295–314, 1967.

[117] L. D. Landau. A possible explanation of the field dependence of the susceptibility at low temperatures. *Phys. Z. Sowjet*, 4:675, 1933.

[118] L. Néel. Propriétés magnétiques des ferrites ; ferrimagnétisme et antiferromagnétisme. *Ann. Phys.*, 12:(3) 137–198, 1948.

[119] J. C. Slater. Magnetic effects and the hartree-fock equation. *Phys. Rev.*, 82:538–541, 1951.

[120] K. Borejsza and N. Dupuis. Antiferromagnetism and single-particle properties in the two-dimensional half-filled hubbard model: Slater *vs*. mott-heisenberg. *Europhysics Letters (EPL)*, 63(5):722–728, 2003.

[121] K. A. Chao, J. Spalek, and A. M. Oles. Kinetic exchange interaction in a narrow S-band. *Journal of Physics C: Solid State Physics*, 10:L271, 1977.

[122] P. C. Hohenberg. Existence of Long-Range Order in One and Two Dimensions. *Phys. Rev.*, 158:383–386, 1967.

[123] N. D. Mermin and H. Wagner. Absence of Ferromagnetism or Antiferromagnetism in One- or Two-Dimensional Isotropic Heisenberg Models. *Phys. Rev. Lett.*, 17:1133–1136, 1966.

[124] M. B. Walker and Th. W. Ruijgrok. Absence of Magnetic Ordering in One and Two Dimensions in a Many-Band Model for Interacting Electrons in a Metal. *Phys. Rev.*, 171:513–515, 1968.

[125] Y.M. Vilk and A.-M.S. Tremblay. Destruction of the fermi liquid by spin fluctuations in two dimensions. *Journal of Physics and Chemistry of Solids*, 56(12):1769–1771, 1995. Proceedings of the Conference on Spectroscopies in Novel Superconductors.

[126] Y.M. Vilk and A.-M.S. Tremblay. Non-Perturbative Many-Body Approach to the Hubbard Model and Single-Particle Pseudogap. *J. Phys. I France*, 102 (46):1309–1368, 1997.

[127] C. Huscroft, M. Jarrell, Th. Maier, S. Moukouri, and A. N. Tahvildarzadeh. Pseudogaps in the 2D Hubbard Model. *Phys. Rev. Lett.*, 86:139–142, 2001.

[128] D. Sénéchal and A.-M. S. Tremblay. Hot Spots and Pseudogaps for Hole- and Electron-Doped High-Temperature Superconductors. *Phys. Rev. Lett.*, 92:126401, 2004.

[129] A.-M. S. Tremblay, B. Kyung, and D. Sénéchal. Pseudogap and high-temperature superconductivity from weak to strong coupling. Towards a quantitative theory (Review Article). *Low Temp. Phys.*, 32(4):424–451, 2006.

[130] A. Macridin, M. Jarrell, T. Maier, P. R. C. Kent, and E. D'Azevedo. Pseudogap and Antiferromagnetic Correlations in the Hubbard Model. *Phys. Rev. Lett.*, 97:036401, 2006.

[131] K. Jin, N. P. Butch, K. Kirshenbaum, J. Paglione, and R. L. Greene. Link between spin fluctuations and electron pairing in copper oxide superconductors. *Nature*, 476:73–75, 2011.

[132] D. Rost, E. V. Gorelik, F. Assaad, and N. Blümer. Momentum-dependent pseudogaps in the half-filled two-dimensional Hubbard model. *Phys. Rev. B*, 86:155109, 2012.

[133] O. Gunnarsson, T. Schäfer, J. P. F. LeBlanc, E. Gull, J. Merino, G. Sangiovanni, G. Rohringer, and A. Toschi. Fluctuation Diagnostics of the Electron Self-Energy: Origin of the Pseudogap Physics. *Phys. Rev. Lett.*, 114:236402, 2015.

[134] W. Wu, M. Ferrero, A. Georges, and E. Kozik. Controlling Feynman diagrammatic expansions: Physical nature of the pseudogap in the two-dimensional Hubbard model. *Phys. Rev. B*, 96:041105, 2017.

[135] W. Wu, M. S. Scheurer, S. Chatterjee, S. Sachdev, A. Georges, and M. Ferrero. Pseudogap and Fermi-Surface Topology in the Two-Dimensional Hubbard Model. *Phys. Rev. X*, 8:021048, 2018.

[136] F. Šimkovic, J. P. F. LeBlanc, A. J. Kim, Y. Deng, N. V. Prokof'ev, B. V. Svistunov, and E. Kozik. Extended Crossover from a Fermi Liquid to a Quasiantiferromagnet in the Half-Filled 2D Hubbard Model. *Phys. Rev. Lett.*, 124:017003, 2020.

[137] T. Schäfer, N. Wentzell, F. Šimkovic, Y.-Y. He, C. Hille, M. Klett, C. J. Eckhardt, B. Arzhang, V. Harkov, F.-M. Le Régent, A. Kirsch, Y. Wang, A. J. Kim, E. Kozik, E. A. Stepanov, A. Kauch, S. Andergassen, P. Hansmann, D. Rohe, Y. M. Vilk, J. P. F. LeBlanc, S. Zhang, A.-M. S. Tremblay, M. Ferrero, O. Parcollet, and A. Georges. Tracking the Footprints of Spin Fluctuations: A Multi-Method, MultiMessenger Study of the Two-Dimensional Hubbard Model. *Phys. Rev. X*, 11:011058, 2021.

[138] V. Harkov, A. I. Lichtenstein, and F. Krien. Parametrizations of local vertex corrections from weak to strong coupling: Importance of the Hedin three-leg vertex. *Phys. Rev. B*, 104:125141, 2021.

[139] G. Sordi, K. Haule, and A.-M. S. Tremblay. Finite Doping Signatures of the Mott Transition in the Two-Dimensional Hubbard Model. *Phys. Rev. Lett.*, 104:226402, 2010.

[140] F. Šimkovic, R. Rossi, A. Georges, and M. Ferrero. Origin and fate of the pseudogap in the doped Hubbard model. page arXiv:2209.09237, 2022.

[141] S. R. White and D. J. Scalapino. Density Matrix Renormalization Group Study of the Striped Phase in the 2D $t - J$ Model. *Phys. Rev. Lett.*, 80:1272–1275, 1998.

[142] Y.-F. Jiang, J. Zaanen, T. P. Devereaux, and H.-C. Jiang. Ground state phase diagram of the doped Hubbard model on the four-leg cylinder. *Phys. Rev. Res.*, 2:033073, 2020.

[143] A. Wietek, Y.-Y. He, S. R. White, A. Georges, and E. M. Stoudenmire. Stripes, Antiferromagnetism, and the Pseudogap in the Doped Hubbard Model at Finite Temperature. *Phys. Rev. X*, 11:031007, 2021.

[144] E. Pavarini, I. Dasgupta, T. Saha-Dasgupta, O. Jepsen, and O. K. Andersen. Band-Structure Trend in Hole-Doped Cuprates and Correlation with T_{cmax}. *Phys. Rev. Lett.*, 87:047003, 2001.

[145] T. Yanagisawa. Kosterlitz–Thouless Transition in Two-Dimensional Hubbard Model Evidenced from Quantum Monte Carlo Calculations of Susceptibilities. *J. Phys. Soc. Jpn.*, 79:063708, 2010.

[146] A. Eberlein and W. Metzner. Superconductivity in the two-dimensional t-t'-Hubbard model. *Phys. Rev. B*, 89:035126, 2014.

[147] E. W. Huang, C. B. Mendl, H.-C. Jiang, B. Moritz, and T. P. Devereaux. Stripe order from the perspective of the Hubbard model. *npj Quant Mater*, 3:22, 2018.

[148] E. W. Huang, R. Sheppard, B. Moritz, and T. P. Devereaux. Strange metallicity in the doped Hubbard model. *Science*, 366(6468):987–990, 2019.

[149] Y. Tang, L. Li, T. Li, Y. Xu, S. Liu, K. Barmak, K. Watanabe, T. Taniguchi, A. H. MacDonald, J. Shan, and K. F. Mak. Simulation of Hubbard model physics in WSe_2/WS_2 moiré superlattices. *Nature*, 579:353–358, 2020.

[150] V. J. Emery. Theory of the quasi-one-dimensional electron gas with strong "on-site" interactions. *Phys. Rev. B*, 14:2989–2994, 1976.

[151] R. T. Scalettar, E. Y. Loh, J. E. Gubernatis, A. Moreo, S. R. White, D. J. Scalapino, R. L. Sugar, and E. Dagotto. Phase diagram of the two-dimensional negative-U Hubbard model. *Phys. Rev. Lett.*, 62:1407–1410, 1989.

[152] R. Micnas, J. Ranninger, and S. Robaszkiewicz. Superconductivity in narrow-band systems with local nonretarded attractive interactions. *Rev. Mod. Phys.*, 62:113–171, 1990.

[153] A. Moreo and D. J. Scalapino. Two-dimensional negative-U Hubbard model. *Phys. Rev. Lett.*, 66:946–948, 1991.

[154] M. Randeria, N. Trivedi, A. Moreo, and R. T. Scalettar. Pairing and spin gap in the normal state of short coherence length superconductors. *Phys. Rev. Lett.*, 69:2001–2004, 1992.

[155] D. J. Scalapino, S. R. White, and S. Zhang. Insulator, metal, or superconductor: The criteria. *Phys. Rev. B*, 47:7995–8007, 1993.

[156] R. R. dos Santos. Spin gap and superconductivity in the three-dimensional attractive Hubbard model. *Phys. Rev. B*, 50:635–638, 1994.

[157] N. Trivedi and M. Randeria. Deviations from Fermi-Liquid Behavior above T_c in 2D Short Coherence Length Superconductors. *Phys. Rev. Lett.*, 75:312–315, 1995.

[158] C. N. Yang. η pairing and off-diagonal long-range order in a Hubbard model. *Phys. Rev. Lett.*, 63:2144–2147, 1989.

[159] Shoucheng Zhang. Pseudospin symmetry and new collective modes of the hubbard model. *Phys. Rev. Lett.*, 65:120–122, 1990.

[160] M. Keller, W. Metzner, and U. Schollwöck. Dynamical Mean-Field Theory for Pairing and Spin Gap in the Attractive Hubbard Model. *Phys. Rev. Lett.*, 86:4612–4615, 2001.

[161] M. Capone, C. Castellani, and M. Grilli. First-Order Pairing Transition and Single-Particle Spectral Function in the Attractive Hubbard Model. *Phys. Rev. Lett.*, 88:126403, 2002.

[162] A. Toschi, M. Capone, and C. Castellani. Energetic balance of the superconducting transition across the BCS—Bose Einstein crossover in the attractive Hubbard model. *Phys. Rev. B*, 72:235118, 2005.

[163] A Toschi, P Barone, M Capone, and C Castellani. Pairing and superconductivity from weak to strong coupling in the attractive Hubbard model. *New J. Phys.*, 7(1):7, 2005.

[164] A. F. Ho, M. A. Cazalilla, and T. Giamarchi. Quantum simulation of the Hubbard model: The attractive route. *Phys. Rev. A*, 79:033620, 2009.

[165] T. Paiva, R. Scalettar, M. Randeria, and N. Trivedi. Fermions in 2D Optical Lattices: Temperature and Entropy Scales for Observing Antiferromagnetism and Superfluidity. *Phys. Rev. Lett.*, 104:066406, 2010.

[166] Q. Chen, J. Stajic, S. Tan, and K. Levin. BCS–BEC crossover: From high temperature superconductors to ultracold superfluids. *Physics Reports*, 412:(1), 1–88, 2005.

[167] A. Privitera, M. Capone, and C. Castellani. Finite-density corrections to the unitary Fermi gas: A lattice perspective from dynamical mean-field theory. *Phys. Rev. B*, 81:014523, 2010.

[168] A. Koga and P. Werner. Low-temperature properties of the infinite-dimensional attractive Hubbard model. *Phys. Rev. A*, 84:023638, 2011.

[169] A. Amaricci, A. Privitera, and M. Capone. Inhomogeneous BCS-BEC crossover for trapped cold atoms in optical lattices. *Phys. Rev. A*, 89:053604, 2014.

[170] A. Tagliavini, M. Capone, and A. Toschi. Detecting a preformed pair phase: Response to a pairing forcing field. *Phys. Rev. B*, 94:155114, 2016.

[171] M. Randeria and E. Taylor. Crossover from Bardeen-Cooper-Schrieffer to Bose-Einstein Condensation and the Unitary Fermi Gas. *Annual Review of Condensed Matter Physics*, 5:209–232, 2014.

[172] L. Del Re, M. Capone, and A. Toschi. Dynamical vertex approximation for the attractive Hubbard model. *Phys. Rev. B*, 99:045137, 2019.

[173] M. Gall, C. F. Chan, N. Wurz, and M. Köhl. Simulating a Mott Insulator Using Attractive Interaction. *Phys. Rev. Lett.*, 124:010403, 2020.

[174] F. C. Zhang, Masao Ogata, and T. M. Rice. Attractive interaction and superconductivity for K_3C_{60}. *Phys. Rev. Lett.*, 67:3452–3455, 1991.

[175] Y. Wang, Z. Chen, T. Shi, B. Moritz, Z.-X. Shen, and T. P. Devereaux. Phonon-Mediated Long-Range Attractive Interaction in One-Dimensional Cuprates. *Phys. Rev. Lett.*, 127:197003, 2021.

[176] V. Meregalli and S. Y. Savrasov. Electron-phonon coupling and properties of doped $BaBiO_3$. *Phys. Rev. B*, 57:14453–14469, 1998.

[177] Z. P. Yin, A. Kutepov, and G. Kotliar. Correlation-Enhanced Electron-Phonon Coupling: Applications of *GW* and Screened Hybrid Functional to Bismuthates, Chloronitrides, and Other High-T_c Superconductors. *Phys. Rev. X*, 3:021011, 2013.

[178] M. Tomczyk, S. Lu, J. P. Veazey, M. Huang, P. Irvin, S. Ryu, H. Lee, C.-B. Eom, C. S. Hellberg, and J. Levy. Electron pairing without superconductivity. *Nature*, 521:196–199, 2015.

[179] G. Cheng, M. Tomczyk, A. B. Tacla, H. Lee, S. Lu, J. P. Veazey, M. Huang, P. Irvin, S. Ryu, C.-B. Eom, A. Daley, D. Pekker, and J. Levy. Tunable Electron-Electron Interactions in $LaAlO_3/SrTiO_3$ Nanostructures. *Phys. Rev. X*, 6:041042, 2016.

[180] M. Tomczyk, G. Cheng, H. Lee, S. Lu, A. Annadi, J. P. Veazey, M. Huang, P. Irvin, S. Ryu, C.-B. Eom, and J. Levy. Micrometer-Scale Ballistic Transport of Electron Pairs in $LaAlO_3/SrTiO_3$ Nanowires. *Phys. Rev. Lett.*, 117:096801, 2016.

[181] G. E. D. K. Prawiroatmodjo, M. Leijnse, F. Trier, Y. Chen, D. V. Christensen, M. von Soosten, N. Pryds, and T. S. Jespersen. Transport and excitations in a negative-U quantum dot at the LaAlO3/SrTiO3 interface. *Nat. Commun.*, 8:395, 2017.

[182] D. van der Marel and G. A. Sawatzky. Electron-electron interaction and localization in d and f transition metals. *Phys. Rev. B*, 37:10674–10684, 1988.

[183] H. U. R. Strand. Valence-skipping and negative-U in the d-band from repulsive local Coulomb interaction. *Phys. Rev. B*, 90:155108, 2014.

[184] T. Esslinger. Fermi-Hubbard Physics with Atoms in an Optical Lattice. *Annu. Rev. Condens. Matter Phys.*, 1(1):129–152, 2010.

[185] D. Mitra, P. Brown, E. Guardado-Sanchez, S. S. Kondov, T. Devakul, D. A. Huse, P. Schauß, and Wa. S. Bakr. Quantum gas microscopy of an attractive Fermi–Hubbard system. *Nature Physics*, 14:173–177, 2018.

[186] T. Hartke, B. Oreg, C. Turnbaugh, N. Jia, and M. Zwierlein. Direct observation of nonlocal fermion pairing in an attractive Fermi-Hubbard gas. *Science*, 381:82–86, 2023.

[187] A. Garg, H. R. Krishnamurthy, and M. Randeria. BCS-BEC crossover at $T = 0$: A dynamical mean-field theory approach. *Phys. Rev. B*, 72:024517, 2005.

[188] M. R. Schafroth, S. T. Butler, and J. M. Blatt. Quasichemical equilibrium approach to superconductivity. *Helv. Phys. Acta*, 30:93–134, 1957.

[189] L. Laloux, A. Georges, and W. Krauth. Effect of a magnetic field on Mott-Hubbard systems. *Phys. Rev. B*, 50:3092–3102, 1994.

[190] V. J. Emery. *Theory of the One-Dimensional Electron Gas*, pages 247–303. Springer US, Boston, MA, 1979.

[191] B. Fourcade and G. Spronken. Real-space scaling methods applied to the one-dimensional extended Hubbard model. I. The real-space renormalization-group method. *Phys. Rev. B*, 29:5089–5095, 1984.

[192] B. Fourcade and G. Spronken. Real-space scaling methods applied to the one-dimensional extended Hubbard model. II. The finite-cell scaling method. *Phys. Rev. B*, 29:5096–5102, 1984.

[193] J. E. Hirsch. Charge-Density-Wave to Spin-Density-Wave Transition in the Extended Hubbard Model. *Phys. Rev. Lett.*, 53:2327–2330, 1984.

[194] Y. Zhang and J. Callaway. Extended Hubbard model in two dimensions. *Phys. Rev. B*, 39:9397–9404, 1989.

[195] J. Callaway, D. P. Chen, D. G. Kanhere, and Q. Li. Small-cluster calculations for the simple and extended Hubbard models. *Phys. Rev. B*, 42:465–474, 1990.

[196] X.-Z. Yan. Theory of the extended Hubbard model at half filling. *Phys. Rev. B*, 48:7140–7147, 1993.

[197] M. Aichhorn, H. G. Evertz, W. von der Linden, and M. Potthoff. Charge ordering in extended Hubbard models: Variational cluster approach. *Phys. Rev. B*, 70:235107, 2004.

[198] B. Davoudi and A.-M. S. Tremblay. Nearest-neighbor repulsion and competing charge and spin order in the extended Hubbard model. *Phys. Rev. B*, 74:035113, 2006.

[199] J. Paki, H. Terletska, S. Iskakov, and E. Gull. Charge order and antiferromagnetism in the extended Hubbard model. *Phys. Rev. B*, 99:245146, 2019.

[200] P. Pudleiner, A. Kauch, K. Held, and G. Li. Competition between antiferromagnetic and charge density wave fluctuations in the extended Hubbard model. *Phys. Rev. B*, 100:075108, 2019.

[201] E. A. Stepanov, V. Harkov, M. Rösner, A. I. Lichtenstein, M. I. Katsnelson, and A. N. Rudenko. Coexisting charge density wave and ferromagnetic instabilities in monolayer InSe. *npj Comput. Mater.*, 8:118, 2022.

[202] M. Vandelli, A. Galler, A. Rubio, A. I. Lichtenstein, S. Biermann, and E. A. Stepanov. Doping-dependent charge- and spin-density wave orderings in a monolayer of Pb adatoms on Si(111). page arXiv:2301.07162, 2023.

[203] T. Ayral, S. Biermann, and P. Werner. Screening and nonlocal correlations in the extended Hubbard model from self-consistent combined *GW* and dynamical mean field theory. *Phys. Rev. B*, 87:125149, 2013.

[204] E. G. C. P. van Loon, A. I. Lichtenstein, M. I. Katsnelson, O. Parcollet, and H. Hafermann. Beyond extended dynamical mean-field theory: Dual boson approach to the two-dimensional extended Hubbard model. *Phys. Rev. B*, 90:235135, 2014.

[205] H. Terletska, T. Chen, and E. Gull. Charge ordering and correlation effects in the extended Hubbard model. *Phys. Rev. B*, 95:115149, 2017.

[206] K. J. Kapcia, S. Robaszkiewicz, M. Capone, and A. Amaricci. Doping-driven metal-insulator transitions and charge orderings in the extended Hubbard model. *Phys. Rev. B*, 95:125112, 2017.

[207] M. Schüler, E. G. C. P. van Loon, M. I. Katsnelson, and T. O. Wehling. First-order metal-insulator transitions in the extended hubbard model due to self-consistent screening of the effective interaction. *Phys. Rev. B*, 97:165135, 2018.

[208] J. Sólyom. The Fermi gas model of one-dimensional conductors. *Adv. Phys.*, 28(2):201–303, 1979.

[209] M. Nakamura. Mechanism of CDW-SDW Transition in One Dimension. *J. Phys. Soc. Jpn.*, 68(10):3123–3126, 1999.

[210] M. Nakamura. Tricritical behavior in the extended Hubbard chains. *Phys. Rev. B*, 61:16377–16392, 2000.

[211] H. Hafermann, E. G. C. P. van Loon, M. I. Katsnelson, A. I. Lichtenstein, and O. Parcollet. Collective charge excitations of strongly correlated electrons, vertex corrections, and gauge invariance. *Phys. Rev. B*, 90:235105, 2014.

[212] E. G. C. P. van Loon and M. I. Katsnelson. The extended Hubbard model with attractive interactions. *J. Phys.: Conf. Ser.*, 1136:012006, 2018.

[213] A. A. Katanin. Extended dynamical mean field theory combined with the two-particle irreducible functional renormalization-group approach as a tool to study strongly correlated systems. *Phys. Rev. B*, 99:115112, 2019.

[214] M. Vandelli, V. Harkov, E. A. Stepanov, J. Gukelberger, E. Kozik, A. Rubio, and A. I. Lichtenstein. Dual boson diagrammatic Monte Carlo approach applied to the extended Hubbard model. *Phys. Rev. B*, 102:195109, 2020.

[215] H. Terletska, S. Iskakov, T. Maier, and E. Gull. Dynamical cluster approximation study of electron localization in the extended Hubbard model. *Phys. Rev. B*, 104:085129, 2021.

[216] E. A. Stepanov, A. Huber, E. G. C. P. van Loon, A. I. Lichtenstein, and M. I. Katsnelson. From local to nonlocal correlations: The Dual Boson perspective. *Phys. Rev. B*, 94:205110, 2016.

[217] E. A. Stepanov, A. Huber, A. I. Lichtenstein, and M. I. Katsnelson. Effective Ising model for correlated systems with charge ordering. *Phys. Rev. B*, 99:115124, 2019.

[218] S. V. Vonsovsky and M. I. Katsnelson. Some types of instabilities in the electron energy spectrum of the polar model of the crystal. I. The maximum-polarity state. *J. Phys. C: Solid State Phys.*, 12(11):2043–2053, 1979.

[219] A.M. Oleś, R. Micnas, S. Robaszkiewicz, and K.A. Chao. Ground state of the half-filled extended Hubbard model beyond the Hartree-Fock approximation. *Phys. Lett. A*, 102(7):323–326, 1984.

[220] M. Schüler, M. Rösner, T. O. Wehling, A. I. Lichtenstein, and M. I. Katsnelson. Optimal Hubbard Models for Materials with Nonlocal Coulomb Interactions: Graphene, Silicene, and Benzene. *Phys. Rev. Lett.*, 111:036601, 2013.

[221] T. Ayral, S. Biermann, P. Werner, and L. Boehnke. Influence of Fock exchange in combined many-body perturbation and dynamical mean field theory. *Phys. Rev. B*, 95:245130, 2017.

[222] S. Robaszkiewicz, R. Micnas, and K. A. Chao. Thermodynamic properties of the extended Hubbard model with strong intra-atomic attraction and an arbitrary electron density. *Phys. Rev. B*, 23:1447–1458, 1981.

[223] A. A. Aligia. Phase diagram of the one-dimensional extended attractive Hubbard model for large nearest-neighbor repulsion. *Phys. Rev. B*, 61:7028–7032, 2000.

[224] E. Dagotto, J. Riera, Y. C. Chen, A. Moreo, A. Nazarenko, F. Alcaraz, and F. Ortolani. Superconductivity near phase separation in models of correlated electrons. *Phys. Rev. B*, 49:3548–3565, 1994.

[225] B. Davoudi and A.-M. S. Tremblay. Non-perturbative treatment of charge and spin fluctuations in the two-dimensional extended Hubbard model: Extended two-particle self-consistent approach. *Phys. Rev. B*, 76:085115, 2007.

[226] Y.-Y. Xiang, X.-J. Liu, Y.-H. Yuan, J. Cao, and C.-M. Tang. Doping dependence of the phase diagram in one-dimensional extended Hubbard model: a functional renormalization group study. *J. Phys. Condens. Matter*, 31(12):125601, 2019.

[227] M. Yao, D. Wang, and Q.-H. Wang. Determinant quantum Monte Carlo for the half-filled Hubbard model with nonlocal density-density interactions. *Phys. Rev. B*, 106:195121, 2022.

[228] W.-C. Chen, Y. Wang, and C.-C. Chen. Superconducting Phases of the Square-Lattice Extended Hubbard Model. page arXiv:2206.01119, 2022.

[229] Ponor. ARPES analyzer cross section. *Wikimedia Commons*, 2020.

[230] R. de L. Kronig. On the Theory of Dispersion of X-Rays. *J. Opt. Soc. Am.*, 12:547–557, 1926.

[231] H. A. Kramers. La diffusion de la lumiere par les atomes. *Atti Cong. Intern. Fisica (Transactions of Volta Centenary Congress) Como*, 2:545–557, 1927.

[232] H. J. Vidberg and J. W. Serene. Solving the Eliashberg equations by means of N-point Padé approximants. *J Low Temp Phys*, 29:179–192, 1977.

[233] O. Gunnarsson, M. W. Haverkort, and G. Sangiovanni. Analytical continuation of imaginary axis data for optical conductivity. *Phys. Rev. B*, 82:165125, 2010.

[234] A. W. Sandvik. Stochastic method for analytic continuation of quantum Monte Carlo data. *Phys. Rev. B*, 57:10287–10290, 1998.

[235] J. Fei, C.-N. Yeh, and E. Gull. Nevanlinna Analytical Continuation. *Phys. Rev. Lett.*, 126:056402, 2021.

[236] R. N. Silver, D. S. Sivia, and J. E. Gubernatis. Maximum-entropy method for analytic continuation of quantum Monte Carlo data. *Phys. Rev. B*, 41:2380–2389, 1990.

[237] M. Jarrell and J. E. Gubernatis. Bayesian inference and the analytic continuation of imaginary-time quantum Monte Carlo data. *Physics Reports*, 269:133–195, 1996.

[238] G. J. Kraberger, R. Triebl, M. Zingl, and M. Aichhorn. Maximum entropy formalism for the analytic continuation of matrix-valued Green's functions. *Phys. Rev. B*, 96:155128, 2017.

[239] J.-H. Sim and M. J. Han. Maximum quantum entropy method. *Phys. Rev. B*, 98:205102, 2018.

[240] P. Curie. Magnetic Properties of Materials at Various Temperatures. *Ann. Chem. Phys.*, 5, 1895.

[241] P. Weiss. Magnetic Properties of Materials at Various Temperatures. *J. Phys.*, 6:661, 1907.

[242] D. R. Hartree. The Wave Mechanics of an Atom with a Non-Coulomb Central Field. *Math. Proc. Camb. Philos. Soc.*, 24:111, 1928.

[243] D. R. Hartree and W. Hartree. Self-consistent field, with exchange, for beryllium. *Proc. R. Soc. Lond. A.*, 150, 1935.

[244] J. C. Slater. The Self Consistent Field and the Structure of Atoms. *Phys. Rev.*, 32:339–348, 1928.

[245] J. C. Slater. Note on Hartree's Method. *Phys. Rev.*, 35:210–211, 1930.

[246] J. C. Slater. A Simplification of the Hartree-Fock Method. *Phys. Rev.*, 81:385–390, 1951.

[247] J. A. Gaunt. A Theory of Hartree's Atomic Fields. *Math. Proc. Camb. Philos. Soc.*, 24:328–342, 1928.

[248] V. A. Fock. Näherungsmethode zur Lösung des quantenmechanischen Mehrkörperproblems. *Z. Physik*, 61:126–148, 1930.

[249] V. A. Fock. Selfconsistent field" mit Austausch für Natrium. *Z. Physik*, 62:795–805, 1930.

[250] J. Jaeckel and C. Wetterich. Flow equations without mean field ambiguity. *Phys. Rev. D*, 68:025020, 2003.

[251] T. Baier, E. Bick, and C. Wetterich. Temperature dependence of antiferromagnetic order in the Hubbard model. *Phys. Rev. B*, 70:125111, 2004.

[252] J. Jaeckel. Understanding the Fierz Ambiguity of Partially Bosonized Theories. page arXiv:0205154, 2002.

[253] R.L. Stratonovich. On a Method of Calculating Quantum Distribution Functions. *Soviet Physics Doklady*, 2:416, 1958.

[254] J. Hubbard. Calculation of Partition Functions. *Phys. Rev. Lett.*, 3:77–78, 1959.

[255] H. J. Schulz. Effective action for strongly correlated fermions from functional integrals. *Phys. Rev. Lett.*, 65:2462–2465, 1990.

[256] J. E. Hirsch. Attractive interaction and pairing in fermion systems with strong on-site repulsion. *Phys. Rev. Lett.*, 54:1317–1320, 1985.

[257] M. Jarrell. Hubbard model in infinite dimensions: A quantum monte carlo study. *Phys. Rev. Lett.*, 69:168–171, 1992.

[258] A. N. Rubtsov, V. V. Savkin, and A. I. Lichtenstein. Continuous-time quantum Monte Carlo method for fermions. *Phys. Rev. B*, 72:035122, 2005.

[259] P. Werner, A. Comanac, L. de' Medici, M. Troyer, and A. J. Millis. Continuous-Time Solver for Quantum Impurity Models. *Phys. Rev. Lett.*, 97:076405, 2006.

[260] E. Gull, A. J. Millis, A. I. Lichtenstein, A. N. Rubtsov, M. Troyer, and P. Werner. Continuous-time Monte Carlo methods for quantum impurity models. *Rev. Mod. Phys.*, 83:349–404, 2011.

[261] M. Caffarel and W. Krauth. Exact diagonalization approach to correlated fermions in infinite dimensions: Mott transition and superconductivity. *Phys. Rev. Lett.*, 72:1545–1548, 1994.

[262] Q. Si, M. J. Rozenberg, G. Kotliar, and A. E. Ruckenstein. Correlation induced insulator to metal transitions. *Phys. Rev. Lett.*, 72:2761–2764, 1994.

[263] O. Sakai and Y. Kuramoto. Application of the numerical renormalization group method to the hubbard model in infinite dimensions. *Solid State Communications*, 89:307–311, 1994.

[264] F. A. Wolf, I. P. McCulloch, O. Parcollet, and U. Schollwöck. Chebyshev matrix product state impurity solver for dynamical mean-field theory. *Phys. Rev. B*, 90:115124, 2014.

[265] F. A. Wolf, A. Go, I. P. McCulloch, A. J. Millis, and U. Schollwöck. Imaginary-Time Matrix Product State Impurity Solver for Dynamical Mean-Field Theory. *Phys. Rev. X*, 5:041032, 2015.

[266] M. Bramberger, B. Bacq-Labreuil, M. Grundner, S. Biermann, U. Schollwöck, S. Paeckel, and B. Lenz. Formation of CuO_2 sublattices by suppression of inter-lattice correlations in tetragonal CuO. *SciPost Phys.*, 14:010, 2023.

[267] A. Erpenbeck, W.-T. Lin, T. Blommel, L. Zhang, S. Iskakov, L. Bernheimer, Y. Núñez Fernández, G. Cohen, O. Parcollet, X. Waintal, and E. Gull. Tensor train continuous time solver for quantum impurity models. *Phys. Rev. B*, 107:245135, 2023.

[268] G. Baym and L. P. Kadanoff. Conservation Laws and Correlation Functions. *Phys. Rev.*, 124:287–299, 1961.

[269] G. Kotliar, S. Y. Savrasov, K. Haule, V. S. Oudovenko, O. Parcollet, and C. A. Marianetti. Electronic structure calculations with dynamical mean-field theory. *Rev. Mod. Phys.*, 78:865–951, 2006.

[270] V. I. Anisimov, A. I. Poteryaev, M. A. Korotin, A. O. Anokhin, and G. Kotliar. First-principles calculations of the electronic structure and spectra of strongly correlated systems: dynamical mean-field theory. *J. Phys. Cond. Matter*, 9:7359, 1997.

[271] S. Sachdev and J. Ye. Gapless spin-fluid ground state in a random quantum Heisenberg magnet. *Phys. Rev. Lett.*, 70:3339–3342, 1993.

[272] Q. Si and J. L. Smith. Kosterlitz-Thouless Transition and Short Range Spatial Correlations in an Extended Hubbard Model. *Phys. Rev. Lett.*, 77:3391–3394, 1996.

[273] O. Parcollet and A. Georges. Non-Fermi-liquid regime of a doped Mott insulator. *Phys. Rev. B*, 59:5341–5360, 1999.

[274] J. L. Smith and Q. Si. Spatial correlations in dynamical mean-field theory. *Phys. Rev. B*, 61:5184–5193, 2000.

[275] R. Chitra and G. Kotliar. Effect of Long Range Coulomb Interactions on the Mott Transition. *Phys. Rev. Lett.*, 84:3678–3681, 2000.

[276] R. Chitra and Gabriel Kotliar. Effective-action approach to strongly correlated fermion systems. *Phys. Rev. B*, 63:115110, 2001.

[277] Q. Si, S. Rabello, K. Ingersent, and J. L. Smith. Locally critical quantum phase transitions in strongly correlated metals. *Nature*, 413:804–808, 2001.

[278] P. Schmidt and H. Monien. Nonequilibrium dynamical mean-field theory of a strongly correlated system. page arXiv:0202046, 2002.

[279] J. K. Freericks, V. M. Turkowski, and V. Zlatić. Nonequilibrium Dynamical Mean-Field Theory. *Phys. Rev. Lett.*, 97:266408, 2006.

[280] H. Aoki, N. Tsuji, M. Eckstein, M. Kollar, T. Oka, and P. Werner. Nonequilibrium dynamical mean-field theory and its applications. *Rev. Mod. Phys.*, 86:779–837, 2014.

[281] P. Sun and G. Kotliar. Extended dynamical mean-field theory and GW method. *Phys. Rev. B*, 66:085120, 2002.

[282] S. Biermann, F. Aryasetiawan, and A. Georges. First-Principles Approach to the Electronic Structure of Strongly Correlated Systems: Combining the *GW* Approximation and Dynamical Mean-Field Theory. *Phys. Rev. Lett.*, 90:086402, 2003.

[283] L. Boehnke, F. Nilsson, F. Aryasetiawan, and P. Werner. When strong correlations become weak: Consistent merging of *GW* and DMFT. *Phys. Rev. B*, 94:201106, 2016.

[284] F. Nilsson, L. Boehnke, P. Werner, and F. Aryasetiawan. Multitier self-consistent GW + EDMFT. *Phys. Rev. Mater.*, 1:043803, 2017.

[285] A. I. Lichtenstein and M. I. Katsnelson. Antiferromagnetism and d-wave superconductivity in cuprates: A cluster dynamical mean-field theory. *Phys. Rev. B*, 62:R9283–R9286, 2000.

[286] G. Kotliar, S. Y. Savrasov, G. Pálsson, and G. Biroli. Cellular Dynamical Mean Field Approach to Strongly Correlated Systems. *Phys. Rev. Lett.*, 87:186401, 2001.

[287] T. Maier, M. Jarrell, T. Pruschke, and M. H. Hettler. Quantum cluster theories. *Rev. Mod. Phys.*, 77:1027–1080, 2005.

[288] M. Harland, M. I. Katsnelson, and A. I. Lichtenstein. Plaquette valence bond theory of high-temperature superconductivity. *Phys. Rev. B*, 94:125133, 2016.

[289] M. H. Hettler, A. N. Tahvildar-Zadeh, M. Jarrell, T. Pruschke, and H. R. Krishnamurthy. Nonlocal dynamical correlations of strongly interacting electron systems. *Phys. Rev. B*, 58:R7475–R7479, 1998.

[290] M. H. Hettler, M. Mukherjee, M. Jarrell, and H. R. Krishnamurthy. Dynamical cluster approximation: Nonlocal dynamics of correlated electron systems. *Phys. Rev. B*, 61:12739–12756, 2000.

[291] K. Aryanpour, M. H. Hettler, and M. Jarrell. Analysis of the dynamical cluster approximation for the Hubbard model. *Phys. Rev. B*, 65:153102, 2002.

[292] G. Rohringer, H. Hafermann, A. Toschi, A. A. Katanin, A. E. Antipov, M. I. Katsnelson, A. I. Lichtenstein, A. N. Rubtsov, and K. Held. Diagrammatic routes to nonlocal correlations beyond dynamical mean field theory. *Rev. Mod. Phys.*, 90:025003, 2018.

[293] A. Toschi, A. A. Katanin, and K. Held. Dynamical vertex approximation: A step beyond dynamical mean-field theory. *Phys. Rev. B*, 75:045118, 2007.

[294] K. Held, A. A. Katanin, and A. Toschi. Dynamical Vertex Approximation: An Introduction. *Prog. Theor. Phys. Suppl.*, 176:117–133, 2008.

[295] A. Galler, P. Thunström, P. Gunacker, J. M. Tomczak, and K. Held. Ab initio dynamical vertex approximation. *Phys. Rev. B*, 95:115107, 2017.

[296] A. Galler, J. Kaufmann, P. Gunacker, M. Pickem, P. Thunström, J. M. Tomczak, and K. Held. Towards ab initio Calculations with the Dynamical Vertex Approximation. *J. Phys. Soc. Jpn.*, 87(4):041004, 2018.

[297] J. Kaufmann, C. Eckhardt, M. Pickem, M. Kitatani, A. Kauch, and K. Held. Self-consistent ladder dynamical vertex approximation. *Phys. Rev. B*, 103:035120, 2021.

[298] T. Ayral and O. Parcollet. Mott physics and spin fluctuations: A unified framework. *Phys. Rev. B*, 92:115109, 2015.

[299] T. Ayral and O. Parcollet. Mott physics and spin fluctuations: A functional viewpoint. *Phys. Rev. B*, 93:235124, 2016.

[300] A. N. Rubtsov, M. I. Katsnelson, and A. I. Lichtenstein. Dual fermion approach to nonlocal correlations in the Hubbard model. *Phys. Rev. B*, 77:033101, 2008.

[301] A. N. Rubtsov, M. I. Katsnelson, A. I. Lichtenstein, and A. Georges. Dual fermion approach to the two-dimensional Hubbard model: Antiferromagnetic fluctuations and Fermi arcs. *Phys. Rev. B*, 79:045133, 2009.

[302] H. Hafermann, G. Li, A. N. Rubtsov, M. I. Katsnelson, A. I. Lichtenstein, and H. Monien. Efficient Perturbation Theory for Quantum Lattice Models. *Phys. Rev. Lett.*, 102:206401, 2009.

[303] S. Iskakov, A. E. Antipov, and E. Gull. Diagrammatic Monte Carlo for dual fermions. *Phys. Rev. B*, 94:035102, 2016.

[304] J. Gukelberger, E. Kozik, and H. Hafermann. Diagrammatic Monte Carlo approach for diagrammatic extensions of dynamical mean-field theory: Convergence analysis of the dual fermion technique. *Phys. Rev. B*, 96:035152, 2017.

[305] S. Brener, E. A. Stepanov, A. N. Rubtsov, M. I. Katsnelson, and A. I. Lichtenstein. Dual fermion method as a prototype of generic reference-system approach for correlated fermions. *Ann. Phys.*, 422:168310, 2020.

[306] A. N. Rubtsov, M. I. Katsnelson, and A. I. Lichtenstein. Dual boson approach to collective excitations in correlated fermionic systems. *Ann. Phys.*, 327(5):1320–1335, 2012.

[307] E. A. Stepanov, E. G. C. P. van Loon, A. A. Katanin, A. I. Lichtenstein, M. I. Katsnelson, and A. N. Rubtsov. Self-consistent dual boson approach to single-particle and collective excitations in correlated systems. *Phys. Rev. B*, 93:045107, 2016.

[308] L. Peters, E. G. C. P. van Loon, A. N. Rubtsov, A. I. Lichtenstein, M. I. Katsnelson, and E. A. Stepanov. Dual boson approach with instantaneous interaction. *Phys. Rev. B*, 100:165128, 2019.

[309] E. A. Stepanov, V. Harkov, and A. I. Lichtenstein. Consistent partial bosonization of the extended Hubbard model. *Phys. Rev. B*, 100:205115, 2019.

[310] V. Harkov, M. Vandelli, S. Brener, A. I. Lichtenstein, and E. A. Stepanov. Impact of partially bosonized collective fluctuations on electronic degrees of freedom. *Phys. Rev. B*, 103:245123, 2021.

[311] E. A. Stepanov, Y. Nomura, A. I. Lichtenstein, and S. Biermann. Orbital Isotropy of Magnetic Fluctuations in Correlated Electron Materials Induced by Hund's Exchange Coupling. *Phys. Rev. Lett.*, 127:207205, 2021.

[312] M. Vandelli, J. Kaufmann, V. Harkov, A. I. Lichtenstein, K. Held, and E. A. Stepanov. Extended regime of metastable metallic and insulating phases in a two-orbital electronic system. *Phys. Rev. Res.*, 5:L022016, 2023.

[313] M. Vandelli, J. Kaufmann, M. El-Nabulsi, V. Harkov, A. I. Lichtenstein, and E. A. Stepanov. Multi-band D-TRILEX approach to materials with strong electronic correlations. *SciPost Phys.*, 13:036, 2022.

[314] X. Cao, T. Ayral, Z. Zhong, O. Parcollet, D. Manske, and P. Hansmann. Chiral d-wave superconductivity in a triangular surface lattice mediated by long-range interaction. *Phys. Rev. B*, 97:155145, 2018.

[315] U. Schollwöck. The density-matrix renormalization group in the age of matrix product states. *Annals of Physics*, 326:96–192, 2011.

[316] S. R. White. Density-matrix algorithms for quantum renormalization groups. *Phys. Rev. B*, 48:10345–10356, 1993.

[317] U. Schollwöck. The density-matrix renormalization group. *Rev. Mod. Phys.*, 77:259–315, 2005.

[318] W. L. McMillan. Ground State of Liquid He^4. *Phys. Rev.*, 138:A442–A451, 1965.

[319] D. Ceperley, G. V. Chester, and M. H. Kalos. Monte Carlo simulation of a many-fermion study. *Phys. Rev. B*, 16:3081–3099, 1977.

[320] R. Blankenbecler, D. J. Scalapino, and R. L. Sugar. Monte Carlo calculations of coupled boson-fermion systems. I. *Phys. Rev. D*, 24:2278–2286, 1981.

[321] E. Gull, P. Werner, O. Parcollet, and M. Troyer. Continuous-time auxiliary-field Monte Carlo for quantum impurity models. *EPL*, 82:57003, 2008.

[322] P. Werner and A. J. Millis. Hybridization expansion impurity solver: General formulation and application to Kondo lattice and two-orbital models. *Phys. Rev. B*, 74:155107, 2006.

[323] F. F. Assaad and T. C. Lang. Diagrammatic determinantal quantum Monte Carlo methods: Projective schemes and applications to the Hubbard-Holstein model. *Phys. Rev. B*, 76:035116, 2007.

[324] N. Prokof'ev and B. Svistunov. Bold Diagrammatic Monte Carlo Technique: When the Sign Problem Is Welcome. *Phys. Rev. Lett.*, 99:250201, 2007.

[325] K. Van Houcke, F. Werner, E. Kozik, N. Prokof'ev, B. Svistunov, M. J. H. Ku, A. T. Sommer, L. W. Cheuk, A. Schirotzek, and M. W. Zwierlein. Feynman diagrams versus Fermi-gas Feynman emulator. *Nature Physics*, 8:366–370, 2012.

[326] K. Van Houcke, E. Kozik, N. Prokof'ev, and B. Svistunov. Diagrammatic Monte Carlo. *Physics Procedia*, 6:95–105, 2010.

[327] R. Rossi, N. Prokof'ev, B. Svistunov, K. Van Houcke, and F. Werner. Polynomial complexity despite the fermionic sign. *EPL*, 118:10004, 2017.

[328] R. Peierls. Model-making in physics. *Cont. Phys.*, 21(1):3–17, 1980.

[329] A. N. Rubtsov. Fluctuating local field method probed for a description of small classical correlated lattices. *Phys. Rev. E*, 97:052120, 2018.

[330] D. Kuznetsova, G. V. Astretsov, and A. N. Rubtsov. Fluctuating local field method for the disordered Ising model. page arXiv:2212.14733, 2022.

[331] A. N. Rubtsov, E. A. Stepanov, and A. I. Lichtenstein. Collective magnetic fluctuations in Hubbard plaquettes captured by fluctuating local field method. *Phys. Rev. B*, 102:224423, 2020.

[332] Y. S. Lyakhova, E. A. Stepanov, and A. N. Rubtsov. Fluctuating local field approach to free energy of one-dimensional molecules with strong collective electronic fluctuations. *Phys. Rev. B*, 105:035118, 2022.

[333] Y. S. Lyakhova and A. N. Rubtsov. Fluctuating local field approach to the description of lattice models in the strong coupling regime. *J. Supercond. Nov. Magn.*, 35:2169–2173, 2022.

[334] E. Linnér, A. I. Lichtenstein, S. Biermann, and E. A. Stepanov. Multichannel fluctuating field approach to competing instabilities in interacting electronic systems. *Phys. Rev. B*, 108:035143, 2023.

[335] E. Linnér, C. Dutreix, S. Biermann, and E. A. Stepanov. Coexistence of s-wave superconductivity and phase separation in the half-filled extended Hubbard model with attractive interactions. *Phys. Rev. B*, 108:205156, 2023.

[336] J. Hubbard. Electron correlations in narrow energy bands III. An improved solution. *Proc. R. Soc. Lond. A*, 281:401–419, 1964.

[337] R. Peierls. On a Minimum Property of the Free Energy. *Phys. Rev.*, 54:918–919, 1938.

[338] N. N. Bogolyubov. On a variational principle in the many-body problem. *Sov. Phys. Dokl.*, 3(2):292–294, 1958.

[339] R. P. Feynman. *Statistical mechanics: A set of lectures*. Reading, Mass: Benjamin/Cummings, 1972.

[340] L. Philoxene, V. H. Dao, and R. Frésard. Spin and charge modulations of a half-filled extended hubbard model. *Phys. Rev. B*, 106:235131, 2022.

[341] N. E. Bickers and D. J. Scalapino. Conserving approximations for strongly fluctuating electron systems. I. Formalism and calculational approach. *Ann. Phys.*, 193(1):206–251, 1989.

[342] N. E. Bickers and S. R. White. Conserving approximations for strongly fluctuating electron systems. ii. numerical results and parquet extension. *Phys. Rev. B*, 43:8044–8064, 1991.

[343] J. R. Engelbrecht, M. Randeria, and C. A. R. Sá de Melo. BCS to Bose crossover: Broken-symmetry state. *Phys. Rev. B*, 55:15153–15156, 1997.

[344] S. N. Klimin, J. Tempere, T. Repplinger, and H. Kurkjian. Collective excitations of a charged Fermi superfluid in the BCS-BEC crossover. *New Journal of Physics*, 25(6):063011, 2023.

[345] E. Linnér and F. Aryasetiawan. Ensemble Green's function theory for interacting electrons with degenerate ground states. *Phys. Rev. B*, 100:235106, 2019.

[346] F. Aryasetiawan. Private communcations.

[347] C. Brouder, G. Panati, and G. Stoltz. Many-Body Green Function of Degenerate Systems. *Phys. Rev. Lett.*, 103:230401, 2009.

[348] J. D. Jorgensen, B. Dabrowski, Shiyou Pei, D. G. Hinks, L. Soderholm, B. Morosin, J. E. Schirber, E. L. Venturini, and D. S. Ginley. Superconducting phase of $La_2CuO_{4+\delta}$: A superconducting composition resulting from phase separation. *Phys. Rev. B*, 38:11337–11345, 1988.

[349] K. Machida. Magnetism in La_2CuO_4 based compounds. *Physica C Supercond.*, 158(1):192–196, 1989.

[350] J. Zaanen and O. Gunnarsson. Charged magnetic domain lines and the magnetism of high-T_c oxides. *Phys. Rev. B*, 40:7391–7394, 1989.

[351] M. Kato, K. Machida, H. Nakanishi, and M. Fujita. Soliton Lattice Modulation of Incommensurate Spin Density Wave in Two Dimensional Hubbard Model -A Mean Field Study-. *J. Phys. Soc. Japan*, 59(3):1047–1058, 1990.

[352] V. J. Emery and S. A. Kivelson. Frustrated electronic phase separation and high-temperature superconductors. *Physica C Supercond.*, 209(4):597–621, 1993.

[353] B. W. Statt, P. C. Hammel, Z. Fisk, S-W. Cheong, F. C. Chou, D. C. Johnston, and J. E. Schirber. Oxygen ordering and phase separation in $La_2CuO_{4+\delta}$. *Phys. Rev. B*, 52:15575–15581, 1995.

[354] M. Fratini, N. Poccia, A. Ricci, G. Campi, M. Burghammer, G. Aeppli, and A. Bianconi. Scale-free structural organization of oxygen interstitials in La_2CuO_{4+y}. *Nature*, 466:841–844, 2010.

[355] N. Poccia, A. Ricci, G. Campi, M. Fratini, A. Puri, D.D. Gioacchino, A. Marcelli, M. Reynolds, M. Burghammer, N.L. Saini, and G. Aeppli. Optimum inhomogeneity of local lattice distortions in La_2CuO_{4+y}. *PNAS*, 109((39)):15685–15690, 2012.

[356] G. Campi, A. Bianconi, N. Poccia, G. Bianconi, L. Barba, G. Arrighetti, D. Innocenti, J. Karpinski, N. D. Zhigadlo, S. M. Kazakov, M. Burghammer, M. v. Zimmermann, M. Sprung, and A. Ricci. Inhomogeneity of charge-density-wave order and quenched disorder in a high-T_c superconductor. *Nature*, 525(7569):359–362, 2015.

[357] J. Wu, O. Pelleg, G. Logvenov, A. T. Bollinger, Y-J. Sun, G. S. Boebinger, M. Vanević, Z. Radović, and I. Božović. Anomalous independence of interface superconductivity from carrier density. *Nature Mater.*, 12(10):877–881, 2013.

[358] T. Misawa, Y. Nomura, S. Biermann, and M. Imada. Self-optimized superconductivity attainable by interlayer phase separation at cuprate interfaces. *Sci. Adv.*, 2(7):e1600664, 2016.

[359] H. Takahashi, K. Igawa, K. Arii, Y. Kamihara, M. Hirano, and H. Hosono. Superconductivity at 43 K in an iron-based layered compound $LaO_{1-x}F_xFeAs$. *Nature*, 453:376–378, 2008.

[360] A. Ricci, N. Poccia, G. Campi, B. Joseph, G. Arrighetti, L. Barba, M. Reynolds, M. Burghammer, H. Takeya, Y. Mizuguchi, Y. Takano, M. Colapietro, N. L. Saini, and A. Bianconi. Nanoscale phase separation in the iron chalcogenide superconductor $K_{0.8}Fe_{1.6}Se_2$ as seen via scanning nanofocused x-ray diffraction. *Phys. Rev. B*, 84:060511, 2011.

[361] M. Bendele, A. Barinov, B. Joseph, D. Innocenti, A. Iadecola, A. Bianconi, H. Takeya, Y. Mizuguchi, Y. Takano, T. Noji, T. Hatakeda, Y. Koike, M. Horio, A. Fujimori, D. Ootsuki, T. Mizokawa, and N. L. Saini. Spectromicroscopy of electronic phase separation in $K_xFe_{2-y}Se_2$ superconductor. *Sci. Rep.*, 4:5592, 2014.

[362] L. Simonelli, T. Mizokawa, M. Moretti Sala, H. Takeya, Y. Mizuguchi, Y. Takano, G. Garbarino, G. Monaco, and N. L. Saini. Temperature dependence of iron local magnetic moment in phase-separated superconducting chalcogenide. *Phys. Rev. B*, 90:214516, 2014.

[363] A. Ricci, N. Poccia, B. Joseph, D. Innocenti, G. Campi, A. Zozulya, F. Westermeier, A. Schavkan, F. Coneri, A. Bianconi, H. Takeya, Y. Mizuguchi, Y. Takano,

T. Mizokawa, M. Sprung, and N. L. Saini. Direct observation of nanoscale interface phase in the superconducting chalcogenide $K_xFe_{2-y}Se_2$ with intrinsic phase separation. *Phys. Rev. B*, 91:020503, 2015.

[364] A. P. Itin and A. I. Neishtadt. Effective Hamiltonians for fastly driven tight-binding chains. *Phys. Lett. A*, 378(10):822 – 825, 2014.

[365] A. P. Itin and M. I. Katsnelson. Effective Hamiltonians for Rapidly Driven Many-Body Lattice Systems: Induced Exchange Interactions and Density-Dependent Hoppings. *Phys. Rev. Lett.*, 115:075301, 2015.

[366] M. Bukov, M. Kolodrubetz, and A. Polkovnikov. Schrieffer-Wolff Transformation for Periodically Driven Systems: Strongly Correlated Systems with Artificial Gauge Fields. *Phys. Rev. Lett.*, 116:125301, 2016.

[367] C. Dutreix and M. I. Katsnelson. Dynamical control of electron-phonon interactions with high-frequency light. *Phys. Rev. B*, 95:024306, 2017.

[368] C. Dutreix, E. A. Stepanov, and M. I. Katsnelson. Laser-induced topological transitions in phosphorene with inversion symmetry. *Phys. Rev. B*, 93:241404(R), 2016.

[369] E. A. Stepanov, C. Dutreix, and M. I. Katsnelson. Dynamical and Reversible Control of Topological Spin Textures. *Phys. Rev. Lett.*, 118:157201, 2017.

[370] V. N. Valmispild, C. Dutreix, M. Eckstein, M. I. Katsnelson, A. I. Lichtenstein, and E. A. Stepanov. Dynamically induced doublon repulsion in the Fermi-Hubbard model probed by a single-particle density of states. *Phys. Rev. B*, 102:220301, 2020.

[371] M. A. Sentef. Light-enhanced electron-phonon coupling from nonlinear electron-phonon coupling. *Phys. Rev. B*, 95:205111, 2017.

[372] E. Berger, P. Valášek, and W. von der Linden. Two-dimensional Hubbard-Holstein model. *Phys. Rev. B*, 52:4806–4814, 1995.

[373] G. Sangiovanni, M. Capone, C. Castellani, and M. Grilli. Electron-Phonon Interaction Close to a Mott Transition. *Phys. Rev. Lett.*, 94:026401, 2005.

[374] P. Werner and A. J. Millis. Efficient Dynamical Mean Field Simulation of the Holstein-Hubbard Model. *Phys. Rev. Lett.*, 99:146404, 2007.

[375] A. Jodorowsky. *The Holy Mountain*. ABKCO Films, 1973.

DOCTORAL SCHOOL

Titre : Fluctuations collectives dans les systèmes de fermions fortement corrélés

Mots clés : Modèles de fermions sur réseau, transitions de phase, corrélations, fluctuations collectives

Résumé : Les systèmes fortement corrélés présentent souvent des diagrammes de phase riches avec différentes phases ordonnées impliquant des degrés de liberté de spin, de charge, d'appariement ou d'orbite. La description théorique de la compétition entre les différentes instabilités dans les systèmes fortement corrélés, qui donne lieu à cette phénoménologie, reste l'un des Saint-Graal de la théorie moderne de la matière condensée. Elle pose un énorme défi de complexité à la fois conceptuelle et informatique, et l'interaction des fluctuations électroniques concurrentes constitue donc un obstacle à la compréhension des diagrammes de phase complexes d'une large gamme de matériaux quantiques corrélés. Cela motive la recherche de méthodes simplifiées pour étudier l'interaction des fluctuations collectives.

Nous présentons une extension multicanal de l'approche du champ fluctuant récemment développée pour les fluctuations collectives concurrentes dans les systèmes électroniques corrélés. La méthode est basée sur une optimisation variationnelle d'une action d'essai qui contient explicitement les paramètres d'ordre des principaux canaux de fluctuation. Elle donne un accès direct à l'énergie libre du système, facilitant la distinction entre les phases stables et métastables du système. Nous appliquons notre approche au modèle de Hubbard étendu, un modèle de réseau fermionique paradigmatique. En utilisant notre technique pour étudier le régime de couplage faible à intermédiaire de l'interaction répulsive, nous constatons qu'elle capture l'interaction de compétition entre la fonction l'onde de densité de charge en compétition et des fluctuations antiferromagnétiques en accord qualitatif avec des méthodes plus coûteuses en termes de calcul. En explorant les régimes attractifs du modèle, nous abordons l'interaction des fluctuations dans les canaux du spin, de la charge et de la supraconductivité. Bien que ce modèle ait été étudié de manière intensive depuis des décennies, notre nouvelle approche nous permet d'identifier une nouvelle phase caractérisée par la coexistence de fluctuations collectives de l'onde s supraconductrice et de la séparation de phase. La nature générale de la théorie proposée, qui permet d'incorporer une grande variété de modes collectifs, en fait un outil prometteur pour l'étude de l'interaction des fluctuations collectives dans les systèmes fermioniques fortement corrélés.

Title : Interplay of collective fluctuations in strongly correlated fermionic systems

Keywords : Fermionic lattice models, phase transitions, correlations, collective fluctuations

Abstract : Strongly correlated systems often display rich phase diagrams exhibiting different ordered phases involving spin, charge, pairing, or orbital degrees of freedom. The theoretical description of the competition between different instabilities in strongly correlated systems giving rise to this phenomenology, remains one of the holy grails of modern condensed matter theory. It poses a tremendous challenge of both conceptual and computational complexity, and thus the interplay of competing electronic fluctuations constitutes a roadblock to the understanding of the complex phase diagrams of a wide range of correlated quantum materials. This motivates the search for constructing simplified methods to study interplaying collective fluctuations.

We introduce a multi-channel extension of the recently developed fluctuating field approach to competing collective fluctuations in correlated electron systems. The method is based on a variational optimization of a trial action that explicitly contains the order parameters of the leading fluctuation channels. It gives direct access to the free energy of the system, facilitating the distinction between stable and metastable phases of the system. We apply our approach to the extended Hubbard model, a paradigmatic fermionic lattice model. Utilising the technique to study weak to intermediate coupling regime of the repulsive interaction, we find it to capture the interplay of competing charge density wave and antiferromagnetic fluctuations with qualitative agreement with more computationally expensive methods. Exploring the attractive regimes of the model, we address the interplay of fluctuations in the spin, charge, and superconducting channels. Despite the fact that this model has been intensively studied for decades, our novel approach allows us to identify a novel phase that is characterised by the coexistence of collective s-wave superconducting and phase separation fluctuations. The general nature of the proposed theory, allowing to incorporate a variety of collective modes, makes it a promising tool for studying the interplay of collective fluctuations in strongly correlated fermionic systems.

Institut Polytechnique de Paris
91120 Palaiseau, France